Electrical excitation of surface plasmons with a scanning tunneling microscope

Tao Wang

Université Paris XI - UFR scientifique d'Orsay

École Doctorale Ondes et Matière

Thèse de doctorat

Discipline : Physique

présentée par

Tao Wang

pour obtenir le grade de Docteur de l'Université Paris XI

Excitation électrique de plasmons de surface avec un microscope à effet tunnel

---

Soutenue le 18 juillet 2012 devant le jury composé de :

M. Renaud Bachelot	rapporteur
M^{me} Elizabeth Boer-Duchemin	(invitée)
M. Fabrice Charra	(invité)
M^{me} Geneviève Comtet	directrice de thèse
M. Yannick De Wilde	rapporteur
M. Christian Girard	examinateur
M. Jean-Jacques Greffet	examinateur
M. Serge Huant	examinateur

Institut des Sciences Moléculaires d'Orsay
Bâtiment 210, 91 405 Orsay

Cette thèse est dédiée à Maman et Papa,
sans lesquels je n'aurais jamais vu le jour.

Fluctuat nec mergitur !

Acknowledgements

First of all, I would like to thank my supervisor Dr. Geneviève Comtet and the group leader Dr Gérald Dujardin. Thank you for giving me the opportunity to conduct my promotion in your group and for all the advice and guidance that you gave me in the last three years. Especially, I really appreciate for the free environment in the group and I really enjoy the free atmosphere during the experiments. The study with you not only broadens my knowledge but also makes me know the methods to do researches.

I would like to thank Dr. Elizabeth Boer-Duchemin. I thank you very much for your carefully and patiently teaching about the AFM and STM. I appreciate for the direct discussions with you. The discussions with you were always very inspiring and they were the breeding ground to develop many new ideas. I also thank you very much for your kindly help in my daily life.

I would like to thank my office mate Dr. Damien Riedel. The discussions with you were always interesting and inspiring. I really learn a lot from the papers you selected and shared and I like the whiteboard in our office. I like very much the badminton and tennis games we played together. Hope we can play again in the future. I also would like to thank Dr. Andrew Mayne and Dr. Eric Le Moal for the help in our experiments.

My colleagues contributed to an enjoyable and inspiring atmosphere over the years. I would like to thank my colleague Yang Zhang, Tamara Ovramenko, Hatem Labidi, Heejun Yang and Benoît Rogez. I really like the boundless discussions with you after lunch and I like the dinners with you. Moreover, I thank Yang for the help in the experiments. I thank Tamara for making the STM tips. I thank Hatem for the liquid nitrogen. I thank Benoît for the software help.

I thank the French ANR (Agence Nationale de la Recherche) which supported my PhD thesis within the Nano-source of Photons (NAPHO) project. The collaboration within the NAPHO project and ARTIST project was a pleasure. I thank Dr. Aurélien Drezet, Dr. Serge Huant and Dr. Joachim Krenn for the understanding of leakage radiation microscopy. I thank Dr. Christian Girard and Dr. Renault Marty for the theoretical understanding of our experiments. I thank Dr. Joachim Krenn for the help of dark field microscopy. I thank Jean-François Motte and Dr. Serge Huant for providing the nanohole samples. I also thank Dr. Wafa Abidi and Dr. Hynd Remita for the synthesis of gold nanoparticles.

I would like to thank my family for their support and their encouragement throughout the years. I had a good time in Paris also because of the friends I met here and with whom I had a lot of fun.

Last but not the least, I thank you for your kindly help when I got illness and I am sorry for my impatience from time to time. I really appreciate for your patience and tolerance.

Abstract

For the first time, using a equipment combining a scanning tunneling microscope (STM) and an inverted optical microscope, we excite and directly image STM-excited broadband propagating surface plasmons on a thin gold film. The STM-excited propagating surface plasmons have been imaged both in real space and Fourier space by leakage radiation microscopy. Broadband localized surface plasmons due to the tip-gold film coupled plasmon resonance have also been detected. Quantitatively, we compare the intensities of STM-excited propagating and localized surface plasmons obtained with different STM tips. We find that the intensity of each plasmon mode can be selectively varied by changing the STM tip shape or material composition. A silver tip produces a high intensity of localized surface plasmons whereas a sharp (radius $<$ 100 nm) tungsten tip produces mainly propagating surface plasmons.

We have investigated the coherence of STM-excited propagating surface plasmons by performing experiments on a 200 nm thick (opaque) gold film punctured by pairs of nanoholes. This work is analogous to Young's double-slit experiment, and shows that STM-excited propagating surface plasmons have a coherence length of 4.7$\pm$0.5 μm. This coherent length is very close to the value 3.7$\pm$1.2 μm expected from the spectrum, which indicates that the spectrum broadening of STM-excited surface plasmons is homogeneous.

We have also studied the in-plane and radiative scattering of STM-excited propagating surface plasmons by gold nanoparticles deposited on a 50 nm thick gold film. In the Fourier space images, interference fringes are observed in the forbidden light region. This interference occurs between STM-excited localized surface plasmons (radiating at large angles from the tip position) and the radiative scattering by the gold nanoparticle of STM-excited propagating surface plasmons. This indicates that STM-excited localized and propagating surface plasmons are different components of the same single plasmon produced by inelastic electron tunneling with the STM tip.

These results not only broaden the understanding about the excitation process of STM-excited surface plasmons but also offer interesting perspectives for the connection between nanoelectronics and nanophotonics.

Keywords:
STM, surface plasmons, coherence, interference, scattering

Résumé

Pour la première fois, en associant un microscope à effet tunnel (STM) et un microscope optique inversé, nous avons imagé les plasmons de surface excités électriquement sur un film d'or avec la pointe d'un STM. Par microscopie de fuite radiative, en observant l'image de l'interface air/or et celle du plan de Fourier associé, nous avons distingué les plasmons propagatifs des plasmons localisés sous la pointe. Les plasmons propagatifs sont caractérisés par une distance de propagation et une direction d'émission en accord avec celles de plasmons propagatifs créés par excitation laser sur des films d'or de mêmes épaisseurs. Les fuites radiatives des plasmons localisés s'étalent jusqu'à l'angle maximum d'observation. Plasmons propagatifs et localisés ont une large bande spectrale dans le visible. Si la pointe est plasmonique (en argent), les plasmons localisés ont une composante supplémentaire due au couplage associé. Pour différents types de pointe, nous avons déterminé les intensités relatives des plasmons localisés et propagatifs. Nous trouvons que chaque mode plasmon (propagatif ou localisé) peut être préférentiellement sélectionné en modifiant le matériau de la pointe et sa forme. Une pointe en argent produit une intensité élevée de plasmons localisés, tandis qu'une pointe fine de tungstène (rayon de l'apex inférieur à 100 nm) produit essentiellement des plasmons propagatifs.

Nous avons étudié la cohérence spatiale des plasmons propagatifs excités par la pointe du STM. Avec un film d'or opaque (épaisseur 200 nm) percé de paires de nanotrous nous avons réalisé une expérience analogue à celle des fentes d'Young. Des franges d'interférences sont observées. La mesure de leur visibilité en fonction de la distance des nanotrous donne une longueur de cohérence des plasmons de 4.7 ± 0.5 μm. Cette valeur, très proche de la valeur 3.7 ± 1.2 μm déduite de la largeur de la distribution spectrale des plasmons, indique que l'élargissement spectral des plasmons propagatifs est homogène.

Nous avons aussi étudié la diffusion des plasmons propagatifs excités par la pointe du STM par des nanoparticules d'or déposées sur un film d'épaisseur 50 nm. Nous observons une diffusion élastique et une diffusion radiative. Des franges d'interférences sont observées dans la région d'émission lumineuse interdite du plan de Fourier, dont la période est inversement proportionnelle à la distance pointe-nanoparticule d'or avec un facteur de proportionnalité égal à la longueur d'onde moyenne des plasmons. Il y a donc interférence entre la radiation des plasmons localisés et la radiation provenant de la diffusion des plasmons propagatifs sur les nanoparticules d'or. Ceci indique que les plasmons localisés et propagatifs excités électriquement par la pointe du STM sont différentes composantes du plasmon unique produit par effet tunnel inélastique avec la pointe du STM.

Ces résultats originaux sur les plasmons créés sur film d'or par un effet tunnel inélastique localisé à l'échelle atomique (i) élargissent la compréhension du processus et (ii) offrent des perspectives intéressantes pour une association de la nanoélectronique et de la nanophotonique.

Mots clés:
STM, plasmons de surface, coherence, interference, diffusion

Contents

Chapter 1

Introduction

1.1 Light emission with a scanning tunneling microscope

The scanning tunneling microscope (STM) was invented in 1982 by Gerd Binnig and Heinrich Rohrer, for which they shared the Nobel prize in physics in 1986. The instrument consists of a sharp metal tip which scans very close ($\leq$ 1nm) to a conducting (or semiconducting) sample surface. When a voltage V is applied between the tip and the sample surface, across the junction, a tunnel junction forms and a tunneling current flows, and this tunneling current is a function of tip position, applied voltage, and the local density of states (LDOS) of the sample.

The first observation of photon emission from a tunnel junction was reported even before the invention of the scanning tunneling microscope. In 1976, Lambe and McCarthy [1, 2] observed that broadband light emission was produced with a planar metal-insulator-metal (MIM) sandwich junction (Al-Al_2O_3-Ag/Au junction) having a roughened Ag external electrode surface or a Au electrode with deposited Ag nanoparticles. They also found a high frequency linear cutoff of the optical spectra that was dependent only upon the applied voltage through the quantum relation: $h\nu_{cutoff} = eV_{applied}$. This was interpreted in terms of inelastic tunneling excitation of surface plasmon modes which were coupled to free photons by scattering on rough metal surface or metal particles.

In 1985 and 1986, Ushioda et al. coupled the surface plasmon modes of a planar MIM (Al-AlO_x-Au) junction excited by inelastic electron tunneling to free photons with a hemicylindrical prism [3, 4]. The light was detected at specific angles, which meant that propagating surface plasmons were excited on the air-Au interface.

The light emission from the STM tunnel junction was first observed by Gimzewski et al. in 1988 [5]. The authors reported isochromatic photon-emission spectra of polycrystalline tantalum and Si(111)-(7 $\times$ 7) at photon energies of 9.5 eV. In 1989, Gimzewski et al. reported the first STM excited light emission spectra of polyscrystalline silver film [6]. Similar to the observations of Lambe and McCarthy in 1976, the high energy threshold of the spectra was found to equal the electron energy with the applied voltage between the tip and the sample $eV_{applied}$. A very interesting phenomenon is that the maximum intensity of the photon emission was at $\approx$1.9 eV and $\approx$2.4 eV, independent of applied voltages. This study suggested that the light emission originates from resonant excitation and radiative decay of localized surface plasmon modes at the silver surface.

In 1991, Berndt et al. reported the first experiment of photon emission from single-crystal surfaces of Ag(111), Au(110) and Cu(111) using the STM in tunnel and field emission modes [7]. Following studies on MIM junctions, they suggested that the light emission from STM tunnel junction originates from the inelastic tunneling process. The inelastic tunneling electrons interact with collective electromagnetic modes and excite a localized surface plasmon between the tip and the sample as shown in figure 1.1 (a). They found that the light emission spectra were sensitive to the cavity size of the tunneling junction, which showed that the localized surface plasmons were not only on the metallic surface, but in the tip-surface gap.

In 1991 and 2010, Takeuchi et al. and Ahamed et al. reported light emission under an STM tip from a gold film deposited on a prism [8, 9]. They detected light both on the tip side (for localized plasmons) and on the prism side (for localized plasmons and leakage radiation of propagating plasmons). Propagating plasmons are recognized by their specific leakage radiation angle.

The schematic diagram of inelastic tunneling is shown in figure 1.1 (b). When the electrons tunnel from the tip to the metal surface, most of them tunnel elastically. However, about 1 in 10^6 electrons tunnel inelastically. The inelastic tunneling electrons lose part of their energy in the tunneling junction and this lost energy turns into the energy of surface plasmons so that inelastic tunneling electrons excite surface plasmons between tip and sample. The lost energy by the inelastic tunneling electron is limited to $eV_{applied}$, so the maximum surface plasmon photon energy $h\nu$ must be lower than this value.

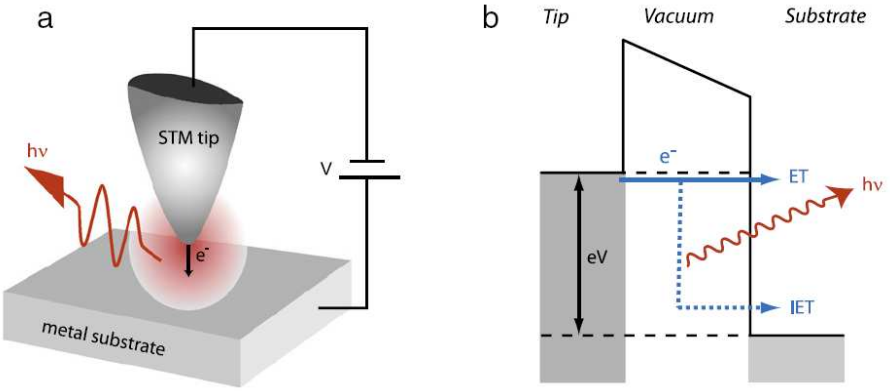

Figure 1.1: (a) The tunneling current in an STM can be used as a nanosource to generate light from the tunnel junction. (b) Schematic potential energy diagram illustrating the mechanism for photon emission in an STM junction. Elastic (ET) and inelastic tunneling (IET) processes are indicated. Inelastic tunneling electrons excite a localized surface plasmon between tip and sample. The photons emitted during the radiative decay of the plasmon may be detected in the far field. [10]

Since these first observations of light emission from the tunnel junctions of a STM, this phenomenon has been reported for a variety of systems, including metal surfaces and nanoparticles, semiconductor surfaces, semiconductor heterostructures and quantum dots, ultrathin dielectric films on metal surfaces, molecules assembled in thin films and even supported single molecules [10]. Benefiting from the atomic scale resolution of the

STM, the STM induced light emission technique provides a powerful method to image and to chemically recognize the constituents of matter down to the molecule and atomic scale optically. This atomic resolution luminescence induced by the tunneling electrons not only reveals the chemical identification of individual molecules [11] or the basic quantum mechanical principle of the tunneling junction [12]but also provides an atomic-scale light emission source.

In my PhD studies, we have optically investigated this atomic-scale light emission source (STM-excited surface plasmons) in the far field. As opposite to previous works, for the first time, we can directly image both the localized and propagating surface plasmons excited with the STM tip by combining a STM with an inverted optical microscope and performing leakage radiation microscopy. We have used this atomic-scale light emission source for nano-optics experiments involving scattering of nanoholes and gold nanoparticles.

1.2 Opportunities and challenges of plasmonics

Benefiting from the ability to manipulate light at the nanoscale, plasmonic research has risen rapidly in the last decade. This manipulation of light consists mainly of the confinement of light to the nanoscale (localized surface plasmons) and the modification of the dispersion relation of light (propagating surface plasmons). The development of nanoscale fabrication techniques (such as electron beam lithography or focused ion beam milling) and nanoparticle synthesis techniques, has opened up new ways to fabricate new metallic structures at the nanoscale. Because of these attributes, plasmonics has found applications in a large range of fields such as sensing, imaging, energy harvesting and waveguiding [13–21].

The light field confined and localized at the surface of metallic structures makes surface plasmons very sensitive to the *local* changes in the permittivity of the surrounding medium. The metallic structures can be thin metal films and stripes, metal nanoparticles, holes, slits, gaps, grooves or corrugations in metal films and so on. By functionalizing the metal surface, molecules can be selectively bound to the surface, shifting the wavelength of the surface plasmons resonance. Because of the large light field confinement and enhancement, single molecules spectroscopy or sensing is also possible [14, 15]. Nowadays, sensors based on the effect of the surface plasmon resonance are commercially available. As the surface plasmons wavelength for a given frequency is shorter than that in air, surface plasmons can be employed to overcome the classical diffraction limit and to be used for nano-scale imaging [17]. The large light confinement can be used to efficiently trap and concentrate sunlight, so the absorption in photovoltaic devices is largely improved. This improvement may permit a considerable reduction in the physical thickness of solar photovoltaic absorber layers and may reduce the price of the solar cells in the future [16, 21]. The modification of dispersion relation of light at the metallic structures makes surface plasmons guided in metallic structures such as thin metal films and stripes, nanowires, and nanoparticles arrays. The waveguiding properties make surface plasmons very useful for integrating optics at nano-scale, especially for the energy and information transfer beyond the diffraction limit[13, 14, 18–20].

Despite these advances and useful applications in the field of plasmonics, there are still

important open questions and problems. For example: how can plasmons be efficiently excited with nano-scale resolution? So far, the excitation of surface plasmons is mostly performed using far-field optical techniques which have a resolution that is larger than plasmonic phenomena under investigation and using near-field optical techniques (e.g., scanning near-field optical microscopy) which have a better resolution for both excitation of SPP and detection of SPP [22–25]. However, for true nano-scale plasmonic studies a point source of surface plasmons with nano-scale dimensions is required. In recent years, high energy electron beams(>30keV) have been used to excite surface plasmons thus reducing the excitation source size down to the nanometer scale [26–30], but the high energy electron beams generators are usually large and not easy to couple to the traditional optical microscope. The high energy electron beams are not compatible with low-voltage electronic devices, so the application is limited. Also, the high energy electron beams should be used in high vacuum ($\leq 10^{-6}$mbar), which is another drawback for future application. So can we find a way to excite surface plasmons very locally and truly at the nano-scale, while easier combining with the traditional optical microscope?

1.2.1 Optical nano-antenna

In recent years, a technique, closely related to plasmonics, named "optical antenna" has attracted much attention [31–39]. Antenna techniques are well known in traditional electrical engineering fields. The antenna are used to emit and receive radiowaves or microwave signals so energy or information can be transmitted through transmission lines from one place to another. Now, antennas are pervasive in almost all areas of modern technology, ranging from satellite communications to cell phones and the design of antennas to control electromagnetic fields on the subwavelength scale is well-established. The objective of optical antenna design is equivalent to that of classical antenna design: to optimize the energy transfer between a localized source or receiver and the free-radiation field, and optical antenna can be looked as an extended concept of antenna to the optical frequency range. Optical antenna techniques provide emerging applications in photodetection, photovoltaics, nano-imaging, nonlinear signal conversion, information processing and among others [39].

One challenge for optical antenna is “electro-optical transduction" [39]. In the traditional radiofrequency and microwave regime, antennas are usually used to convert electric currents into electromagnetic radiation, and vice versa. However, most of the optical antennas studied so far operate on a “light-in, light-out" basis. A mean for electro-optical transduction is vital. One possible way for optical antenna assisted electro-optical transduction can be inspired from STM induced light emission experiments, especially the STM-excited surface plasmons experiments. Although there are problems such as low “electro-optical transduction” efficiency, it can be expected that electro-optical antennas based on electron-plasmon coupling with a scanning tunneling microscope will be a promising choice for optical antenna in the near future [39].

1.3 Outline of this thesis

This thesis focuses on the fundamental understanding of surface plasmons excited with a scanning tunneling microscope and also gives several typical applications.

In Chapter 2, we give a general theoretical background of surface plasmons. We discuss the dispersion relations of surface plasmons polaritons on a gold film with different gold film thicknesses. We also discuss the basic principle of leakage radiation microscopy. In Chapter 2, we also introduce the dipole radiation near an air-dielectric interface and air-gold film interface. The angular distribution of the dipole radiation is discussed. In Chapter 2, we also present our experimental setup and the general experimental techniques.

In Chapter 3, we show that propagating surface plasmons can be excited with the STM on a thin gold film. In the Fourier space (back focal plane), the plasmons peaks which related to the propagating surface plasmons are clearly seen. There are also localized surface plasmons excited under the STM which are attributed to a tip-gold film coupled plasmon resonance.

In Chapter 4, we demonstrate that the sizes and materials of the STM tips have effects on the STM-excited surface plasmons on gold films. The size and material of the STM tip both have effects on the relative ratio between the propagating surface plasmons intensity to the total intensity (I_{SPP}/I_{total}). In our experiments, the sharpest W tip has the highest ratio of I_{SPP}/I_{total}. The spectra of electrically excited surface plasmons does not depend on the tip shapes. However, the spectra have a blue shift when the gold film thickness increases.

In Chapter 5, we present experiments involving the STM-excited surface plasmons scattered by nanoholes in thick (opaque) gold films. In both real space images and Fourier space images, we see that the STM excited surface plasmons are scattered by nanoholes along the tip-nanohole direction. In the experiments with a nanohole pair (double holes), interference fringes are seen in Fourier space (back focal plane). By changing the separation between the nanoholes, the coherent length of STM-excited surface plasmons is measured at 4.7$\pm$0.5 μm. This coherent length is very close to the value estimated from the spectrum 3.7$\pm$1.2 μm, which indicates that the spectrum broadening of STM-excited surface plasmons is homogeneous.

In Chapter 6, we present experiments involving the STM-excited surface plasmons scattered by gold nanoparticles deposited on thin gold films. In real space images, we record both the in-plane (elastic) scattering and the radiative (out of plane) scattering of STM-excited surface plasmons by the gold nanoparticles. In Fourier space images, we see the interference between the radiative scattering of STM-excited propagating surface plasmons by the gold nanoparticles and STM-excited localized surface plasmons under the STM tip, which indicates that STM-excited propagating and localized surface plasmons are coherent.

Chapter 7 gives the conclusions and future prospects.

This thesis gives an overview of the opportunities that the STM technique provides for the field of plasmonics. The presented results show that inelastic tunneling electrons can be used to excite propagating SPP on an atomic scale. Our work provides a new way to generate a nano-scale photon source for nano-scale energy transfer. These insights can

lead to novel applications of surface plasmons in (bio-)sensing or addressing, nano-scale optical integrated circuits, opto-electronic integration and electro-optical nano-antenna techniques.

Chapter 2

Theoretical Background and Experimental Techniques

2.1 Surface plasmons

2.1.1 Optical constant of gold films

The optical properties of metals can be described by a complex dielectric function that depends on the frequency of light. The properties are determined mainly by two facts: first, the electrons can move freely within the bulk of material and second, interband excitations can occur if the photon energy exceeds the bandgap energy of the respective metals [40].

It is well known that the free electrons in metals are modeled in the "Drude-Sommerfeld model" as a free electron gas. In the low photon energy region, the "Drude-Sommerfeld model" fits well with the dielectric function of gold. But in the high photon energy region where the interband transitions may occur, the "Drude-Sommerfeld model" is no longer valid and a "Lorentz" term describing the damping of bound electrons should be added. We can thus use the "Drude-Lorentz model" to fit the dielectric function of gold.

The Drude-Lorentz model for gold is written as [41]:

$$\varepsilon_{gold}(\omega) = \varepsilon_r - \frac{\omega_p^2}{\omega(\omega + i\gamma)} - \frac{\Delta\varepsilon * \Omega^2}{\omega^2 - \Omega^2 + i\omega\Gamma} \tag{2.1}$$

with ε_r=5.967 (relative dielectric constant considering both bound and free electrons), ω_p=8.729 eV (bulk plasma frequency), γ=0.065 eV (bulk plasma damping), Γ=0.433 eV (interband transition damping), Ω=2.684 eV (interband transition frequency) and $\Delta\varepsilon$=1.09 (interband transition dielectric constant displacement).

In equation 2.1, the first two terms are the "Drude-Sommerfeld model" term and the last term is the "Lorentz" term which relates to an interband transition.

Figure 2.1 plots the dielectric constant (real and imaginary parts) of gold as a function of wavelength. The blue dots show the data taken from the paper of Johnson and Christy [42] and the black lines show the Drude-Lorentz model curves from equation 2.1. For wavelengths above 500 nm the behavior clearly follows the Drude-Lorentz theory. For wavelengths below 500 nm obviously interband transitions become significant. Because in

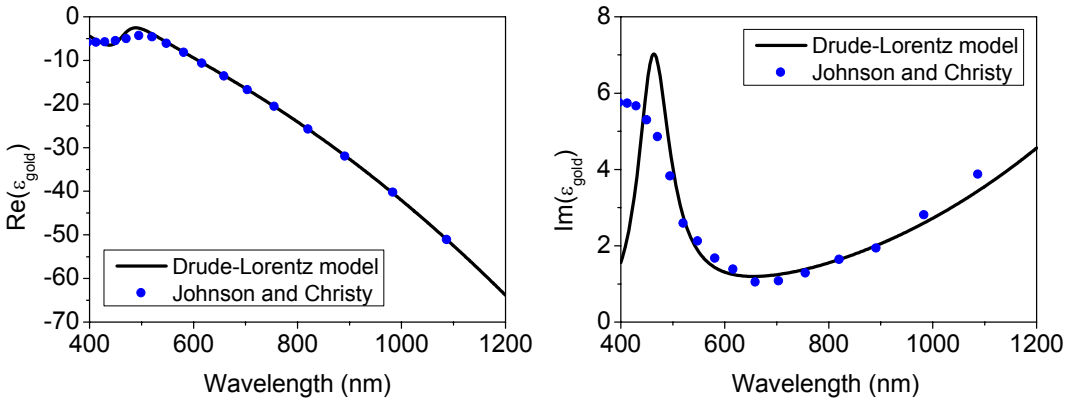

Figure 2.1: Optical constants of gold as a function of the wavelength. The real part and imaginary part of the optical constants are drawn in black lines based on equation 2.1 separately. The experimental data from Johnson and Christy [42] are plotted as blue dots.

equation 2.1 only one interband transition is taken into account, the model curves still fail to reproduce the data below 500 nm [40].

2.1.2 Surface plasmon polaritons

Surface plasmons are collective surface charges oscillation that exist at a metal-dielectric interface. When surface plasmons couple with photons, the resulting hybridized excitation is called surface plasmon polaritons (SPP or SPPs). These SPPs can propagate along the metal surface until energy is lost either via internal absorption in the metal or radiation damping [43]. The propagating SPP wave has the properties of a transverse magnetic (TM) electromagnetic field. The elementary propagating SPP wave can be written as:

$$E_d(x,z,t) = E_{d,0}\, e^{ik_x x} e^{ik_{z_0} z} e^{-i\omega t}; \qquad E_m(x,z,t) = E_{m,0}\, e^{ik_x x} e^{ik_{z_1} z} e^{-i\omega t} \tag{2.2}$$

where E_d, the field in the dielectric, E_m, the field in the metal and $k_{SPP} = k_x = k_x^{'} + k_x^{''}$ is the in-plane wave vector of the SPP propagating in the x direction along the interface. $k_{zj} = \pm\sqrt{k_j^2 - k_x^2}$ are the wave vectors in the medium j= [0 (dielectric),1 (metal)] along the direction z normal to the interface (the conventions for the axes x and z can be seen in figure 2.3(b)). By applying boundary conditions to the Maxwell's equations, we can deduce the dispersion relation of the propagating SPP [40, 43, 44]:

$$k_{z0}/\varepsilon_d - k_{z1}/\varepsilon_m = 0 \tag{2.3}$$

which implies:

$$k_{SPP} = k_x = \frac{\omega}{c}\sqrt{\frac{\varepsilon_d \varepsilon_m}{\varepsilon_d + \varepsilon_m}} \tag{2.4}$$

where ε_d and ε_m are the permittivity of the dielectric medium and the metal respectively. Because the permittivity of the metal is complex, the k_x is also complex with real and imaginary parts. The real part of k_x gives the dispersion relation of the SPP waves propagating along the dielectric/metal interface and the imaginary part of k_x is involved

in the field decay of the SPP waves propagating along the dielectric/metal interface and is related to the propagation length of SPP waves.

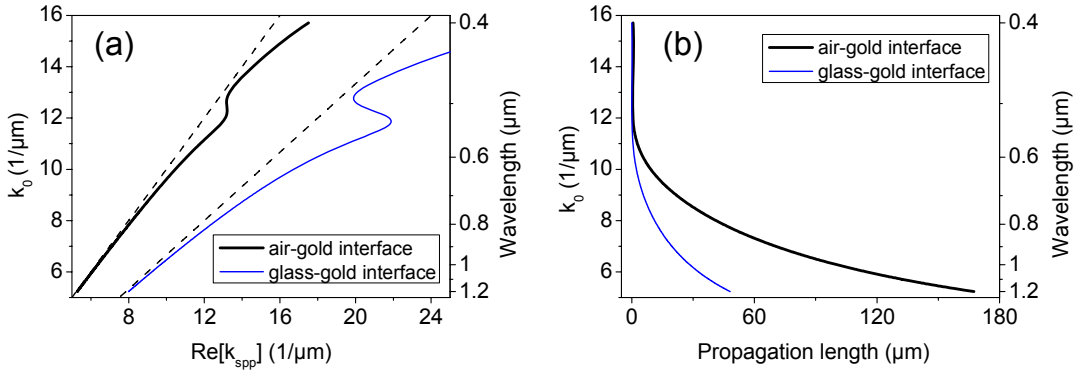

Figure 2.2: (a) Dispersion relation of SPP waves propagating along the air/gold (thick black curve) and glass/gold (thin blue curve) interfaces. (b) Propagation length of SPPs along the air/gold (thick black curve) and glass/gold (thin blue curve) interfaces.

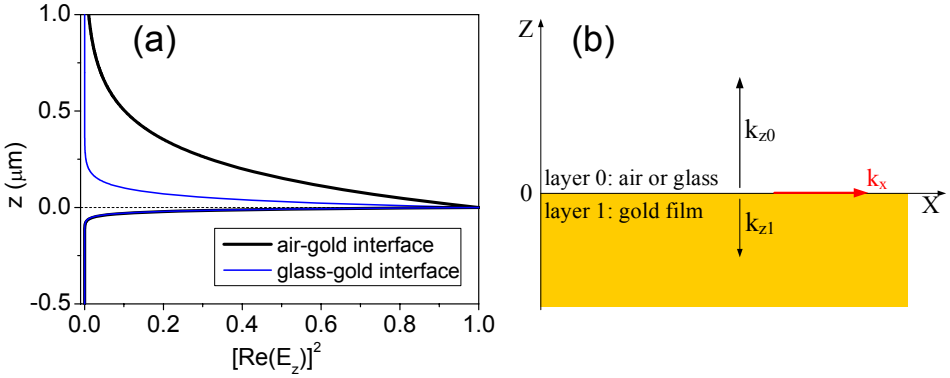

Figure 2.3: (a) Intensity distribution of the SPP field $Re[E_z]$ along the z direction across an air/gold (black thick line) and glass/gold (blue thin line) interface. The optical wavelength considered is $\lambda = 700$ nm. The permittivity of glass is taken to be 2.25. (b) shows the conventions for the x and z axes. The arrows indicate the direction of the real part of the wave vectors normal and parallel to the interface.

Figure 2.2(a) gives the dispersion relation curves of SPP waves along an air (ε_d=1)/gold (thick black curve) and glass (ε_d=2.25)/gold (thin blue curve) interface ((ε_m=ε_{gold}=$\varepsilon_{gold}(\omega)$ in equation 2.1). A very important point is that the air/gold dispersion curve is located inside of the light cone for glass defined by $K = (\omega/c)n_{glass}$ where K is a real light wave vector and n_{glass}=1.5, so according to the coupling condition the SPP propagating along the air/gold interface can radiate into the glass medium if the x component of the wave vector of the radiative light in glass medium is equal to the in-plane wave vector of the SPP (this is called leakage radiation and a more detailed discussion may be found in section 2.1.4). Similarly we know that the SPPs propagating along either interface cannot radiate into the air side and the SPPs along the glass/gold interface cannot radiate into

the glass medium.

Figure 2.2(b) presents the propagation length of SPP along the air/gold and glass/gold interfaces for different wavelengths. The intensity of SPP propagating along the interfaces exponentially decreases as $e^{-2Im(k_x)x}$, so the propagation length is defined as:

$$L_{SPP} = \frac{1}{2Im(k_x)} \tag{2.5}$$

From figure 2.2(b) we see that the propagation length L_{SPP} increases when the SPP wavelength increases. We also see that at the same wavelength, the propagation length along air/gold interface is always larger than the propagation length along glass/gold interface.

Another important parameter is the k_{zj}. From the equation above we can get: $k_{zj} = (\omega/c)\sqrt{\varepsilon_j^2/(\varepsilon_0 + \varepsilon_1)}$ with j= [0(dielectric),1(metal)]. On the air-gold interface, the permittivity of gold is complex and the real part is negative, and the absolute value of the real part is much larger than the absolute value of the imaginary part. So the k_{zj} can be considered as a pure imaginary number. This pure imaginary wave vector indicates that the SPP cannot propagate along the z direction and the SPP wave exponentially decays along z direction. The decay length of the SPP $field$ along z direction is defined as $1/Im[k_{zj}]$ [43] and the decay length of the SPP *intensity* along the z direction can be defined as $1/2Im[k_{zj}]$.

Figure 2.3(a) gives the intensity distribution of the SPP field $Re[E_z]$ along the z direction across an air/gold (black thick line) and glass/gold (blue thin line) interface. It is clear that the decay length of the SPP intensity along the z direction is much longer in the dielectric medium than in the metal. The decay length of the SPP intensity in the metal medium does not vary so much between the air/gold interface and the glass/gold interface, and at $\lambda = 700$ nm, the decay length (also called skin depth) in gold is ≈13nm. On the other hand, the decay length of the SPP intensity in the dielectric medium varies quite a bit between air and glass. At $\lambda = 700$ nm, the decay length of the SPP intensity along the z direction is ≈220nm in air and ≈44nm in glass.

From the discussion above we see that the energy of the SPP is well confined to the dielectric-metal surface and propagates along the interface. The SPPs wavevector in the x direction, k_x, indicates how the SPP propagate along the dielectric-metal interface. The real part of k_x presents the dispersion relation of the SPP and imaginary part of k_x defines the propagation length L_{SPP}. The SPP wavevector in the z direction, k_{zj}, shows how the SPP energy is confined along the z direction.

2.1.3 Dispersion relation of gold films

In the last subsection we discussed the SPP dispersion properties for a dielectric-metal interface. In practice, we make the sample by depositing a thin metal film on a glass substrate, so the sample is a dielectric-metal-dielectric sandwich structure with a finite metal film thickness. The SPP dispersion relation of this sandwich structure is very important.

To calculate this SPP dispersion relation, we follow the method proposed by H. Raether [43] and A. Drezet [44]. In this method, we try to find the zeros of the denominator of the Fresnel reflectivity coefficient for a TM wave (p-polarized) coming from the

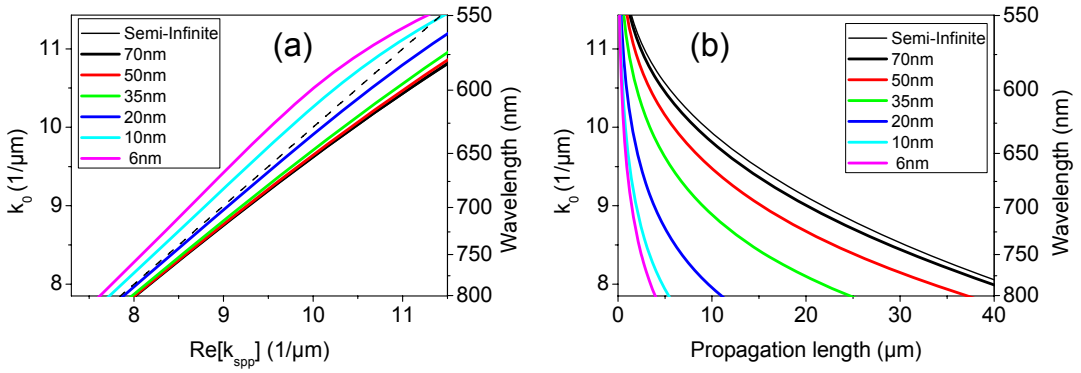

Figure 2.4: (a) Dispersion relation of SPP waves propagating along air/gold interface with different gold film thicknesses and (b) The propagating length of SPP waves propagating along air/gold interface with different gold film thicknesses and with different wavelengths.

dielectric side. For example, on the dielectric-metal (0-1) structure the Fresnel reflectivity coefficient for a TM wave from the dielectric side is [43, 44]:

$$r^p_{0,1} = \frac{k_{z0}/\varepsilon_0 - k_{z1}/\varepsilon_1}{k_{z0}/\varepsilon_0 + k_{z1}/\varepsilon_1} \tag{2.6}$$

where $k_{zj} = \pm\sqrt{k_j^2 - k_x^2}$ are still the wave vectors in the medium j= [0 (dielectric),1 (metal)] along the direction z normal to the interface. We see the denominator is exactly the same as equation 2.3. In the same way, we define the Fresnel coefficient of the glass-gold-air (2-1-0) sandwich structure for a TM wave from the glass side as [40, 43, 44]:

$$r^p_{2,1,0} = \frac{r^p_{2,1} + r^p_{1,0}\, e^{2ik_{z1}d}}{1 + r^p_{2,1} r^p_{1,0}\, e^{2ik_{z1}d}} \tag{2.7}$$

where d is the gold film thickness. To find the zeros of the denominator and get the dispersion relation, we solve the equation:

$$r^p_{2,1} + r^p_{1,0}\, e^{2ik_{z1}d} = 0 \tag{2.8}$$

From this equation it follows:

$$\left(\frac{k_{z2}/\varepsilon_2 - k_{z1}/\varepsilon_1}{k_{z2}/\varepsilon_2 + k_{z1}/\varepsilon_1}\right) + \left(\frac{k_{z1}/\varepsilon_1 - k_{z0}/\varepsilon_0}{k_{z1}/\varepsilon_1 + k_{z0}/\varepsilon_0}\right) e^{2ik_{z1}d} = 0 \tag{2.9}$$

with $k_{zj} = \pm\sqrt{k_j^2 - k_x^2}$ as the wave vectors in the medium j= [0 (air),1 (gold),2 (glass)] along the direction z normal to the interface. By solving the equation (2.9)[1], we get the SPP dispersion relations for different gold film thicknesses as shown in Figure 2.4. From Figure 2.4 we see that the dispersion curves for the 70 nm thick gold film is nearly the same as the dispersion curve of a semi-infinite gold film. When the gold film thickness decreases, the dispersion curve turns towards the light line. When the gold film thickness is smaller than 20 nm, the dispersion curve jumps to the left side of the light line which indicates the light along the air-gold interface can radiate into the far field and there is no SPP bound on the interface.

[1] In order to solve the equation, we follow the method by H. Raether [43], page 120-121

2.1.4 Leakage radiation microscopy

In the last section we discussed how SPPs propagate on gold films of different thicknesses. In this section, we will discuss how to image the SPP which propagates on gold films.

Having been studied for more than ten years [44, 45], leakage radiation microscopy (LRM) is a very useful optical far-field method allowing the direct imaging of propagating SPP on thin metal films. The LRM is easy to set up: a standard epifluorescence microscope with an oil objective(numerical aperture(NA) larger than 1) is sufficient. Compared to near field optical techniques, with LRM one can directly obtain the two-dimensional SPP image without scanning point by point, so the imaging speed is more rapid. Normally in LRM one records the two-dimensional SPP image on a CCD camera. With accessory optical elements, the LRM can be used for both the direct space imaging and reciprocal space (k-space) imaging of the propagating SPP. Because LRM is a far field imaging technique, the optical resolution of LRM is limited by the diffraction of the optical microscope.

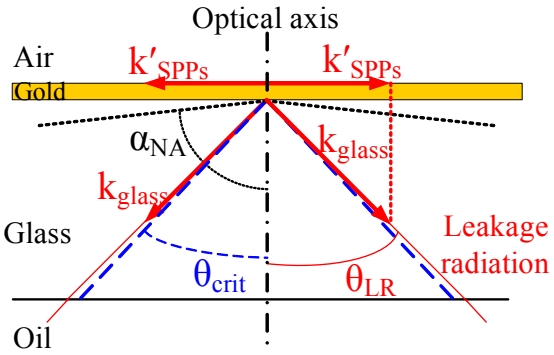

Figure 2.5: Principle of leakage radiation.

Figure 2.5 presents the principle of leakage radiation. On the air-gold interface this k'_{SPP} is the real part of the in-plane wavenumber of the propagating SPP and in the glass medium k_{glass} is the wavenumber of the leakage radiation light. The leakage radiation relation can be written as:

$$Real[k_{SPP}(\omega)] = k_{glass} sin(\theta_{LR}) = nk_0(\omega) sin(\theta_{LR}) \tag{2.10}$$

with n the refractive index of the glass substrate, θ_{LR} the leakage angle and k_0 the wavevector in free space. Because of the dispersion relation, the leakage angle θ_{LR} also depends on the light angular frequency ω. From the dispersion relation shown in figure 2.2 and figure 2.4, we know that the $Real[k_{SPP}(\omega)]$ is larger than $k_0(\omega)$, so if we define $\theta_{critical}$ as the critical angle at the glass/air interface ($nsin(\theta_{critical}) = 1$), we get:

$$nsin(\theta_{LR}) = Real[k_{SPP}(\omega)]/k_0(\omega) > 1; \qquad \theta_{LR} > \theta_{critical} \tag{2.11}$$

This is a very important relation for leakage radiation microscopy. From this relation, we know that in order to get leakage radiation images we need an oil objective with an NA larger than 1. Using an air objective we cannot get leakage radiation images.

To understand more about leakage radiation, we study the electric field distribution in the air-gold-glass (0-1-2) sandwich structure (figure 2.6(b)). As it is well known for waveguide structures [40, 44, 46], we write the SPP waves in the three layers as:

$$\begin{aligned} E_0(x,z,t) &= \gamma e^{ik_x x} e^{ik_{z0}(z-d)} e^{-i\omega t} \\ E_1(x,z,t) &= e^{ik_x x}[\alpha sin(k_{z1}z) + \beta cos(k_{z1}z)] e^{-i\omega t} \\ E_2(x,z,t) &= e^{ik_x x} e^{ik_{z2}z} e^{-i\omega t} \end{aligned} \tag{2.12}$$

with

$$\begin{aligned} \alpha &= i\frac{k_{z2}\varepsilon_1}{k_{z1}\varepsilon_2} \\ \beta &= 1 \\ \gamma &= i\frac{k_{z2}\varepsilon_1}{k_{z1}\varepsilon_2} sin(k_{z1}d) + cos(k_{z1}d) \end{aligned} \tag{2.13}$$

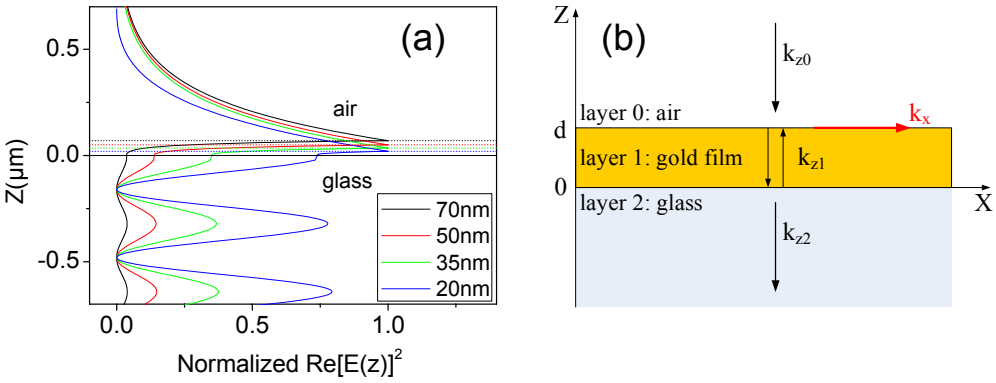

Figure 2.6: (a) Electric field intensity transmission of a propagating SPP mode leaking through gold films of different thicknesses (medium 1) from the air side (medium 0) to the glass side (medium 2). The evolution is represented along the Z axis (the direction normal to the interfaces) at x=0. The optical wavelength considered is λ = 700 nm. The horizontal lines show the interfaces of different gold films. The electric field intensity $\mathrm{Re}[E(z)]^2$ is normalized to $\mathrm{Re}[E(d)]^2$ for each sample of gold film thickness d. (b) shows the conventions for the x and z axes. The arrows indicate the direction of the real part of the wave vector normal and parallel to the interface.

Figure 2.6(a) shows the electric field intensity $\mathrm{Re}[E(z)]^2$ associated with a propagating SPP mode leaking through gold films of different thicknesses (medium 1) from the air side (medium 0) to the glass side (medium 1). The electric field intensity $\mathrm{Re}[E(z)]^2$ is normalized to $\mathrm{Re}[E(d)]^2$ for each sample of gold film thickness d. The evolution is represented along along the Z axis (the direction normal to the interfaces) at x=0, and the wavelength is λ = 700 nm. It is very clear that with the same SPP field intensity on the air-gold interface (z=d, d is the thickness of the gold film) there is less intensity transmitted to the glass substrate for thick gold films. In other words, with the gold film thickness increases, the intensity transmission by leakage radiation through the gold film decreases. By comparing the electric field intensity of a propagating SPP mode at the air-gold interface $\mathrm{Real}[E(z=d)]^2$ and the electric field intensity of leaked light $\mathrm{Real}[E(z=0)]^2$, we can find the leakage radiation transmission ratio.

Figure 2.7 shows the leakage radiation transmission ratio as a function of free-space light wavelength for different gold film thicknesses. From this figure we clearly see the different transmission ratios for different wavelengths and for different gold film thicknesses. It clearly shows that at $\lambda = 700$ nm (see the dashed vertical line) while the gold film thickness increases from 20 nm to 70 nm, the leakage radiation transmission decreases from $\sim$0.75 to $\sim$0.05. With the same gold film thickness, the leakage radiation transmission is larger at near infrared wavelengths.

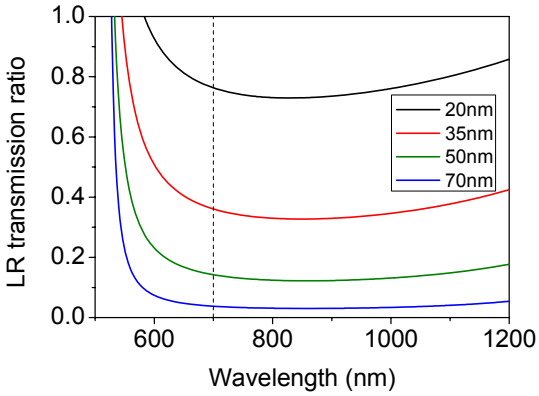

Figure 2.7: Leakage radiation(LR) transmission ratio as a function of free-space wavelength for different gold film thicknesses. The dashed line guides the eyes for $\lambda = 700$ nm.

2.2 Dipole radiation near an interface

An oscillating dipole is the basic light source in electromagnetic radiation systems. In many nano-optics experiments or theoretical calculations the nano-scale light source may be also considered as an oscillating dipole or an ensemble of oscillating dipoles. For example, single molecule emission [47, 48], CdSe quantum dot emission[49], the surface plasmon resonances of nanoparticles [40], the surface plasmon resonances of nanoholes [50, 51], scanning near-field optical microscope probes [36, 40], the optical response of the atomic force microscope probes [52] and even the scanning tunneling microscope tunneling junction [53] have been considered as oscillating dipoles. Such a wide variety of applications makes it very important to understand the radiation properties of oscillating dipoles. Most of the time we study the system near an interface, either an air-dielectric interface or an air-metal interface, so here we will focus on the radiation properties of a dipole near an interface.

2.2.1 Dipole radiation near an air-dielectric interface

Dipole radiation near an air-dielectric interface was well studied by W. Lukosz in the 1970s [54–56]. The air-dielectric interface can transmit and reflect the radiation of a dipole near the interface. As is well known, the Fresnel transmission ($t^{(p)}$, $t^{(s)}$) and reflection ($r^{(p)}$, $r^{(s)}$) coefficients are different for different polarizations [40], so we need to consider

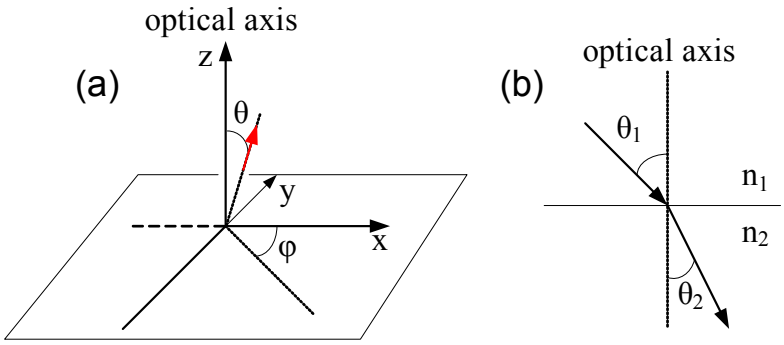

Figure 2.8: The coordinate system used for the dipole radiation near an interface. In (a), the red arrow indicates the position and orientation of the dipole. The angle θ is between the dipole and the optical axis, and the angle φ is between the X axis and the dipole's projection in the X–Y plane. In (b), θ_1 is the angle between the light emitted from the dipole and the optical axis, and θ_2 is the angle between the transmitted light and the optical axis. n_1 and n_2 represent the refractive indices of air and dielectric medium respectively.

the polarization when we calculate the dipole radiation near an interface. Here, we give the angular distribution of a dipole at an air-dielectric interface (z_0=0) [40, 54–57]:

$$I = \frac{3}{8\pi} sin^2(\theta) sin^2(\varphi) \left(\frac{t_{12}^{(s)} cos(\theta_2)}{\sqrt{1-(\frac{n_2}{n_1} sin(\theta_2))^2}}\right)^2 + \frac{3}{8\pi} cos^2(\theta_2) (t_{12}^{(p)})^2 \left(\frac{(cos(\theta) sin(\theta_1) - sin(\theta) cos(\varphi) cos(\theta_1))}{\sqrt{1-(\frac{n_2}{n_1} sin(\theta_2))^2}}\right)^2 \tag{2.14}$$

with θ, φ, θ_1 and θ_2 defined in figure 2.8. The Fresnel transmission coefficients ($t^{(p)}$, $t^{(s)}$) are as follows:

$$\begin{aligned} t_{12}^{(p)} &= (\frac{n_1}{n_2})(1 + \frac{n_2 cos(\theta_1) - n_1 cos(\theta_2)}{n_2 cos(\theta_1) + n_1 cos(\theta_2)}) \\ t_{12}^{(s)} &= 1 + \frac{n_1 cos(\theta_1) - n_2 cos(\theta_2)}{n_1 cos(\theta_1) + n_2 cos(\theta_2)} \end{aligned} \tag{2.15}$$

So, putting equation 2.15 into equation 2.14 we get:

$$I = \frac{3}{2\pi} n_1^2 sin(\theta)^2 sin(\varphi)^2 \left(\frac{cos(\theta_2)}{n_1 cos(\theta_1) + n_2 cos(\theta_2)}\right)^2 + \frac{3}{2\pi} n_1^2 cos(\theta_2)^2 \left(\frac{(cos(\theta) sin(\theta_1) - sin(\theta) cos(\varphi) cos(\theta_1))}{n_2 cos(\theta_1) + n_1 cos(\theta_2)}\right)^2 \tag{2.16}$$

In figure 2.8(a), the red arrow indicates the position and orientation of the dipole. The angle between the dipole and the optical axis is θ. In the interface (X–Y plane), the angle between the X axis and the projection of the dipole in the X–Y plane is φ. In figure 2.8(b), θ_1 is the angle between the light emitted from the dipole and the optical axis, and θ_2 is the angle between the transmitted light and the optical axis. When $\theta = 0°$, the dipole is perpendicular to the X–Y plane, and the dipole is vertical. When $\theta = 90°$, the dipole is parallel to the X–Y plane, and the dipole is horizontal. For these two special cases, based on the equation 2.16, the vertical dipole ($\theta = 0°$) and horizontal dipole ($\theta = 90°$) emission intensity can be written respectively as:

$$I_{vertical} = \frac{3}{2\pi} n_1^2 sin(\theta_1)^2 \left(\frac{cos(\theta_2)}{n_2 cos(\theta_1) + n_1 cos(\theta_2)}\right)^2 \tag{2.17}$$

and

$$I_{horizontal} = \frac{3}{2\pi} n_1^2 sin(\varphi)^2 (\frac{cos(\theta_2)}{n_1 cos(\theta_1)+n_2 cos(\theta_2)})^2 + \frac{3}{2\pi} n_1^2 cos(\varphi)^2 cos(\theta_1)^2 (\frac{cos(\theta_2)}{n_2 cos(\theta_1)+n_1 cos(\theta_2)})^2 \quad (2.18)$$

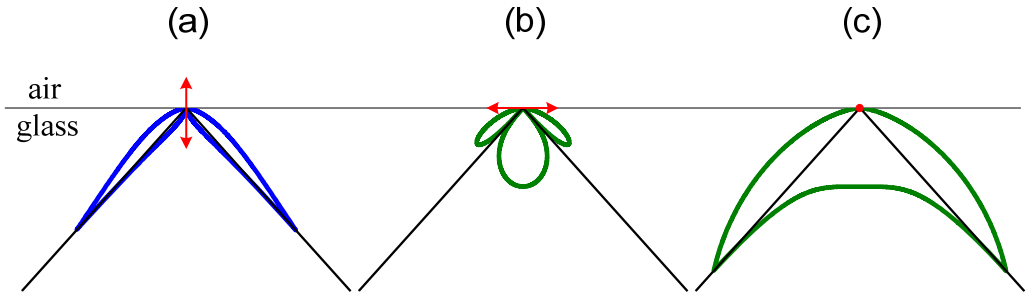

Figure 2.9: Angular distribution in the X–Z plane of the radiation from (a) a vertical dipole (θ=0°), (b) a horizontal dipole (θ=90°, φ=0°) and (c) a horizontal dipole (θ=90°, φ=90°) through an air-glass interface. These dipoles are located at the air-glass interface, z_0=0. The emission is calculated only for the glass side.

The angular distribution in the X–Z plane of the light emitted through an air-glass interface by a vertical dipole or a horizontal dipole is shown in figure 2.9. Figure 2.9(a) shows the angular distribution of the emission intensity (in the glass) for a vertical dipole located at the air-glass interface. The red double arrow shows the orientation of the dipole. The black line indicates the critical angle. Thus, the emission of a vertical dipole through an air-glass interface is mainly at angles larger than the critical angle.

Figure 2.9(b) and (c) show the angular distribution of the emission intensity (in the glass) of a horizontal dipole located at the air-glass interface. In figure 2.9(b), the red double arrow shows the direction of the horizontal dipole. In this case the horizontal dipole is in the X–Z plane (φ=0°, figure 2.8). Again, the black line indicates the critical angle, so in this case the dipole emission through the air-glass interface is mainly at angles smaller than the critical angle in the plane containing a dipole horizontal to the interface. In figure 2.9(c), the red dot again shows the direction of the horizontal dipole, so in this case the horizontal dipole is in the Y–Z plane (φ=90°, figure 2.8). The black line indicates the critical angle, so in this case the dipole emission through the air-glass interface is again mainly at angles larger than the critical angle, but there is still a significant amount of light emitted at small angles in the plane perpendicular to a dipole horizontal to the interface.

In figure 2.10, we plot the angular radiation pattern in the horizontal plane (parallel to the X–Y plane) in the glass medium for a vertical (figure 2.10(a)) and a horizontal (figure 2.10(b)) dipole. The dipoles are located at the air-glass interface, z_0=0. It is clear that the vertical dipole gives rise to a central symmetric pattern which means that angular distribution of the emission is the same for all values of φ. On the other hand, it is also clear that the horizontal dipole gives rise to a pattern which is symmetric with respect to the X or Y axis. This means that angular distribution is not the same for all values of φ. The emission intensity along the direction (in the X–Y plane) of the horizontal dipole

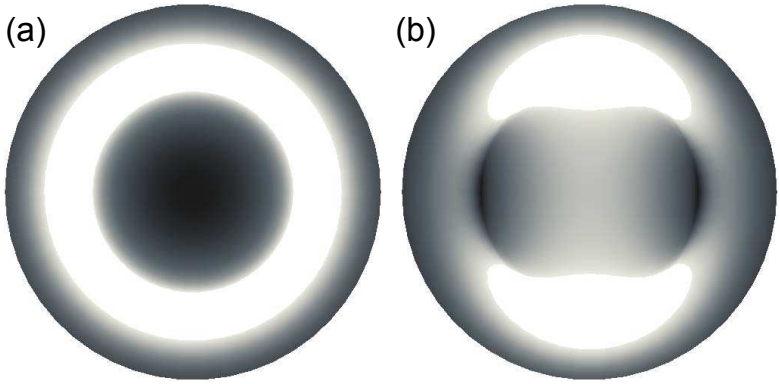

Figure 2.10: Angular radiation pattern in the horizontal plane (parallel to the X–Y plane) in the glass medium for (a) a vertical dipole (θ=0°) and (b) a horizontal dipole (θ=90°, φ=0°). The dipoles are located at the air-glass interface, z_0=0.

orientation is much smaller than the emission along the direction perpendicular to the horizontal dipole orientation (in the X–Y plane).

In general case, the dipole is neither vertical nor horizontal, so the angle θ may be between 0° and 90°. Figure 2.11 gives the angular radiation pattern for a dipole oriented 45° to the optical axis (θ=45°, φ=0°). The angular radiation pattern is not central symmetric. Especially in the small angle range (smaller than critical angle), there is more radiation along the direction perpendicular to the dipole (in the X–Z plane) than along the direction parallel to the dipole (in the X–Z plane, see figure 2.11(b)).

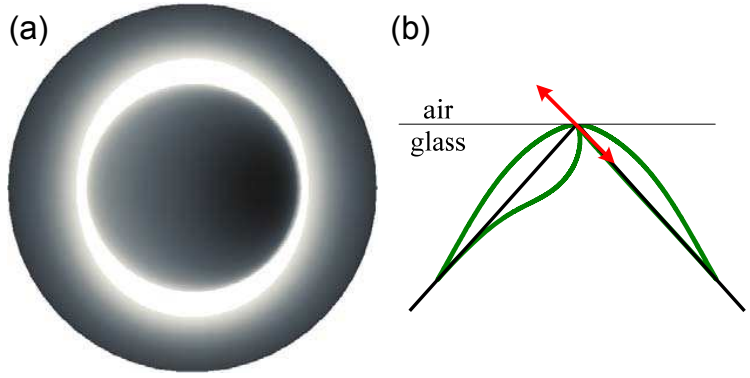

Figure 2.11: Angular distribution (a) in the X–Y plane and (b) the X–Z plane for a dipole (θ=45°, φ=0°). The dipole is located at the air-glass interface, z_0=0.

Dipole above the air-dielectric interface (z_0>0)

We have also investigated the case where $z_0 > 0$ (the dipole is above the air-dielectric interface). In this case, we need to add a multiplicative term to equation 2.14 in order to describe the distance effect, so the equation 2.14 can be modified to [40]:

$$I = (equation\ 2.16) \times Re[e^{i\frac{2\pi}{\lambda}z_0 cos(\theta_1)}]^2 \tag{2.19}$$

The angular distribution of a dipole oriented 60° to the optical axis for different distances z_0 are shown in figure 2.12. Here we choose z_0=0.01λ, z_0=0.1λ and $z_0 = \lambda$. With the three different distances, we see that when the z_0 increases, the radiation at large angles (larger than critical angle) decreases, but the radiation at small angles (smaller than critical angle) does not change. The radiation at large angles is called "forbidden light" and the radiation at small angles is called "allowed light" [40]. The forbidden light is always symmetrical with respect to the optical axis. But, the allowed light is not symmetrical with respect to the optical axis because of the dipole orientation of 60°. Moreover, the allowed light originates from traveling waves and the forbidden light arises from the evanescent waves of the electric dipole radiation [58]. It is shown in figures 2.9-2.12 that when the dipole is very close to the air-glass interface, almost all the far field intensity is from evanescent waves. But when the dipole is one wavelength away from the interface, no radiation is observed in the forbidden light region, because the evanescent waves from the dipole die out before reaching the interface.

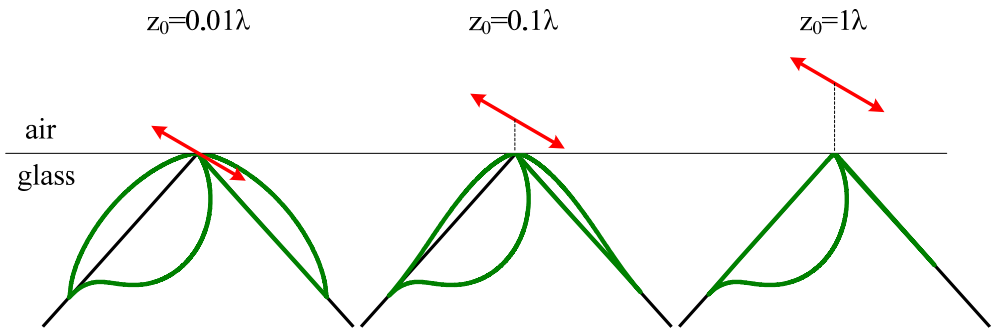

Figure 2.12: Angular distribution in the X–Z plane of a dipole (θ=60°, φ=0°) for different distances z_0. The distances z_0 of the dipole are indicated in the figure. The radiation patterns are shown in the X–Z plane. Note that the allowed light does not depend on z_0 and that the forbidden light is always symmetrical with respect to the optical axis.

2.2.2 Dipole radiation near an air-gold film interface

Now we consider how a dipole radiates near an air-gold-glass sandwich structure shown in figure 2.13.

Vertical dipole radiation through an air-gold-glass structure

When a dipole radiates near an air-gold interface, the dipole can excite surface plasmons on the gold film [59–62]. Similar to the air-glass interface case, with the consideration of dipole-excited surface plasmons, we can write the angular distribution of the radiation from a **vertical** dipole (θ=0°) through an air-gold-glass sandwich structure as [53]:

$$E(k_x) = \frac{ip_z}{8\pi^2\varepsilon_0} \frac{k_x t^{(p)}(k_x)}{\sqrt{1-k_x^2/k_0^2}} \, e^{ik_0 z_0 \sqrt{1-k_x^2/k_0^2}} \tag{2.20}$$

where k_x is the wavenumber of the propagating surface plasmons at the air-gold interface, k_0 is the wavenumber of the light in free space, p_z represents the vertical oscillating dipole.

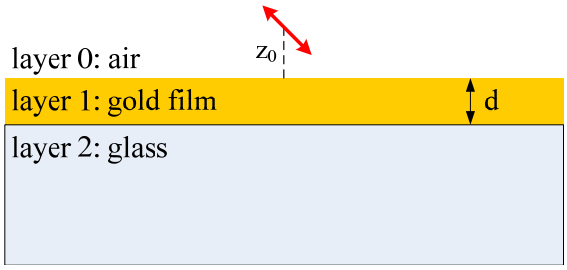

Figure 2.13: Schematic image of a dipole near an air-gold-glass sandwich structure (cross section in the X–Z plane). The coordinate system is shown in figure 2.8. The red double arrow indicates the position and orientation of the dipole. z_0 is the distance between the dipole and the gold film and the d is the thickness of the gold film.

If $z_0 = 0$, the angular distribution of intensity I can be written as:

$$I(k_x) \propto \frac{(k_x)^2 \left| t^{(p)}(k_x) \right|^2}{1 - k_x^2/k_0^2} \tag{2.21}$$

with [43, 44]

$$\begin{aligned} t^{(p)} &= \frac{t_{01}^p t_{12}^p e^{ik_{z1}d}}{1 + r_{01}^p r_{12}^p e^{2ik_{z1}d}} \\ r_{ik}^p &= \frac{\frac{k_{zi}}{\varepsilon_i} - \frac{k_{zk}}{\varepsilon_k}}{\frac{k_{zi}}{\varepsilon_i} + \frac{k_{zk}}{\varepsilon_k}} \\ t_{ik}^p &= (1 + r_{ik}^p)\sqrt{\varepsilon_i/\varepsilon_k} \\ k_{zi} &= \sqrt{k_i^2 - k_x^2} \end{aligned} \tag{2.22}$$

The schematic is shown in figure 2.13 and figure 2.6(b).

Vertical dipole radiation through an air-gold-glass structure for different gold film thicknesses at λ=700 nm ($z_0 = 0$)

Figure 2.14 shows the angular distribution in the horizontal plane (parallel to the X–Y plane) in the glass medium of the radiation from a vertical dipole radiation through an air-gold-glass structure for different gold film thicknesses from 6 nm to 70 nm at wavelength λ=700 nm based on equation 2.21. Figure 2.15 presents the corresponding cross-sections of the images in figure 2.14.

In figure 2.14, it is very clear that the angular distribution image (in the X–Y plane) on a 6 nm gold film is very similar to figure 2.10(a) which shows the radiation of a vertical dipole on an air-glass interface. This means there are no propagating surface plasmons excited by the vertical dipole on the 6 nm gold film. It is clearer in figure 2.15(a) that the cross-section of the angular distribution image of a vertical dipole on a 6 nm gold film is very "flat", i.e., there is no propagating SPP peak. Actually, as already shown in figure 2.4(a), a 6 nm gold film does not support propagating SPPs, so there is no SPP ring in figure 2.14 or SPP peak in figure 2.15(a). Instead, the angular distribution (in the X–Y plane) image features a uniform intensity pattern with a discontinuity at the critical angle.

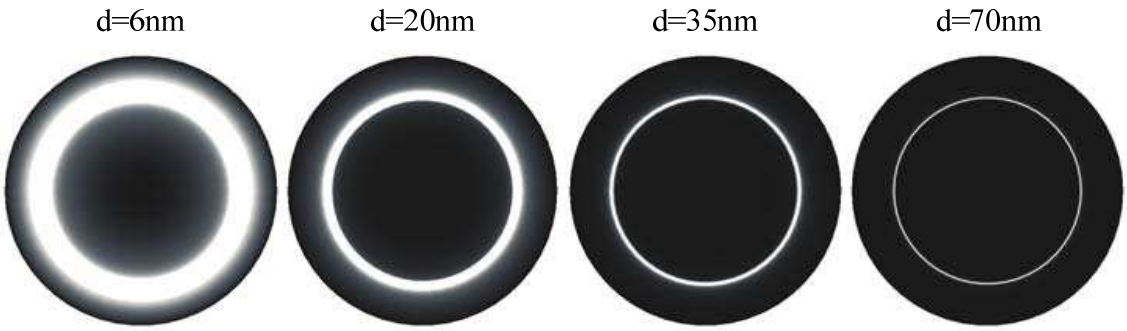

Figure 2.14: Angular distribution in the X–Y plane of the radiation from a vertical dipole through an air-gold-glass structure for different gold film thicknesses at λ=700nm. The film thickness d is indicated for each image.

For other thicknesses (20 nm to 70 nm), they all have a significant plasmon ring in figure 2.14 or plasmon peak in figure 2.15, and the plasmon peaks are all at angles larger than the critical angle. We also notice that the *maximum* intensities are higher than that from the 6 nm gold film. If we only consider the transmission properties, this peak intensity increasing effect is very surprising because the transmission decreases when the gold film thickness increases. However, due to the fact that the propagating SPPs are excited by dipole radiation on these gold films and the fact that thicker gold films support more propagating SPPs, so we can understand this phenomenon. More precisely, we see the peak intensity from the 70 nm gold film is lower than that from the 50 nm gold film since the film starts to become opaque. Moreover, the full width at half maximum (FWHM) of the plasmon peak decreases as gold film thickness increases. This because the reciprocal of the FWHM of these plasmon peaks is related to the propagating length of the SPP, and when the gold film thickness increases, the propagating length of the SPPs also increases as shown in figure 2.4(b).

Vertical dipole radiation through an air-gold-glass structure for a 50 nm gold film at different wavelengths ($z_0 = 0$)

Figure 2.16 shows the angular distribution in the X–Y plane of the radiation from a vertical dipole through an air-gold-glass structure (gold film thickness 50 nm) for different dipole radiation wavelengths λ. Figure 2.17(a) presents the corresponding cross-sections (from 40° to 50°) of the images in figure 2.16. From figure 2.16, we see that at λ=500 nm the angular distribution image (in the X–Y plane) is similar to figure 2.10(a) which is a vertical dipole on an air-glass interface. In figure 2.17(a) we see that the cross-section of the angular distribution image at λ=500 nm is very "flat", and there is no significant SPP peak (grey curve). This means that there are no propagating SPPs excited by the vertical dipole at λ=500 nm [63].

For other wavelengths (550 nm to 900 nm), a significant SPP ring in figure 2.16 or SPP peak in figure 2.17(a) is observed, and the SPP peaks are all at angles larger than the critical angle. In figure 2.17(a), it is very clear that the SPP peak positions change with the dipole radiation wavelengths. When the wavelength decreases, the SPP peak shifts to a larger angle. In figure 2.17(b) we plot the dispersion curve of SPP

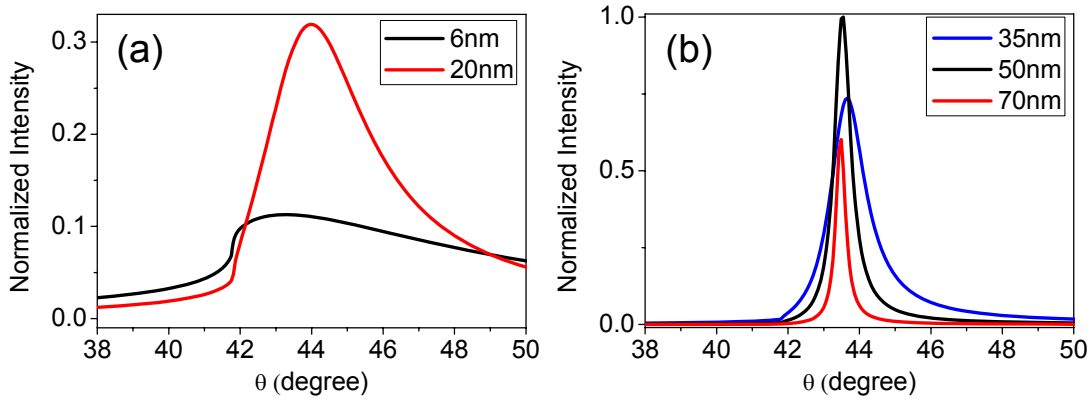

Figure 2.15: Cross-sections through the center of the images in figure 2.14. The cross-sections are normalized to the maximum intensity for the 50 nm gold film case and show the relative intensity. For clarity, the plot range is from 38° to 50° and the cross-sections are separated into two groups of gold film thicknesses: (a) 6 and 20 nm, (b) 35, 50 and 70 nm. The critical angle of an air-glass interface is 41.8°.

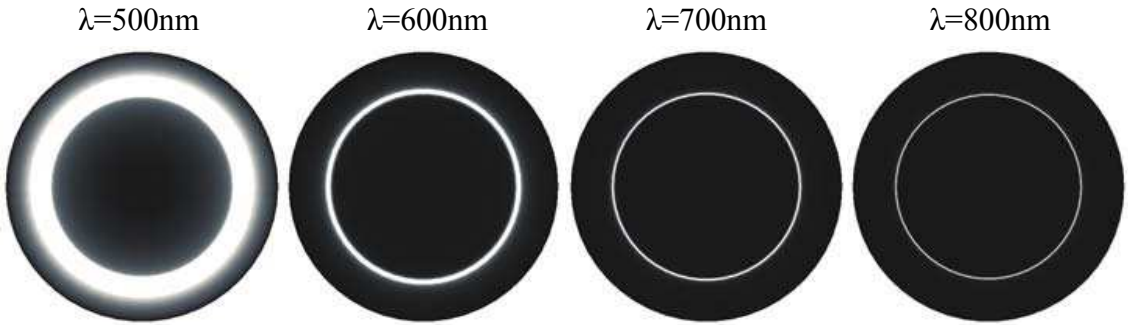

Figure 2.16: Angular distribution in the X–Y plane of the radiation from a vertical dipole through an air-gold-glass structure for a fixed gold film thickness (50 nm) and for different dipole radiation wavelengths. The wavelength λ is indicated for each image.

waves propagating along the air/gold interface for a 50 nm thick gold film again (already shown in figure 2.4(a)). From the SPP peak positions in figure 2.17(a), we determine the propagating SPP wavenumbers (real part) for different dipole radiation wavelengths ($Re[k_{SPP}(\omega)] = n_{glass} sin(\theta) k_0(\omega)$). We see that the determined value fits very well with the theoretical dispersion curve. This give us another way to calculate the dispersion relation for gold films. The FWHMs of the SPP peaks (in figure 2.17(a)) also indicate the propagation length L_{SPP} of SPP at different wavelengths ($L_{SPP} = 1/FWHM$ [64]). For example, the FWHM of the SPP peak at 550 nm is much larger than that at 700 nm which means the propagation length of SPP at λ_{SPP}=550 nm is much smaller than that at λ_{SPP}=700 nm.

From the figures 2.14-2.17 we see that propagating SPPs can be excited when a vertical dipole with an appropriate wavelength is near an air-gold-glass sandwich structure with an appropriate gold film thickness. When propagating SPPs are excited, the angular

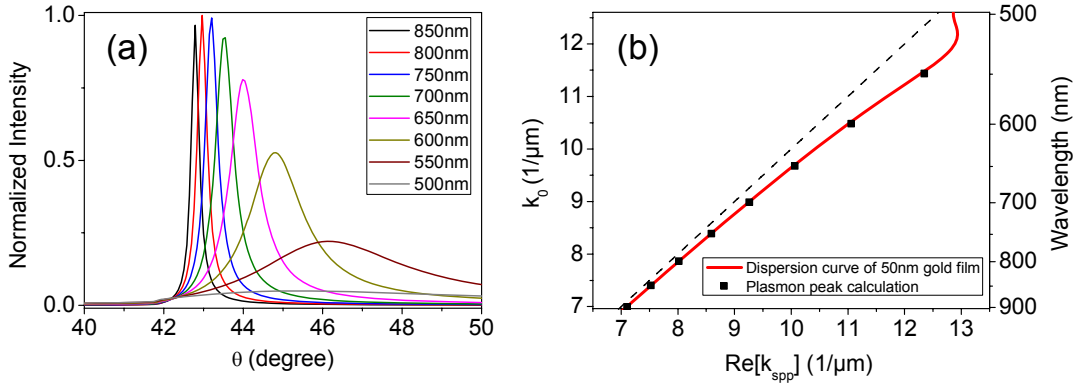

Figure 2.17: (a) Partial cross-sections through the center of the images in figure 2.16. The cross-sections are normalized to the maximum intensity for the λ=800 nm case and show the relative intensity. For clarity, the plot range is from 40° to 50°. (b)The red curve is the dispersion curve of SPP waves propagating along the air/gold interface for a 50 nm thick gold film (already shown in figure 2.4(a)). The black squares are the propagating SPP wavevectors (real part) as determined from the SPP peaks in (a). The values from the angular distribution images fit very well with the theoretical dispersion curve.

distribution of the radiation through an air-gold-glass structure is different from that of a vertical dipole on an air-glass interface. The angular distribution (in the X–Y plane) is very useful for checking whether propagating SPPs are excited. Moreover, we can calculate the dispersion curve and propagation length from the the angular distribution of the radiation.

2.3 Experimental setup

Our experimental setup has two main parts: the scanning tunneling microscope (STM) and the inverted optical microscope. We combine them together so that we can excite surface plasmons on thin metal films (deposited on quartz or glass substrates) with the STM and record the surface plasmons images through the thin metal film with the optical microscope. The setup is shown in figure 2.18 and figure 2.19.

2.3.1 Scanning tunneling microscope

In general, there are two types of imaging modes for STM: constant height mode and constant current mode. In constant height mode, the relative distance between the tip and the reference plane is fixed and the tunneling current changes with the lateral tip position. However, in constant current mode, the tunneling current is maintained and the relative tip-sample distance (z position of the tip) is adjusted by a feedback loop. By recording the feedback signal at each tip position, a “topography” image is produced.

In our experiments, we use the STM mode (constant current mode) of a Veeco Dimension 3100 system (nanoscope IV). The STM tips are made of PtIr, W and Ag. The PtIr tips are bought from Veeco and were just mechanically cut. The W tips and Ag tips were homemade by an electrochemical etching process.

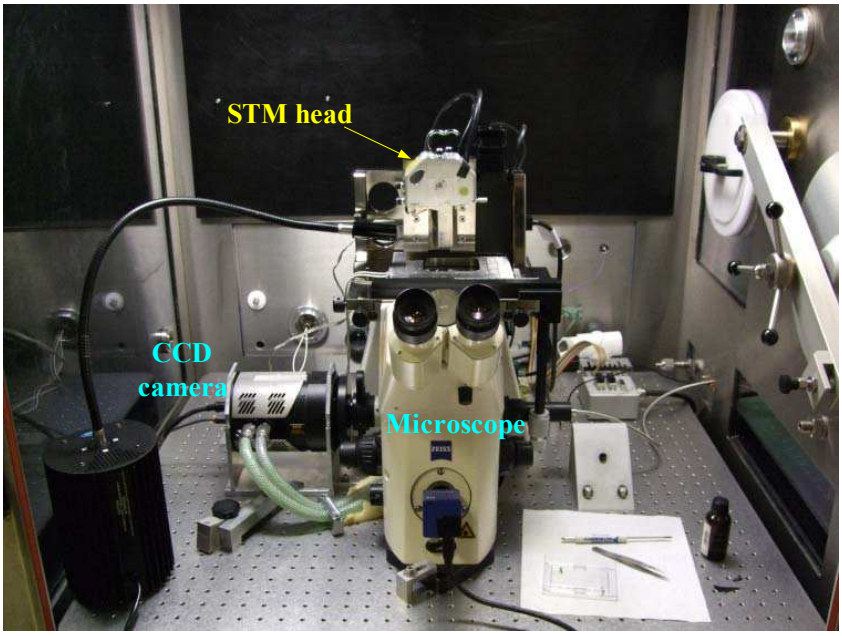

Figure 2.18: The combination experimental setup. In a glove box, a STM/AFM head is mounted on an inverted optical microscope. A cooled Roper camera is mounted on the left port, a live Axiocam camera is on the front port and a collection fiber is on the right port. The collection fiber is connected to a spectrometer outside the glove box.

The W tips are etched in a 2 mol/L NaOH solution. The solution is prepared with: 80 g Na_2O, 650 ml distilled H_2O and 350 ml glycerin. The applied bias can be either alternating current (AC) pulses or direct current (DC). The electrode used in the NaOH solution is made with nickel wire. Normally, when etched with direct current, the tip is sharper and has a symmetrical shape.

The Ag tips are etched in a 25% (in volume fraction) NH_3OH solution. The NH_3OH solution is prepared using a 32% NH_3OH solution diluted with distilled H_2O. For example, 100 ml of a 32% NH_3OH solution diluted with 28 ml distilled H_2O, gives us a 25% NH_3OH solution.

2.3.2 Optical microscope

The inverted optical microscope we used is a Zeiss Axiovert 200. With dichroic cubes (dichroic mirrors and bandpass filters for excitation and emission), the inverted optical microscope can be used for *epifluorescence* microscopy experiments using lamp or laser excitation. During the lamp (X-cite 120) excitation, the excitation intensity on the sample can be adjusted with the aperture diaphragm by changing the beam diameter of the lamp in the microscope and the emission area size on the samples can be adjusted by the field diaphragm. For the laser excitation, by adding a focus module, the beam size of a 488nm argon laser is reduced and the FWHM (full width at half maximum) of the laser beam can reach around 1 μm. With the help of a high numerical aperture oil objective, the laser excitation can be also operated in the total internal reflection fluorescence (TIRF) mode.

The emission can be recorded either by an uncooled color Axio camera (AxioCam ICc,

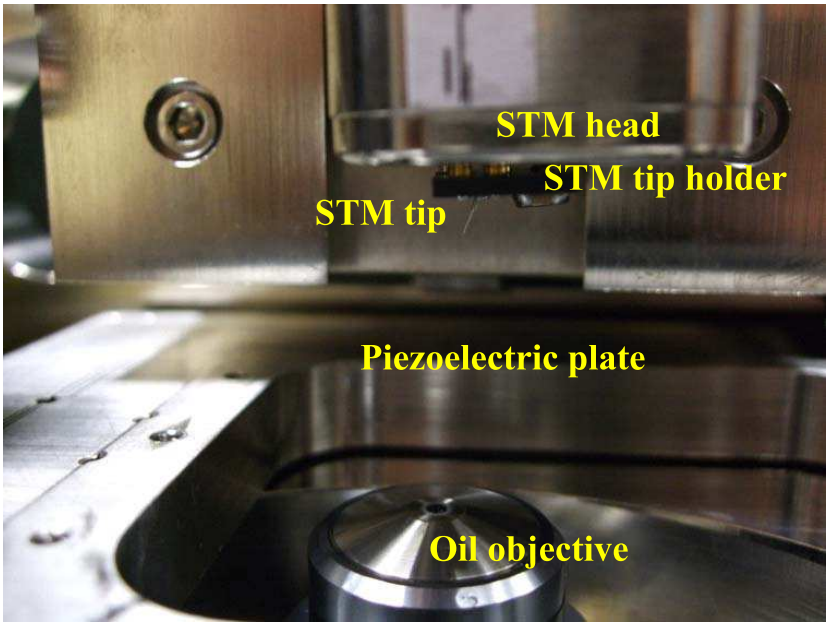

Figure 2.19: The core part of the experimental setup. The spectrum is recorded without a sample during XX s.

Zeiss) or by a liquid cooled Roper camera (PIXIS 1024B, Princeton Instruments). The Axio camera has a 1.4 megapixel resolution (1388 × 1038) and one pixel is 4.65 μm × 4.65 μm in size. The Roper camera has a 1 megapixel resolution (1024 × 1024) and one pixel is 13 μm × 13 μm in size. While the Axiocam has better resolution, the Roper camera is used most because of its better signal to noise ratio (cooled to $-70°C$. If we use an 100× objective, one pixel of the Axio camera in the image plane corresponds to 46.5 nm (4.65 μm/100) in the object plane and one pixel of the Roper camera in the image plane corresponds to 130 nm (13 μm/100) in the object plane. It is important to notice that in our setup before the Axio camera, there is an 0.63 × optical translator, so one pixel of Axio camera in the image plane corresponds to 74 nm (4.65 μm/(100×0.63)) in the object plane.

The emission can also be recorded by a liquid nitrogen cooled spectrometer (Jobin-Yvon, Triax 190). A collection fiber made of 49 single fibers collects the light from the right port of the microscope. The spectrometer uses a CCD for light detection, so the spectral information can be presented either as spectral curves or 2D spectral maps. The spectrometer CCD works at around 150K. There are several gratings with different spectral ranges. The most frequently used grating for our spectral measurements is the one with a blazed wavelength at 600 nm, a grating density of 300 grooves/mm (grating per millimeter) and a grating width of 120 mm. Theoretically, the 300 grooves/mm grating with a width of 120 mm that is used in first order has a numerical resolving power R = 300×120 = 36,000= $\lambda/\Delta\lambda$. Therefore, at 700 nm, the spectral resolution $\Delta\lambda$ of the grating is equal to 0.0194 nm (λ/R) [65].

A transmission curve of our spectrometer system has been calculated including the transmission of the objective, the tube lens and prism of the microscope, the collection fiber, the response of the grating in the spectrometer and the quantum efficiency of the

CCD in the spectrometer (figure 2.20(a)). According to this transmission curve, our recorded experimental spectra (central wavelength around 700 nm) need to be red shifted by 10 nm. Most of the spectra in this thesis are not corrected for instrumental response since the shift is small, except for some special cases. The transmission curves of the spectrometer system are given in figure 2.20(a) and the transmission curves of the Roper camera system are given in figure 2.20(b). Figure 2.21 is a comparison between the spectrometer and the Roper camera systems.

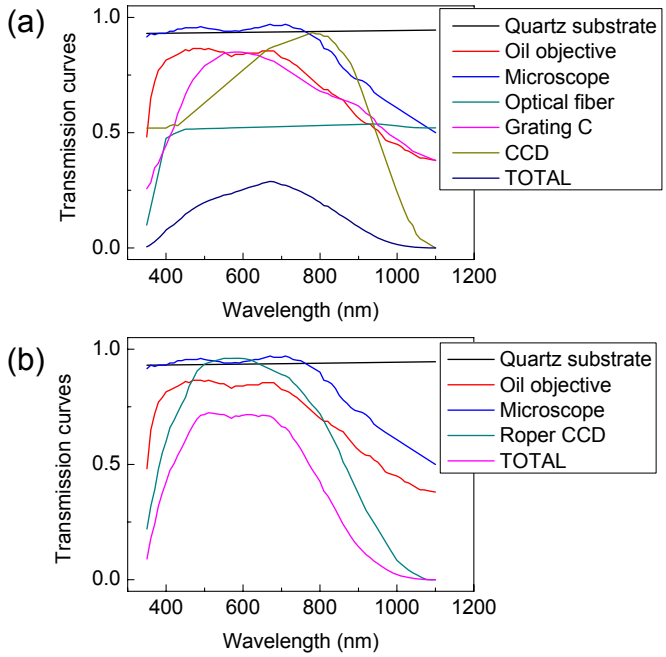

Figure 2.20: Transmission curves of (a) our spectrometer system and (b) Roper camera system (b). In each image, we show the transmission curves for each component in the detection system. The total transmission curve is also plotted.

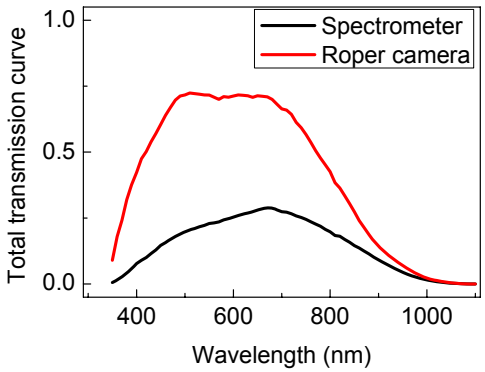

Figure 2.21: Total transmission curves of our spectrometer and Roper camera systems.

Figure 2.22 shows the near infrared light from the AFM/STM head of our setup. This near infrared light is always there when the AFM/STM head is electrically connected to

the controller and it may be related to the feedback system in the AFM/STM head. By a Gaussian fit, we see that this near infrared light has a central peak position around 893 nm and a FWHM around 40 nm. This near infrared light is a noise for our experiments, so we use a 842 nm shortpass filter to cut this near infrared light.

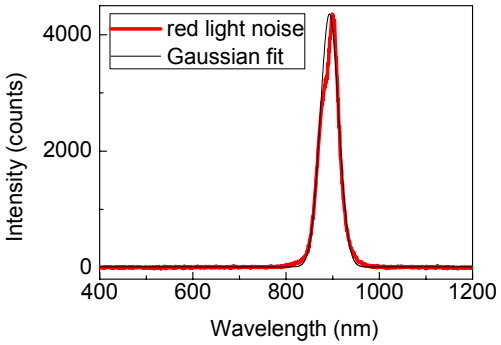

Figure 2.22: Near infrared light from the AFM/STM head of our setup. The spectrum is recorded using an oil objective (×100, NA=1.45). An ITO deposited glass substrate is used to focus the oil objective. The acquisition time is 60 s.

Back focal plane imaging

The back focal plane is also called the rear focal plane or Fourier plane and the back focal plane image is usually called the Fourier space image. A converging lens has both a front focal point and back (rear) focal point. Any ray passing through the front focal point will exit parallel to the optical axis when it leaves the converging lens. The back (rear) focal point of the system has the reverse property: rays that enter the system parallel to the optical axis are focused so that they pass through the rear focal point.

Back focal plane imaging gives information on the angular distribution of the light emitted in the object plane. Figure 2.23 shows the principle of the back focal plane. There is an emitter at point A in the object plane (front focal plane of the objective) which emits at an angle θ.

As shown in figure 2.23, in the object plane the distance between point A and the optical axis is r, and in the back focal plane the distance between point A' and the optical axis is r'. According to the "Abbe sine condition", there is a relation [66, 67]:

$$rnsin(\theta) = r'n'sin(\theta') \tag{2.23}$$

where n is the refractive index of front focal plane and n' is the refractive index of back focal plane. Because θ' is rather small, $sin(\theta') \approx tan(\theta')$. The focal length of the objective is defined as f, thus $tan(\theta')$= r/f. So equation 2.23 can be written as:

$$rnsin(\theta) = r'n'tan(\theta') = r'n'r/f \tag{2.24}$$

So we have:

$$r' = fnsin(\theta)/n' \tag{2.25}$$

Because the refractive indices n, n' and focal length of the objective f do not change for a specific objective, the distance r' between image point A' and the optical axis in the back focal plane only depends on the light emission angle in the object plane.

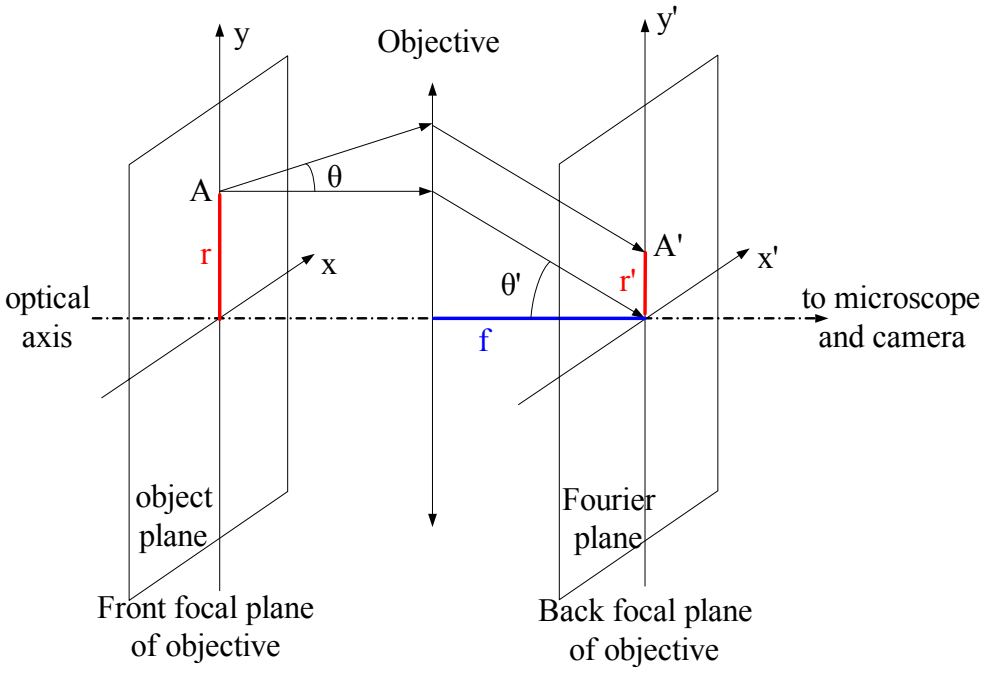

Figure 2.23: Principle of the back focal plane.

On the other hand, the image in the back focal plane may be considered as the "Fraunhofer diffraction" pattern of the point source emission in the object plane. In this case, the field emission in the back focal plane can be calculated as [66, 67]:

$$U(x',y') = \iint_{Aperture} A(x_0,y_0)\, e^{-ik(lx+my)} dxdy = A(x_0,y_0)\, e^{-iky'r/f} \tag{2.26}$$

where $A(x_0, y_0)$ represent the field amplitude at point (x_0, y_0) in the object plane and $U(x', y')$ represents the field amplitude in back focal plane at point (x', y'). The l and m are the direction cosines of the emission at point A. For the case shown in figure 2.23, l=0 and $m = r'/f = y'/f$.

Back focal plane calibration

To understand the back focal plane images, it is very important to calibrate the back focal plane image. Once the back focal plane image is calibrated, we can quantify the angular distribution of the emitted light. Here we do the back focal plane calibration for oil objectives by obtaining back focal plane (or Fourier space, see subsection 2.3.2) images with molecular fluorescence and attributing a value of 1 to the inflection point, as shown in the following.

The fluorescence sample is made by using a a fluorescence marker on a glass substrate. The photoluminescence of the fluorescence marker is excited by a lamp (x-cite 120, Lumen Dynamics Group Inc.) and detected by our inverted optical microscope (epifluorescence microscopy). The back focal plane images with oil objectives NA=1.45 (figure 2.24(a)) and NA=1.3 (figure 2.24(b)) both have a ring shaped pattern. The ring pattern with

the oil objectives NA=1.45 (figure 2.24(a)) is larger than the one with the oil objectives NA=1.3 (figure 2.24(b)). This also can be seen in figure 2.24(c) with the cross-section curves.

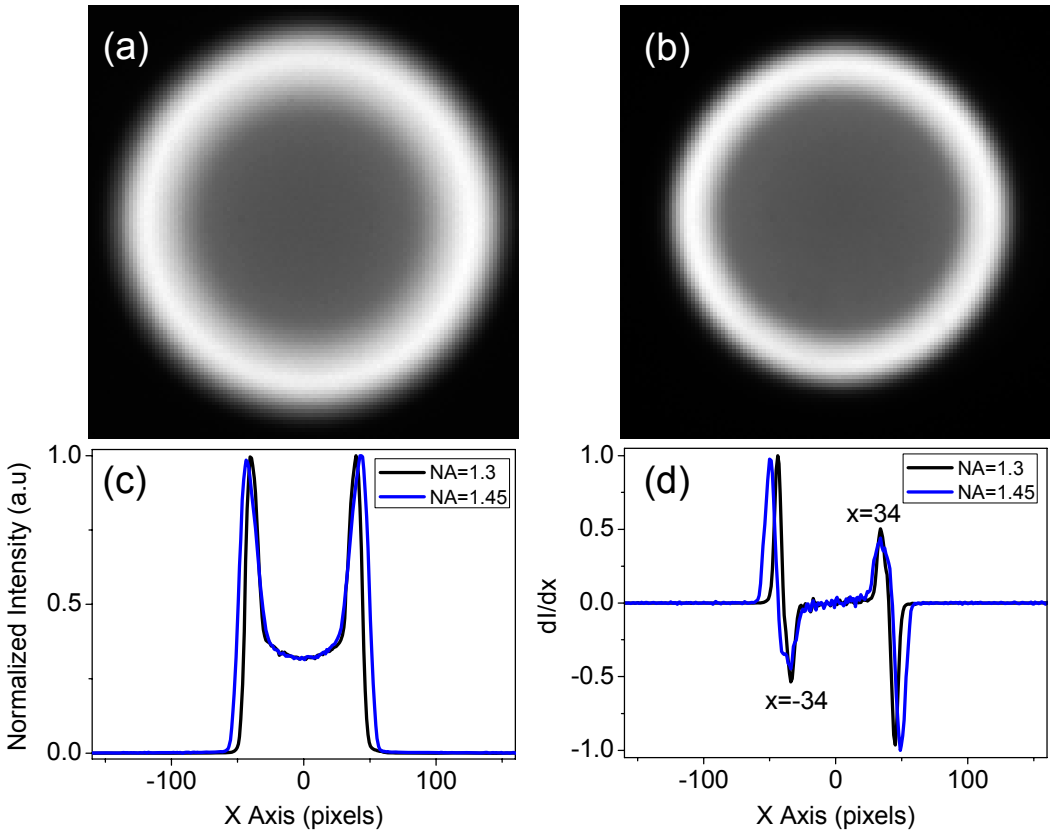

Figure 2.24: Back focal plane images of fluorescent molecule photoluminescence emission with oil objectives NA=1.45 (a) and NA=1.3 (b). (c) Corresponding cross-sections of (a) and (b). (d) The derivative curves of the cross-sections in (c).

To find the NA=1 point, we take the derivative of the cross-sections in figure 2.24(c). From the derivative curves in figure 2.24(d) we see that for each objective there are four peaks. The outer two peaks corresponding to the numerical aperture of the objectives. The inner two peaks have been assigned to the critical angle[47, 68], so we can use 34 pixels as NA=1 to find the measured numerical aperture of the objectives by the intensity rapid decreasing point divided by the intensity rapid increasing point. Here for oil objective NA=1.45, the measured numerical aperture is 49/34=1.44, and for the oil objective NA=1.3, the measured numerical aperture is 44/34=1.29. The measured numerical apertures fit well with the nominal values for both objectives, so the calibration is quite good. In the future, for all the back focal plane images with oil objectives, we will use the calibration "34 pixels corresponding to NA=1". Similarly, for air objectives, the abrupt cutoff of the back focal plane image is assigned to be the numerical aperture of the air objective. An important point is that the air objective back focal plane calibration may be different from that of the oil objectives because of the different coverslip correction thicknesses.

Figure 2.25 shows the radiation angle θ as a function of numerical aperture $nsin(\theta)$. Figure 2.25(b) is a zoom of figure 2.25(a) around $nsin(\theta)$=1. It shows that around $nsin(\theta)$=1, the resolution of angle θ is around 1.5°. When numerical aperture $nsin(\theta)$ increases and $nsin(\theta) < \sim 1.25$, the resolution of angle θ nearly does not change (or decreases slightly). When numerical aperture $nsin(\theta)$ is larger than ∼1.25, the resolution of angle θ decreases rapidly.

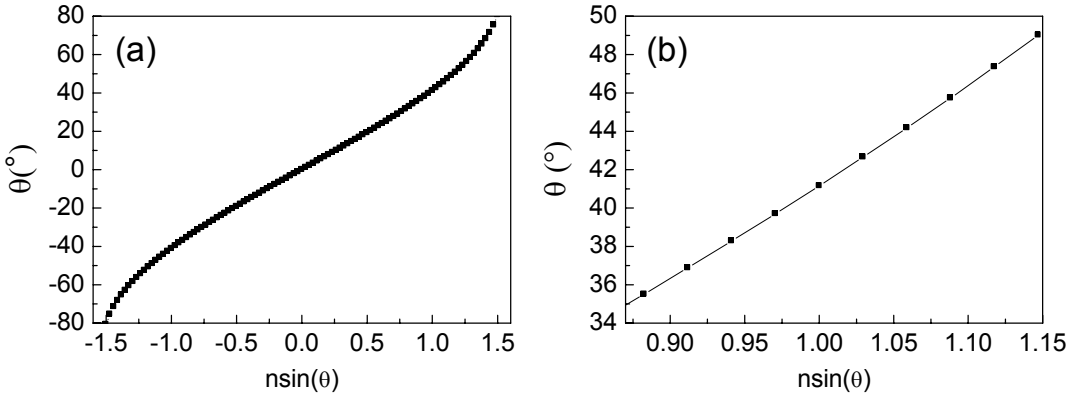

Figure 2.25: The radiation angle θ as a function of the numerical aperture $nsin(\theta)$. (b) is a zoom of (a) around $nsin(\theta)$=1.

Chapter 3

STM Excitation of Surface Plasmons on Gold Films

Inelastic electron tunnelling excitation of propagating surface plasmon polaritons (SPP) on a thin gold film is demonstrated. This is done by combining a scanning tunnelling microscope (STM) with an inverted optical microscope. Analysis of the leakage radiation in both the image and Fourier spaces unambiguously shows that the majority of the detected photons originate from propagating SPP with propagation lengths of the order of 10 μm. The remaining photon emission is localized under the STM tip and is attributed to a tip-gold film coupled plasmon resonance as evidenced by the bimodal spectral distribution and enhanced emission intensity observed using a silver STM tip for excitation.

T Wang, E Boer-Duchemin, Y Zhang, G Comtet and G Dujardin, Excitation of propagating surface plasmons with a scanning tunnelling microscope, *Nanotechnology*, **22**, 175201 (2011)

3.1 Introduction

Propagating surface plasmon polaritons (SPP) in metallic nanostructures offer new perspectives for integrating optics at the nanoscale. In particular, SPP provide new methods for the transfer of information and energy at dimensions below the diffraction limit [13, 14, 17, 18]. Excitation of such propagating SPP on noble metal nanostructures has been demonstrated by using photon excitation [69, 22, 70, 64, 71] and high energy ($\geq$ 30 keV) electron beams [26, 27, 29]. Recently, the use of a near-field scanning optical source made of a single fluorescent nanodiamond [63] has opened the possibility of quantum plasmonics. Another possibility, the electrical excitation of propagating SPP using inelastic electron tunnelling from the tip of a scanning tunnelling microscope (STM), would have unique advantages over the methods of [26, 27, 29, 63, 69, 22, 70, 64, 71]: (i) inelastic electron tunnelling can be extremely localized (down to the picometre scale) [72], (ii) there is no background light from an excitation source when an STM is used, and (iii) the STM can be easily coupled to optical devices for photon emission detection. Despite these advantages, the excitation of propagating SPP on noble metal surfaces with the STM has not been unambiguously demonstrated so far. Optically excited SPP propagating on a thin homogeneous noble metal film sandwiched between air on one side and a quartz or glass substrate on the other are often detected by leakage radiation microscopy, i.e. by detecting the light emitted into the substrate of higher index of refraction [22, 70, 64, 71]. In most of the previous STM experiments, photon emission was detected on the air/vacuum side of the noble metal film [7, 73–83], i.e. on the same side as the STM tip, where leakage radiation of propagating SPP cannot occur. Thus in this configuration the detection of propagating SPP is not possible, unless the noble metal surface is very rough. Others have detected the light induced by the STM tip through a thin gold film at specific angles [8, 84]. Egusa et al [85] have detected the light induced by the STM tip through a thin gold film in the leakage radiation configuration. In their Fourier space image, they observe a peak at zero numerical aperture ($NA = 0$) and assign this peak to propagating SPP. However, this does not fit with the expected leakage emission from propagating SPP which occurs at large angles (larger than the critical angle of the substrate/air interface, i.e., NA $>$ 1 [70]). Therefore, the origin and nature of plasmons excited with an STM tip on noble metal surfaces is still a very puzzling problem, raising a number of questions: is it possible to excite propagating SPP with the STM and to detect them? What is the nature of those plasmons which are excited with the STM?

In this chapter, we use an STM operating in air to electrically induce light from a thin gold film on a quartz substrate. The STM is combined with an inverted optical microscope and the emitted photons are collected through the quartz by leakage radiation microscopy. Both the image and Fourier space results are analyzed. We show that the majority of the emitted photons originate from propagating SPP with propagation lengths of the order of $10\mu m$. In addition, the remaining light emission, which was the only detected light in previous STM experiments [7, 73–83], is shown to be localized under the STM tip and is attributed to a tip-gold film plasmon resonance. Replacing the tungsten STM tip by a silver tip splits the spectral distribution of this localized emission into a bimodal distribution as expected for a Ag-Au localized plasmon resonance [86]. It is also shown that using a silver tip instead of a tungsten tip enhances the intensities of the propagating

SPP and the localized plasmon emission by a factor of 2 and 20 respectively.

3.2 Experimental Setup

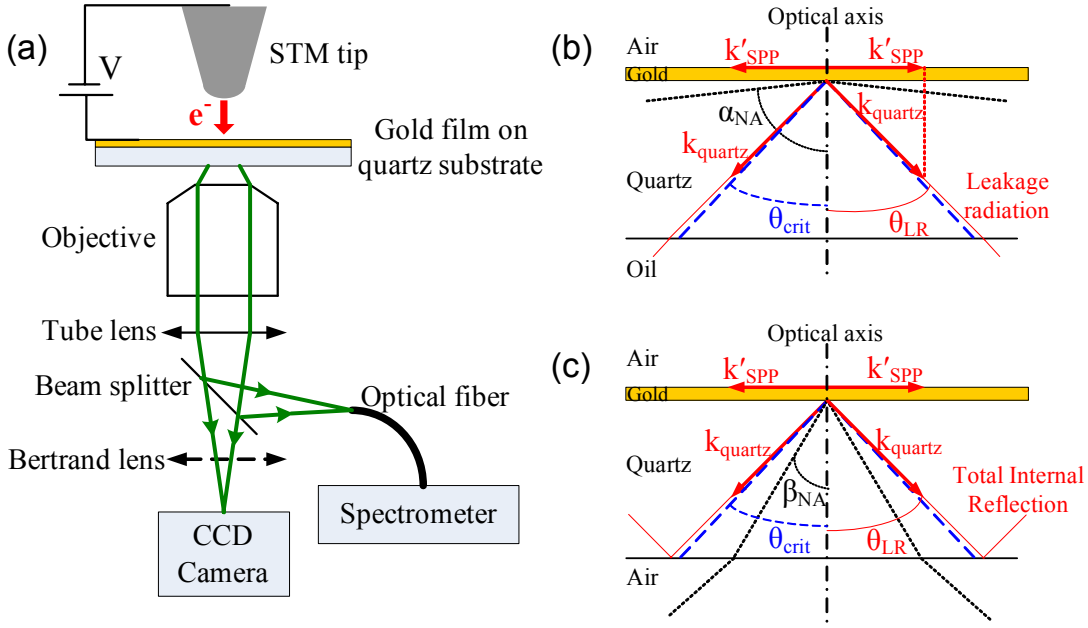

Figure 3.1: Experimental setup (a) and schematics defining the different angles in the experiment for the case of the (b) oil and (c) air objective.

The experimental setup is shown in figure 3.1(a). A scanning tunneling microscope (Veeco Bioscope/Nanoscope IV) operating in air is mounted on an inverted optical microscope(Zeiss Axiovert 200). Photon emission produced by inelastic electron tunneling is detected through the sample made of a thin gold film (35 nm) deposited on a 0.2mm thick quartz substrate (GE 214, refractive index n = 1.4585) by electron beam evaporation under high vacuum (1×10^{-7} Torr). The rootmean square surface roughness as measured by atomic force microscopy is found to be about 1.5 nm (Figure 2.2). Both air (100×, NA = 0.75) and oil immersion (100×, NA = 1.45) optical microscope objectives are used for small (i.e., less than the critical angle, θ_{crit}) and large ($>\theta_{crit}$) angle photon emission detection through the sample, respectively (see figures 3.1(b) and (c)). For each value of the tunnel current I and surface voltage V (the tip is grounded), we successively record (i) the image plane with the CCD camera, (ii) the Fourier space by focusing the back focal plane onto the CCD camera(PIXIS 1024B, Princeton Instruments), and (iii) the photon emission spectrum using a spectrometer (Jobin-Yvon, Triax 190). In order to focus the back focal plane onto the CCD camera, an extra lens, called a Bertrand lens, is added to the optical path in front of the CCD (see figure 1(a)). Three different types of STM tips are compared: commercial cut PtIr tips, electro-chemically etched W tips and electro-chemically etched Ag tips [87]. The tips have been imaged with a scanning electron microscope. Whereas the W and Ag tips have a regular shape with a radius of about 50 nm, the PtIr tips have a completely erratic shape with a radius of several micrometres.

The gold film surface is imaged with the STM before and after each experiment to verify that no change in the surface has occurred.

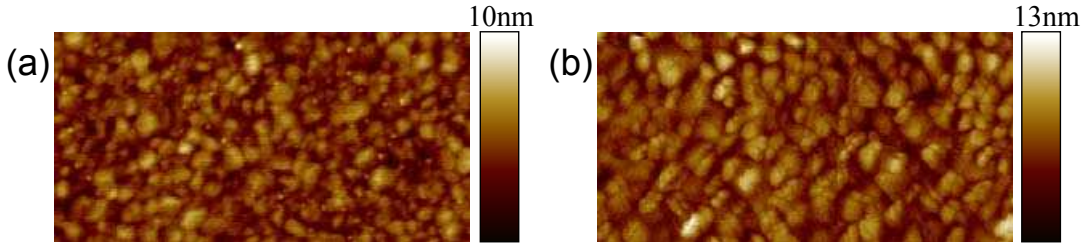

Figure 3.2: Atomic force microscope (AFM) topography image (a) and STM topography image (b). The roughness measured from the topography images is around 1.5nm. The AFM topography image is recorded in tapping mode with a Si tip and the STM image is recorded with a PtIr tip.

Figure 3.1(b) and 3.1(c) shows the schematics defining the different angles in the experiment for the case of the (b) oil and (c) air objective. The red arrows k'_{spp} and k_{quartz} represent the real parts of the wavevectors of the SPP and leakage radiation respectively. The blue dashed lines designate the critical angle, θ_{crit}. The black dotted lines show the collection angles of the two objectives. From the sketch (b), we see that in order that the component of k_{quartz} parallel to the interface be equal to the real part of the SPP wavevector, i.e., $k^{\parallel}_{quartz} = k'_{spp}$, k_{quartz} must make an angle θ_{LR} with respect to the optical axis. This leakage radiation angle θ_{LR} is slightly larger than the critical angle. In (b) we see that $\theta_{LR} < \theta_{NA}$, the maximum collection angle for the oil objective (NA = 1.45), so that the leakage radiation may be collected in this configuration. In (c), for the air objective (NA = 0.75), not only is $\theta_{LR} > \theta_{NA}$, the maximum collection angle for the air objective, but since $\theta_{LR} > \theta_{crit}$, the leakage radiation undergoes total internal reflection at the quartz/air interface.

3.3 Results and discussions

3.3.1 Propagating surface plasmons on a gold film

We use leakage radiation microscopy to investigate the STM excitation of propagating SPP on a gold film sandwiched between air and a quartz substrate. Leakage radiation microscopy has been used in previous experiments where SPP have been excited optically [69, 22, 70, 64, 71]. An important difference between STM and optical excitation is that a whole range of radiation frequencies ν, with $h\nu <$ eV , may be produced with the STM (V is the surface bias voltage) [81, 82].

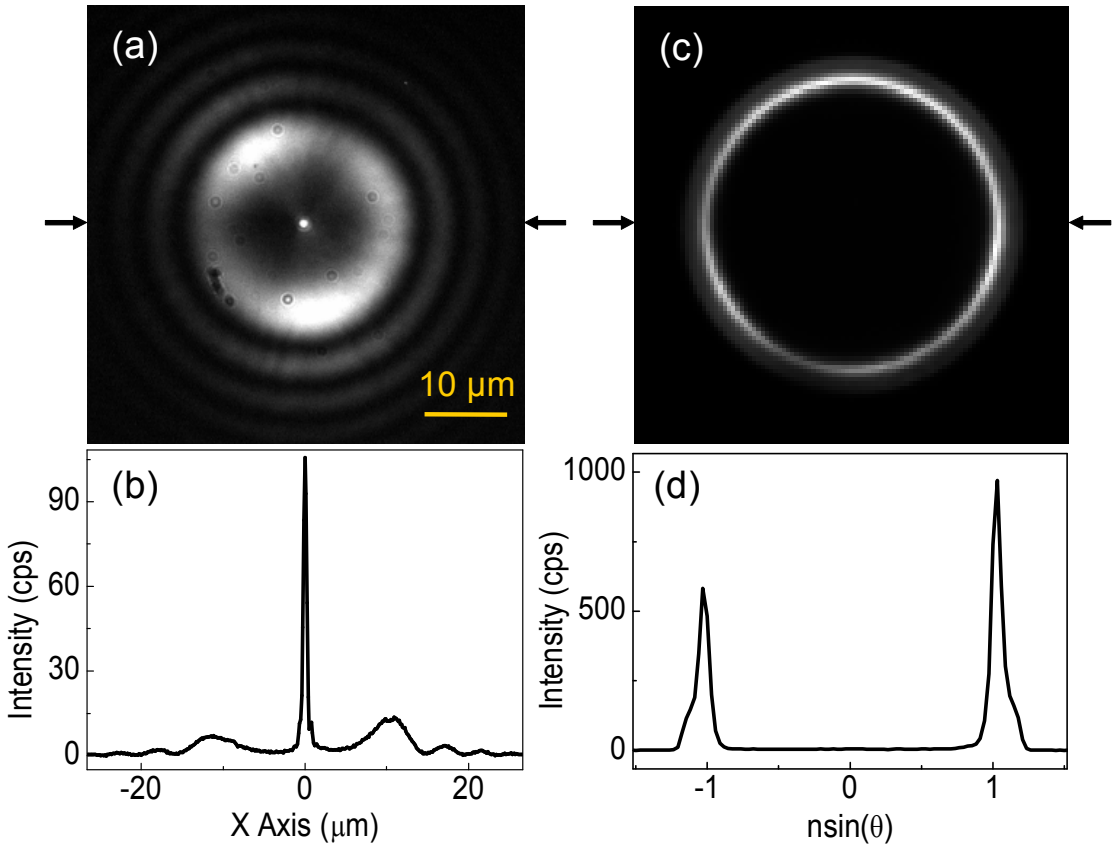

Figure 3.3: Light collected through the quartz substrate of an air/Au film/quartz system during STM excitation (oil immersion objective, NA = 1.45). Images are recorded for 60 s with I = 5 nA and V = +2.5 V, using a tungsten STM tip. (a) Two-dimensional image plane data showing the spatial distribution of the collected light and (b) the corresponding cross-section (average of three measurements) along the X axis (see arrows in (a)). (c) Corresponding two-dimensional Fourier space data showing a bright ring and (d) the horizontal cross-section (see arrows in (c)). In (d), n = 1.4585 is the quartz refractive index and θ is the angle (with respect to the optical axis) of the emitted light excited by the STM. The scale for (d) was determined by back focal plane calibration.

Leakage radiation microscopy has already been discussed in subsection 2.1.4, in this case, the leakage radiation relation (coupling condition) can be written as:

$$Real[k_{spp}(\nu)] = k'_{spp}(\nu) = k^{\parallel}_{quartz}(\nu) = nsin(\theta_{LR})k_0(\nu) \tag{3.1}$$

with k'_{spp} and $k^{\parallel}_{quartz}$ represent the real parts of the wavevectors of the SPP and the in-plane component of leakage radiation wavevectors parallel to the gold/quartz interface, n is the refractive index of the quartz substrate 1.4585. The θ_{LR} is the leakage angle. The k_0 is the wavevector in free space and $k_0 = 2\pi\nu/c$ with frequency ν. Since as discussed in 2.1.4, $\theta_{LR} > \theta_{critical}$, so this is expected that leakage radiation may be detected through the quartz substrate using an oil immersion objective ($NA = nsin(\theta) > 1$) but not an air objective ($NA < 1$, see figure 3.1(c)).

Electrically induced photon emission is recorded by placing the STM tip at a fixed

position on the film surface and maintaining a constant tunnel current I (e.g., I = 5 nA) and surface voltage V (e.g., V = 2.5 V). A tungsten tip is used for the images shown in figures 3.3 and 3.5. The recording time for each image is 60 s. Image plane and Fourier space data recorded with the high numerical aperture (NA = 1.45) oil immersion objective are shown in figures 3.1(a) and (c) respectively. The image plane (figure 3.1(a)) shows a narrow central peak whose full width at half maximum (FWHM) is approximately 0.6 μm and is limited by diffraction. Furthermore, a broad feature, made of several concentric bright rings, extends up to more than 30 μm from the centre. broad feature is assigned to leakage radiation from propagating SPP whose intensity decreases with increasing distance from the excitation point. The dark circular fringes in the image plane (figure 3.3(a)) are an artifact caused by refractive index mismatch as previously observed with similar experimental setups [63, 88] and we will discuss this artifact in section 3.4.

The Fourier space image in figure 3.3(c) consists of a bright ring. This result shows that the maximum intensity of the emission occurs at large angles, confirming the existence of propagating SPP. From our data we estimate θ_{LR} to be $\approx 45° \pm 1°$, i.e., larger than the critical angle for the quartz.air interface ($\theta_{crit} = arcsin(1/1.4585) = 43.3°$), as expected for leakage radiation from propagating SPP. Moreover, $k'_{spp}(\nu)/k_0(\nu) = nsin(\theta_{LR}) = 1.4585 * sin(45° \pm 1°) = 1.03 \pm 0.015$. From SPP dispersion relation shown in figure 2.4, we can then estimate that the wavelength of this leakage radiation should be in the range 650-800 nm. We emphasize that our Fourier space image (figure 3.3(c)) is markedly different from that which was previously reported for similar experimental conditions [85]. Here, our Fourier space result shows intense emission at large leakage radiation angles, i.e., for $NA > 1$, whereas in [85], the Fourier space image shows a peak at NA = 0 which was assigned to propagating SPP.

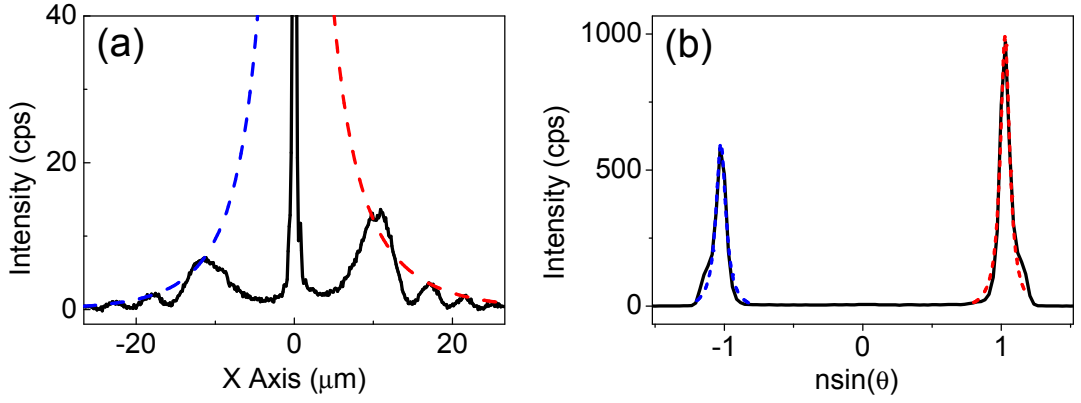

Figure 3.4: Propagation length analysis with the cross-sections from real space image (a) and Fourier space image (b). The cross-section of real space image is the same cross-section as in figure 3.3(b). The blue (left) and red (right) dashed lines are the 2D exponential decay fitting. The fitting lines fit well the peaks. The left (blue) dashed line give a propagation length ≈ 8 μm, and the right (red) dashed line give a propagation length ≈ 10 μm. The cross-section of Fourier space image is the same cross-section as in figure 3.3(d). The blue (left) and red(right) dashed lines are Lorentzian profile fitting.

The propagation length (L_{SPP}) of the propagating SPP is deduced from the cross-sections from real space image (see figure 3.4(a)). Figure 3.4(a) is the same as figure 3.3(b). The blue (left) and red(right) dashed lines are the 2D exponential decay fitting because the STM-excited SPP are circular waves. The function used is $e^{-\frac{r}{L_{spp}}}/r$, where r is the distance from the excitation point (tip position)[22]. The fit does not look good due to the artifact of refractive index mismatch (section 3.4). But at least, the fit agrees well with the peaks. The left (blue) dashed line gives a propagation length of 8 μm, and the right (red) dashed line gives a propagation length of 10 μm. With more statistics, we obtain a propagation length 10 $\pm$ 5 μm which is in good agreement with the theoretical calculation shown in figure 2.4(b) and other measurements of the damping constant of propagating SPP on gold film surfaces, albeit for different film thicknesses [26, 63, 22]. We note that this decay length varies with gold film thickness.

Figure 3.4(b) shows the same cross-section of Fourier space image as in figure 3.3(d). The blue (left) and red(right) dashed lines are Lorentzian profile fitting. In principle, by measuring the FWHM of the Lorentzian profiles, we can obtain the propagation length L_{SPP}= 1/(FWHM*k_0) [64]. The measured FWHM= 0.102 (left) and 0.095 (right) and k_0=8.97 1/μm (at λ=700 nm) which gives a propagation length of only $\approx$ 1.1 μm (left) and $\approx$ 1.17 μm (right). So it is very clear that the propagation lengths determined in this way are much shorter. One reason may be that the plasmon peaks are broaden because of the broad spectra of STM-excited propagating surface plasmons (see section 3.3.2). Another reason may be our poor back focal plane resolution. In our back focal plane image, one pixel is equal to 0.02941 (k_{SPP}/k_0), so if the plasmon peak FWHM is only 1 pixels, we deduce a propagation length of L_{SPP}=3.8 μm. Thus in our experiments, it is best to deduce the propagation lengths of the propagating surface plasmons from the real space images.

It is important to realize that the central peak in figures 3.3(a) and 3.3(b), although intense, accounts for a little amount of the total detected emission when integrated over the two dimensions of the image plane. This means that the majority of the detected emission originates from propagating SPP. The exact percentage depends on the tip in our experiments. As mentioned previously, this emission from propagating SPP could not be detected in previous STM experiments when the light was detected above the air or vacuum/gold interface (i.e., on the same side as the STM tip) [7, 73–83]. We also emphasize that the central peak emission could not be detected, even if it existed, in previous experiments using optical excitation, since any induced radiation from the excitation point is indistinguishable from the excitation source [63].

Similar experiments are reported in figure 3.5, this time using a small numerical aperture (NA = 0.75 $<$ 1) air objective instead of the high NA (NA $>$ 1) oil immersion objective. Only the narrow central peak emission is observed in figure 3.5(a). The corresponding Fourier space image in figure 3.5(c) consists of a disc of low intensity. The abrupt cutoff of the Fourier space signal occurs at the numerical aperture of the air objective, i.e., at its maximum collection angle (see figure 3.1(c)). The fact that the Fourier space image consists of a disc means there is no preferential angle at which the light is emitted-in other words, there is no detected leakage radiation from propagating SPP. The absence of any detected leakage radiation from propagating SPP is easily explained. Using the oil immersion objective we showed in figures 3.3(c) and 3.3(d) that the leakage radiation from

propagating SPP is at large angles i.e., $\theta_{LR} > \theta_{crit}$, and thus cannot be detected with the air objective (see figure 3.1(c)).

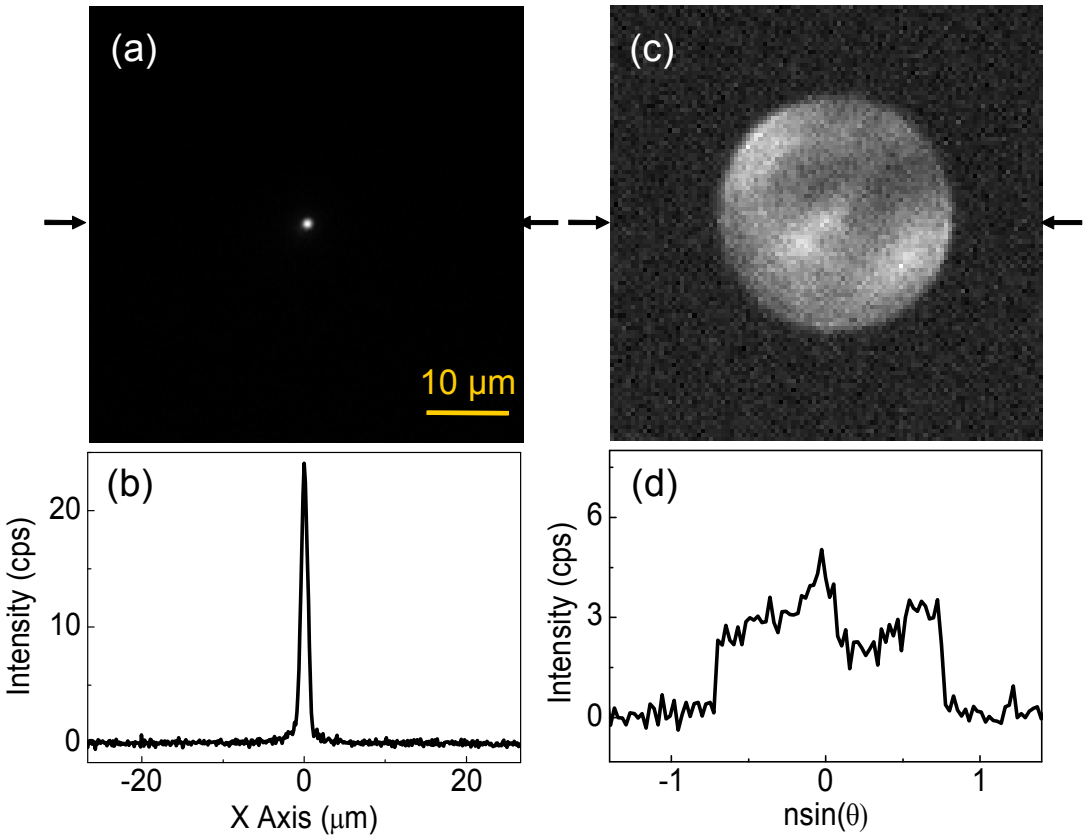

Figure 3.5: Light collected through the quartz substrate of an air/Au film/quartz system during STM excitation (air objective, NA = 0.75). Images are recorded for 60 s with I = 5 nA and V = +2.5 V, using a tungsten STM tip. (a) Two-dimensional image plane data showing the spatial distribution of the collected light and (b) the corresponding cross-section (average of three measurements) along the X axis (see arrows in (a)). Note that in this case only the central peak is observed. (c) Corresponding two-dimensional Fourier space data showing a disc and (d) the horizontal axis cross-section (see arrows in (c)). In (d), n = 1.4585 is the quartz refractive index and θ is the angle (with respect to the optical axis) of the emitted light excited by the STM. The scale for (d) was determined by attributing a value of NA = 0.75 to the abrupt cut-off of the Fourier space signal.

The experiments reported in figures 3.3 and 3.5 were performed using a tungsten tip freshly prepared to avoid tungsten oxidation and whose regular shape was verified by scanning electron microscopy. Similar results are obtained using PtIr tips. However, with PtIr tips, whose shapes are much more irregular, the observed patterns in the image plane due to the leakage radiation of propagating SPP are not as symmetric as with the W tips (figure 3.3(a)). This indicates that the propagating SPP can be perturbed by the STM tip.

3.3.2 Voltage dependence of the emission spectra

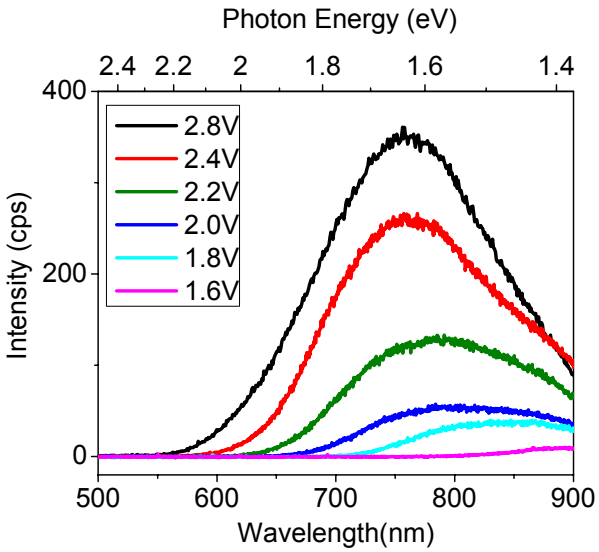

Figure 3.6: Light emission spectra obtained with a PtIr STM tip using an oil objective (NA=1.45). The voltage bias increases from 1.6 V to 2.8 V.

Emission spectra are recorded using the oil objective (NA=1.45) and the spectrometer as shown in figure 3.1(a). A PtIr tip (in figure 3.6 by different sample voltage biases. It shows that when the voltage bias increases from 1.6 V to 2.4 V, the central peak of the relative spectra decreases and the spectra are "blue shifted". However, when the voltage bias is larger than 2.4 V (e.g, 2.8 V), the central peaks of the spectra are stable around 720 nm. This is because the interband transition happens when the voltage bias is higher than 2.4 V, which opens new decay channels [6, 10]. Another phenomenon is that the maximum photon energies of the light emission spectra are smaller than the electron energies of the relative sample bias, i.e, $h\nu_{photon} < eV_{bias}$, and this is because that the light(plasmons) are excited by inelastic tunneling electrons and the energy is conserved during the excitation process.

3.3.3 Localized tip-gold film coupled plasmon resonance

In order to investigate the nature of the central peak emission as observed in figures 3.3 and 3.5, we compare results obtained with tungsten and silver STM tips. Silver is a material which has a large plasmonic response in the visible region of light, unlike the case of tungsten. Cross-sections of the spatial distribution of the light detected in the image plane with the oil immersion objective are compared in figure 3.7 for W and Ag tips. As the detected emission intensities may fluctuate from one tip to the other and even for the same tip from one experiment to the other, the experiments were repeated for several different W and Ag tips in order to confirm the results. Figure 3.7 shows that when using a silver tip the central peak intensity is increased by a factor of ≈20 whereas the leakage radiation from propagating SPP is only increased by a factor of ≈2. This clearly demonstrates that the central peak emission and propagating SPP are two distinct optical

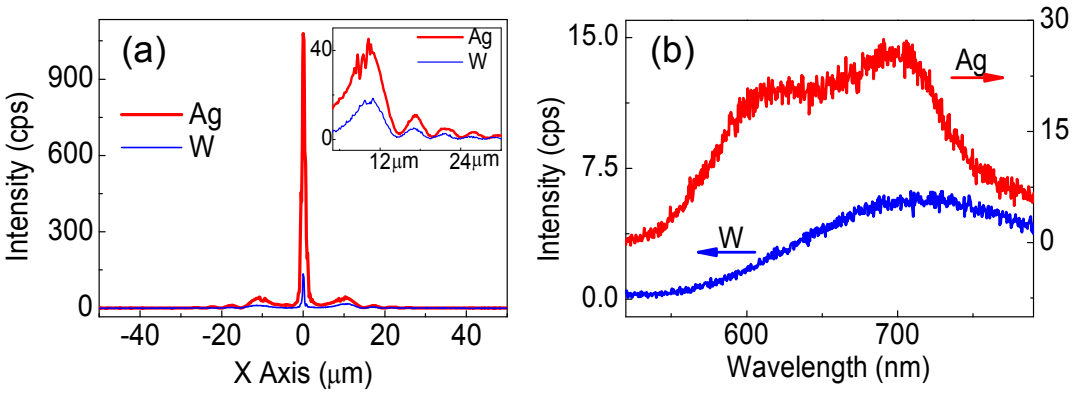

Figure 3.7: (a)Cross-sections of real space images recorded with W (thin blue curve) and Ag (thick red curve) tips using the oil immersion objective (NA=1.45). The data are recorded for 60 s with I = 5 nA and V = +2.5 V. The inset is a zoom showing the propagating SPP part of the two cross-section curves.(b)Emission spectra recorded with W (lower blue curve) and Ag (upper red curve) tips using the air objective (NA = 0.75). Each spectrum is recorded for 20 s with I = 5 nA and V = +2.8 V. Note the two peaks seen in the Ag tip case.

processes. More insight is deduced from the emission spectra (figure 3.6) recorded with the air objective lens which has been shown to select only the central peak emission at small angles (see figure 3.5). The emission spectra are not corrected for the transmission of the detection system. With the W tip, a broad emission spectrum centered around 720 nm is observed. This is consistent with the peak wavelength range estimated in section 3.3.1 above and with the fact that $h\nu_{photon} <$ eV . With the Ag tip, two bands centred around 600 and 700 nm are observed. The emission spectrum with the Ag tip is very similar to the optical scattering spectrum of a Ag nanoparticle (60 nm) on top of a 50 nm gold film [86]. This suggests that the end of the STM tip plays the role of a metallic nanoparticle and, by interacting with the gold surface, creates a localized tip-gold film plasmon resonance.

3.4 Refractive index mismatch

In this experiment, the gold films are deposited on *quartz* substrates. Because the refractive index of quartz (GE 214) at 589.6nm is around 1.4585, it is slightly different than the refractive index of the immersion oil (1.52). Although this slight mismatch does not contradict the fact that the propagating surface plasmons are excited by the scanning tunneling microscope, it influences both the real space and the back focal plane images. The influence is more important for large emission angles, for example, the leakage radiation angle of the propagating surface plasmons.

Figure 3.8(a) shows the schematic image of the defocus effect on a oil-quartz interface. The defocus effect is due to the spherical abberation caused by the mismatching of the refractive indexes of the quartz substrate and the immersion oil. The t is the thickness of the quartz substrate. The light with an angle α is supposed to focus on the top surface of the quartz substrate, but due to the refractive indexes mismatching, the real focus position

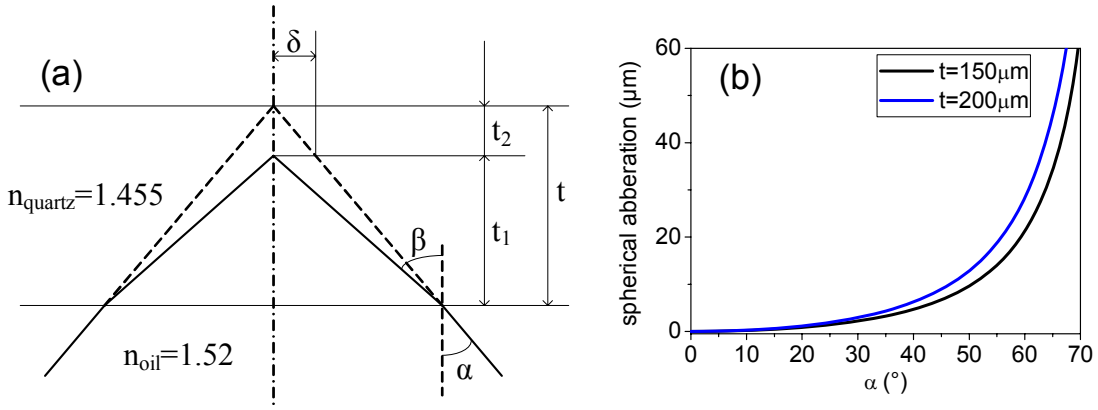

Figure 3.8: (a) Schematic image of the defocus effect on a oil-quartz interface. The defocus effect is due to the spherical abberation caused by the mismatching of the refractive indexes of the quartz substrate and the immersion oil. (b) Spherical abberation as a function of the angle α with different quartz substrate thicknesses (150 μm and 200 μm).

is lower(defocus), and the focus shift is t_2. From Snell equations we have that $n_{oil}\ sin\ (\alpha) = n_{quartz}\ sin(\beta)$. So we find a relation between t_2 and angle α:

$$t_2 = (1 - \frac{tg(\alpha)}{tg(\beta)}) \times t = (1 - \frac{n_{quartz}}{n_{oil}} \frac{\sqrt{1 - (\frac{n_{oil}}{n_{quartz}})^2 sin(\alpha)^2}}{\sqrt{1 - sin(\alpha)^2}}) \times t \tag{3.2}$$

So for small angles around 0°, t_2 = (1-n_{quartz}/n_{oil}) × t=0.0428 t. For large angles the t_2 increases, and the spherical abberation δt_2 between the large angle and the small angle light is [89–91]:

$$\Delta t_2 = t_2(\alpha) - t_2(\alpha = 0) = \frac{n_{quartz}}{n_{oil}} (1 - \frac{\sqrt{1 - (\frac{n_{oil}}{n_{quartz}})^2 sin(\alpha)^2}}{\sqrt{1 - sin(\alpha)^2}}) \times t \tag{3.3}$$

The spherical abberation as a function of the angle α with different quartz substrate thicknesses (150 μm and 200 μm) is shown in figure 3.8(b). At the leakage radiation angle of 45°, the abberation is around 6.7 μm for a 150 μm quartz substrate and 9 μm for a 200 μm quartz substrate.

Because of this spherical abberation, the real space image (figure 3.3(a)) of the propagating surface plasmons on the 35 nm thin gold film deposited on the top surface of the quartz substrate is defocused, so there is a dark ring round the central peak. In figure 3.3(a), the radius of the dark ring is around 6μm which is nearly the same as the calculation above, which means that this theoretical deduction is reasonable.

From the discussion above, we know that in figure 3.3(a), the central peak is actually related to the small angle radiation (smaller than critical angle) of the local emission under the STM tip. The first bright ring from the central peak is related to the large angle radiation (larger than critical angle) of the local emission under the STM tip and the propagating surface plasmons radiation close to the STM tip.

This defocus effect is demonstrated further in the defocusing experiments of STM excited surface plasmons on a 50nm gold film with glass substrates (see Appendix B and

figure B.2). To avoid this artifact, we must use glass substrates with a refractive index very close to 1.52 for gold film deposition and must focus well on the gold film surface.

3.5 Conclusion

We have analysed the light induced by inelastic electron tunneling in an air/thin gold film/quartz system. Detection of the photon emission through the quartz substrate enables us to unambiguously demonstrate STM excitation of propagating SPP on the gold film with propagation lengths of the order of 10 μm. Moreover, this leakage radiation from propagating SPP accounts for the majority of the total detected photon emission. The remaining minority part is localized under the STM tip. The two-peak spectrum found with Ag tips suggests that this localized emission is due to a tip-gold film plasmon resonance.

These results provide new insight on light emission induced by STM on gold films. In most of the previous studies [7, 73–83]„ the excitation of propagating SPP on gold films was not considered. This is due to the fact that under typical experimental conditions the light emission is detected above the air or vacuum-Au interface (i.e., on the same side as the STM tip). In this case, the propagating SPP cannot be detected since there is no leakage radiation into the medium with n $\sim$ 1. From the present results, we learn that the excitation of propagating SPP by inelastic tunneling is in fact a very efficient process, as it gives rise to the overwhelming majority of the detected photons in our experiment. The light emission detected in previous studies [7, 73–83], is probably due to a localized tip-gold film plasmon resonance that we have also investigated. This resonance is considerably enhanced when a W STM tip is replaced by a Ag tip. At the same time, the excitation efficiency of propagating SPP is only weakly affected by the nature and the shape of the tip. This ability to excite very locally, with a spatial resolution smaller than one nanometre, propagating SPP with tunnelling electrons from the STM tip offers interesting perspectives to combine nanoelectronics with nanophotonics.

Chapter 4

The Tip Effects of STM-excited Surface Plasmons on Gold Films

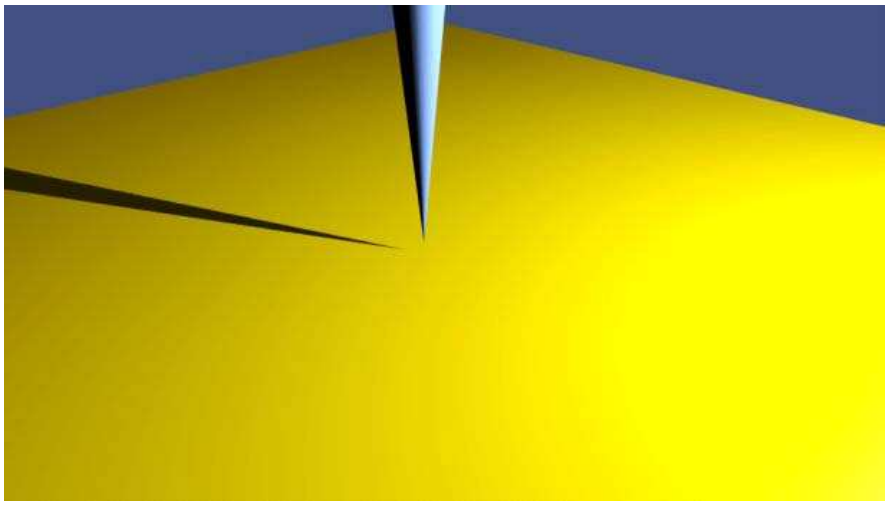

4.1 Introduction

The role of the tip shape (size) and material in light emission from the scanning tunneling microscope (LESTM) has been studied both theoretically and experimentally since 1990s [7, 92–98]. But in most of the previous LESTM experiments, photon emission was detected on the tip side (in other words the air or vacuum side) where propagating SPP do not radiate, unless the noble metal surface is very rough. Consequently previous calculations and experiments on the role of the tip shape and material involve only the localized surface plasmons excited in the tunneling junction. Combining an STM with an inverted optical microscope and recording light emission excited from the STM on the glass side of the gold film samples, we have demonstrated that both localized surface plasmons and propagating surface plasmons are excited on a thin gold film with an STM tip in chapter 3 and ref.[99]. What is more important is that the majority of the detected photons originate from propagating SPP. In this case, it is possible to investigate the tip effects with our setup not only for the STM-excited localized surface plasmons but also for the major source of the intensity : STM-excited propagating surface plasmons.

Another interesting point is central peak pattern of the STM-excited surface plasmons in the real space images. The central peak pattern shown in chapter 3 (figure 3.3) and ref.[99] is different from the pattern reported by Bharadwaj et al [53] with a very similar setup. In our case, we used a W tip to excite surface plasmons on a gold film and we found a high intensity peak at the tip position. In the paper by Bharadwaj et al. they used a Au tip to excite surface plasmons on a gold film and they found a dip at the tip position. What is reason for these different central peak patterns? How does the tip affect the central peak pattern? Can we use the STM tip to selectively excited different plasmon modes (localized and propagating modes)? What parameters of the STM tip are crucial for exciting the propagating surface plasmons?

In this chapter, we demonstrate how the shape and material of STM tips affect the STM-excited localized and propagating surface plasmons on thin gold films. We find that in the real space with a sharp (symmetric) W tip or a Ag tip the central peak pattern is a donut shape and with a blunt (asymmetric) W tip the central peak pattern is a high intensity peak. Furthermore, with a deeper understanding of the real space and Fourier space images, we quantitatively calculate the relative ratio between the STM-excited localized surface plasmons and the STM-excited propagating surface plasmons on gold films with different film thicknesses. The spectrum of the STM-excited surface plasmons does not depend on the tip shape but does depend on the tip material. It is also shown that the spectrum of the STM-excited surface plasmons is blue shifted when the gold film thickness increases.

4.2 Experiment preparation

The experimental setup is shown in figure 3.1. A scanning tunneling microscope operating in air is coupled to an inverted optical microscope. Photons induced in the sample by the inelastic tunneling of electrons from the STM are detected through the substrates. To match the refractive index of the immersion oil, thin gold films are deposited on glass substrates (n_{glass}=1.52, thickness 170 μm). The optical microscope is equipped with a

x100 oil immersion objective (numerical aperture NA= 1.45). The light emitted through the sample may be focused on a cooled charge-coupled device (CCD) camera to investigate the real space distribution of the emitted light or dispersed with a diffraction grating in order to obtain the emission spectrum. A third possibility is to add an extra (Bertrand) lens in front of the CCD camera to study the Fourier space image and thus determine the angular distribution information of the light emission excited with the STM tip.

For all real space and Fourier space images shown in this chapter, the STM parameters are I_{tunnel}=6 nA, sample bias V_s=2.8 V and the integration time of the CCD camera is 60 s.

Preparation of gold film samples

Gold film samples are prepared by electron beam evaporation under high vacuum (1x 10^{-7} torr). Gold film samples with different gold film thicknesses (6, 20, 35, 50 and 70 nm) are made at CTU (Centrale de Technologie Universitaire) IEF-Minerve in Orsay. The root-mean-square surface roughness as measured by atomic force microscopy is found to be about 1.5 nm. The AFM topography images of a 6 nm and a 50 nm gold film are shown in figure 4.1. It is clear that the 6 nm gold film is not uniform and it seems that there are randomly distributed big particles on the 6 nm gold film. On the contrary, the 50 nm gold film is more uniform.

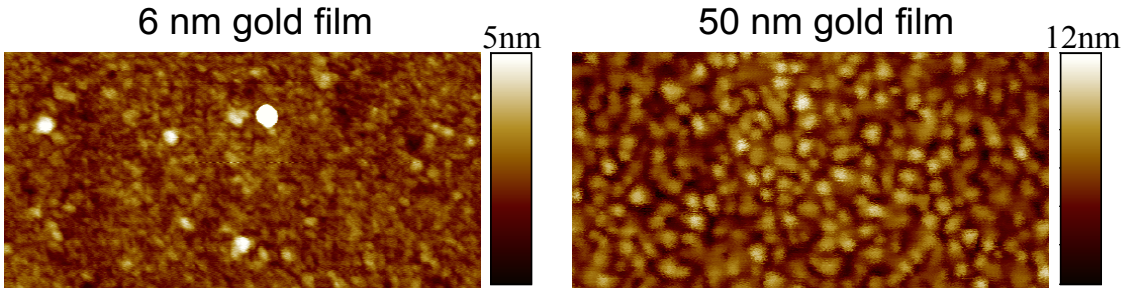

Figure 4.1: AFM topography images of (a) a 6 nm and (b) a 50 nm gold film. The AFM image size is 1 μm $\times$ 0.5 μm.

Preparation of the three types of STM tips

Three types of STM tips have been used for this study. The first two are made of tungsten, and have been fabricated by two different processes, leading to different tip shapes; the third is made of silver. The blunt W tip is made by electrochemical etching with an AC power supply using an NaOH solution (80g Na_2O_2 dissolved in 650ml H_2O and mixed with 350 ml glycerin) and results in a somewhat blunted, slightly asymmetrical shape as seen in figure 4.2(a). From scanning electron microscope (SEM) images the radius of curvature is estimated at $\sim$ 400 nm. The sharp W tip is made by electrochemical etching with a DC power supply (no glycerin is used) and is much finer and more symmetric (figure 4.2)(b); the radius of curvature is measured to be $\sim$ 70 nm. The silver tip is made by electrochemical etching in ammonia solution (25% volume ratio) with a DC power supply (see figure 4.2)(c). The radius of curvature is measured to be $\sim$ 400 nm.

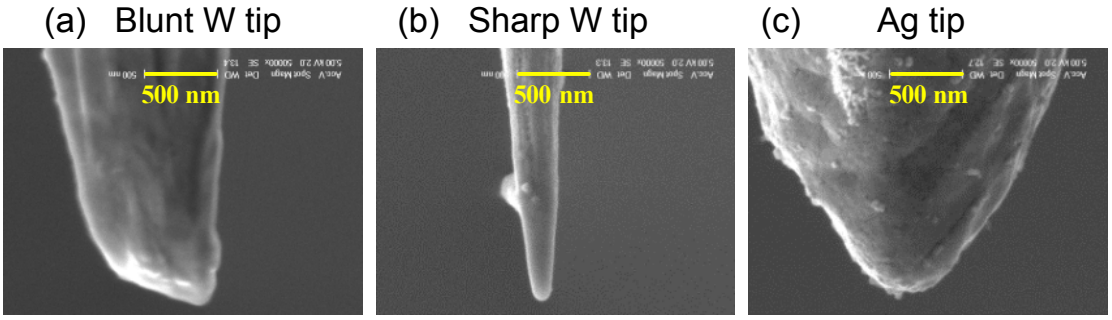

Figure 4.2: Scanning electron microscope images of the three types of tips. The yellow scale bar is 500 nm. The radius of curvature are ∼400 nm (a), ∼70 nm (b), ∼400 nm (c) respectively.

The three types of STM tips are used to electrically excite surface plasmons on gold film sample of different gold film thicknesses respectively. For each case, both real space images and Fourier space images are recorded. Meanwhile, the corresponding spectra are also recorded.

4.3 Real space images on gold films of different thicknesses obtained with the three types of STM tips

4.3.1 Propagating SPP in real space images

With the three types of STM tips (blunt W tips, sharp W tips and Ag tips), we excite surface plasmons on gold films of different thicknesses. The real space images are recorded using an oil objective (NA=1.45) on a cooled ($-70°C$) Roper CCD camera.

Figure 4.3 presents the real space image of light emission excited by blunt W tip on a 50 nm gold film with different gray scales. The images are recorded using an oil objective (×100, NA=1.45) by leakage radiation microscopy. In (a), only the central peak is seen. In (b), the image gray scale has been chosen so that the lateral extent of the propagating surface plasmons is visible, thus saturating the central peak. It is clear that other than the high intensity central spots, we also see the surface plasmons which propagate on the surface from the tip position (center of the image). The large concentric rings in (b) are due to the diffraction limitation of the leakage radiation microscopy, the detail explanation can be found in Ref.[100].

Figure 4.3(c) and (d) show the corresponding cross-sections obtained on samples of different gold film thicknesses with different intensity scale. In figure 4.3(c), we clearly see that the maximum intensities of these cross-sections are the same so that we can compare the relative intensities of these cross-sections. The FWHMs of these cross-sections are all around 1μm, actually the actual size of the excitation is much smaller than 2 μm [94]. From figure 4.3(d) we see that on gold films thicker than 20nm, the cross-sections exponentially decay from the tip position (center of the image). In order to see the change of these cross-sections at large x value, the maximum intensities at (x=0) in these cross-sections are the same. Furthermore, we see qualitatively that the decay length of the

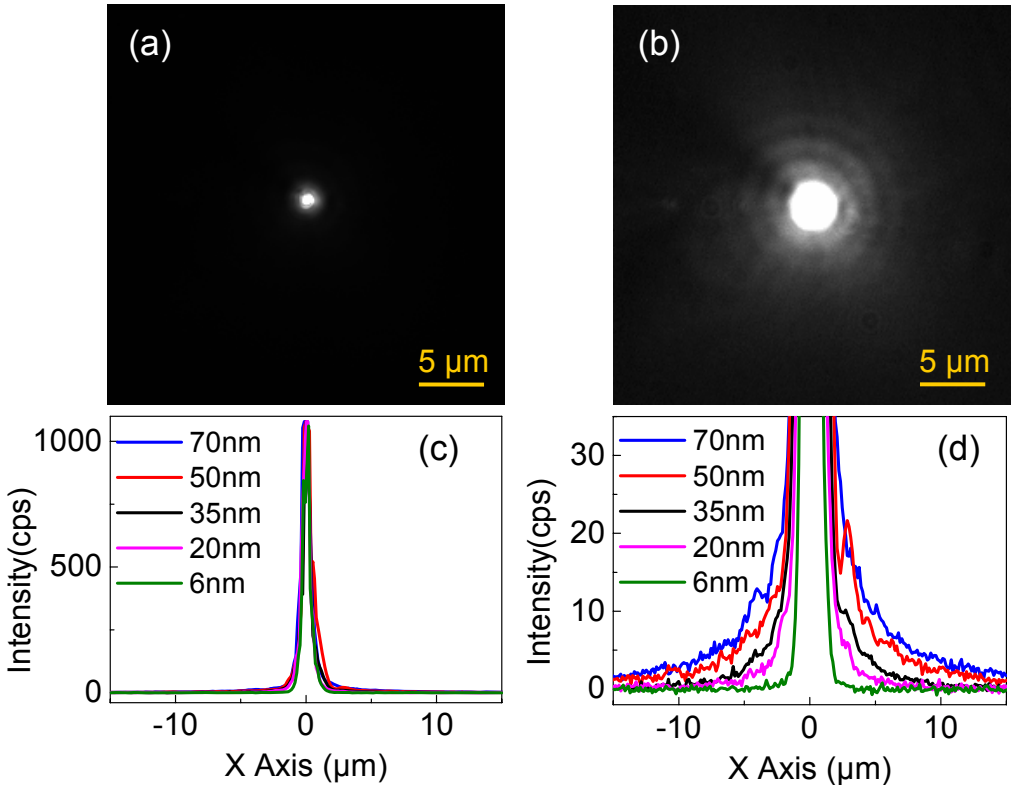

Figure 4.3: Real space image of light emission excited with a blunt W tip on a 50 nm gold film with different gray scales shown in (a) and (b). The image is recorded with an oil objective (×100, NA=1.45) in the leakage radiation microscopy configuration. The tip is in the center of the images. In (a), only the central peak is seen. In (b), the central peak is saturated in order to clearly see the propagating surface plasmons. The corresponding cross-sections obtained on samples of different gold film thicknesses are shown in (c) and (d) with different intensity scale. Note that the images of the propagating surface plasmons with a sharp W tip and a Ag tip (not shown) are very similar to the image with a blunt W tip.

cross-sections increases when the gold film thickness increases. This exponential decay strongly suggests that the surface plasmons propagate on the gold films, and that this decay length is the propagation length [22]. In the cross-section from the 6 nm gold film, there is no exponential decay, so we can say there are no propagating SPP excited on 6 nm gold films. This is because 6 nm gold film does not support propagating surface plasmons (see subsection 2.1.3).

Figure 4.4 shows the real space image obtain on a 50 nm thick gold film with a polarizer (a dichroic sheet polarizer (03FPG003, CVI Melles Griot)) placing after the oil objective and before the tube lens. The images in (a) and (b) are the same real space image but with different gray scale. The polarizer is parallel to the object plane. This dichroic sheet polarizer strongly absorbs the light whose electric field direction is perpendicular to the polarizer axis. In figure 4.4, the propagating SPP which propagate along the same direction (y axis) as the polarizer are seen; and the propagating SPP which propagate

along the perpendicular direction (x axis) of the polarizer are not seen. The corresponding cross-sections along x and y axis are shown in figure 4.4(c) and (d). This is very similar to the image of propagating SPP excited with a polarized laser (figure 3 in [22]). This phenomenon clearly indicates that the in-plane electric field direction of the propagating SPP is the same as the propagation direction of the propagating SPP and the propagating SPP are TM-waves propagating on the gold films. The images of STM-excited propagating surface plasmons with sharp W tips and Ag tips are very similar to the images with blunt W tips. In this case, the images of STM-excited propagating surface plasmons with sharp W tips and Ag tips are not shown.

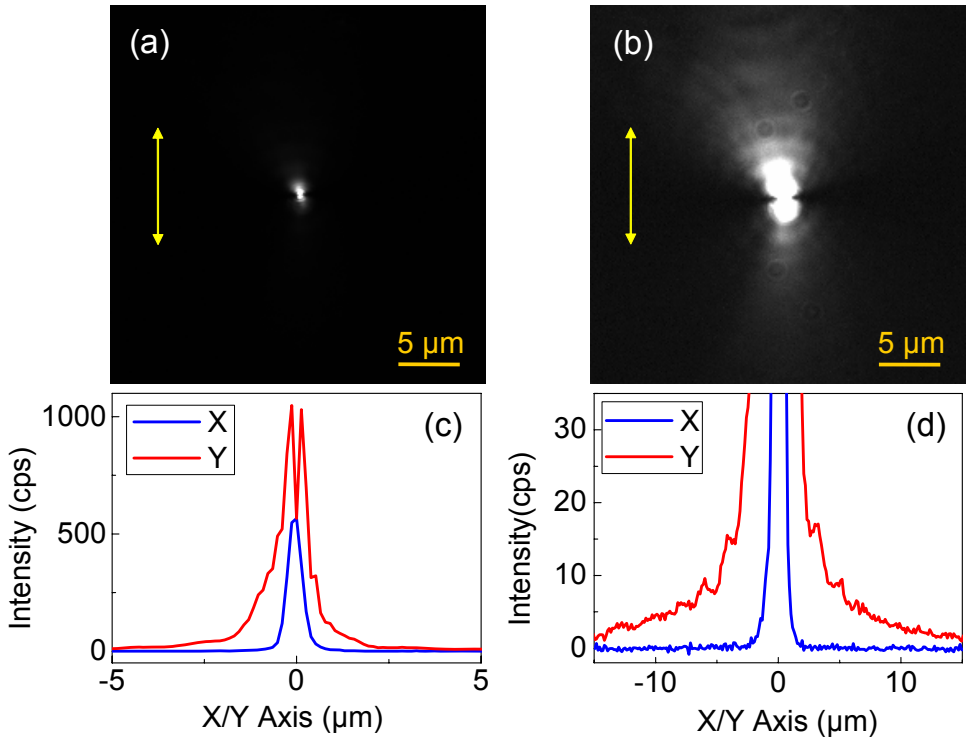

Figure 4.4: Real space images of light emission excited with a blunt W tip on a 50 nm gold film using a polarizer with different gray scales shown in (a) and (b). The images are recorded with an oil objective (×100, NA=1.45) in the leakage radiation microscopy configuration. The tip is in the center of the images. The yellow arrow line indicates the polarizer direction. In (a), only the central peak is seen. In (b), the central peak is saturated in order to clearly see the propagating surface plasmons. The corresponding cross-sections obtained on samples of different gold film thicknesses are shown in (c) and (d) with different scales.

One very important point is that the propagating SPP excited by the STM are 2D circular waves propagating on the gold film surfaces radially away from the tip (STM excitation position). This is quite different from the optically excited propagating SPP where the propagating surface plasmons are often plane waves (such as Kretschmann excitation or grating excitation case) or circular waves with a polarization direction (such as SNOM excitation case). 2D circular SPP waves propagating on the gold film surfaces

may be used as a new type of circular light source for nano-optics experiments. One thing very important is that the real space image is not perfectly symmetric in all the directions because of the tip condition, the surface roughness and so on. For example, in figure 4.4(b) we see the STM-excited propagating surface plasmons in the upper part of the image is more intense.

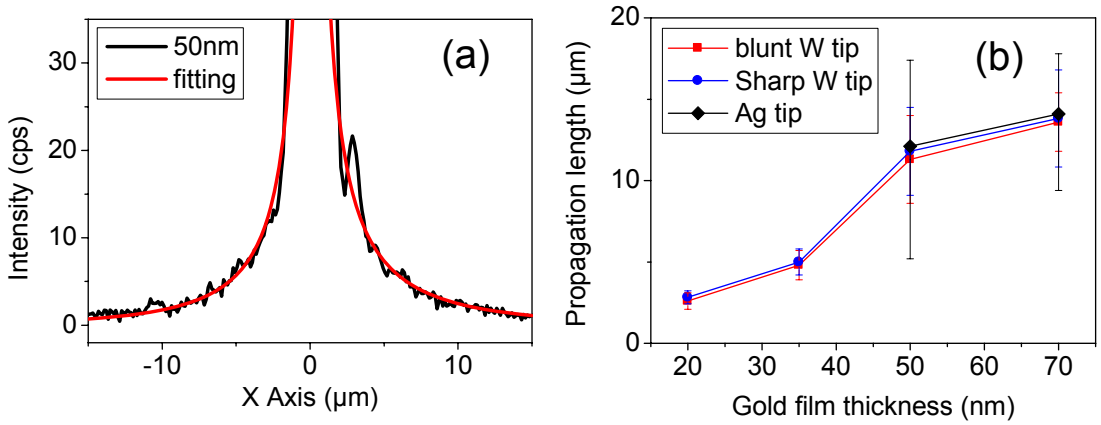

Figure 4.5: (a) Calculating the propagation length of propagating SPP by 2D exponential decay. The experimental data (black line) is the cross-section from figure 4.3 on 50 nm gold film. The red lines are fitted curves. The propagation length is found around 11μm. (b) Propagation lengths of propagating SPP excited with different types of STM tips on gold films with different gold film thicknesses. For the three types of STM tips, the propagation lengths are nearly the same. The propagation length increases as the gold film thickness increases.

From the cross-sections in the real space images we can quantitatively calculate the propagation lengths (L_{SPP}). Figure 4.5(a) shows the method to calculate the propagation length of propagating SPP. We use 2D exponential decay same as in figure 3.4: $e^{-\frac{x}{L_{SPP}}}/x$ (x, distance to the tip position). The experimental data (black line) is the cross-section from figure 4.5 on a 50 nm gold film. The red lines are fitted curves. The propagation length is found around 11μm.

Figure 4.5(b) presents the propagation lengths of propagating SPP excited with different types of STM tips (blunt W tip, sharp W tip and Ag tip) on gold films with different thicknesses. Each point of the data is the average of more than 20 fits as in figure 4.5(a) (the cross-sections are from different real space images obtained with several tips of the same kind). For the three types of STM tips, the propagation lengths are nearly the same. This is because that the propagation length is the intrinsic properties of the gold films. It indicates the damping of the propagating SPP on gold films and it shows the relation between the propagating SPP and the gold films which does not depends on the STM tips. When the gold film thickness increases, the propagation length of propagating SPP increases. The propagation lengths presented in figure 4.5(b) fit well with the theoretical results as shown in figure 2.4(b). Note that in figure 4.5(b), there is a large uncertainties for the results with Ag tips. This is because the Ag tips are soft and fragile. The real space images obtained with Ag tips are less symmetric and the propagation lengths along

different directions vary more.

4.3.2 Central peak intensities and patterns in real space images

To compare the central peak patterns in real space images, we excite surface plasmons on a 50 nm gold film sample with the three types of STM tips (blunt W tips, sharp W tips and Ag tips). Like in last subsection, the real space images are recorded using an oil objective (NA=1.45) on a cooled ($-70°C$) Roper CCD camera. Figure 4.6 shows the real space central peak patterns and corresponding cross-sections obtained with the blunt W tip (a) (same image as figure 4.2(a) with different lateral and gray scales), the sharp W tip (b) and the Ag tip (c). The indicated intensity in the cross-section is an averaged intensity of more than 70 images for each kind of tip.

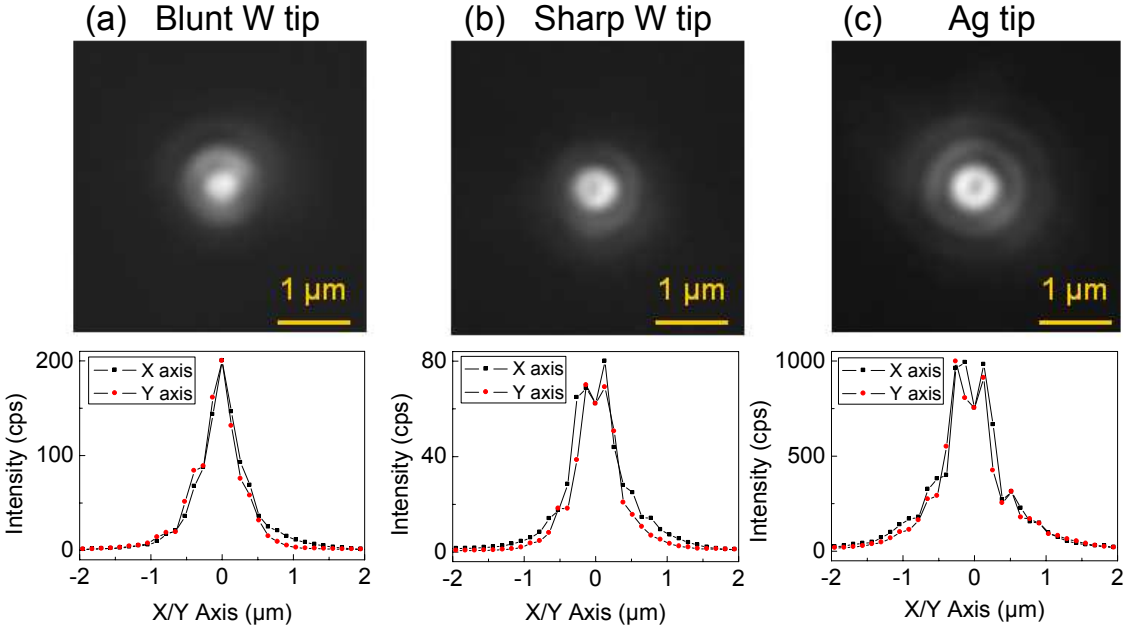

Figure 4.6: Central peak images in real space with blunt W tip (a), sharp W tip (b) and Ag tip (c). The corresponding cross-sections are also shown. The images are obtained on a 50 nm gold film. The SEM images of the tips are shown in figure 4.2. The indicated intensity in the cross-section is an averaged intensity of more than 70 images for each kind of tip.

Central peak intensities comparison

From figure 4.6 (a) and (b), we see that the intensity obtained with blunt W tips (radius of curvature $\sim$ 400 nm) is higher than that of sharp W tips (radius of curvature $\sim$ 70 nm). This phenomenon is already seen and discussed by Johansson et al. that with a larger curvature the interaction area between the STM tip and sample is increased, giving rise to an enhancement of the local field [92–94] (tip-side light detection).

From figure 4.6 (a) and (c), we see that the intensity obtained with Ag tips (radius of curvature $\sim$ 400 nm) is higher than that of blunt W tips (radius of curvature $\sim$ 400 nm). In this case, the radius of curvature is the same. This phenomenon is owing to the fact

that with a plasmonic tip (Ag or Au tip), the light emission from the tunneling junction can be enhanced around 10 times (1 order of magnitude) [7, 92, 93, 96, 97] (tip-side light detection).

In conclusion, the central peak intensity depends on the tip shape (size) and material, which is similar to the previous experiments where the light emission from STM (LESTM) is collected on the tip-side. Because the LESTM on the tip-side is explained by the localized surface plasmons resonance in the tunneling junction, we say that the central peak intensity represents mainly the localized surface plasmons.

Central peak patterns comparison

From figure 4.6 it is clear that the image obtained with the blunt W tip is different from the others (Note that in all the real space central peak patterns, the rings are the Airy pattern of diffraction). For the image obtained with the sharp W tip and the Ag tip, there is a dip in intensity (an intensity minimum) at the center and the central peak pattern has a *donut* shape. This phenomenon is also seen in the x and y cross-sections of the central peaks. For the cross-section of the blunt W tip, the central position (x=0, y=0) has the maximum intensity, but for the cross-section of the sharp W tip and the Ag tip, there is a drop in intensity at the central position. We conclude that the central peak pattern of the STM-excited light emission depends on the shape and the material of the STM tip.

First, we compare the central peak patterns obtained with the blunt W tip and the sharp W tip. The two types of tips are made of the same material and the difference is the shape of the tip. From figure 4.6(a) and (b), it is clear that the size of the central peak patterns does not depend on the the radius of curvature. It may indicate that the emission size of the tunneling junction is smaller than the diffraction limitation (similar to a point source). Actually, the symmetry of the tip is very important for the central peak pattern. The electromagnetic modes in the tip-surface cavity excited by the inelastic electron tunneling can be modeled by an oscillating dipole [7, 10, 92, 94, 97, 101], and the direction of the oscillating dipole largely depends on the symmetry of the tip, especially the symmetry at the end of the tip. If the tip is perfectly symmetric, the oscillating dipole used in the model is perpendicular to the gold film surface; otherwise the oscillating dipole is not perpendicular to the gold film. From the SEM image of the tips, we see that the sharp W tip is symmetric and the blunt W tip is asymmetric. So the tunneling between the sharp W tip and the gold film may be modeled as a vertical oscillating dipole, but not the one of the blunt W tip. From the theoretical calculation of a dipole near an interface, we know that for an oscillating dipole which is perpendicular to the interface, the central peak pattern is a *donut* shape and for oscillating dipole which is parallel to the interface, the central peak pattern is a high intensity peak [40]. Note that because of background noise, surface roughness of the film, finite detector pixel size, and the slightly asymmetry of the sharp tip, the minimum in figure 4.6(b) is not a perfect null, which is also seen in ref. [53].

Second, we compare the central peak patterns obtained with the sharp W tip and the Ag tip. The two types of tips are made of different materials but central peak patterns both have *donut* shapes. Although the central peak patterns are the same, the physical principle

is different. For sharp W tip, the *donut* shape pattern is due to the symmetry of the W tip and the related oscillating dipole orientation. But for Ag tip, the *donut* shape pattern is due to the local tip-film plasmon resonance (see subsection 3.3.3) [86, 99, 102, 103]. The Ag tip has plasmonic resonance in visible range, and during the STM excitation the Ag tip is predominantly excited [98]. The end of the Ag tip is most easily modeled as a Ag nanosphere [7, 10, 92, 93, 97], so an oscillating dipole can form in the Ag nanosphere during the STM excitation. This oscillating dipole excited in the end of the Ag tip is also similar to the case in ref.[104] where they use a high electron beam to excite individual silver sphere on a silver film: If the Ag tip is perfectly symmetric, the induced oscillating dipole is perpendicular to the gold film surface; otherwise the induced oscillating dipole is not perpendicular to the gold film.

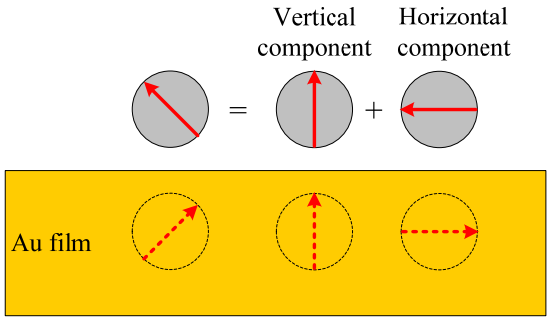

Figure 4.7: Simplified representation of interaction of a plasmonic sphere with a gold film. The oscillating dipole induced in the plasmonic sphere can be considered as the sum of the vertical component and the horizontal component. The vertical component induces an image dipole vertical to the gold film with the same direction. The horizontal component induces an image dipole parallel to the gold film with an opposite direction.

This nanosphere-film system is already well studied experimentally using laser excitation [86, 102, 103], the donut shape pattern is always seen no matter the polarization direction of the nanosphere. The explanation is that at low frequencies (well below the plasma frequency of the metal film), the oscillating dipole in the metal particle near a gold film can induce an oscillating dipole in the gold film. According to the "boundary conditions" at the air-gold interface, the vertical (perpendicular to the gold film) component of the oscillating dipole in the metal particle can induce an image dipole in the gold film that is aligned in the same direction. The horizontal (parallel to the gold film) component of the oscillating dipole in the metal particle can induce an antiparallel image dipole in the gold film. In this case, in the vertical direction, we can assume that a new vertical dipole with a longer oscillating length forms with the sum of the vertical components of the oscillating dipole in the metal particle and the corresponding image dipole. While in the horizontal direction, a quadrupole (with a shorter oscillation length) forms with the sum of the parallel component of the oscillating dipole in the metal particle and the corresponding image dipole [86]. Both a vertical dipole or a quadrupole near an interface give a donut shape pattern in the real space image [105], so for a nanosphere-film system there is always a donut shape pattern in the real space image no matter the polarization direction of the nanospheres.

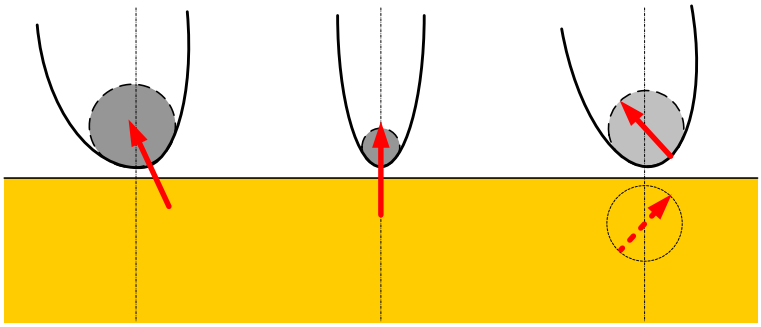

Figure 4.8: Schematic representation of the induced oscillating dipole by the tunneling junction between the STM tips and the gold film. The orientation of the induced oscillating dipole depends on the tip shape and the tip materials.

Similar to nanospheres, for STM-excited surface plasmons experiments with Ag tips, no matter the shape (symmetry) of the Ag tip, we always get a donut shape cental peak pattern in the real space image. The schematic representation of the induced oscillating dipole by the tunneling junction between the STM tips and the gold film is shown in figure 4.8. A more detailed numerical analysis of the local electric field in the STM tunneling junction based on static approximation is shown in "Appendix A". One thing that needs to be emphasized is that the polarization of the W tip can be ignored because of its small polarizability compared to that of the Ag tip. In other words, the W tip is not excited and cannot induce an image dipole in the gold film.

A very important point is that the model described in "Appendix A" is limited. In this model, the interaction between the tip and the film is not fully treated, especially for the case when the STM tip is very close and tunnel to the gold film as in our experiments. Detail discussions about the tip-film interactions are recently done in ref.[98, 106]. In these two papers, they both found two localized modes in the tip-film junction: "the high energy particle dipolar plasmon modes" and "the low energy evanescent plasmon waves of the film". "the high energy particle dipolar plasmon modes" is the same as in the model described in "Appendix A". "the low energy evanescent plasmon waves of the film" has a similar behavior as the propagating surface plasmons. These localized modes can both affect the central peak pattern, so it could be also a reason why the dips at the center obtained with the sharp W tip and the Ag tip (figure 4.6(b) and (c)) are not a perfect null.

4.3.3 Propagating and localized surface plasmons in real space images

In the subsection 4.3.1, we calculate the propagation lengths of propagating SPP on gold films with different thicknesses using 2D exponential decay fitting. For the same equation, we can transform the 2D exponential decay fitting to linear fitting:

$$\begin{aligned} I &= I_0 \, \frac{e^{\frac{-x}{Lspp}}}{x} \\ Ln[I \times x] &= Ln[I_0 \, e^{\frac{-x}{L_{SPP}}}] \\ Ln[I \times x] &= A + \frac{-x}{Lspp} \end{aligned} \tag{4.1}$$

In this way, we can use a linear fitting procedure to fit the cross-sections from the real space images. We use the intensity I in figure 4.3(a) and time I with x. The Ln[I × x] as a function of x is shown in figure 4.9(a). The cross-section shows different behavior at large (x > 2μm) and small (x < 2μm) distances from the tip position. The red line is the linear fit for x > 2μm and the propagation length is found to be around 11μm. However, when x is smaller than 2μm (close to the STM tip), the red line does not fit the experimental data. Thus, we cannot assign this part of light to propagating surface plasmons. However, we may assign it as the component of localized surface plasmons trapped in the tip-film junction because this part of light is very close to the tip position and does not propagate.

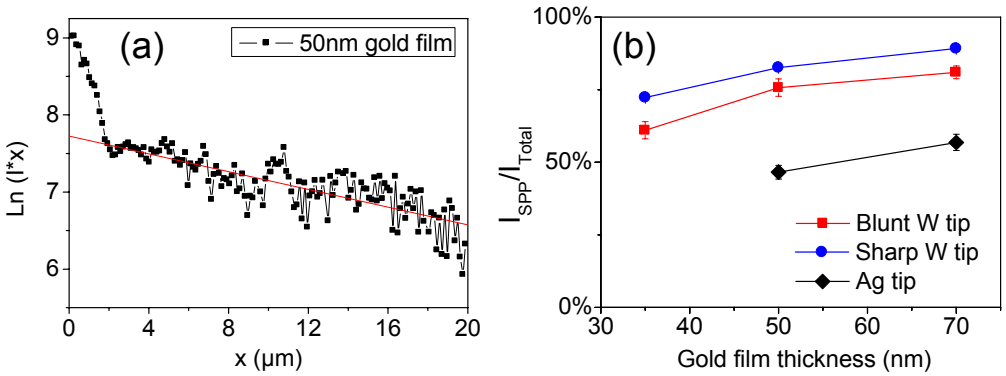

Figure 4.9: (a) Calculating the propagation length of propagating surface plasmons by linear fitting using equation 4.1. The experimental data (black line with black squares) is the cross-section from figure 4.3 on the 50 nm gold film. The red line is the linear fit for x > 2μm from the tip position. (b) The ratio between the intensity of propagation SPP and the total intensity calculated from the real space images on gold films with different thicknesses obtained with blunt W tip, sharp W tip and Ag tip. The ratio varies with the tip shape and material and also with the thickness of the gold films.

In figure 4.9(a), the intensity corresponding to the red line fit can be considered as propagating part. By using the parameters from the fit on a linear scale and integrate the fitted curves for the whole real space image, we can get the intensity of propagating SPP I_{SPP} in the real space image. Then, we can calculate the ratio I_{SPP}/I_{Total} between the propagating SPP and the total intensity of the real space image (More data on gold films with different thicknesses as figure 4.9(a) are shown in figure 4.10). Similarly, the data obtained by a sharp W tip are shown in figure 4.11. Apparently the intensity of localized surface plasmons I_{LSP} is equal to the difference between I_{Total} and I_{SPP}.

Figure 4.9(b) presents the ratio between the intensity of propagation SPP and the total intensity calculated from the real space images on gold films with different thicknesses obtained with blunt W tip, sharp W tip and Ag tip. From figure 4.9(b) we see that the ratios are all larger than 50%, on 70 nm, the ratios are even higher than 75%, so we can say that the propagating SPP dominate the light emission excited with a STM tip on gold films.

From figure 4.9(b) we also see that the ratios I_{SPP}/I_{Total} varies with the tip shape, the tip material and the thickness of the gold films. The variation with the tip shape (blunt

W tip and sharp W tip) may be due to the oscillating dipole direction in the tunneling junction between the STM tip and the gold film surface. For the very symmetry tip (sharp W tip), the oscillating dipole in the tunneling junction is perpendicular to the gold film. For the asymmetry tip (blunt W tip), the oscillating dipole in the tunneling junction is not perpendicular to the gold film and the oscillating dipole can be looked as partially perpendicular and partially parallel to the gold film. To excite propagating SPP, a dipole vertical to the gold film excites more efficiently than the dipole parallel to the gold film [62]. The variation with the tip shape (blunt W tip and sharp W tip) may be also due to the fact that the diameter of the blunt tip is larger than that of the sharp W tip. The tip with a larger diameter can trap more light in the tunneling junction [94], so that the localized emission intensity is larger and the ratios I_{SPP}/I_{tot} is smaller. The variation with gold film thickness is due to the fact that thicker gold film support better the propagating surface plasmons (more oscillating electrons, less leakage damping) [43, 106].

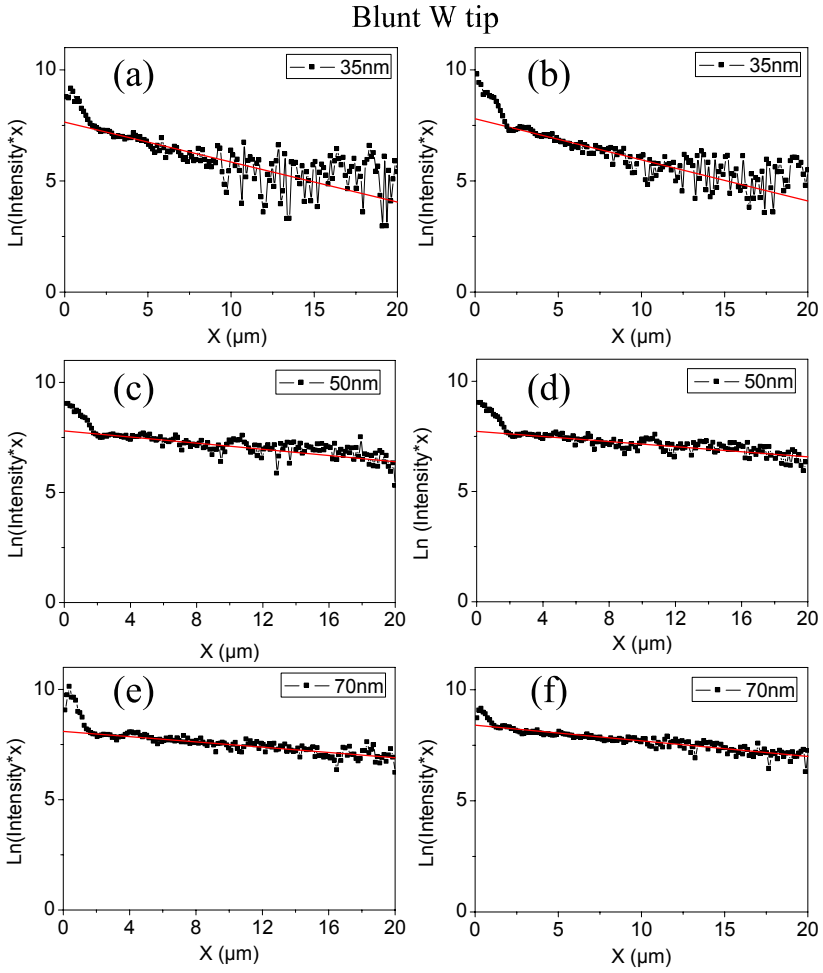

Figure 4.10: Calculating the propagation length of propagating surface plasmons by linear fitting using equation 4.1. The experimental data (black line with black squares) is the cross-section obtained with a blunt W tip from figure 4.3 on 35 nm ((a) and (b)) , 50 nm ((c) and (d)) and 70 nm ((e) and (f)) gold film. The red lines are the linear fits for x > 2μm from the tip position.

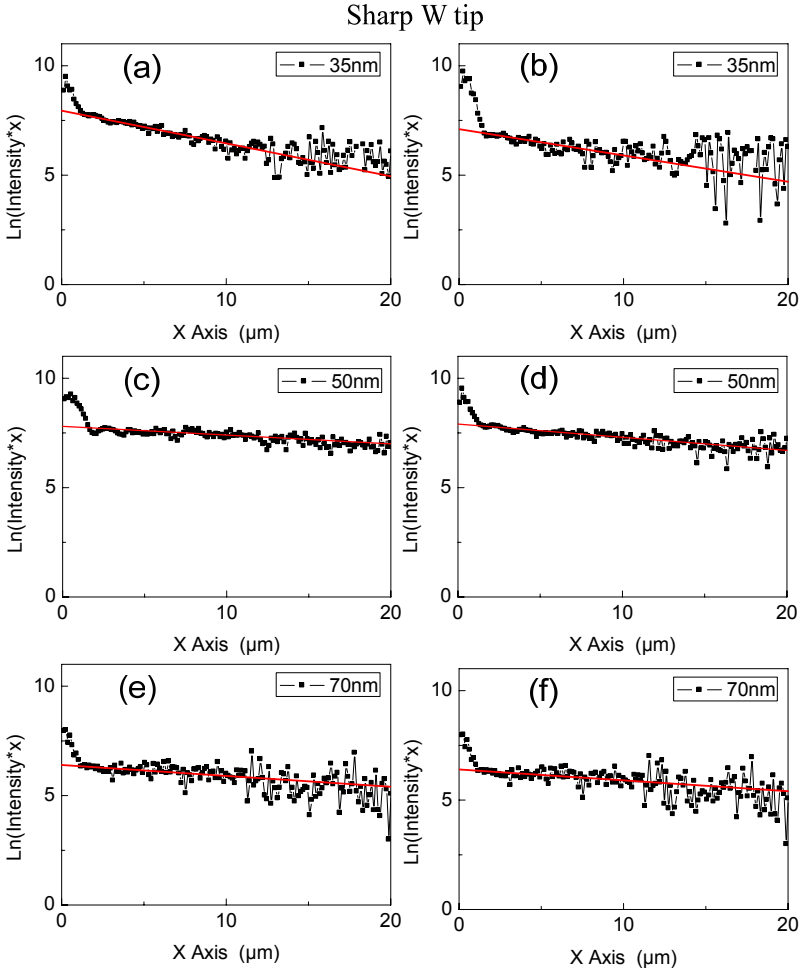

Figure 4.11: Calculating the propagation length of propagating surface plasmons by linear fitting using equation 4.1. The experimental data (black line with black squares) is the cross-section with a sharp W tip on 35 nm ((a) and (b)) , 50 nm ((c) and (d)) and 70 nm ((e) and (f)) gold film. The red lines are the linear fits for x $>$ 2μm from the tip position.

4.4 Fourier space images on gold films of different thicknesses obtained with the three types of STM tips

The Fourier space images present the angular distribution of the light emission from the object plane. It is very important to fully understand the Fourier space images in order to better comprehend the light emission excited by STM.

Figure 4.12(a) shows the Fourier space images of light emission excited by a blunt W tip on a 50 nm gold film. Figure 4.12(b) shows the corresponding cross-sections on samples with 6 nm, 20 nm, 35 nm, 50 nm and 70 nm gold film thicknesses. It is very clear that there is a propagating surface plasmons ring (in figure 4.12(a)) and peaks (in figure 4.12(b)) for gold film thickness thicker than 20 nm. In figure 4.12(b), we see that the peak positions are all slightly larger than the critical angle and exactly at the same position as the theoretical calculated propagating surface plasmon peaks in Fourier space (see figure 2.15).

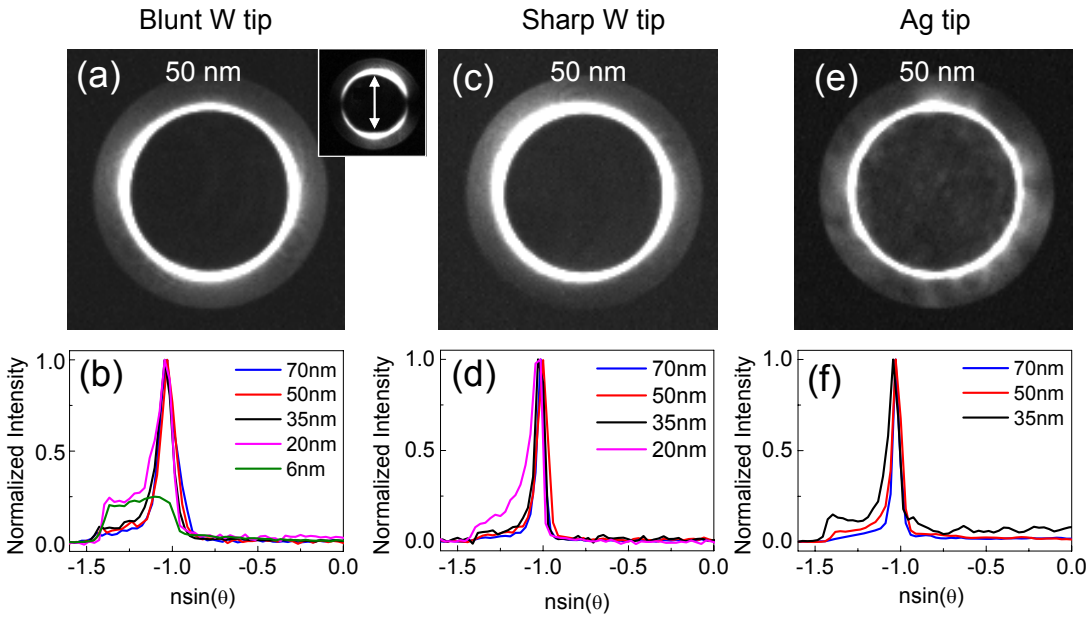

Figure 4.12: Fourier space images of light emission excited with a blunt W tip (a), a sharp W tip (c) and a Ag tip (e) on a 50 nm gold film. The corresponding cross-sections are shown in (b) for 6 nm - 70 nm gold films with a blunt W tip, (d) for 20 nm - 70 nm gold films with a sharp W tip and (f) for 35 nm - 70 nm gold films with a Ag tip. Note that in (b) the 6 nm cross-section is normalized to 0.25 for clarity. The inset to (a) is the Fourier space image with a polarizer, and the double arrow indicates the polarizer direction. Note that the cross-sections are only half range for a better view of the peaks.

In figure 4.12(b), it is very clear that there is no propagating surface plasmons peak for the 6 nm gold film. From the dispersion relation (as shown in figure 2.4(a)) we know that gold film $\approx$ 6 nm does not support propagating SPP, so no propagating surface plasmons are excited by the STM tip and hence no propagating surface plasmon peak can be observed.

The inset of figure 4.12 (a) shows the result when a polarizer (oriented in the direction of the double arrow) is placed in front of the CCD camera. The result is reminiscent of that which is obtained when exciting SPP with a near field optical probe with polarized light [22], confirming that the polarization of the leakage radiation is as expected for propagating SPP.

Figure 4.12(c) shows the Fourier space images of light emission excited by a sharp W tip on a 50 nm gold film. Figure 4.12(d) shows the corresponding cross-sections on samples with 20 nm, 35 nm, 50 nm and 70 nm gold film thicknesses. As in figure 4.12(a), there is also a propagating surface plasmons ring in figure 4.12(c). A slight difference compare to those cross-sections in figure 4.12(d) may be that the peaks in figure 4.12(d) seem a little narrower.

Figure 4.12(e) and (f) show the Fourier space images of the light emission excited with a Ag tip on a 50 nm gold film and the corresponding cross-sections on gold films with 35 nm, 50 nm and 70 nm thicknesses. As in figure 4.12(a), there is also a propagating surface plasmons ring in figure 4.12(e). However, in figure 4.12(e) we see that there is

more intensity at small angles (nsin(θ<1), which indicates more "localized" light emission (especially for the 35 nm gold film case). A slight difference compare to those cross-sections in figure 4.12(b) may be also that the peaks in figure 4.12(f) seem a little narrower.

Except this plasmon peak, there is also light emission at large angles which looks like "shoulder" in the cross-sections. From figure 4.12, it is clear that the "shoulder" in the cross-sections obtained with a sharp W tip or a Ag tip is lower than that obtained with a blunt W tip.

4.4.1 The dispersion relation of SPP deduced from Fourier space images

The propagating surface plasmons ring at the correct angle in the Fourier space images is direct evidence of propagating SPP. The width of the propagating surface plasmons ring is related to the damping of the propagating SPP, so one can calculate the propagation length of the propagating SPP from the width of the plasmon ring [64].

Here, we demonstrate that the dispersion relation of the propagating surface plasmons can also be deduced from the plasmon ring of electrical excited surface plasmons with a STM tip. The reason is that the light emission of the electrical excited propagating SPP is broadband (see figure 3.6). Due to the dispersion relation of the propagating SPP (figure 2.4) and the leakage radiation properties (subsection 2.1.4), different wavelengths have different leakage radiation angles, so in the Fourier space the position of the propagating surface plasmons ring changes for different wavelengths (theoretical calculation shown in figure 2.17(a)).

In this case, on the same 50 nm gold film we record the Fourier space images of the STM-excited surface plasmons with different bandpass filters to see the changes of propagating surface plasmons ring. The cross-sections of these propagating surface plasmons rings at different wavelengths are shown in figure 4.13(a). In figure 4.13(a) one thing very obvious is that the positions of the plasmons peaks are all larger than 1. Also, the position of the peaks are different for different wavelengths. From these peak positions we calculate the related propagating SPP wavevectors (real part). The calculated value fits well with the theoretical dispersion curve (figure 4.13(b)).

From this experiment, we are sure that these peaks originate from propagating surface plasmons. We also know that we can deduce the dispersion relation of thin gold films from the Fourier space images of the broadband propagating SPP excited using a STM tip with the help of bandpass filters. It is a new way to experimentally determine the dispersion relation of thin metal films.

In the other hand, we understand that these propagating surface plasmons rings in the Fourier space images contains the dispersion information, and the widths of the propagating surface plasmons rings are certainly broadened because of the different positions of the propagating surface plasmons rings with different wavelengths. From the dispersion relation (figure 2.4), we can calculate the width broadening due to the dispersion of the broadband propagating SPP.

Figure 4.14 clearly shows the range of this Fourier space propagating surface plasmons peaks width extension which is due to the dispersion of the broadband propagating SPP. It is quite obvious that on 50 nm gold films the maximum ratio between Re[k_{SPP}] and k_0 is $\approx$ 1.08 at λ=520 nm and at λ=800 nm the ratio is only $\approx$ 1.02. This indicates that the

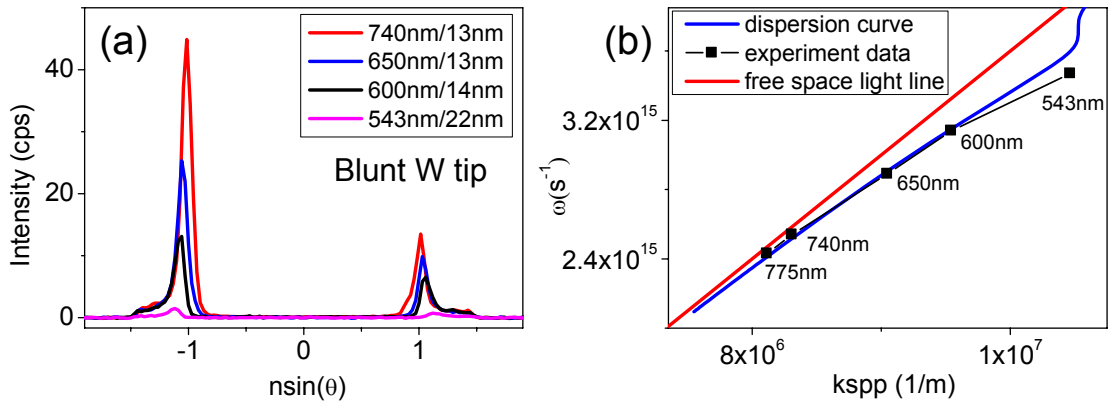

Figure 4.13: (a) Cross-sections of the plasmon rings with different bandpass filters. (b) The blue curve is the dispersion curve of SPP waves propagating along the air/gold interface of a 50nm gold film (already shown in figure 2.4(a)). The black squares are the calculated propagating SPP wavevectors (real part) from the plasmon peaks in (a). The calculated value fits very well with the dispersion curve. The central wavelengths of the plasmon rings are also indicated in (b)

width of the propagating surface plasmons peak in the Fourier space can be enlarged by $\sim$ 0.06 (1.08-1.02) due to the dispersion of the broadband propagating SPP. In figure 4.12, the FWHM of the propagating surface plasmons ring on 50 nm gold film is $\approx$ 0.11, larger than 0.06. This is because other parameters such as the damping of the propagating SPP and limited Fourier space resolution also needs to be considered.

4.4.2 Propagating and localized surface plasmons in Fourier space images

From the discussion above, we know that there are two contributions of light recorded in the Fourier space images: the propagating SPP and the localized surface plasmons. In this subsection, we propose a method to quantify the intensity of propagating SPP and local surface plasmons respectively in the Fourier space images and give the relative ratio between them. The contribution of the propagating SPP is very clear: the plasmon rings (in the Fourier space images) or peaks (in the corresponding cross-sections). So we integrate the intensities of the plasmons peaks to get the intensity of the propagating SPP and then the rest is assigned to localized surface plasmons.

Figure 4.15(a) shows the propagating SPP intensity and the localized surface plasmons intensity in the half cross-section curves. In the half cross-section, above the green dash line, is the SPP peaks. The rest, below the green dashed line, is assigned to the localized surface plasmons contribution. If we integrate the intensity of the whole SPP peaks, we can quantitatively calculate the intensity of propagating SPP and get the ratio between the propagating SPP and the total intensity I_{SPP}/I_{Total} from the Fourier space images.

Figure 4.15(b) gives the I_{SPP}/I_{Total} from the Fourier space images for gold films of different thicknesses obtained using different STM tips. From figure 4.15(b) we see that similar to figure 4.9(b), the ratios with W tips are all larger than 50%, and on 70 nm the

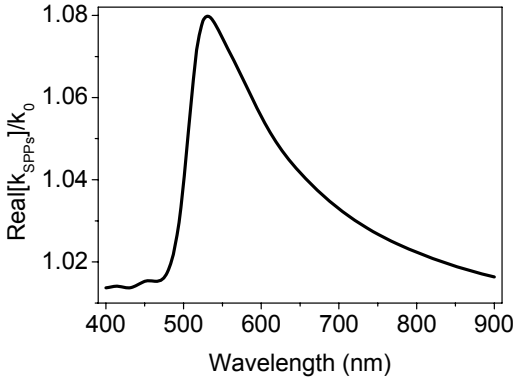

Figure 4.14: Wavelength dependence of the ratio between the Real$[k_{SPP}]$ and k_0 on 50nm gold film. Real$[k_{SPP}]$ is the real part of the in-plane wavevector of propagating SPP. k_0 is the wavevector of the light in free-space. From equation 2.11, Real$[k_{SPP}]/k_0$ equals to nsin(θ) (θ is the leakage radiation angle (plasmon angle)). It is very clear for different wavelengths the positions of the plasmon rings are different.

ratios are even higher than 75%, so we can also say that the propagating SPP dominate the STM-excited light emission on gold films.

From figure 4.15(b) we also see that on gold films of the same thickness, the ratios I_{SPP}/I_{Total} with W tips are obviously higher than the ratios with the Ag tip. This may be because of the local tip-film plasmon resonance between the Ag tip and the gold film. This local tip-film plasmon resonance largely enhances the local emission owing to the gap plasmons enhancement [99]. Because the local tip-film plasmon resonance, the light emission in the allowed light region ($I_{nsin(\theta<1)}$) should be enhanced. This phenomenon is seen in figure 4.16(b) where we clearly see that for Ag tips the ratio between the allowed light intensity and the total intensity ($I_{NA<1}/I_{Total}$) is higher than that for W tips.

There is also a difference between the I_{SPP}/I_{Total} of blunt W tip and sharp W tip (similar to figure 4.9(b)). One reason of this difference may be explained by considering the fact that the localized surface plasmons result from the coupling of the STM tip with the sample. If we assume that the tunneling occurs through a small cluster of atoms of the same size at the apex of the two types of W tips, the tip-sample separation is the same in the two cases. However, due to the larger radius of the blunt tip, the interaction area between the tip and sample is increased and more localized surface plasmons is trapped in the tunneling junction, giving rise to an enhancement of the local field [94]. This increases the local emission intensity and decreases the ratio I_{SPP}/I_{Total}. Another reason (not very obvious) may be the different propagating surface plasmons excitation efficiency of different oscillating dipole orientations. As discussed above, a vertical oscillating dipole model (perpendicular to the gold film surface) is used for the sharp W tip and an oscillating dipole that is not perpendicular to the gold film is used for the blunt W tip. The vertical oscillating dipole has a higher coupling efficiency to propagating surface plasmons because the radiation light of a vertical dipole is p-polarized. For a dipole that is not perpendicular to the gold film, the horizontal component which contains the s-polarized radiation light will decrease the coupling efficiency to propagating surface plasmons [40, 62]. This also

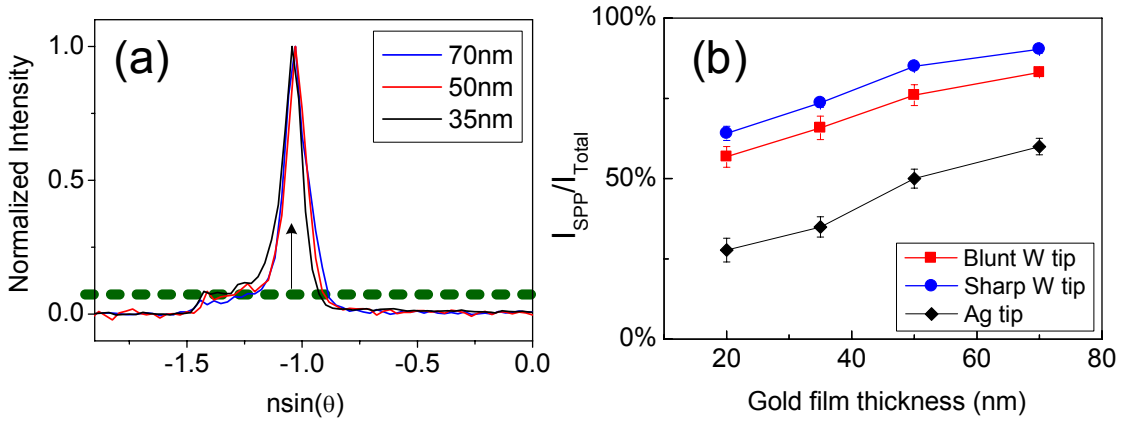

Figure 4.15: (a) The propagation SPP intensity and the local emission intensity in the cross-section curves. Above the green dash line is the intensity of propagation SPP, the rest is the local emission. (b) The ratio between the intensity of propagation SPP and the total intensity calculated from the Fourier space images for different gold film thicknesses with different STM tips. The ratio varies considerably with STM tip shape, material as well as the thickness of the gold film.

makes the I_{SPP}/I_{Total} higher for the blunt W tip.

Another interesting point in figure 4.15 (b) is that the I_{SPP}/I_{Total} varies with the gold film thicknesses (also seen in figure 4.9(b)). It is clear that the I_{SPP}/I_{Total} increases when the gold film thickness increases. The variation with gold film thickness is due to the fact that thicker gold film support better the propagating surface plasmons (more oscillating electrons, less leakage damping) [43, 106].

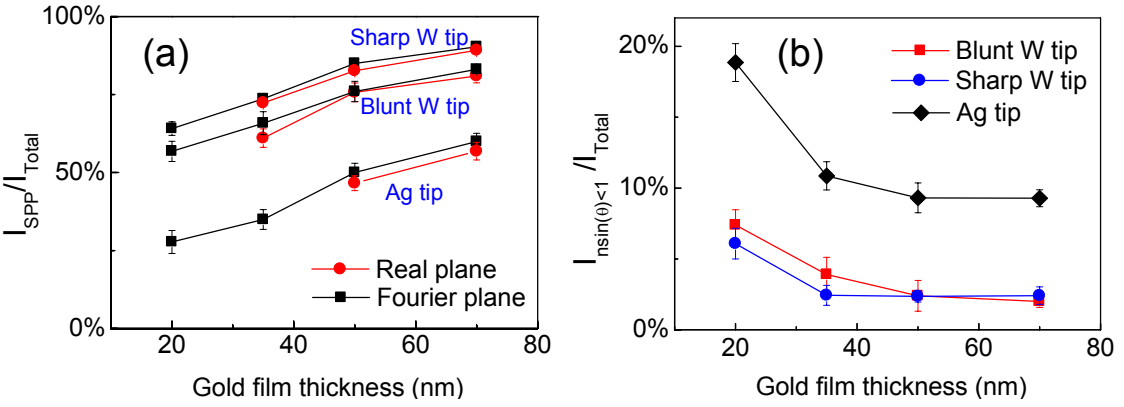

Figure 4.16: (a)I_{SPP}/I_{Total} calculated from both real space and Fourier space. (b)The ratio between the allowed light intensity and the total intensity ($I_{NA<1}/I_{Total}$) on gold films with different thicknesses using the three tips.

Putting the I_{SPP}/I_{Total} ratios deduced from the real space and Fourier space together, we get figure 4.16 (a) which clearly shows that the two methods give a very similar result. This confirms that our deduction of I_{SPP}/I_{Total} ratio from both real space and Fourier space is reasonable.

4.5 Mode Selection between propagating and local surface plasmons with different STM tips

From the previous discussion in this chapter, we clearly see that different surface plasmon modes are excited on gold films by inelastic electron tunneling with the STM, namely localized and propagating plasmons. Both types of plasmon modes are of interest: localized plasmons are of crucial importance for the excitation of quantum emitters in the plasmonic nano-cavity formed between the STM tip and the substrate [107], while propagating plasmons are essential for information transfer at the nanoscale [14, 18]. In this section, we show how we can preferentially excite one type of plasmon mode over another by changing the tip shape or material based on the quantitative calculation of I_{SPP} and I_{LSP} from real space and Fourier space images.

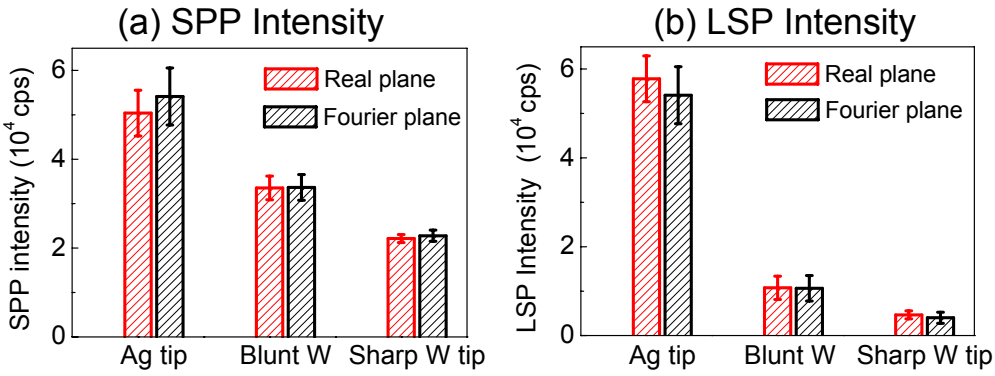

Figure 4.17: The average propagating surface plasmons intensities I_{SPP} (a) and the local surface plasmons intensities I_{LSP} (b) on a 50 nm gold film with the three tips. The average intensities are calculated based on the ratios I_{SPP}/I_{Total} for both real space and Fourier space in figure 4.16.

Figure 4.17 shows the average propagating surface plasmons intensities I_{SPP} (a) and the local emission intensities I_{LSP} (b) on a 50 nm gold film for the three tips calculated from both real space and Fourier space. The way we calculate I_{SPP} and I_{LSP} is described as follows. First, for each type of tip, we integrate all the STM-excited light intensities I_{Total} (on a 50 nm gold film) in a real space image and average for more than 70 images. The averaged I_{Total} reflects the ability of the STM-excited surface plasmons for each type of tip. Then, with the ratio I_{SPP}/I_{Total} (calculated from both real space and Fourier space), we calculate I_{SPP} for each tip. The difference between I_{Total} and I_{SPP} is attributed to I_{LSP}. From figure 4.17, it is clear that I_{SPP} and I_{LSP} calculated from both real space and Fourier space intensity ratio (I_{SPP}/I_{Total}) are very similar.

It is also clear that the localized emission intensities I_{LSP} of the Ag tip are around 10 times higher than the I_{LSP} of W tips (figure4.17(b)), which is similar to the results observed before [7, 53, 92–94, 96, 97]. However, a very interesting point is that the propagating surface plasmons intensities I_{SPP} of Ag tip is just around 2 times higher than the I_{SPP} of W tips, which means the propagating surface plasmons are not greatly influenced by the STM tip material (figure4.17(a)).

Figure 4.18 shows the ratio between I_{SPP} and I_{LSP} based on the data in figure 4.17.

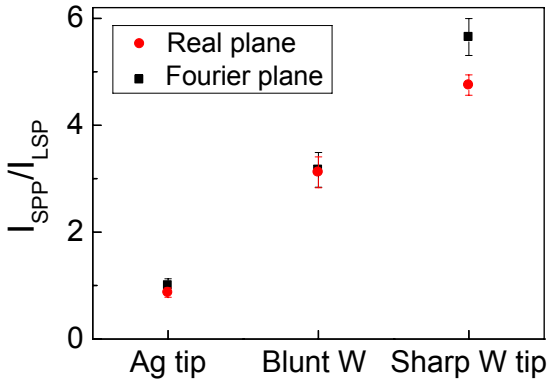

Figure 4.18: The ratio I_{SPP}/I_{LSP} on a 50 nm gold film with the three types of STM tips.

From figure 4.18 we clear see that a silver tip produces a high intensity of localized plasmons whereas a sharp (radius $<$ 100 nm) tungsten tip produces mainly propagating plasmons.

4.6 Spectra of STM-excited surface plasmons

4.6.1 Spectra obtained with the three types of tips on a 50 nm gold film

The spectra of STM-excited surface plasmons on gold films are also very interesting. Figure 4.19 shows the spectra of STM-excited surface plasmons when the three types of STM tips are used on the same 50 nm gold film. It is clear that all the spectra have a similar peak position of $\sim$ 700 nm and similar bandwidth of $\sim$ 150 nm. This indicates that the different STM tips do not influence the spectra very much.

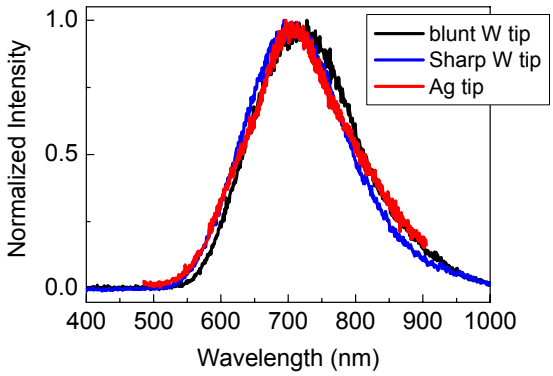

Figure 4.19: The spectra of STM-excited surface plasmons with the three types of STM tips on the same 50 nm gold film. The spectra are recorded using the oil objective ($\times$100, NA = 1.45). The tunneling condition is V=2.8 volts, I=6 nA.

4.6.2 Spectra obtained with the three types of tips on gold films of different thicknesses

Figure 4.20 shows the spectra of STM-excited surface plasmons with a blunt W tip (a) and a Ag tip (b) on gold films of different thicknesses. It is clear that the spectrum depends on the gold film thicknesses! When the gold film thickness increases, the spectra of STM-excited surface plasmons are blue shifted for both types of STM tips (blunt W tip and Ag tip). The spectra peaks on 35 nm, 50nm and 70nm gold film are at $\sim$ 730 nm, 700 nm and 670 nm respectively.

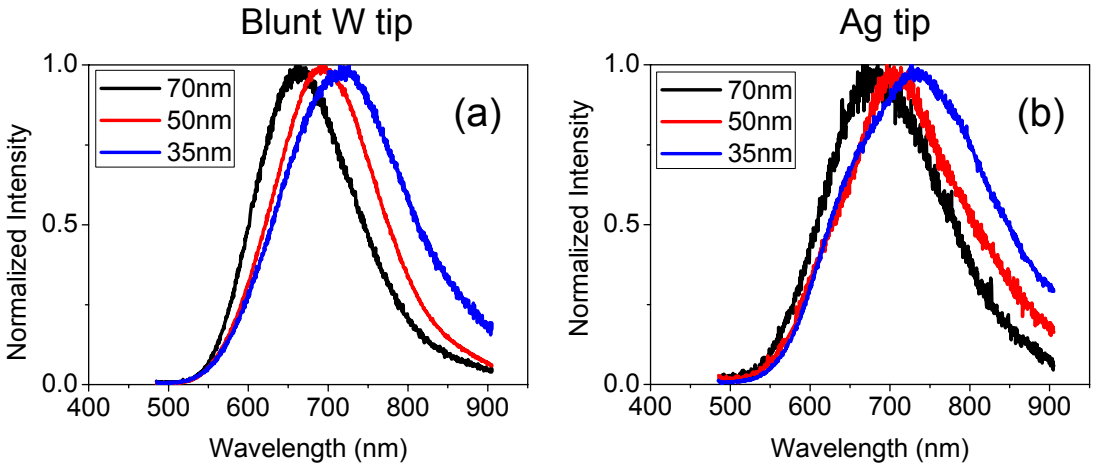

Figure 4.20: The spectra of STM-excited surface plasmons with the same blunt W tip (a) and the same Ag tip (b) on gold films of different thicknesses. The spectra are recorded using the oil objective ($\times$100, NA = 1.45). The tunneling condition is V=2.8 volts, I=6 nA.

Actually, during the STM inelastic tunneling, two modes are excited: a low energy "film-like" propagating surface plasmons mode bound at the air-gold interface and a high energy "particle-like" localized surface plasmons mode [106].

When the gold film thickness increases, the interaction between the two modes decreases which leads to less repulsion between the two modes. This makes the spectra of the two modes closer to each other. Because the localized mode does not change its spectrum during this process (mainly depends on the tip shape and material), the spectrum of the "film-like" propagating surface plasmons mode is blue shifted [106]. The peak position of the spectrum shifts from around 730 nm for 35 nm gold film to 670 nm for 70 nm gold film. This phenomenon is also seen in Ref [106] by theoretical calculation.

In principle, the spectrum with the Ag tip has two peaks which are related to the low energy "film-like" propagating surface plasmons mode and the high energy "particle-like" localized surface plasmons mode respectively. Here, because the two peaks excited with the Ag tip are very close, they merge into a broader spectrum which makes the two peaks difficult to be distinguished [106]. While, with the W tip, the spectrum only has one peak of the low energy "film-like" propagating surface plasmons mode because the high energy "particle-like" localized surface plasmons mode is very weak for a non-plasmonic tip.

4.6.3 Spectra obtained with a Ag tip on a 70 nm gold film

Figure 4.21 shows the spectra obtained with a same Ag tip on a 70 nm gold film. We see that a *"tip" mode peak* [86, 106] is around 600 nm on the red curve. But, on the black curve the *"tip" mode peak* cannot be easily seen. This spectrum variation may be because the tip shape changes during the experiment. We know that the Ag is very soft, so during the experiment, the tip becomes less sharp and the radius of curvature becomes larger, so the *"tip" mode peak* peak becomes less clear. However, in figure 4.21, the *"film" mode peaks* do not change.

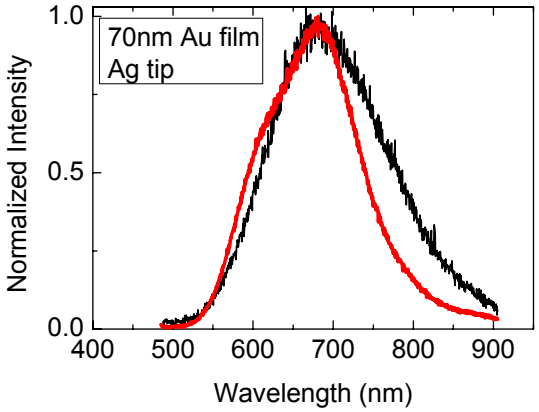

Figure 4.21: The spectra of STM-excited surface plasmons with a same Ag tip on a 70 nm gold film. The spectra are recorded using the oil objective (×100, NA = 1.45). The spectrum variation may be due to the change of the tip shape during the experiment. The tunneling condition is V=2.8 volts, I=6 nA.

4.7 Simulation of Fourier space images using the vertical dipole model

4.7.1 Fourier space images without bandpass filters

Figure 4.22 shows Fourier space images of STM-excited surface plasmons on (a) 50 nm (c) 20 nm and (e) 6 nm thick gold films, obtained with the blunt W tip. It is clear that when the gold film thickness increases, the propagating surface plasmons peak becomes higher and the contribution of propagating surface plasmons increases. This is because there are more electrons in the thicker film which can couple in the oscillation of propagating surface plasmons.

The red curves in figure 4.22 (b), (d) and (f) are the calculated cross section determined by considering the STM tunnel junction as a sum of monochromatic vertical point dipoles all located at the same point 1 nm above the gold film surface [108]. The sum of a series of dipoles of different wavelengths is necessary to take into account the broadband nature of the resulting emission. The dipoles' wavelengths and relative strengths are determined from measured spectra of light from STM-excited surface plasmons. The spectra of the STM excited SPP on gold films of 50 nm, 20 nm and 6 nm are shown in (g)-(i), respectively

(The transmissions of our spectrometer and Roper camera systems have been taken into account). In figure 4.22 (b) and (d), the calculation predicts well the peak positions for SPP, but it does not reproduce the small shoulder present at angles much larger than the critical angle and up to the numerical aperture of the objective. Similarly, in figure 4.22 (f), the calculation has a discontinuity at $nsin(\theta) = 1$, typical for a vertical dipole at an interface, but the calculated result does not explain the emission at large angles up to NA=1.45, the objective numerical aperture. The root-mean-square roughness of the 6 nm film was measured by AFM and found to be 1.5 nm, so radiation loss due to scattering is assumed to be negligible. From these data we see that the vertical dipole model of the tunnel junction does not completely explain the results.

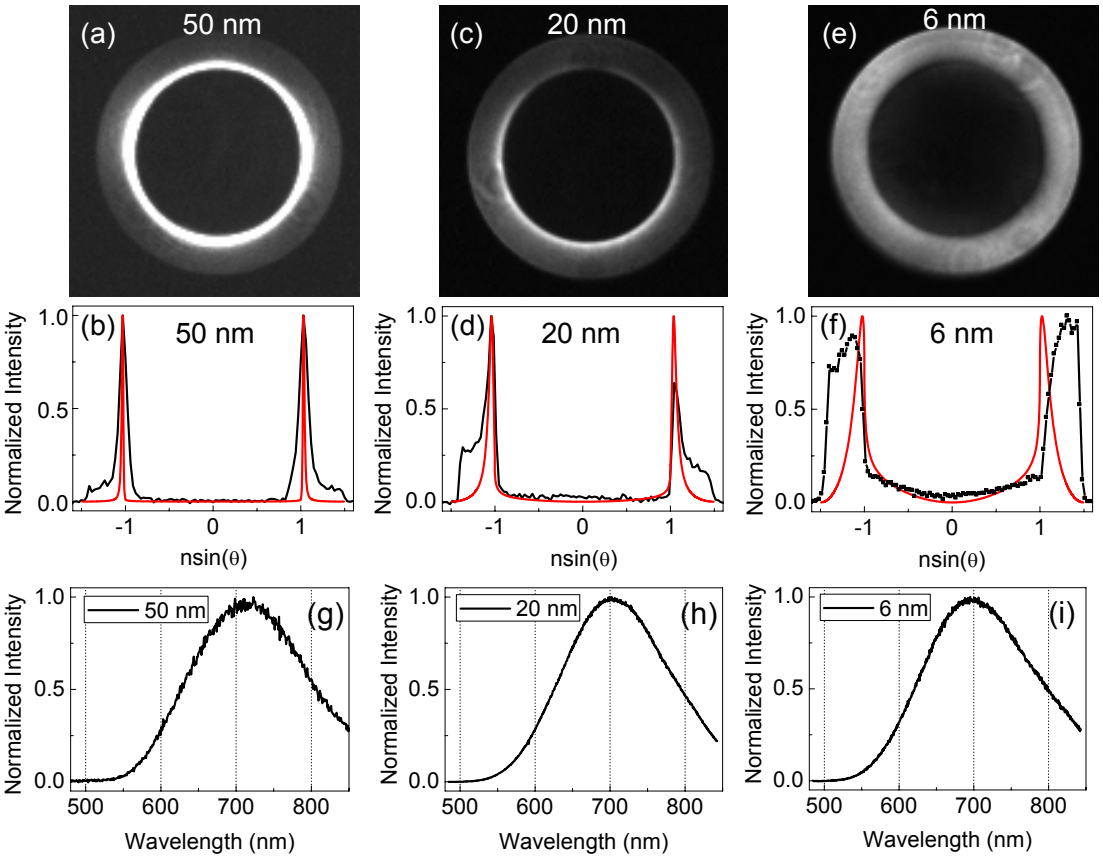

Figure 4.22: Fourier space images of STM-excited surface plasmons on (a) 50 nm (c) 20 nm and (e) 6 nm thick gold films, obtained with the blunt W tip. The black curves in (b), (d) and (f) are the corresponding cross sections. The sharp cut-off seen at large angles is due to the objective numerical aperture (NA=1.45). For (a) to (d) a sharp peak at the Kretschmann angle is observed, consistent with the generation of propagating surface plasmons. Using the oscillating point vertical dipole model for the tunnel junction gives rise to the calculated red curves in (b), (d), and (f). The emission at large angles is clearly not taken into account in this model, and is assigned to the modes that result from the interaction of the film with the STM tip, i.e., the localized modes. The spectra of the STM excited SPP on gold films of 50 nm, 20 nm and 6 nm are shown in (g)-(i), respectively.

Similarly, the comparison between the experimental cross-sections obtained with a

sharp W tip and the calculated cross-sections are shown in figure 4.23(b). It is also clear that the experimental plasmon peaks are well fitted with the vertical dipole model, but the emission at large angles ("shoulder") cannot be fitted by this model. However, comparing the blunt W tip and the sharp W tip, the experimental cross-sections obtained with the sharp W tip fit better with the vertical dipole model. This means that the electron tunneling of the sharp W tip is more similar to a vertical dipole. This is consistent with the fact that with a sharp W tip we obtained donut shape real space central peak patterns (already discussed in subsection 4.3.2).

Since no STM tip is present in this simple vertical dipole model, the tip must play an important role and the large angle emission is thus attributed to the tip-induced or localized plasmon modes.

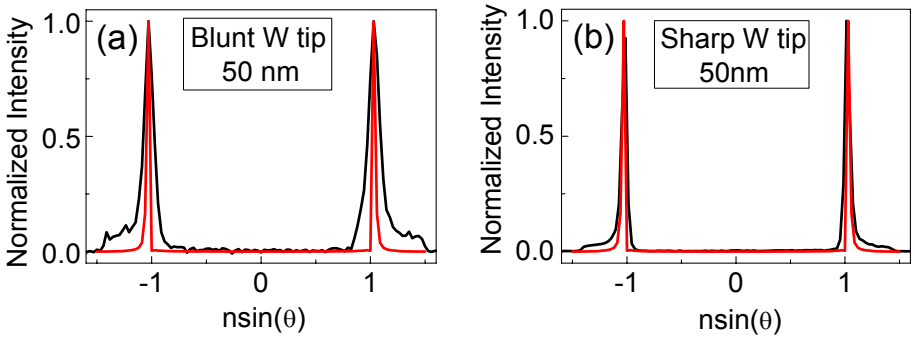

Figure 4.23: The vertical dipole model for the blunt W tip (a) and for the sharp W tip (b). The black curves in (a) and (b) are the Fourier space cross-sections obtained on a 50 nm thick gold film (already shown in figure 4.12). The sharp cut-off seen at large angles is due to the objective numerical aperture (NA=1.45). The sharp peak at the Kretschmann angle is observed, consistent with the generation of propagating surface plasmons. Using the oscillating point vertical dipole model for the tunnel junction gives rise to the corresponding calculated red curves in (a) and (b).

4.7.2 Fourier space images with bandpass filters

Another comparison is shown in figure 4.24. Figure 4.24 presents the experimental cross-sections in the Fourier plane images (with bandpass filters) compared to the theoretical cross-sections. The theoretical cross-sections are calculated using a vertical dipole located on the gold film with an emission wavelength same as the central wavelengths of the bandpass filters (see Chapter 2, subsection 2.2.2). The experimental data are from figure 4.13.

Similar to figure 4.22, we see that the plasmon peaks of the experiments fit well with the plasmon peaks of theoretical curves in figure 4.24(a)-(d). There are also two main differences: the widths of the plasmon peaks and the "shoulders" at large angles. For the widths of the experimental plasmon peaks, the differences may come from the fact that the theoretical curves are calculated for perfect flat gold films. In reality, the deposited gold films have a roughness which makes the damping larger than perfect gold films. From

figure 4.24(a)-(d), we can see that the shorter the wavelength, the better the *width* fitting between the theoretical curves and the experimental data. The widths of the plasmon peaks may also be influenced by the finite pixels of the CCD camera. For the "shoulders" at large angles, they cannot be attributed as propagating SPP and they are related to the the tip-induced or localized plasmon modes.

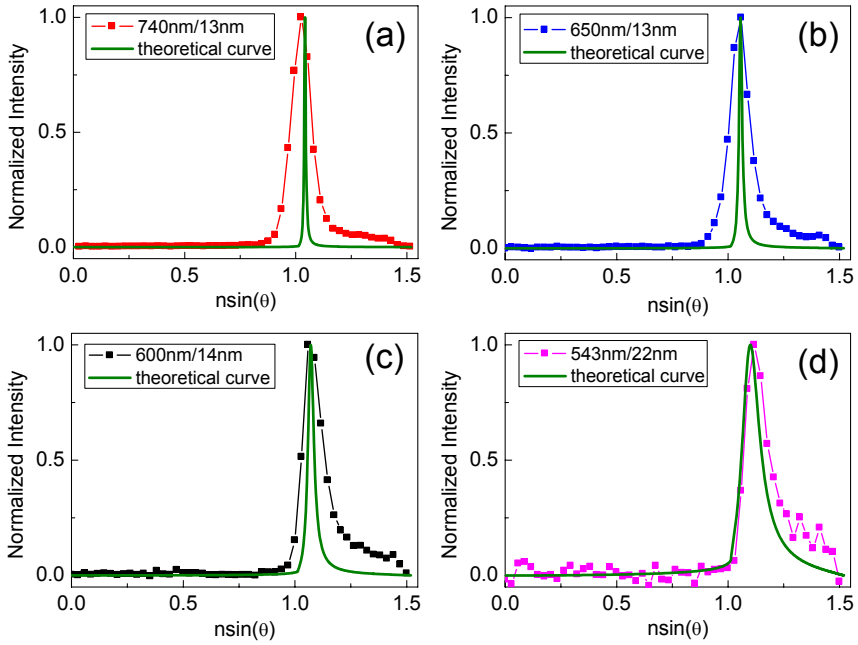

Figure 4.24: Experimental cross-sections in the Fourier space image compared to the theoretical cross-sections. The experimental data are from figure 4.13. The theoretical cross-sections are calculated at the central wavelengths of the bandpass filters in the same way as for figure 2.17.

4.8 Conclusion

In conclusion, we have shown that an STM electrically excites both localized and propagating plasmon modes on thin gold films on glass. For the first time we have characterized the plasmon modes and measured their intensities in both real and Fourier space images obtained from leakage radiation microscopy. We have shown that by varying the tip shape and material we can selectively excite one mode over the other: a sharp "non-plasmonic" tip (e.g. a sharp W tip) is the best choice for the preferential excitation of propagating surface plasmons as compared to localized surface plasmons while a "plasmonic" tip (e.g. a Ag tip) is recommended for the excitation of localized surface plasmons. Furthermore, calculations show that approximating the STM tunnel junction as a vertical dipole is appropriate for the propagating plasmon modes but this model does not take into account the tip-film interactions and the tip-induced or localized plasmon modes. These results provide more control over the STM plasmon excitation process, offer insight into the physical mechanisms involved, and lead to interesting prospects for low energy electrically excited plasmonics.

Chapter 5

Coherence of STM-excited Propagating Surface Plasmons

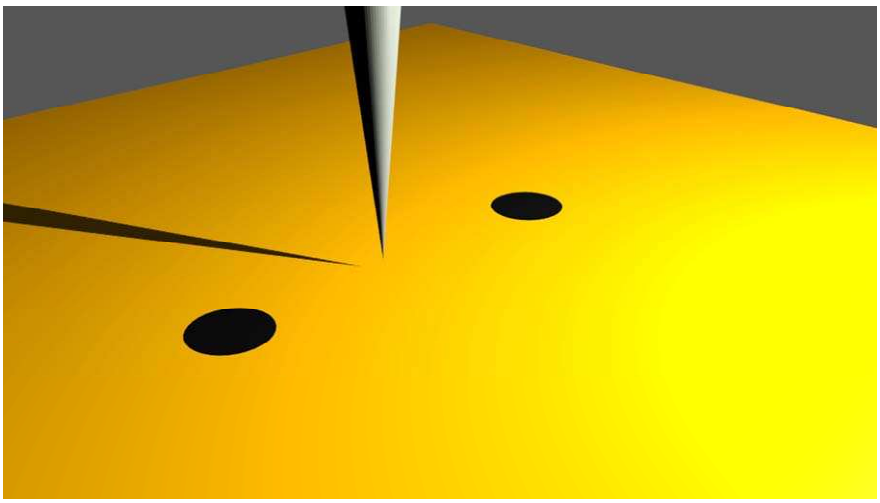

5.1 Introduction

Optically excited propagating surface plasmons (SPP) can interfere with the laser excitation light [109, 110]. For the electrically excited SPP [53, 99] which have a broadband emission spectrum, the investigation of the coherence of such electrically excited SPP is important in the context of their use in future integrated nano-optics devices such as optical nano-antennas [39].

Recently, combining a scanning tunneling microscope (STM) with an inverted optical microscope, we have excited propagating surface plasmons on a thin gold film with an STM [99]. Now, for the first time, we measure the coherence length of these STM-excited SPP.

We excite SPP on a 200 nm opaque gold film containing two nanoholes of the same diameter (250 nm, 500 nm, or 1 μm) using the STM. The STM-excited SPP propagate on the gold film surface and are scattered by the nanoholes. This scattered light is detected both in real space and Fourier space. In real space images, diffraction-limited patterns are seen at the hole positions. In Fourier space images, interference fringes are clearly seen and the period of the interference fringes depends on the separation between the two nanoholes. This experiment is analogous to Young's double-slit experiment. By varying the relative position between the STM tip and the nanoholes, we have studied the visibility of the interference fringes as a function of the plasmonic path difference between the tip and the nanoholes. This enables us to measure the coherence length of STM-excited propagating SPP.

5.2 Young's double-slit experiment for measuring light source coherence

Figure 5.1 shows the Young's double-slit setup for coherence studies of quasi-monochromatic light [111]. A parallel light beam (central wavelength λ) is diffracted by two slits, and the two diffracted light radiations interfere on a screen. The fields diffracted by the slits are $E_1 exp(i\varphi_1)$ and $E_2 exp(i\varphi_2)$ (see figure 5.1). If the distance between the screen and the slits is significantly larger than the slit separation, the interference pattern takes the approximate expression [66, 67]:

$$I(x) = I_1 + I_2 + 2\sqrt{I_1 I_2}\,|\gamma_{12}|\,cos(\frac{2\pi(|R_1| - |R_2|)}{\lambda} + \Delta\varphi) \tag{5.1}$$

where $I_1 = |E_1|^2$, $I_2 = |E_2|^2$, $\Delta\varphi = \varphi_1 - \varphi_2$, and $|\gamma_{12}|$ is the degree of coherence [67]. $|\gamma_{12}|$ is the absolute value (module) of the normalized mutual correlation function γ_{12} (complex degree of coherence) of the electric fields at the two points A and B.[1] Usually $|\gamma_{12}|$ is related to time delay τ between the two diffracted fields and can be written as $|\gamma_{12}(\tau)|$. When $|\gamma_{12}(\tau)| = 1$, the light beam is perfect coherent. When $|\gamma_{12}(\tau)| = 0$, the light beam is incoherent. When $0 < |\gamma_{12}(\tau)| < 1$, the light beam is partially coherent.

1. $\gamma_{12}(\tau) = \frac{\langle E_1(t+\tau)E_2^*(t))\rangle_T}{\sqrt{\langle|E_1|^2\rangle_T \langle|E_2|^2\rangle_T}}$ [67], page 570

The sharpness of the interference fringes is quantified by the visibility V:

$$V = \frac{2\sqrt{I_1 I_2}}{I_1 + I_2} |\gamma_{12}(\tau)| = 2(\sqrt{\frac{I_1}{I_2}} + \sqrt{\frac{I_2}{I_1}})^{-1} |\gamma_{12}(\tau)| \tag{5.2}$$

So by measuring the visibility V and the intensity ratio I_1/I_2, we can deduce the degree of coherence $|\gamma_{12}(\tau)|$ which shows the coherence information of the light source. A special case is when $|E_1|$ equals $|E_2|$, then the visibility $V = |\gamma_{12}(\tau)|$.

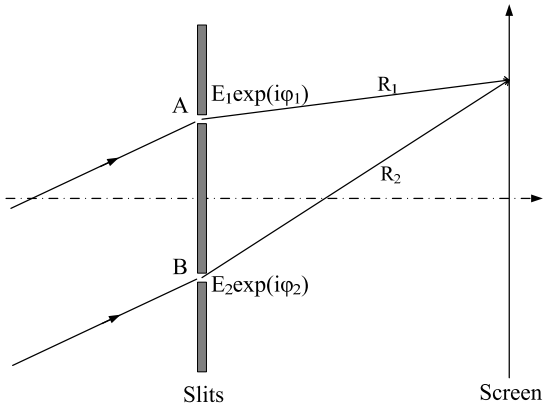

Figure 5.1: The Young's double-slit experiment setup for coherence studies of quasi-monochromatic light. Two slits located at A and B diffract a parallel light beam on a screen. If the diffracted lights from the two slits are coherent or patially coherent, there will be interference fringes on the screen.

5.3 Young's double-slit experiment for measuring plasmonic source coherence

In our experiments (figure 5.2), we use a STM tip to excite propagating surface plasmons (SPP) on a 200 nm gold film containing two nanoholes (separation d). If the paths of the STM-excited propagating SPP from the STM tip to each nanohole (r_1 and r_2) are different, there will be a phase difference $\Delta\varphi_{(SPP)}$ between the two diffracted electric fields. This phase difference is written as:

$$\Delta\varphi_{(SPP)} = k_{SPP}(|r_1| - |r_2|) = \frac{2\pi}{\lambda_{SPP}}(|r_1| - |r_2|) \tag{5.3}$$

where k_{SPP} is the wavenumber of the SPP and λ_{SPP} is the wavelength of the SPP. Our name for this phase difference will be the "plasmonic path difference". Also the amplitudes of the electric fields at the two nanoholes are different since the SPP attenuations are related to the path length (r_1 or r_2).

The time delay τ of the two diffracted fields is proportional to the plasmonic path difference(PPD) L_{PPD} (τ=L_{PPD}/v, v is the velocity of the SPP), so we define "$|\gamma_{12}(L_{PPD})|$" as the "degree of coherence".

The scattered light along the same radiation angle α will go to the same point in the Fourier space with an optical path difference $dsin(\alpha)$. This optical path difference causes

a phase difference:

$$\Delta\varphi_{(photon)} = k_{glass} d sin(\alpha) = \frac{2\pi}{\lambda/n} d sin(\alpha) = \frac{2\pi}{\lambda} d\, n sin(\alpha) \tag{5.4}$$

where k_{glass} is the wavenumber of light in glass and n is the refractive index of the glass substrate. For a fixed nanohole pair separation d and a certain wavelength λ, this optical phase difference is only related to the radiation angle α.

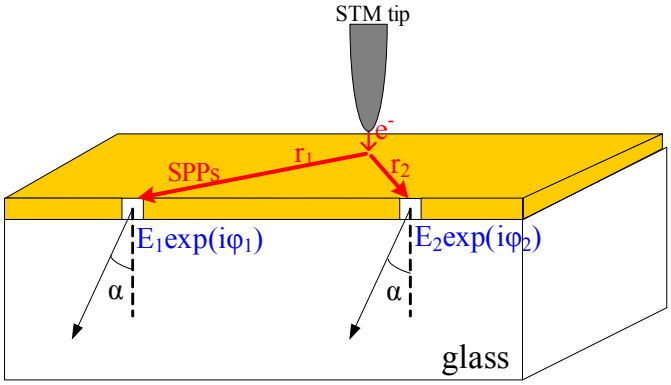

Figure 5.2: Schematic image of our experiment. Two nanoholes scatter the STM-excited propagating SPP. Note that when $r_1 = r_2$, $\Delta\varphi_{(SPP)} = 0$ and $E_1 = E_2$. Otherwise, $\Delta\varphi_{(SPP)} \neq 0$, $E_1 \neq E_2$.

Thus, if the scattered lights from the nanoholes are coherent, there will be an interference fringe pattern in Fourier space. This interference fringe pattern depends on these two kinds of phase difference contributions: the plasmonic path difference and the optical path difference.

5.4 Sample design, fabrication and characterization

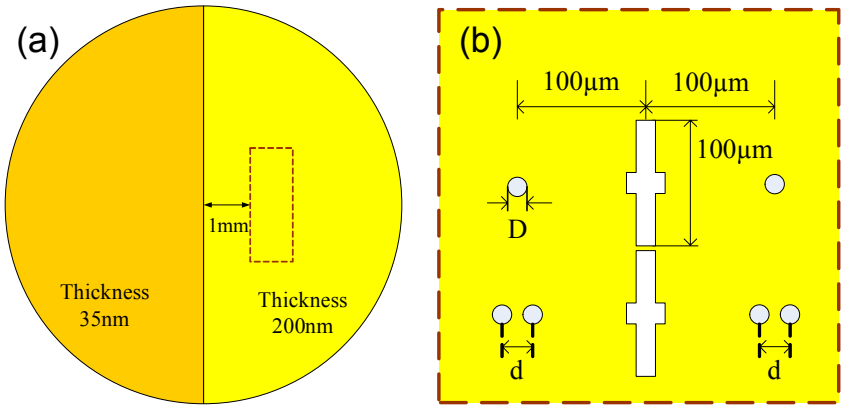

Figure 5.3: Design of the sample with nanoholes.

The design of the sample is shown in figure 5.3. Glass substrates are used (diameter 20 mm, thickness 150 μm). One half of the glass substrate is coated with a 200 nm gold

film pierced with single nanoholes and pairs of nanoholes aligned along markers. The other half of the glass substrate is coated with a 35 nm gold film which is used for the STM tip alignment.

We first designed a sample containing single nanoholes and pairs of nanoholes with diameters of 250 nm. Single nanoholes and pairs of nanoholes are 100 μm apart from each other so that they are well isolated. The nanoholes are aligned 100 μm away from the markers which have a width of 3 μm and a length of 100 μm. These markers help us to find the nanoholes during the initial transmission imaging experiments (see figure 5.3 (b)). The markers are far enough from the nanoholes to prevent their influence on the nanohole radiation. After the experiments with the first sample, we designed samples with larger diameters (500 nm and 1 μm) to increase the light intensity scattered by the nanoholes. For the simplicity of the text, the diameter of the nanoholes is defined as D and the distance between the nanoholes (for the nanohole pairs) is defined as d (figure 5.3(b)).

The samples were fabricated at the "Pôle Nanofab" of the Institut Néel (Grenoble) by Jean-François Motte and Dr. Serge Huant using a focused ion beam etching. The samples were observed using scanning electron microscope right after the fabrication (figure 5.4).

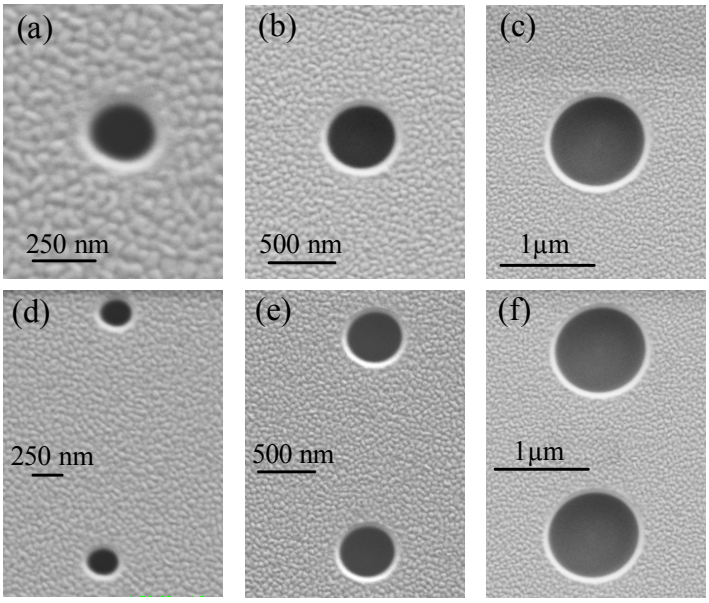

Figure 5.4: SEM (scanning electron microscope) images of single nanoholes and nanohole pairs. (a) D=250 nm, (b) D=500 nm, (c) D=1 μm, (d) D=250 nm, d=2 μm, (e) D=500 nm, d=2 μm and (f) D=1 μm, d=2 μm . D is the diameter of the nanoholes and d is the separation of the nanohole pairs. Note that we also use nanohole pairs with separations d= 4 μm and 6 μm.

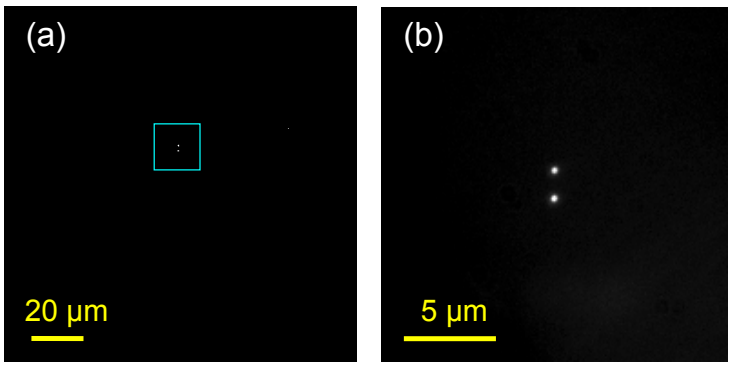

Figure 5.5: Transmission image of a nanohole pair with D=250 nm d=2 μm. In a very large area of 130 $\mu m \times 130$ μm, we can only see the light transmitted from the two nanoholes.

The single nanoholes and nanohole pairs are also characterized by optical transmission imaging and STM topography imaging using our setup. Here we show an example of this characterization. Figure 5.5 shows a transmission image of a nanohole pair with D=250 nm and d=2 μm. There is only one nanohole pair in the large area of about 130 μm $\times$ 130 μm. Figure 5.5(b) is a zoom. The STM topography image of the nanohole pair is shown in figure 5.6(a). From the cross-section along the two holes (figure 5.6(b)), we clearly see that the diameter D is around 250$\pm$20 nm and the distance d between the two nanoholes is about 2$\pm$0.05 μm.

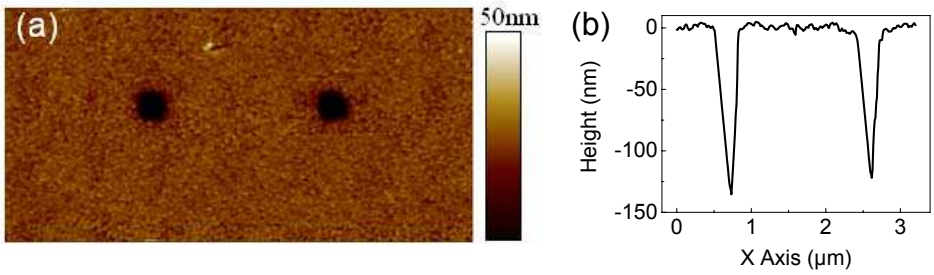

Figure 5.6: (a) STM topography image of the nanohole pair with D = 250 nm d = 2 μm. (b) Cross-section along the two nanoholes.

In all the STM experiments of this chapter, the tunneling parameters are V=2.8 volts, I=6 nA. The STM tips used in this chapter are blunt W tips (see figure 4.2).

5.5 Radiative scattering of STM-excited propagating SPP by single nanoholes

For the first set of experiments, we excite propagating surface plasmons (SPP) on the 200 nm gold film near a single nanohole with a W STM tip. The STM-excited SPP propagate on the gold film surface and are scattered by the nanohole. Due to the 200 nm thickness of the gold film, leakage radiation of the propagating SPP is not detected. With the oil objective, we only detect the radiative scattering of the SPP. The real and Fourier

space images of the radiative scattering of propagating SPP from a 250 nm nanohole are presented in the upper part of figure 5.7(a-f). The lower part of figure 5.7(g-l) shows the radiative scattering from a 1 μm nanohole. It is very clear that the image patterns in both the real space and Fourier space follow the STM tip position.

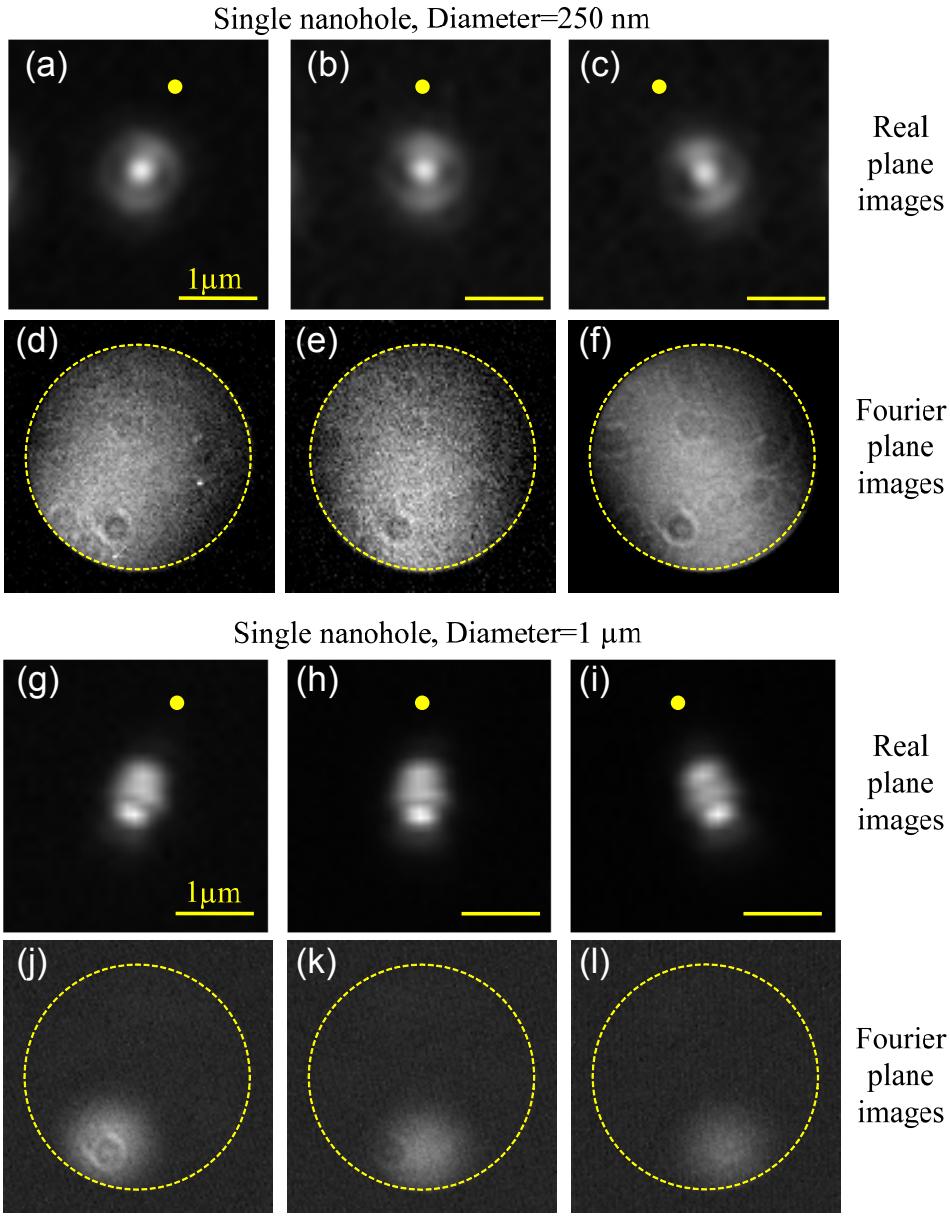

Figure 5.7: STM-excited propagating SPP are radiatively scattered by a single nanohole. Real (a-c) and Fourier (d-f) plane images of the radiative scattering from a 250 nm nanohole. Real (g-i) and Fourier (j-l) plane images of the radiative scattering from a 1 μm nanohole. In (a-c) and (g-i), the yellow spot indicates the tip position. The scale bar is 1 μm. In (d-f) and (j-l), the yellow dashed circle indicates the numerical aperture of the oil objective, i.e., NA=1.45.

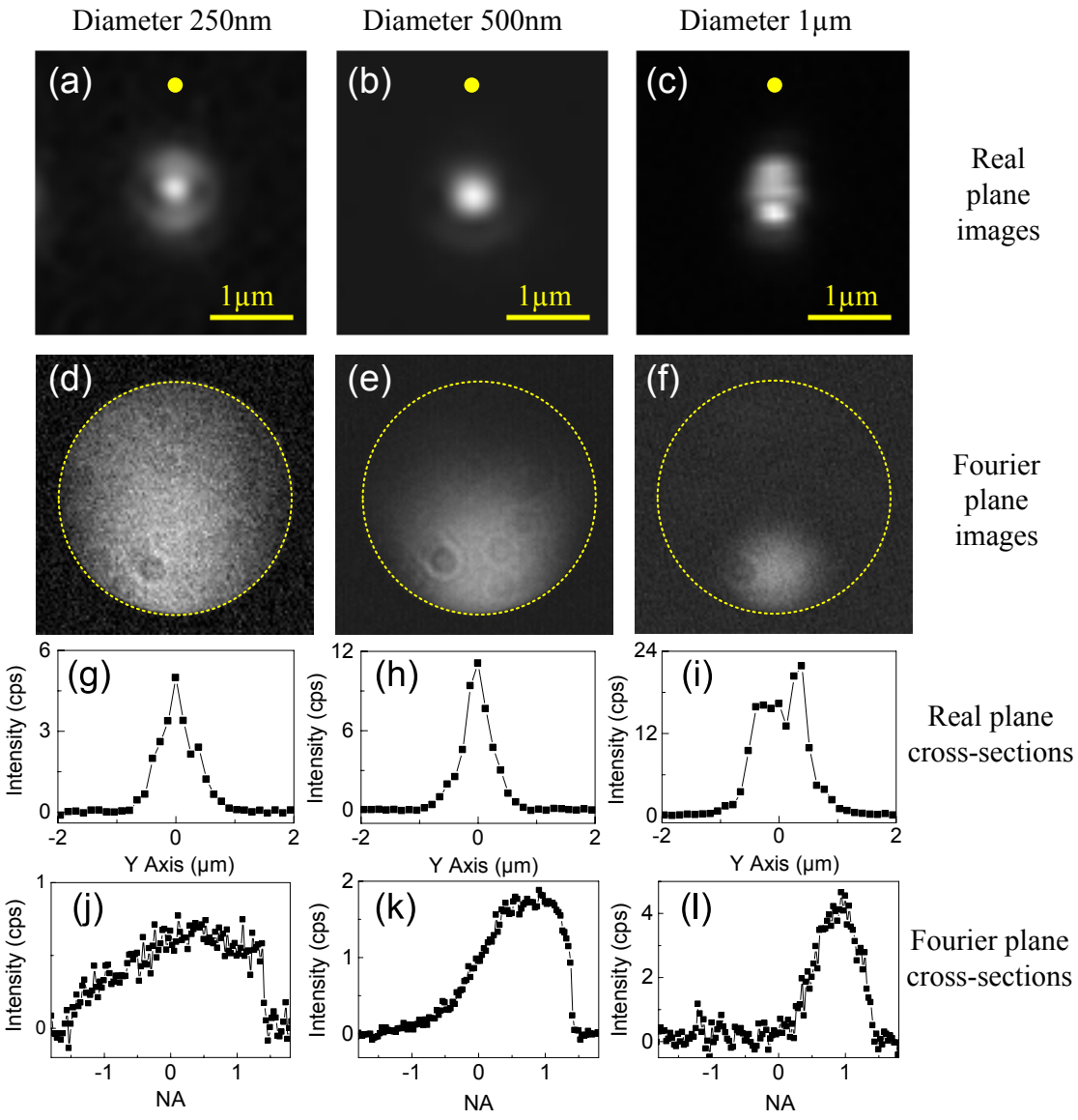

Figure 5.8: STM-excited propagating SPP are radiatively scattered by a single nanohole. Real and Fourier plane images of the radiative scattering from a 250 nm nanohole (a, d), a 500 nm nanohole (b, e) and a 1 μm nanohole (c, f). Images (g-i) are the corresponding cross-sections of (a-c) along the tip-nanohole direction. Images (j-l) are the corresponding cross-sections of (d-f) along the tip-nanohole direction. In (a-c), the yellow spot indicates the tip position. The scale bar is 1 μm. In (d-f), the yellow dashed line circle indicates the numerical aperture of the oil objective, i.e., NA=1.45.

Looking closely at figure 5.7(a)-(c) (nanohole diameter 250 nm) we see that there is more intensity along the tip-hole axis than that along the direction perpendicular to this tip-hole direction. This phenomenon is also seen in the corresponding Fourier space images (figure 5.7(d)-(f)). From figure 5.7(g)-(i) (nanohole diameter 1 μm) we see that the real space patterns are elongated along the tip-hole direction. This also means that there is more intensity along the tip-hole direction than that along the direction perpendicular to the tip-hole axis. This phenomenon is also seen in the corresponding Fourier space images

(figure 5.7(j)-(l)).

Figure 5.8 presents the radiative scattering images of STM-excited propagating SPP from single nanoholes of different diameters (250 nm, 500 nm and 1 μm) with similar tip-hole orientations. Figure 5.8(a-c) and (d-f) are the real space images and Fourier space images respectively. Figure 5.8(g-i) and (j-l) are the cross-sections along tip-nanohole direction (i.e. y axis) of the real and Fourier space images respectively. All the images have a symmetry axis, the tip-nanohole direction.

The real space image of the scattered light from a 250 nm nanohole (figure 5.8(a) and (g)) has a three spot pattern. The three spots are aligned along the tip-nanohole direction. The central spot is located on the nanohole position. It is slightly more intense than the others. This three spot pattern presents similarities with the emission pattern of a horizontal dipole near a air-glass interface. The real space image of the scattered light from a 500 nm nanohole (figure 5.8(b) and (h)) has a one spot pattern. The spot is located on the nanohole. The real space image of the scattered light from a 1 μm nanohole (figure 5.8(c) and (i)) has a three spot pattern elongated along the tip-nanohole direction. Two spots are located on the nanohole edges along the tip-hole direction and one is located at the center of the nanohole. Of these three spots, the spot of highest intensity is the one which is furthest from the tip while the one of lowest intensity is the one centered on the nanohole.

Let us now discuss the angular distribution of the scattered light. The Fourier space image pattern is rather uniform for the 250 nm nanohole (figure 5.8(d) and (j)). It becomes smaller, for the 500 nm nanohole (figure 5.8(e) and (k)), and concentrated on the lower half part of the Fourier space image. It becomes even smaller for the 1 μm nanohole (figure 5.8(f) and (l)), and concentrated on the bottom of the Fourier space image with maximum intensity around the critical angle.

The propagating SPP launched by the STM tip on the gold film are transverse magnetic waves. Their electric field has two components in the "incident plasmonic plane": one is along the tip-nanohole direction, and the other one is perpendicular to the gold film. We have observed the response of the nanoholes, 200 nm in depth and with 250 nm, 500 nm and 1 μm diameters, to this STM-excited propagating SPPs. The radiative response is mainly concentrated in the "incident plasmonic plane". Calculations are needed to understand better the scattering of propagating SPP by nanoholes with different diameters.

For the same tip-nanohole distance, the radiative scattering intensity is more than 5 times higher for 1 μm nanoholes than for 250 nm nanoholes.

5.6 Radiative scattering of STM-excited propagating SPP by two 250 nm nanoholes (2 μm apart)

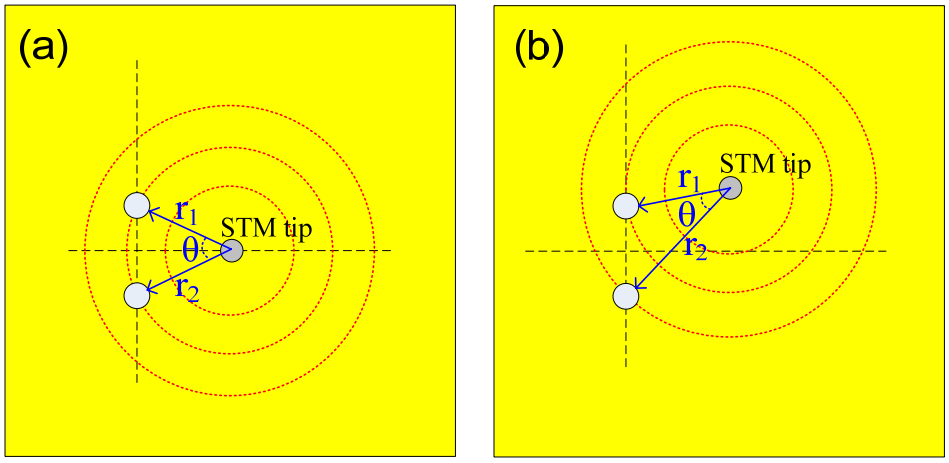

Figure 5.9: Two different positions of the STM tip (which launches the SPP) relative to the nanoholes. (a) Equal tip-nanohole plasmonic paths (b) Different tip-nanohole plasmonic paths. The tip-nanohole distances are $|r_1|$ and $|r_2|$, and the angle between the unit vectors $\widehat{r}_1$ and $\widehat{r}_2$ is θ. The red lines represent the 2D circular propagating SPP waves excited by the STM.

In the next set of experiments, we excite propagating surface plasmons (SPP) on a 200 nm gold film near a pair of 250 nm nanoholes, 2 μm apart. The propagating SPP (excited with a blunt W tip) are 2D circular plasmonic waves, which are radiatively scattered by each of the nanoholes. If the radiation from the two nanoholes overlaps in Fourier space, we might see some interference features. If we put the STM tip on the "perpendicular bisector" of the two nanoholes, the SPP propagating paths from the tip to each of the nanoholes are equal (figure 5.9(a)). The propagating SPP wave, launched by inelastic electron tunneling (IET) at the tip position, reaches the two nanoholes at the same time, so the propagating SPP wave has the same phase and the same intensity attenuation at the nanoholes. On the other hand, if we put the STM tip somewhere else, the SPP propagating paths from the tip to each of the nanoholes are different (figure 5.9(b)). The propagating SPP wave, launched by inelastic electron tunneling at the tip position, first reaches the closer nanohole and then the other one, so the propagating SPP wave at the nanoholes has different phases and different intensities. We will investigate successively these two cases.

5.6.1 Radiative scattering by two 250 nm nanoholes: equal SPP path cases

Real space images when the tip is in the center of the nanohole pair

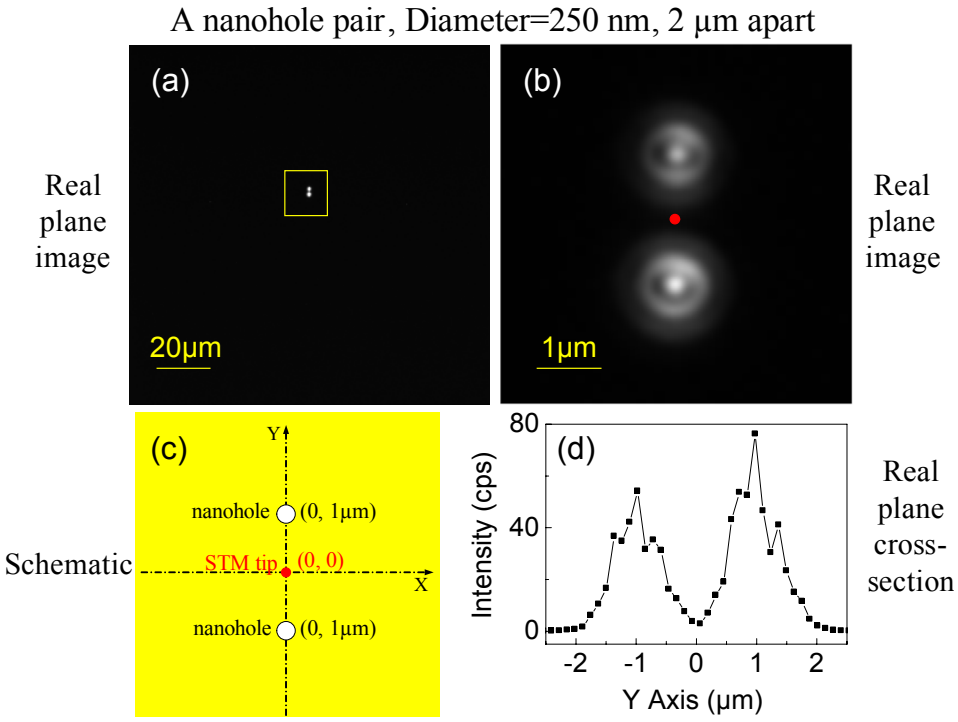

Figure 5.10: Real space image of the scattered propagating SPP from a nanohole pair. (a) Large scale (130 μm $\times$ 130 μm) image. (b) Zoom-in view. (c) Schematic image of the relative position of the STM tip and the nanoholes. (d) Cross-section along y axis of (b). In (b) and (c) the red spot indicates the tip position.

Figure 5.10(a-b) shows real space images of the propagating SPP scattered by a pair of 250 nm nanoholes, 2 μm apart, when the STM tip is located at the center of the two nanoholes. Figure 5.10(c) is a schematic showing the relative position of the STM tip and the two nanoholes. Here, the red dot indicates the tip position. We used a W tip. The real space images are recorded using an oil objective. Because the 200 nm gold film is opaque, in a large area around (130 μm $\times$ 130 μm), only the scattered light emission at the nanohole positions is detected and there is no contribution from leakage radiation (figure 5.10(a)). Figure 5.10(d) shows the cross-section along the nanohole axis of figure 5.10(b). From figure 5.10 (b) and (d) we clearly see that the scattered light emission pattern of each of the two nanoholes is similar to the scattered light emission pattern from a single 250 nm nanohole (see figure 5.8 (a) and (g)). From figure 5.10(d) we clearly see that the light emission patterns are diffraction limited.

Fourier space images for different tip positions for equal SPP path lengths

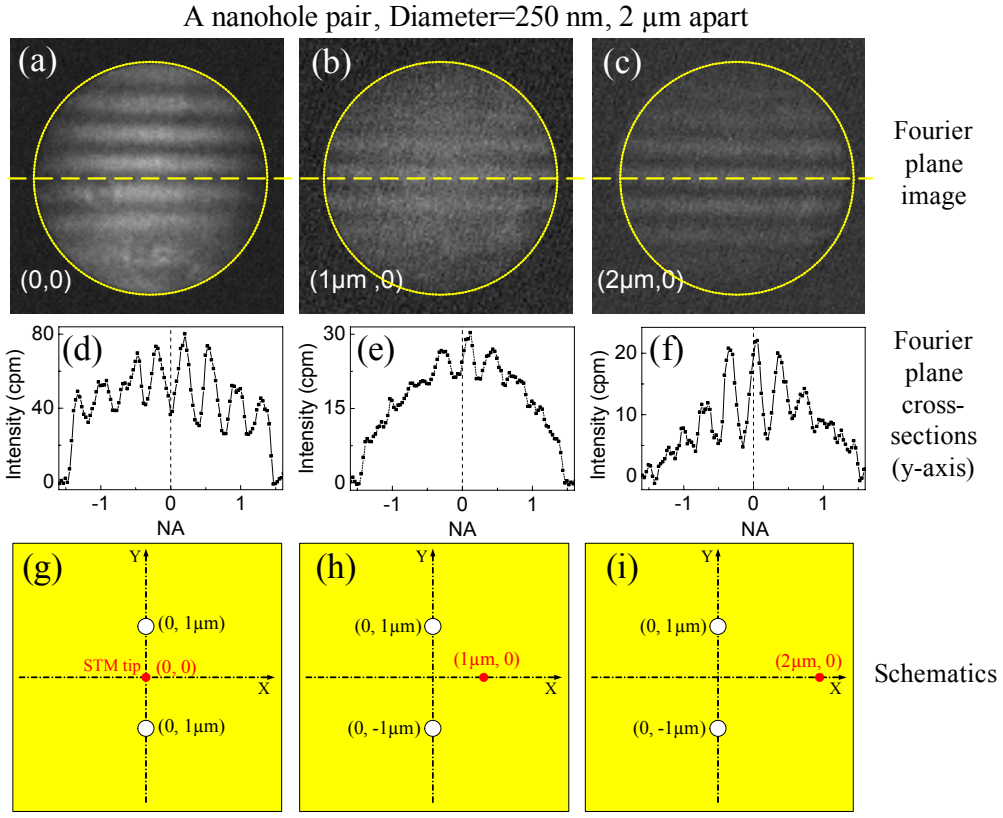

Figure 5.11: (a-c) Fourier space images of the scattered light from the nanohole pair (D=250 nm and d=2 μm) for three different positions of the STM tip. The dashed yellow line (a-c) represents the central axis of the Fourier space image. The yellow circle indicates the numerical aperture of the oil objective, NA=1.45. (d-f) Fourier cross-sections (y axis) associated with (a-c). The vertical dashed line in (d-f) denotes NA=0. In the schematics (g-i), the red dot indicates the tip position.

Figure 5.11 shows the Fourier space images (a-c) of the scattered light from the nanohole pair for different relative positions of the tip and the nanohole pair (g-i).

We see fringes in figure 5.11(a-c). These fringes are believed to be the interference fringes of the light (originating from propagating surface plasmons) scattered from the two nanoholes. This experiment is analogous to Young's double-slit experiment. The angular periods of the interference fringes for the three tip-nanohole positions are the same. The period is measured to be 0.353 $\pm$ 0.015 in NA units ($NA = nsin(\theta)$). In Young's double-slit experiment, the angular period of the interference fringes is calculated as:

$$\theta_f = \frac{\lambda}{d} = \frac{700\ nm}{2\ \mu m} = 0.35 \tag{5.5}$$

So it is clear that the angular period we measured is the same as the calculated value. One interesting thing is that the interference fringes shift when the relative position between the STM tip and the nanoholes changes. This phenomenon is clearest in the cross-sections

of the interference (figure 5.11(d-f)).

Fourier space interference fringes from two in-plane dipolar point sources

In case of a nanohole pair, we have observed interference fringes in Fourier space (figure 5.11). We propose to check whether this interference pattern can be understood in terms of the emission of two in-plane (i.e., parallel to the Au film) point sources $\mathbf{P_1}$ and $\mathbf{P_2}$ located at the nanohole positions. Owing to their similar shape, we may assume that the two nanoholes have the same polarizability and for simplicity we set the polarizability to 1. So the two point sources can be written as:

$$\begin{aligned} &\vec{P_1} = \frac{e^{i\vec{k}_{r_1}\vec{r}_1}}{\sqrt{r_1}}\widehat{r}_1, \quad \vec{P_2} = \frac{e^{i\vec{k}_{r_2}\vec{r}_2}}{\sqrt{r_2}}\widehat{r}_2 \\ &with \\ &\vec{k}_{r_1} = \vec{k}_{r_2} = \vec{k}_{SPP} = \vec{k}'_{SPP} + i\vec{k}''_{SPP} \end{aligned} \tag{5.6}$$

In the Fourier space, the intensity of the light from the two point sources can be written as:

$$I(K) = (\vec{P_1}e^{-iK\frac{d}{2}} + \vec{P_2}e^{iK\frac{d}{2}})^2 = |\vec{P_1}|^2 + |\vec{P_2}|^2 + \vec{P_1}\vec{P_2}^*e^{-iKd} + \vec{P_1}^*\vec{P_2}e^{iKd} \tag{5.7}$$

where d is the distance between the two nanoholes which are along the y axis. From the discussion of back focal plane in Chapter 2 (section 2.3.2), we have $K = \frac{2\pi}{\lambda_0}NA$ (λ_0 is the photon wavelength in free space). So from equation 5.6 and equation 5.7 we get [112]:

$$\begin{aligned} &I(K) = I_1 + I_2 + 2cos(\theta)\sqrt{I_1 I_2}\,|\gamma_{12}|\,cos[Kd + \Delta\varphi] \\ &with \\ &I_1 = \frac{e^{-2k''_{SPP}|r_1|}}{r_1} \quad and \quad I_2 = \frac{e^{-2k''_{SPP}|r_2|}}{r_2} \\ &\Delta\varphi = k'_{SPP}(|r_2| - |r_1|) \\ &cos(\theta) = \widehat{r}_1 \cdot \widehat{r}_2 \end{aligned} \tag{5.8}$$

where the $|\gamma_{12}|$ is the degree of coherence of the light emitted from the two nanoholes (see section 5.2).

This expression is similar to the equation 5.4 for Young's double slit experiments of a parallel beam, except the factor $cos(\theta)$. θ is the angle between $\widehat{r_1}$ (tip-nanohole 1 direction) and $\widehat{r_2}$ (tip-nanohole 2 direction). It is also the angle between the horizontal components of the plasmonic electromagnetic fields at nanohole 1 and 2. So it means that the factor $cos(\theta)$ is provided by the radial polarization of the electromagnetic wave launched by STM tip. The equation 5.8 can also be written as:

$$\begin{aligned} &I(K) = I_0(1 + Vcos[Kd + \Delta\varphi]) \\ &or \quad I(NA) = I_0(1 + Vcos[\tfrac{2\pi}{\lambda_0}d\,(NA + \delta\varphi)]) \\ &with \\ &I_0 = I_1 + I_2 = \frac{e^{-2k''_{SPP}|r_1|}}{r_1} + \frac{e^{-2k''_{SPP}|r_2|}}{r_2} \\ &V(visibility) = 2cos(\theta)\frac{\sqrt{I_1 I_2}}{I_1 + I_2}\,|\gamma_{12}| \\ &\delta\varphi(phase\,shift) = \frac{k'_{SPP}}{k_0}\frac{(|r_2| - |r_1|)}{d} \end{aligned} \tag{5.9}$$

Understanding the shift of the interference fringes

For tip positions along the perpendicular bisector of the nanohole axis, the SPP propagation paths from the tip to each of the nanoholes are equal (figure 5.9(a)). The propagating SPP wave launched by the inelastic electron tunneling (IET) at the tip position reaches each of the nanoholes with the same phase and intensity. So equation 5.9 becomes:

$$\begin{aligned} &I(NA) = I_0(1 + V cos[\tfrac{2\pi}{\lambda_0} d\ NA]) \\ &with \\ &I_0 = 2\tfrac{e^{-2k''_{SPP}|r|}}{r} \\ &V(visibility) = cos(\theta)\,|\gamma_{12}| \end{aligned} \tag{5.10}$$

where $|\gamma_{12}|$ is the degree of coherence of the light emitted from the two nanoholes. Normally $|\gamma_{12}|$ equals 1 if the optical paths are equal [67]. At the center of the Fourier space image, i.e., NA=0, the equation 5.10 can be written as:

$$\begin{aligned} &I(NA = 0) = I_0(1 + V) = I_0(1 + cos(\theta)) \\ &with \\ &I_0 = 2\tfrac{e^{-2k''_{SPP}|r|}}{r} \\ &cos(\theta) = \tfrac{x^2 - (d/2)^2}{x^2 + (d/2)^2} \\ &r = \sqrt{x^2 + (d/2)^2} \end{aligned} \tag{5.11}$$

where θ is the angle between $|r_1|$ and $|r_2|$ (see figure 5.9). For a fixed nanohole pair separation d, the equation 5.11 means that the intensity of the central fringe (NA=0) depends on the position of the tip x (y=0). The normalized intensity of the central fringe is:

$$Normalized \;\; I(NA = 0) = (1 + cos(\theta))/2 \tag{5.12}$$

Especially, if the STM tip is at the middle of the two nanoholes, then the angle θ= 180°. In this case, the normalized intensity of the central fringe $(1 + cos(180°))/2$= 0, which means that in the Fourier space image the central fringe is a dark fringe.

From the cross-sections in figure 5.11 (d-f), we measured the normalized $I(NA = 0)$ at different x values and plot them as blue dots in figure 5.12. Note that the closest maximum and minimum intensity near NA=0 in the cross-sections is normalized to be 1 and 0. We also plot equation 5.12 in figure 5.12. We see that the measured values fit well with equation 5.12. It is clear that when the value of $|x|$ becomes larger $I(NA = 0)$ increases and saturates at 1. Furthermore, the black line in figure 5.12 also represents the shift at different tip positions along the x axis comparing to the cross-section of x=0. When $|x|$ becomes larger the shift increases and saturates at a half period.

It is very important to emphasize that this interference fringe pattern shift is not due to a phase difference between the radiation from the two nanoholes. This shift occurs because of the $cos(\theta)$, the angle between the tip-nanohole axes.

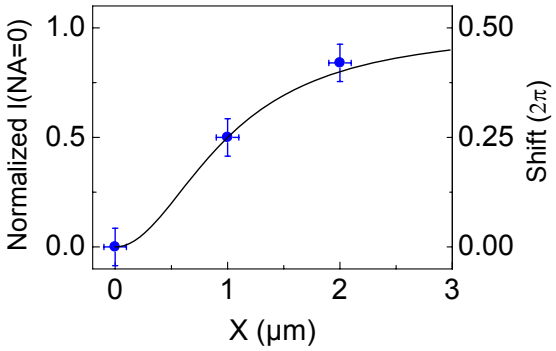

Figure 5.12: Shift of the interference fringe pattern in Fourier space when the STM tip moves along x axis. The blue dots show the measured value of I(NA=0) from the cross-sections. The solid line is the theoretical curve of I(NA=0) from equation 5.11 with d=2 μm. Theoretical curve of I(NA=0) also represents the phase shift of the interference fringes. The experimental data fit well with the theoretical curves.

Understanding the intensity distribution of the interference fringe pattern

To completely model the intensity of the interference fringe pattern in Fourier space, we need to consider more parameters. The first parameter we need to add is the single slit(hole) diffraction profile. During the double slit interference experiments, if the widths of the slits are comparable to the wavelength of the light, the interference fringes are modulated by the single slit diffraction profile. So the equation 5.10 can be modified as:

$$\begin{aligned} &I(NA) = I_0(1 + Vcos[\tfrac{2\pi}{\lambda_0} d\ NA])Sinc^2(\tfrac{\pi D\ NA}{n\lambda_0}) \\ &V(visibility) = cos(\theta)\,|\gamma_{12}| \\ &I_0 = 2\tfrac{e^{-2k''_{SPP}|r|}}{r} \end{aligned} \tag{5.13}$$

where D is the diameter of the nanoholes, d is the separation of the nanohole pair, n=1.52 is the refractive index of the glass substrate and θ is the angle between the tip-nanohole directions (see figure 5.9).

The second thing we need to consider is the broadband spectra of the STM-excited propagating SPP. In principle, the interference fringes of different wavelengths beat with each others and diminish the interference. In our experiments, we need to integrate the whole spectra to model well the interference fringe pattern in the Fourier space. So equation 5.13 should be written as:

$$I(NA) = \sum_{\lambda_{min}}^{\lambda_{max}} I_0(\lambda)(1 + Vcos[\frac{2\pi}{\lambda} d\ NA])Sinc^2(\frac{\pi D\ NA}{n\lambda}) \tag{5.14}$$

where λ_{min} and λ_{max} are the minimum wavelength and the maximum wavelength of the scattered light spectrum.

We use equation 5.14 to fit the cross-sections shown in figure 5.11 (d-f). Note that during the fitting in equation 5.14 there is only one unknown parameter V. So it is by means of this fit that we can get the visibilities of the three cross-sections. For simplicity,

we use just three wavelengths: λ_0=700 nm, λ_0=650 nm and λ_0=750 nm. In this case, equation 5.14 can be written as:

$$\begin{aligned} &I(NA) = \textstyle\sum_{\lambda=650,700,750\ nm} I_0(\lambda)(1 + V cos[\frac{2\pi}{\lambda} d\ NA])Sinc^2(\frac{\pi D\ NA}{n\lambda}) \\ &V(visibility) = cos(\theta)\,|\gamma_{12}| \end{aligned} \tag{5.15}$$

where D is the diameter of the nanoholes, d is the separation of the nanohole pair, n=1.52 is the refractive index of the glass substrate and θ is the angle between the tip-nanohole directions (see figure 5.9). According to the measured spectra, we set the relative normalized intensity to $I_0(700nm)$=0.5, $I_0(650nm)$=$I_0(750nm)$=0.25.

Figure 5.13 shows the results of fits. It is clear that the theoretical curves using equation 5.15 fit the experimental data well. The visibility for the tip position (0, 0) is 0.55 (figure 5.13 (a)), for tip position (1 μm, 0) is 0.15 (figure 5.13 (b)), and for the tip position (2 μm, 0) is 0.60 (figure 5.13 (c)).

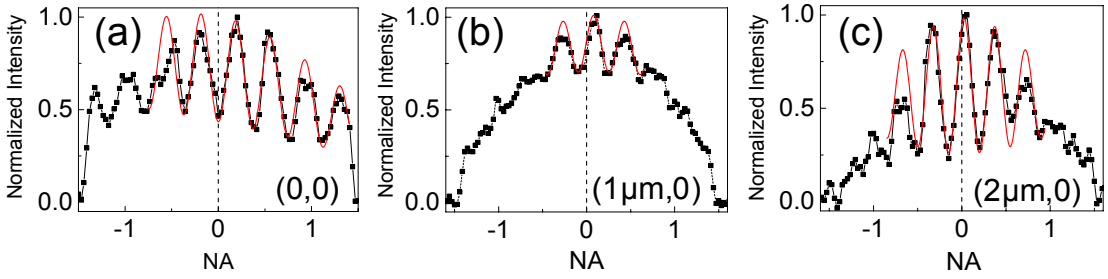

Figure 5.13: Fits to the interference cross-sections using equation 5.15. The cross-sections are from figure 5.11 (d-f).

Understanding the visibility of the interference fringes

Another interesting point may be observed for the visibility. In the case where the tip is along the perpendicular bisector of the nanohole axis, the visibility V can be written as a function of x as:

$$V = cos(\theta)\,|\gamma_{12}| = \frac{x^2 - (d/2)^2}{x^2 + (d/2)^2}\,|\gamma_{12}| \tag{5.16}$$

From equation 5.16, it is clear that when x=d/2=1 μm (i.e., $\theta = 90°$), the visibility V decreases to 0. From the cross-sections in figure 5.11 (d-f) or figure 5.13, we clearly see that the visibility of the cross-section at x=1 μm is smaller than the other two cross-sections. Note that the visibility measured at x=1 μm is not exact 0, is 0.15. This may due to the precision of our tip position. The tip position has a $\sim$ 100nm uncertainty in both x and y axes.

5.6.2 Radiative scattering by two 250 nm nanoholes: different SPP path cases

Measurement of propagation length of STM-excited propagating SPP

As indicated in figure 5.9, the distance between the STM tip and the two nanoholes are r_1 and r_2, so the propagating SPP intensities at the two nanohole positions are:

$$\begin{aligned} I_1 &= I_0 \frac{e^{-r_1/L_{SPP}}}{r_1} \\ I_2 &= I_0 \frac{e^{-r_2/L_{SPP}}}{r_2} \end{aligned} \tag{5.17}$$

where I_0 is the propagating SPP intensity at the tip position and L_{SPP} is the propagation length of the SPP.

From equation 5.17, the intensity ratio between I_2 and I_1 is calculated as:

$$I_2/I_1 = \frac{r_1}{r_2} e^{-\frac{|r_1-r_2|}{L_{SPP}}} \tag{5.18}$$

where $|r_1 - r_2|$=L_{PPD}, the plasmonic path difference. Thus, if we know the intensity ratio I_2/I_1, r_1 and r_2, we can obtain the propagation length L_{SPP}.

Table 5.1 shows the measured I_2/I_1 and calculated L_{SPP} values for different tip positions. Here, the data are from a nanohole pair with a separation d=2 μm. The nanohole diameter is 250 nm. By averaging the six calculated L_{SPP} values, we obtain the propagation length for STM-excited propagating SPP on a 200 nm gold film: 20.7± 2.5 μm. This is very close to the theoretical value 22 μm at λ = 700 nm [44].

Table 5.1: Measured I_2/I_1 (acquisition time 300 s) and calculated L_{SPP} values for different tip positions.

d (μm)	Tip Position (x μm, y μm)	r_1 (μm)	r_2 (μm)	I_1 (counts)	I_2 (counts)	Measured I_2/I_1	Calculated L_{SPP} μm
2	(3.0, 0.0)	2.00	4.00	25668	11583	0.451	19.5
2	(2.0, 1.0)	1.41	3.16	46885	19162	0.412	21.6
2	(2.0, 2.0)	2.24	3.61	43729	25631	0.586	24.3
2	(2.0, 3.0)	3.16	4.24	71582	49879	0.700	17.6
2	(2.0, 4.0)	4.12	5.00	22566	17688	0.793	22.4
2	(1.0, 4.0)	4.00	4.47	57376	66072	0.872	18.8

Fourier space images when the STM tip is along the y axis

Figure 5.14 (g-i) presents three different positions of the tip relative to the nanohole pair along the y axis. The distance between the tip and the nearest nanohole is L. The separation of the nanohole pair is d. In these cases, the angle θ is 0° (see figure 5.9), the plasmonic path difference is d and the shift in the Fourier space $\delta\varphi$ is equal to $\frac{k'_{SPP}}{k_0}$. Thus, the equation 5.9 can be written as:

$$\begin{aligned} I(NA) &= I_0(1 + V cos[\tfrac{2\pi}{\lambda_0} d(NA + \tfrac{k'_{SPP}}{k_0})]) \\ V(visibility) &= 2\tfrac{\sqrt{I_1 I_2}}{I_1+I_2} |\gamma_{12}| \\ I_0 = I_1 + I_2 &= \frac{e^{-2k''_{SPP}|r_1|}}{r_1} + \frac{e^{-2k''_{SPP}|r_2|}}{r_2} \end{aligned} \tag{5.19}$$

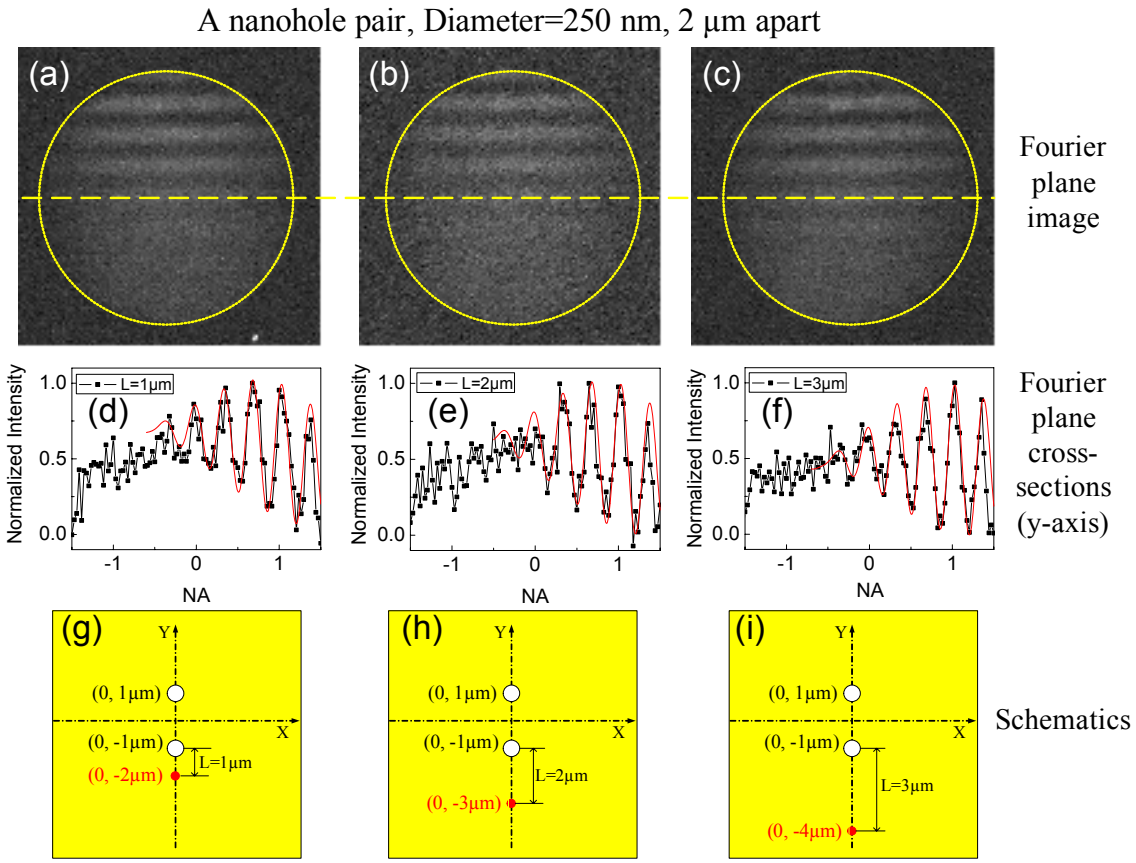

Figure 5.14: The Fourier space images of the scattered light emission from a nanohole pair with three different relative positions of the tip and the nanohole pair. (a-c) The Fourier space images of the scattered light emission from the nanohole pair. (d-f) The corresponding cross-sections. In the schematics (g-i), the red dot indicates the tip position. The yellow dashed line crossing (a-c) represents the central axis of the Fourier space image.

Figure 5.14 shows the Fourier space images (a-c) and the corresponding cross-sections (d-f) for three values of L (1 μm, 2 μm, 3 μm). The interference patterns are very similar. The interference fringes are all shifted along the tip-nanohole direction towards the upper half of the Fourier space images. From the cross-sections (d-f), we find that the central fringes all shift +1.03 NA from the central axis of the Fourier space image. This value is exactly as we predicted (see equation 5.19) because at λ_0=700 nm, on 200 nm gold film, $\frac{k'_{SPP}}{k_0}$ equals 1.03 [44].

In figure 5.14, the red lines are fits to the cross-sections using equation 5.20 (similar to equation 5.15):

$$I(NA) = \sum_{\lambda=650,700,750\ nm} I_0(\lambda)(1 + V cos[\tfrac{2\pi}{\lambda} d\ (NA + \tfrac{k'_{SPP}(\lambda)}{k_0(\lambda)})])Sinc^2(\tfrac{\pi D\ (NA+\frac{k'_{SPP}(\lambda)}{k_0(\lambda)})}{n\lambda})$$
$$V = 2cos(\theta)\tfrac{\sqrt{I_1 I_2}}{I_1+I_2}\,|\gamma_{12}| \tag{5.20}$$

where n=1.5 is the refractive index of the glass substrate, d=2μm is the separation of the nanohole pair, D=250 nm is the diameter of the nanoholes and $\frac{k'_{SPP}}{k_0}$ equals 1.03. We use

the following relative normalized intensities: $I_0(700nm)$=0.5, $I_0(650nm)$=$I_0(750nm)$=0.25. It is clear that the fits agree well with the experimental cross-sections. From the fits, we can determine the visibility $V = 0.8 \pm 0.05$ for L=1 μm, $V = 0.88 \pm 0.05$ for L=2 μm and $V = 0.91 \pm 0.05$ for L=3 μm.

Degree of coherence for a 2 μm SPP path difference (nanohole diameter 250 nm

For the case in figure 5.14, the visibility V can be calculated as:

$$V = 2cos(\theta)\frac{\sqrt{I_1 I_2}}{I_1 + I_2}|\gamma_{12}| = \frac{2\frac{e^{-k''_{SPP}(L+L+d)}}{\sqrt{L}\sqrt{(L+d)}}}{\frac{e^{-2k''_{SPP}L}}{L} + \frac{e^{-2k''_{SPP}(L+d)}}{(L+d)}}|\gamma_{12}| \tag{5.21}$$

where k''_{SPP}= $1/2L_{SPP}$ (L_{SPP} = 20.7 μm, calculated in 5.6.2) and d is 2 μm.

The measured visibilities from the cross-sections of figure 5.14 are plotted in figure 5.15(b). It is clear that the measured visibilities fit well with the theoretical curve from equation 5.21 when $|\gamma_{12}|$ equals 0.95. In these experiments, the plasmonic path difference is always 2 μm, so the degree of coherence $|\gamma_{12}|$ is 0.95±0.05 when the plasmonic path difference is 2 μm.

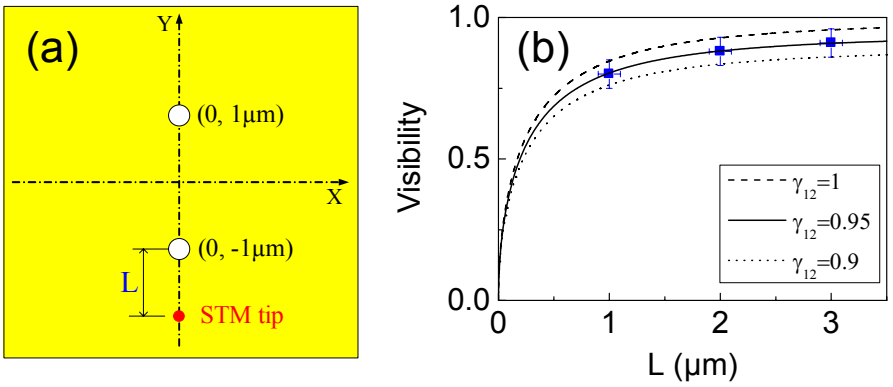

Figure 5.15: (a) Schematic showing the relative position of the STM tip to the nanohole pair. (b) The visibility as a function of L. The blue squares are the measured visibilities from figure 5.14. The lines are the theoretical curves based on equation 5.21 with $|\gamma_{12}|$=1 (dash line), $|\gamma_{12}|$=0.95 (solid line) and $|\gamma_{12}|$=0.9 (dot line).

Arbitrary STM tip position with respect to the nanohole pair

In most cases, the STM tip is put at an arbitrary position on the gold film surface neither along x axis nor along y axis. Figures 5.16 (e) and (f) show the schematics with the STM tip at (-1 μm, 2.5 μm) and (-1.5 μm, 1 μm) respectively. Figure 5.16 shows the Fourier space images (a-b) and the corresponding cross-sections (c-d) with these two tip-nanohole relative positions (indicated in figure 5.16 (e-f)). The corresponding values of r_1, r_2, $cos(\theta)$ and $\delta\varphi$ (defined in equation 5.9 as $\frac{k'_{SPP}}{k_0}\frac{(|r_2|-|r_1|)}{d}$) for the two tip positions are given in table 5.2.

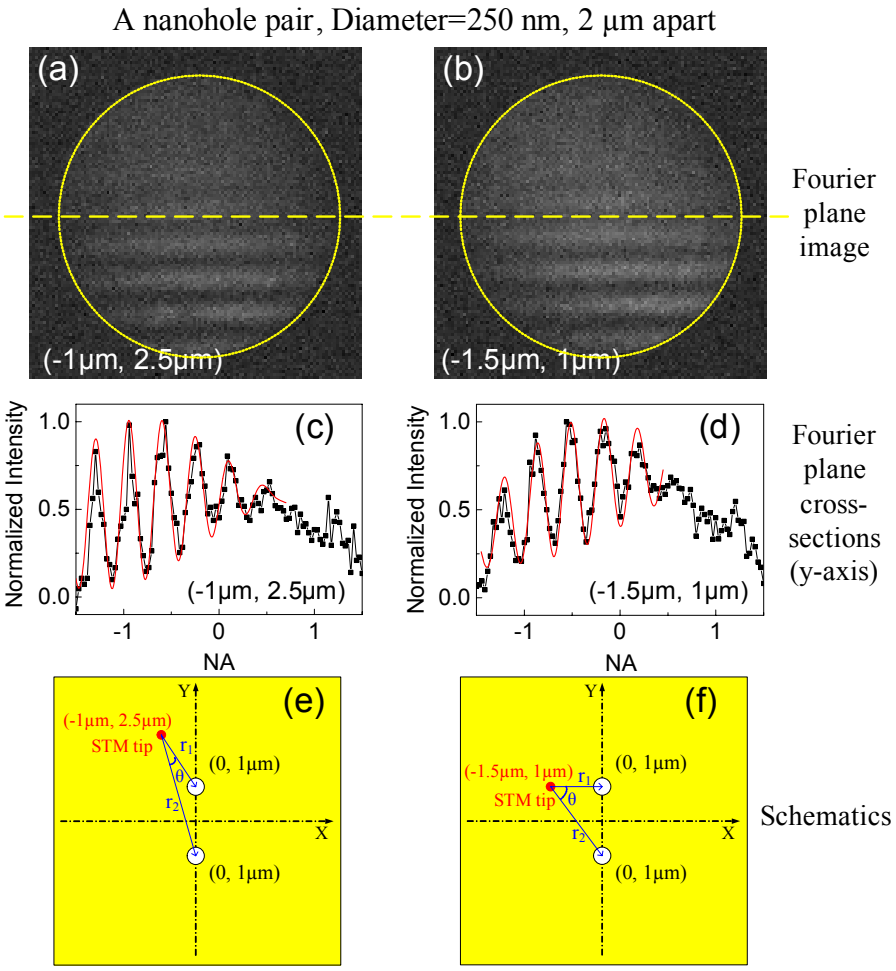

Figure 5.16: The tip is neither along the x axis nor y axis. Fourier space image with the tip at (-1 μm, 2.5 μm) (b) and (-1.5 μm, 1 μm) (a) . The corresponding cross-sections are shown in (c) and (d) with the theoretical fits (red lines) from equation **??** and equation **??** respectively.

Table 5.2: The corresponding values of different parameters for the two tip positions shown in figure 5.16 (e) and (f)

d μm	Tip Position (x μm, y μm)	r_1 μm	r_2 μm	$cos(\theta)$	Calculated I_2/I_1	V	$\delta\varphi$
2	(-1, 2.5)	1.8	3.64	0.95	0.45	0.88 $\lvert\gamma_{12}\rvert$	$0.92\frac{k'_{SPP}}{k_0}$
2	(-1.5, 1)	1.5	2.5	0.6	0.57	0.58 $\lvert\gamma_{12}\rvert$	$0.5\frac{k'_{SPP}}{k_0}$

In figure 5.16 (c) and (d), the red lines are fits to the cross-sections using equation 5.22

(similar to equation 5.15 and equation 5.20):

$$
\begin{aligned}
&I(NA) = \textstyle\sum_{\lambda=650,700,750\ nm} I_0(\lambda)(1 + Vcos[\frac{2\pi}{\lambda} d\ (NA + \delta\varphi)])\ Sinc^2(\frac{\pi D\ (NA+\delta\varphi)}{n\lambda}) \\
&V = 2cos(\theta)\frac{\sqrt{I_1 I_2}}{I_1+I_2}\ |\gamma_{12}| \\
&\delta\varphi(phase\ shift) = \frac{k'_{SPP}}{k_0}\frac{(|r_2|-|r_1|)}{d}
\end{aligned}
\tag{5.22}
$$

It is clear that the theoretical curves fit well with the experimental data. From these Fourier space images and the cross-sections we see that although $\delta\varphi$ is quite different for these two tip positions, the interference fringes for the two tip positions are not so different owing to another important parameter: $cos(\theta)$. This also means that the relative tip-hole position (represented by $cos(\theta)$) plays an important role in the interference fringes.

5.6.3 Conclusion

In conclusion, from these radiative scattering experiments discussed above involving nanohole pairs (D=250 nm, d=2 μm), we clearly see that with SPP path difference smaller than 2 μm there is interference in the Fourier space image and the interference fringes can be well simulated by including the diffraction profile of single slits and the multi-wavelengths beating. With a 2 μm SPP path difference, the interference in the Fourier space has a degree of coherence of 0.95, very close to 1, so the coherence length is longer than 2 μm.

We also tried to repeat these radiative scattering experiments of nanohole pairs with a larger nanohole separation (d) and tried to find the exact value of the coherence length. But when d increases, with 250 nm diameter nanoholes, the radiative scattering intensity decreases due to the longer tip-nanohole distance and thus greater attenuation. So we designed a sample with nanoholes that have a larger diameter (1 μm) to increase the radiative scattering intensity. In this way, we can repeat these radiative scattering experiments with nanohole pairs with larger separations d and try to find the coherence length of the STM-excited propagating SPP.

5.7 Radiative scattering of STM-excited propagating SPP by two 1 μm nanoholes

In the last part of these experiments, we excite propagating SPP on a 200 nm opaque gold film near a nanohole pair with a diameter around 1 μm using a W STM tip. The STM-excited propagating SPP propagate on the gold film surface and are scattered by the nanoholes. This scattered light is detected both in the real space and Fourier space images.

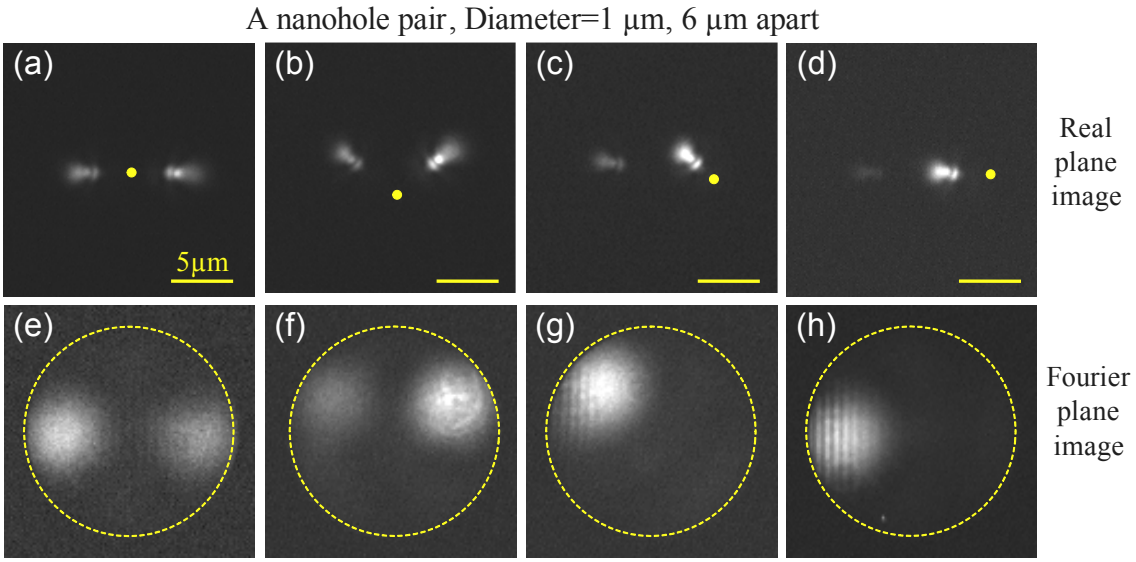

Figure 5.17: Real space (a-d) and Fourier space (e-h) images of the light emission from a nanohole pair with a diameter 1 μm for different tip positions. The propagating SPP are scattered by the nanoholes. In (a)-(d), the yellow spot indicates the tip position. The scale bar is 5 μm. In (e)-(h), the yellow dashed circle indicates the numerical aperture of the oil objective, i.e., NA=1.45.

Figure 5.17 shows real space images obtained with the STM tip at four different locations with respect to the nanohole pair. Similarly to the single hole experiments, the STM-excited propagating SPP are scattered along the tip-hole direction as shown in both real space and Fourier space images (figure 5.17). A very interesting phenomenon appears in the Fourier space. When the scattered light from the two nanoholes has no component along the same direction, there are no interference fringes (figure 5.17 (e) and (f)). On the contrary, when the scattered light has components along the same direction, there are interference fringes (figure 5.17 (g) and (h)). It is clear that when the tip is along the nanohole direction the fringes are clearer. In the following experiments, we will put the tip along the perpendicular bisector of the nanohole axis or along the nanohole axis.

5.7.1 Radiative scattering by two 1 μm nanoholes: equal SPP paths cases

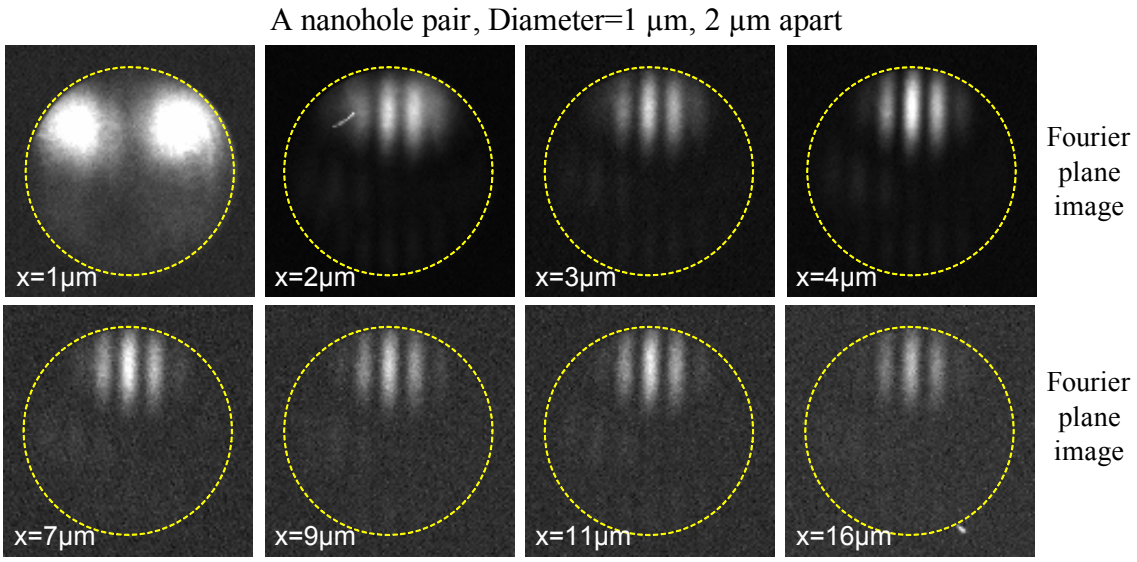

Figure 5.18: The interference patterns in the Fourier space of the scattered propagating surface plasmons from a nanohole pair (diameter 1 μm) with the STM tip displaced along the x axis.

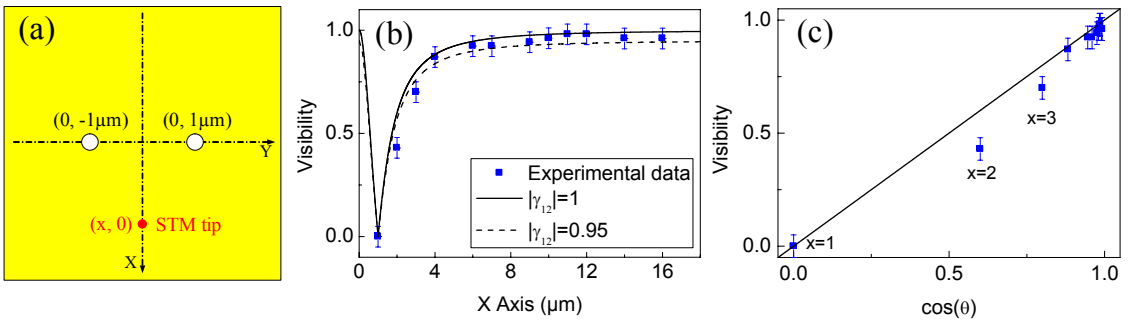

Figure 5.19: (a) Schematic showing the tip position in the experiments. (b) The visibility as a function of the STM tip position along x axis. The blue square points are experimental data and are measured from figure 5.18. The black curves are based on the equation 5.23 with $\gamma_{12} = 1$ and $\gamma_{12} = 0.95$. (c) The visibility as a function of $cos(\theta)$. The blue square points are experimental data and measured from figure 5.18. The black line is $V = cos(\theta)$.

When we put the STM tip along the perpendicular bisector of the nanohole axis, the SPP paths are equal (same situation as in section 5.6.1). In this case, the visibility can be written as (same as equation 5.16, the separation of the nanoholes is d=2 μm):

$$V = cos(\theta)|\gamma_{12}(L_{PPD})| = \frac{x^2 - 1}{x^2 + 1}|\gamma_{12}(L_{PPD})| \tag{5.23}$$

where θ is the angle between $\hat{r}_1$ and $\hat{r}_1$ (as shown in figure 5.9). Here, the plasmonic path difference L_{PPD} is equal to 0.

Figure 5.18 presents the interference patterns in the Fourier space for different positions of the STM tip along the x axis. It is clear that the interference pattern is seen even when the STM tip is more than 16 μm away from the hole. The visibilities of the interference fringes are measured and plotted in figure 5.19 as a function of x and as a function of $cos(\theta)$. To find the $|\gamma_{12}(L_{PPD} = 0)|$, we plot the theoretical curve based on equation 5.23 and try to fit with the experimental data. Thus, from figure 5.19 (b) and (c) we find that the experimental data fit well with the theoretical curve when $|\gamma_{12}(L_{PPD})|$ equals 1. Therefore, we find that the degree of coherence $|\gamma_{12}|$ for L_{PPD}=0 is 1.

It is important to note that it is very difficult to deduce the $|\gamma_{12}|$ using nanohole pairs with diameter=250 nm. This is because the scattered intensity from 250 nm nanoholes is very low.

5.7.2 Radiative scattering by two 1 μm nanoholes: different SPP paths cases

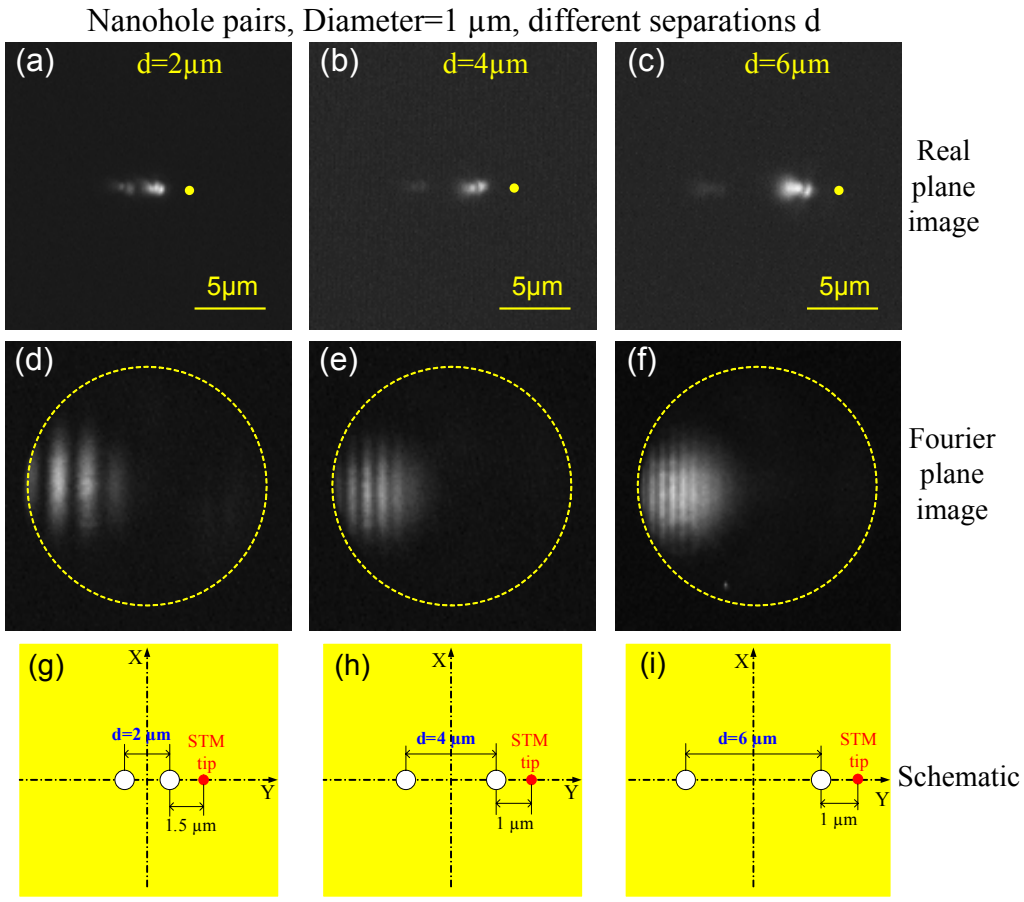

Figure 5.20: Real space (a-c) and Fourier space (d-e) images of the scattered propagating SPP from a 1 μm nanohole pair with three different nanohole separations d (2 μm, 4 μm, 6 μm). The tip is along the nanohole axis as indicated with the yellow spots in (a-c). (g-i) are the corresponding schematics.

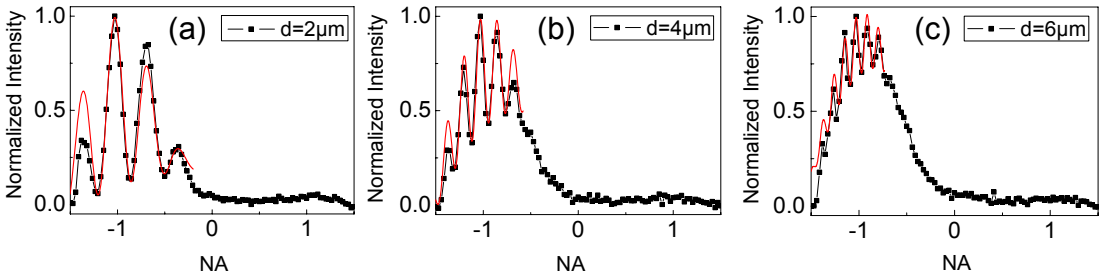

Figure 5.21: The corresponding cross-sections of the interference fringes in the Fourier space images of figure 5.20.

Figure 5.20 shows a series of experiments performed in the same way as in figure 5.17(d). Here, we change the distance d between the nanoholes: d=2 μm ((a) and (d)), d=4 μm ((b) and (e)) and d=6 μm ((c) and (f)). The SPP path differences in the three cases are all equal to the corresponding d. In the schematics (g-i), the relative position between the STM tip and the nanohole pair are presented. In Fourier space images (d-f), it is clear that the period of the interference fringes decreases when d increases. The periods are 0.353 $\pm$ 0.015, 0.176 $\pm$ 0.015 and 0.118 $\pm$ 0.015 in NA units for d=2 μm, d=4 μm and d=6 μm respectively. These periods are all equal to λ/d, the angular period of the Young's double slit experiment.

The corresponding cross-sections of the interference fringes are shown in figure 5.21. From the Fourier space images and the cross-sections, we see that the visibility V of the interference fringe pattern decreases when the distance d between the nanoholes increases. In these experiments, the nanohole separation d is equal to the plasmonic path difference L_{PPD}, so it means that visibility V decreases as the L_{PPD} increases. The visibilities V are 0.8, 0.42 and 0.2 for L_{PPD}=2 μm, L_{PPD}=4 μm and L_{PPD}=6 μm respectively. This may be related to a decrease of $|\gamma_{12}(L_{PPD})|$ when the plasmonic path difference L_{PPD} increases. This phenomenon may indicate that the STM-excited propagating surface plasmons have a certain coherence length L_c between 2 μm and 6 μm. However, in these experiments, the decrease of the visibility V may be also due to the increasing difference of the relative intensities scattered from the two nanoholes (see real space image in figure 5.20(a-c)).

Figure 5.22 shows two models for the radiative scattering intensity at the two nanoholes. In figure 5.22(a), the red circles represent the STM-excited propagating SPP. The STM-excited SPP first reaches nanohole No.1 and then nanohole No.2. Here, the in-plane scattering of nanohole No.1 is ignored. The separation of the nanohole pair is d. The distance between the STM tip and nanohole No.1 is r_1 and the distance between the STM tip and nanohole No.2 is r_2 , so the propagating SPP intensities at the two nanohole positions are:

$$\begin{aligned} I_1 &= I_0 \frac{e^{-r_1/L_{SPP}}}{r_1} \\ I_2 &= I_0 \frac{e^{-r_2/L_{SPP}}}{r_2} \end{aligned} \tag{5.24}$$

where I_0 is the propagating SPP intensity at the tip position and L_{SPP} is the propagation length of SPP. r_1, r_2 and d are indicated in figure 5.22.

In figure 5.22(b), the in-plane scattering of nanohole No.1 is considered and represented

by the blue circles. The propagating SPP intensities at the two positions are:

$$\begin{aligned} I_1 &= I_0 \frac{e^{-r_1/L_{SPP}}}{r_1} \\ I_2 &= \alpha I_0 \frac{e^{-r_2/L_{SPP}}}{r_2} + \beta I_1 \frac{e^{-d/L_{SPP}}}{d} \end{aligned} \tag{5.25}$$

where α is the transmission coefficient when the STM-excited propagating SPP passes the nanohole No.1 along the tip-nanohole axis and β is the coefficient of the in-plane scattering by the nanohole No.1 along the tip-nanohole axis. In principle, the model in (b) is more precise but more complicated because of the unknown parameters α and β.

In the next section, we will show that the model of figure 5.22(a) is sufficient for describing the intensity ratio between I_1 and I_2.

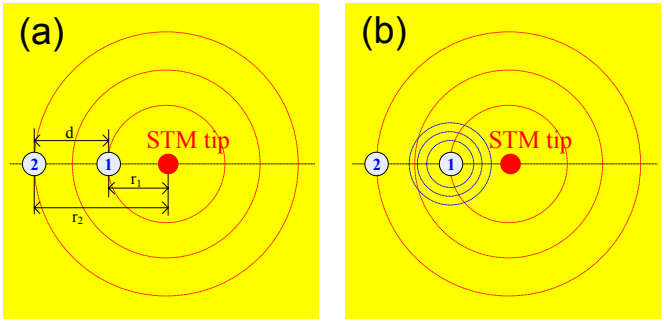

Figure 5.22: Two models presenting the scattering of STM-excited propagating SPP by a nanohole pair. The STM tip is along the nanohole axis. In (a-b) the red circles represent the STM-excited propagating SPP, in (b) the blue circles represent the in-plane scattering of nanohole No.1.

5.8 Coherence length of STM-excited propagating SPP deduced from the interference fringes

We define the coherence length L_c as the length where the $|\gamma_{12}(L)|$ decreases to 1/2 of the value measured at L_{PPD}=0 [113]. From the discussion above, $|\gamma_{12}(L_{PPD}=0)|$ is equal to 1. To calculate $|\gamma_{12}(L_{PPD})|$, based on equation 5.9, we have:

$$|\gamma_{12}(L_{PPD})| = \frac{V}{cos(\theta)\times\frac{2\sqrt{I_1 I_2}}{I_1+I_2}} = \frac{V}{2cos(\theta)}\left(\sqrt{\frac{I_1}{I_2}}+\sqrt{\frac{I_2}{I_1}}\right) \tag{5.26}$$

Thus, to obtain $|\gamma_{12}(L_{PPD})|$, we need to measure the visibility V, $cos(\theta)$ and the intensity ratio I_2/I_1 for different L_{PPD}. The measurement of the visibility V is from the interference fringe pattern in the Fourier space images. $cos(\theta)$ can be determined from the tip-nanohole relative positions. The intensity ratio I_2/I_1 can be measured from the real space images and also can be calculated with the tip-nanohole relative positions based on equation 5.24 (model in figure 5.22(a)). Here, the propagation length is 20.7 μm as calculated in subsection 5.6.2.

Table 5.3: Comparison of calculated and measured I_2/I_1 values at different tip positions.

nanohole separation (μm)	Tip Position (x μm, y μm)	r_1 (μm)	r_2 (μm)	Calculated I_2/I_1	Measured I_2/I_1
6	(-3.5, 3)	3.50	6.95	0.431	0.426
6	(-2.5, 2)	2.70	5.60	0.422	0.419
6	(-3.5, 2)	3.64	6.10	0.533	0.529
6	(1.0, -4.5)	1.80	7.57	0.183	0.180
6	(1.5, -4.5)	2.12	7.65	0.216	0.212
6	(0, -4.5)	1.00	7.00	0.100	0.107

Table 5.3 presents the calculated and measured I_2/I_1 for different tip positions (tip-nanoholes distances r_1 and r_2). It is clear that the calculated and measured light intensity ratios at the two nanoholes I_2/I_1 are very similar. Later on, we will use the calculated I_2/I_1 value for the deduction of $|\gamma_{12}(L_{PPD})|$. This also shows that the model in figure 5.22(a) is good enough to describe the propagating SPP intensities at the two nanoholes.

Table 5.4: The deduction of $|\gamma_{12}(L_{PPD})|$ for different tip positions based on equation 5.26. For all the cases, the center of the nanohole pairs is at (0,0) and the nanohole pairs are along y axis.

d (μm)	Tip Position (x μm, y μm)	measured V	r_1 (μm)	r_2 (μm)	L_{PPD} (μm)	Calculated I_2/I_1	$cos(\theta)$	$\lvert\gamma_{12}(L_{PPD})\rvert$
2	(2.5, 3.5)	0.873	3.54	5.15	**1.61**	0.514	0.962	**0.931**
2	(1.5, 3.5)	0.862	2.91	4.74	**1.83**	0.566	0.976	**0.919**
2	(0.5, 3.5)	0.810	2.55	4.53	**1.98**	0.638	0.996	**0.858**
2	(0.0, 2.5)	0.800	1.50	3.50	**2.00**	0.391	1.000	**0.890**
4	(2.0, 3.0)	0.312	2.24	5.39	**3.15**	0.360	0.747	**0.728**
4	(2.0, -5.0)	0.578	3.61	7.28	**3.67**	0.419	0.952	**0.665**
4	(1.0, -4.0)	0.505	2.24	6.09	**3.85**	0.309	0.956	**0.622**
4	(0.0, 3.0)	0.420	1.00	5.00	**4.00**	0.167	1.000	**0.600**
6	(1.5, 3.0)	0.091	1.50	6.18	**4.68**	0.196	0.243	**0.506**
6	(2.0, -4.0)	0.255	2.24	7.28	**5.04**	0.244	0.676	**0.476**
6	(1.5, -4.0)	0.217	1.50	6.18	**5.36**	0.197	0.717	**0.408**
6	(2.0, -5.0)	0.274	2.83	8.25	**5.42**	0.268	0.858	**0.391**
6	(3.5, -6.0)	0.315	3.90	9.34	**5.44**	0.327	0.912	**0.402**
6	(0.5, -4.0)	0.205	1.12	7.02	**5.90**	0.122	0.924	**0.357**
6	(0.0, 4.0)	0.194	1.00	7.00	**6.00**	0.110	1.000	**0.337**

Table 5.4 shows the value of $|\gamma_{12}(L_{PPD})|$ deduced for different tip positions from equation 5.26. Figure 5.23 shows the degree of coherence $|\gamma_{12}(L_{PPD})|$ as a function of the plasmonic path difference L_{PPD} according to the data in Table 5.4. $|\gamma_{12}(L_{PPD})|$ is deduced from the measured visibility V and the calculated I_2/I_1 and $cos(\theta)$ for different tip positions. The solid curve is a gaussian fitting. We can find that when L_{PPD} is around 4.7 μm, the degree of coherence $|\gamma_{12}(L_{PPD})|$ is 0.5. Thus, the coherence length L_c is measured at 4.7$\pm$0.5 μm.

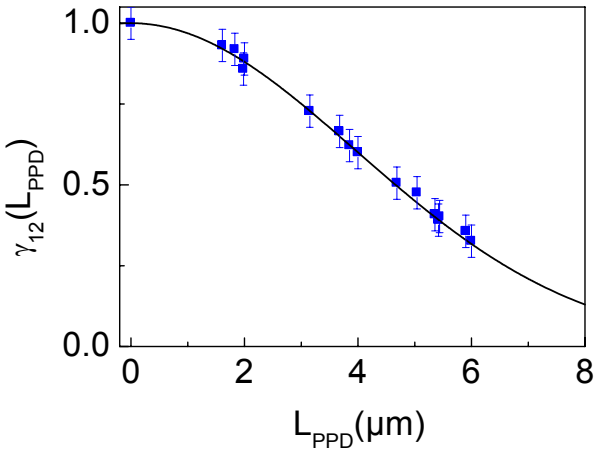

Figure 5.23: The degree of coherence $|\gamma_{12}(L_{PPD})|$ as a function of the plasmonic path difference L_{PPD}. The blue square points are the degree of coherence listed in Table 5.4. The solid curve is a gaussian fit.

5.9 Coherence length of SPP as deduced from the radiative scattering spectra

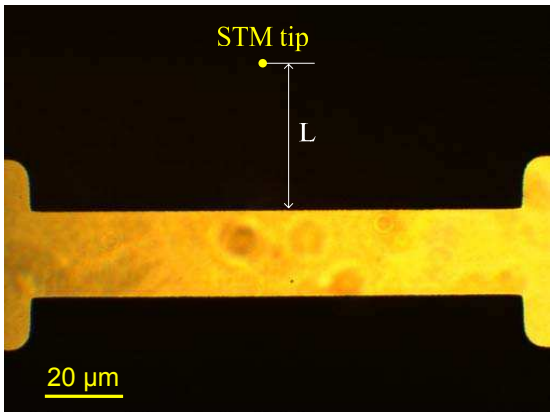

Figure 5.24: The transmission image showing the relative position between the STM tip and a etched line. The distance between the STM tip and the etched line is defined as L. The gold film thickness is 200 nm, so no light can transmit through the gold film (dark area in this image).

For a 200 nm thick gold film, light cannot transmit through it. In order to measure the spectrum of STM-excited propagating SPP on a 200 nm thick gold film, we use an etched line with a width of ~ 20 μm as shown in figure 5.24. The STM-excited propagating SPP are scattered into the far field by the etched line and may be detected by our spectrometer.

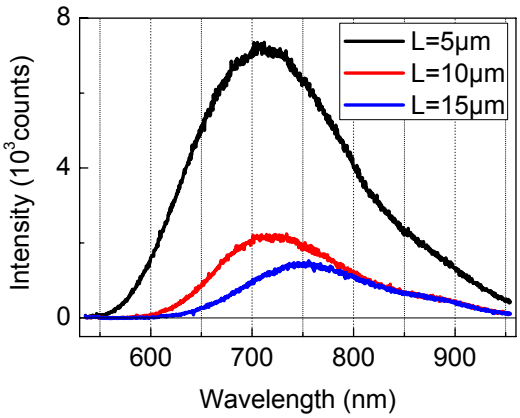

Figure 5.25: The radiation spectra of scattered STM-excited SPP by the etched line as a function of L. The acquisition time of each spectrum is 60 s.

Figure 5.25 shows the spectra of scattered STM-excited SPP by the etched line as a function of L. The spectra are recorded with the following tunneling conditions: 2.8V, 6nA. It is clear that the spectra are broadband and the spectrum is red shifted when L increases from 5 μm to 10 μm. It is also clear that the intensity of the spectra decreases when L increases. This is because of the 2D exponentially decay of the STM-excited propagating surface plasmons. Figure 5.25 also shows that the full-width-half-maximum (FWHM) of the spectrum decreases when L increases. This is because of a shorter propagation length for a smaller wavelength of SPP (see figure 2.2). Thus, when the STM tip is close to the etched line (small L), nearly all the STM-excited SPP can propagate to the etched line. On the contrary, when the STM tip is far from the etched line (large L), only the long wavelength part of STM-excited SPP can propagate to the etched line. Figure 5.26 clearly shows the central peak position and FWHM of scattered STM-excited SPP by the etched line as a function of L.

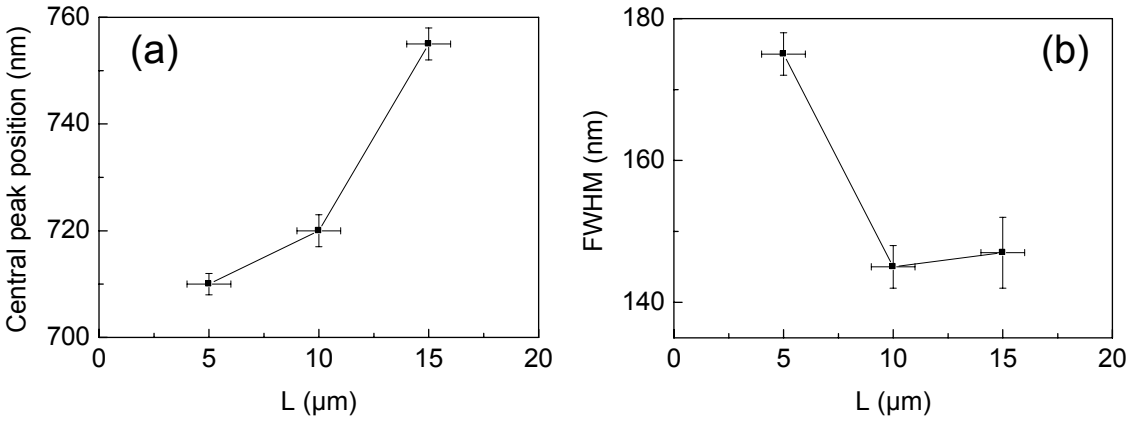

Figure 5.26: The central peak position (a) and FWHM (b) of scattered STM-excited SPP by the etched line as a function of L.

From figure 5.27, we see that the spectra of STM-excited propagating surface plasmons scattered by a nanohole pair are also broadband, with central wavelength λ_0=700 nm, and

FWHM $\Delta\lambda$=150±50 nm. The spectra are recorded with the same tunneling conditions: 2.8V, 6nA. Figure 5.27(a) shows the spectrum of the STM-excited propagating SPP scattered by a nanohole pair with 250 nm diameter and 2 μm separation. The tip is in the center of the nanohole pair. Figure 5.27(b) shows the spectrum of the STM-excited propagating SPP scattered by a nanohole pair with 1 μm diameter and 2 μm separation. The tip is along the perpendicular bisector and 2 μm away from the nanohole pair center. The two spectra in figure 5.27 are very similar. They are also similar to the spectrum in figure 5.25 with L=5 μm. This is because during our experiments the tip-nanohole distances are close to 5 μm. From this comparison, we can say that the nanoholes do not influence a lot on the spectrum of STM-excited SPP, when the SPP is scattered by the nanoholes.

If the spectrum of STM-excited propagating surface plasmons is homogenously broadened, the coherence length can be calculated using the equation $L_c=(\lambda_0)^2/\Delta\lambda$ [114]. Here, with λ_0=700 nm and $\Delta\lambda$=150±50 nm, the coherence length L_c=3.7±1.2 μm which is close to the 4.7±0.5 μm coherence length as measured from the interference fringe patterns.

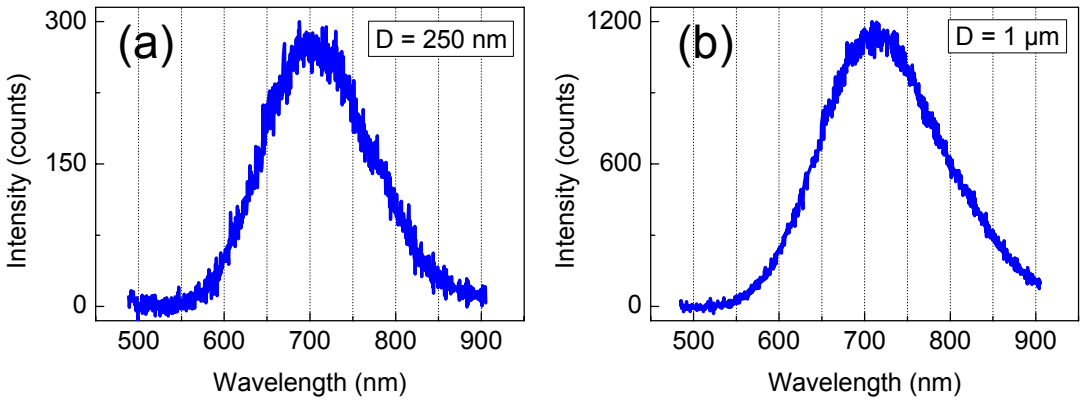

Figure 5.27: The spectra of STM-excited propagating surface plasmons scattered by a nanohole pair with (a) diameter D=250 nm, separation d=2 μm and (b) a nanohole pair with diameter D=1 μm, separation d=2 μm . Both of the spectra are centered around 700 nm and with a FWHM around 150 nm. For both (a) and (b), the tunneling condition is V=2.8 volts, I=6 nA and the acquisition time of each spectrum is 300 s.

5.10 Homogeneous broadening of STM-excited propagating SPP

The coherence length derived from the emission spectrum by assuming homogeneous broadening is 3.7±1.2 μm. This value is very close to the coherence length of STM-excited propagating SPP that we measured from the interference fringe patterns 4.7±0.5 μm. Thus, it may be concluded that STM-excited propagating SPP are homogeneously broadened. This means that each individual plasmon has the same broadband energy spectrum seen in figure 5.27.

Until now, it was believed that the broadband spectrum was inhomogeneous, i.e., that individual plasmons have different energies within the observed energy spectrum. The

homogeneous broadening of STM-excited propagating SPP that we have deduced in this chapter has important consequences. It indicates that each individual plasmon can interact at any energy (within the energy spectrum) with a quantum device.

5.11 Conclusion

In conclusion, we have shown the scattering of STM-excited propagating SPP on a 200 nm gold film from single nanoholes and nanohole pairs. The scattered light from the nanoholes is recorded both in real space and Fourier space. In real space images, diffraction-limited light spots are seen at the nanohole positions. In Fourier space images with nanohole pairs, interference fringes are clearly seen and the periods of the interference fringe patterns depend on the separations of the nanohole pairs.

The experiment is analogous to Young's double-slit experiment. From the Fourier space interference fringe patterns with different nanohole separations, it is seen that STM-excited propagating surface plasmons are coherent, with a coherence length of 4.7±0.5 μm. This value is similar to the coherence length of 3.7±1.2 μm expected when considering a homogeneously broadened spectrum for the surface plasmons produced by the STM. The coherence length can be measured because it is much smaller than the propagation length of the STM-excited propagating SPP 20.7±2.5 μm. In usual experiments, where propagating SPP are excited by a narrow-band optical source (e.g. a laser), the coherence length cannot be measured as it is much larger than the propagation length of the SPP.

The result obtained here is very important as it demonstrates a method to produce homogeneously broadened surface plasmons which could be used for the fabrication of "white" nano-lasers or plasmonic lasers. Our result is also of crucial importance for the understanding of the mechanism for plasmonic inelastic electron tunneling (IET). Until now, there exists no complete theory for plasmonic IET. On one side, the Fermi golden rule in the dipole approximation [10, 12, 115] has been used to account for (*i*) the coupling between tunneling electrons and the electromagnetic field and (*ii*) the energy distribution of the density of electronic states on the surface. On the other hand, the time fluctuations of the tunneling current [92, 116] is also believed to play a role in the plasmonic IET mechanism. The homogeneous broadening of surface plasmons excited by IET with the STM is certainly a key feature which will validate future theories of plasmonic IET.

Chapter 6

Scattering of STM-excited propagating SPP by Gold Nanoparticles

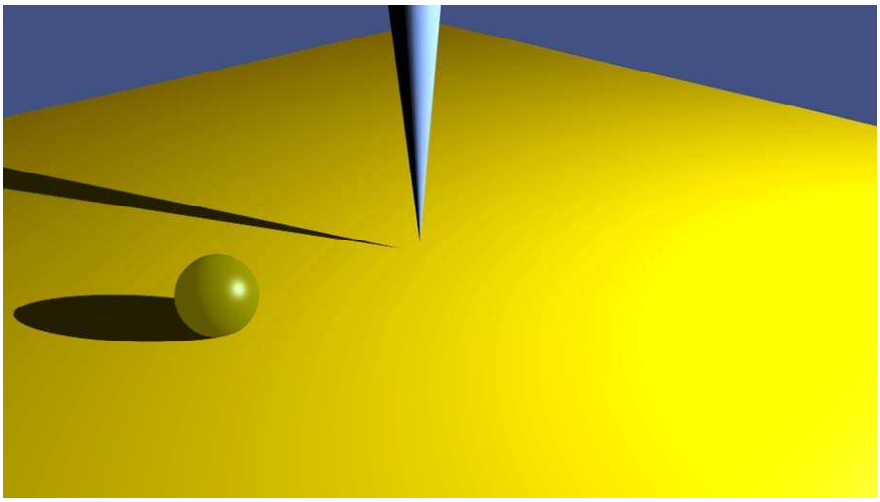

6.1 Introduction

Propagating surface plasmon polaritons (SPP) in metallic nanostructures offer new perspectives for integrating optics at the nanoscale owing to the possibility of confining and guiding electromagnetic field at a subwavelength scale. One of the main goals in SPP research is the ability to control and manipulate the propagation properties (such as the propagation direction and propagation length) of surface plasmons. This control is essential for many prospects of new nanophotonic devices [13, 14, 17, 18, 20]. To control and manipulate the propagation properties of surface plasmons, the propagating SPP scattering plays the main role [117–121]. So it is very useful to know how propagating SPP are scattered by typical optical elements such as nanoparticles.

Experimental studies have shown that nanoparticles on metal surfaces can be used to create efficient micro-optical components for SPP, such as mirrors, beam splitters and interferometers [117, 122–124]. Furthermore, periodic arrays of metal nanoparticles have been shown to exhibit bandgap properties for the propagation of SPP [125–131]. Because of these interesting applications, it is also important to understand how STM-excited propagating SPP are scattered by gold nanoparticles.

In this chapter, we have used colloidal gold nanoparticles as scatterers on a 50 nm thick gold film. The diameter of the nanoparticles are several hundred nanometers. The 2D circular propagating surface plasmons (SPP) wave is generated by IET (inelastic electron tunneling) in the tunneling junction between the STM tip and the gold film surface. We observe the elastic (*in-plane*) and radiative (out of plane) scattering of STM-excited 2D circular SPP by the colloidal gold nanoparticles in both the real and Fourier space. SPP scattering in the surface plane (*in-plane* scattering) is denoted as *elastic* SPP scattering, since SPP scattering into a free space (radiative scattering) is an unwanted process leading to the additional radiative losses experienced by the SPP [132]. The *in-plane* and radiative scattering experiments will be presented successively.

6.2 Sample preparation and characterization

The experimental setup is the same one used for film studies (see figure 3.1). A scanning tunneling microscope (STM) operated in air is mounted on an inverted optical microscope. A 50 nm gold film deposited on a glass substrate (refractive index n=1.52, thickness 170 μm)) is used for the gold nanoparticles deposition. The gold film roughness, measured by atomic force microscopy, is about 1 nm.

Gold nanoparticles (NPs) with diameters of several hundred nm are synthesized by Dr. Wafa Abidi and Prof. Hynd Remita with γ ray radiation in LCP (Laboratoire de Chimie Physique), Orsay [133]. During the synthesis, absorption spectra of gold nanoparticle solution are recorded to follow the growing of the nanoparticles. Figure 6.1(a) shows the absorption spectrum recorded in the end of the synthesis. In the spectrum, we see an absorption peak at around 600 nm which gives a first information of the nanoparticle size. After the synthesis, transmission electron microscopy (TEM) images are recorded to verify the gold nanoparticle morphology. A TEM image in figure 6.1(b) shows that the gold nanoparticles are around 150 nm.

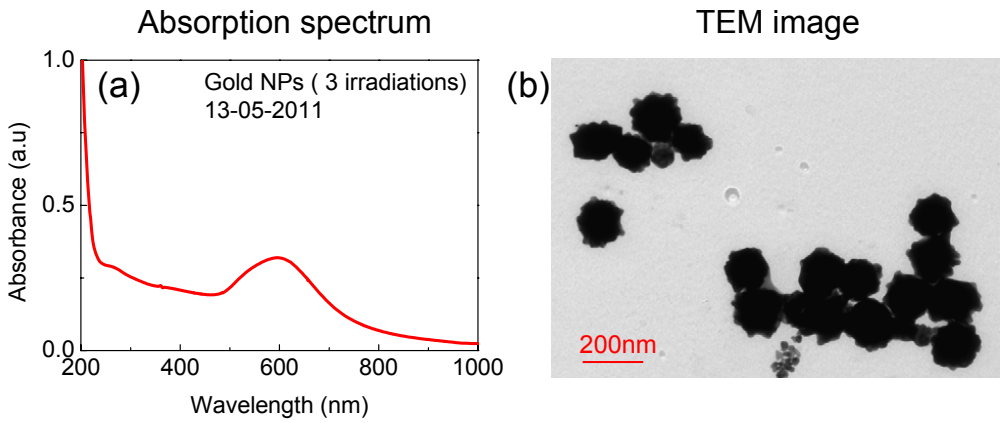

Figure 6.1: The absorption spectrum (a) and TEM image (b) of the gold nanoparticles.

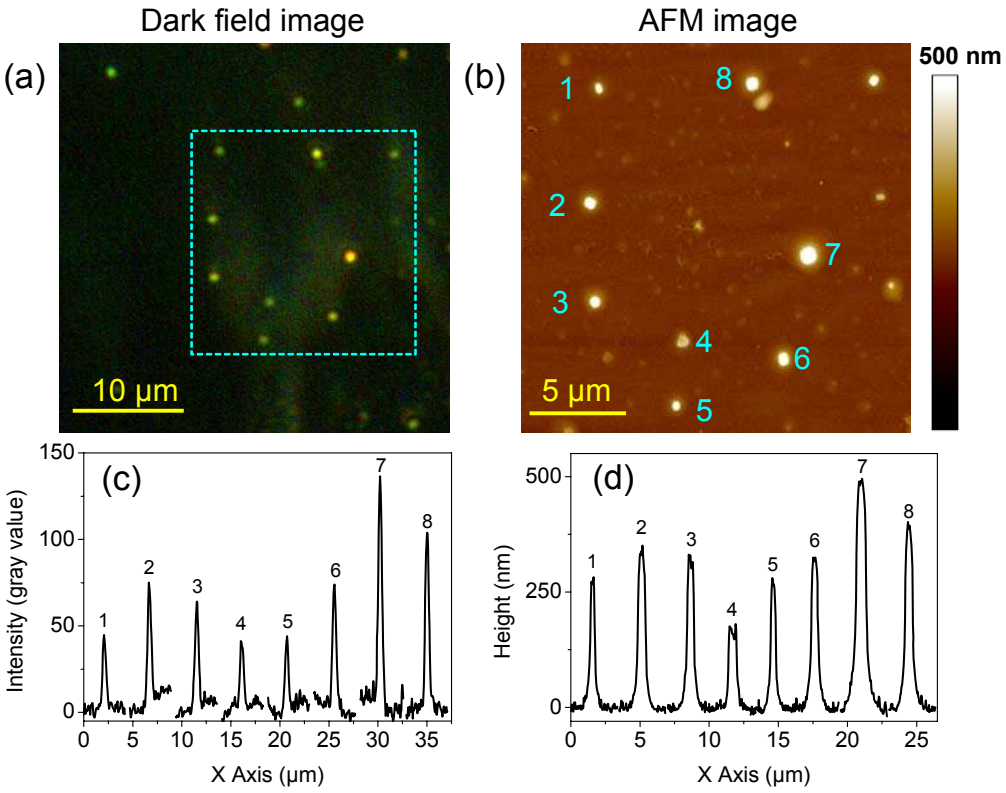

Figure 6.2: (a) Dark field image of gold nanoparticles deposited on a 50 nm gold film on a glass substrate. The cyan dashed square indicates an interesting area for our experiments. There are several gold nanoparticles in this area and the different light scattering colors of these nanoparticles may be due to the different sizes of the gold nanoparticles. The corresponding cross-sections of the gold nanoparticles emission in the dark field image is shown in (c). (b) AFM image (tapping mode) of the gold nanoparticles. The nanoparticles are numbered from 1 to 8. The AFM image clearly shows the different sizes of the nanoparticles. The cross-sections of the gold nanoparticles in the AFM image is shown in (d). The average height of the nanoparticles is around 250 nm.

The dark field image of the gold nanoparticles (deposited on the 50 nm gold film sample) is shown in figure 6.2(a). During the dark field experiments, a white excitation light shines on the sample with a large angle to the optical axis (>60°). In this case, only the scattered light from the gold nanoparticles are collected using an air objective (100×, NA=0.75) and recorded on an Axio color camera (Axio ICc1, Zeiss). In figure 6.2(a), the cyan dashed square indicates an interesting area for our experiments with several gold nanoparticles. The different dark field scattering colors of these nanoparticles are due to the different size of the gold nanoparticles. Figure 6.2(b) shows the AFM image (tapping mode) of the area indicated in figure 6.2(a). The nanoparticles are numbered from 1 to 8. The AFM image and the corresponding cross-sections (figure 6.2(b) and (d)) clearly show the different sizes and heights of the nanoparticles in the area. We see that the dark field scattering is red shifted when the size of the gold nanoparticles increases. For example, nanoparticle No.7 is largest among these nanoparticles and the dark field scattering color is red; and nanoparticle No.1, No.4 and No.5 are smaller among these nanoparticles and the dark field scattering color is green. From figure 6.2 (c) and (d), we also see that the intensities of the dark field scattering is proportional to the nanoparticle size. The larger the gold nanoparticle, the higher the dark field scattering intensity.

6.3 Real space images

6.3.1 Scattering of STM-excited propagating SPP by gold nanoparticles

Two types of experiments have been performed in this section. First (figure 6.3 (a)), we will excite the propagating SPP on the 50 nm gold film with a STM tip and see how the STM-excited propagating SPP are scattered by the gold nanoparticles. Second (figure 6.3 (b)), we will see if propagating SPP can be excited when a STM tip is positioned on a gold nanoparticle deposited on the 50 nm gold film and see how the propagating SPP are scattered by the other gold nanoparticles.

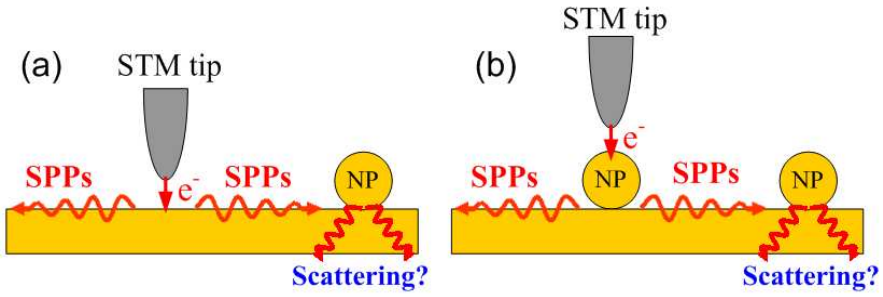

Figure 6.3: Two types of experiments: (a) The propagating SPP are excited (with a STM tip) on the 50 nm gold film and scattered by a gold nanoparticle. (b) The propagating SPP are excited (with a STM tip) when the STM tip excites on a gold nanoparticle deposited on the 50 nm gold film. The propagating SPP are then scattered by another gold nanoparticle.

To record the real space and Fourier space images, both air (100×, NA = 0.75) and immersion oil (100×, NA = 1.45) objectives are used. Both real space images and Fourier

space images are recorded with the Roper CCD camera.

Real space images with the air objective: radiative scattering

With an air objective, the propagation of SPP cannot be *directly* imaged because its numerical aperture is smaller than 1 and the leakage radiation of propagating SPP emits at an angle above the critical angle (a detail discussion is already shown in subsection 2.1.4). But with the help of gold nanoparticles, the propagating SPP electrically excited by the W STM tip and propagating on the gold film surface, can be radiatively scattered into the far field and detected by the air objective. Note that propagating SPP are bounded in the air-gold interface and by radiative scattering they can convert into free-space photons, radiating along all the directions.

Figure 6.4(a) shows the same dark field image as figure 6.2(a). It also reminds the named number of the gold nanoparticle. Figure 6.4(b-c) shows the real space radiative scattering of STM-excited propagating SPP by gold nanoparticles deposited on the 50 nm gold film surface. The images are obtained with the air objective (100×, NA = 0.75).

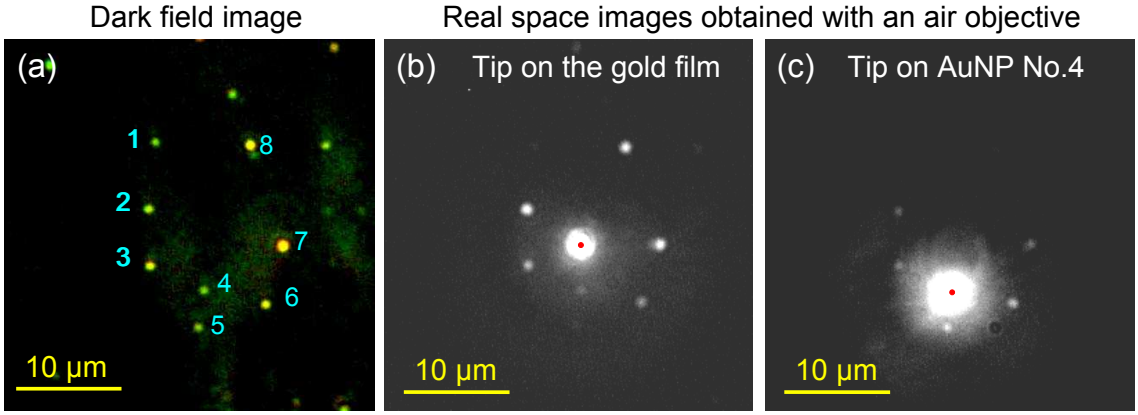

Figure 6.4: (a) The same dark field image as figure 6.2(a) shows the area we study. (b-c) real space radiative scattering of STM-excited propagating SPP by gold nanoparticles deposited on the 50 nm gold film surface. The images are obtained with the air objective (100×, NA = 0.75). The red dot indicates the tip position. In (b) the W tip excites on the gold film and in (c) the W tip excites on gold NP No.4.

In figure 6.4(b), the red dot indicates the STM tip position. The light spot at the tip position is the localized light emission (localized surface plasmons) from the tunneling junction between the STM tip and the gold film (also see in figure 3.5(a)). In figure 6.4(b), we clearly see the bright spots at the nanoparticle positions, which indicates that the STM-excited propagating SPP are radiatively scattered by the gold nanoparticles. The scattered light is especially seen from gold nanoparticles No.2, No.3, No.6, No.7 and No.8. The intensity of the scattered light from gold nanoparticles largely depends on the sizes of gold nanoparticles. In figure 6.4(b), we see that although the tip-particle distance for gold nanoparticle No.4 is smaller than the tip-particle distance for gold nanoparticles No.7 and No.8, the radiatively scattered light intensity is much lower because of the smaller size of gold nanoparticle No.4. The fact we see radiative scattered light from gold nanoparticles

is a significant evidence of the existence of the propagating SPP electrically excited with a STM tip on the 50 nm gold film surface.

A similar experiment is shown in figure 6.4(c). In (c), the STM tip excites on gold nanoparticle No.4. Firstly, the local light emission at the tip position (from the tunneling junction between the STM tip and the gold nanoparticle-gold film system) is more intense ($\sim$ 10 times) than the local light emission at the tip position (from the tunneling junction between the STM tip and the gold film system) in figure 6.4(b). The reason for this difference may be the enhancement of the localized surface plasmon resonance from the gap between the gold nanoparticle and the gold film (see Appendix C). Secondly, similarly to figure 6.4(b), radiatively scattered light is seen from other gold nanoparticles (No.2, No.3, No.5, No.6 and No.7). This clearly shows that propagating SPP can be launched when a STM tip excites on a gold nanoparticle which is deposited on the 50 nm gold film surface. However, the radiatively scattered light in figure 6.4(c) is less intense compare to that in figure 6.4(b), even the localized light emission under the STM tip is more intense than that in figure 6.4(b). This indicates that electrical excitation on a gold nanoparticle which is deposited on the gold film with a STM tip excites propagating SPP with a lower efficiency. This low excitation efficiency of propagating SPP may be due to the extra tunneling barrier introduced by the gold nanoparticle. This phenomenon also indicates that the excitation of propagating surface plasmons does not depend on the localized surface plasmons.

Real space images with the oil objective: *in-plane* and radiative scattering

With an oil objective, the propagation SPP can be *directly* imaged because it has a large numerical aperture which is needed for the leakage radiation imaging of propagating SPP (a detail discussion is already shown in subsection 2.1.4). With the help of the oil objective, other than the radiatively scattering, we can also record the *in-plane* scattering of the propagating SPP on the gold film surface by the gold nanoparticles [132].

Different from radiative scattering, the *in-plane* scattering means that the scattered light is in the surface plane and does not radiate in to far field. Actually, by in-plane scattering, the propagating SPP are *in-plane* scattered into SPP which radially propagate in the surface plane with the same wavenumber. Thus, in order to image the in-plane scattering, we need to use the leakage radiation microscopy configuration [132].

Figure 6.5(a) shows the same dark field image again to remind the named number of the gold nanoparticle. Figure 6.5(b-c) shows the real space radiative and *in-plane* scattering of STM-excited SPP by gold nanoparticles deposited on the 50 nm gold film surface. The images are obtained with the oil objective (100×, NA = 1.45).

In figure 6.5(b), the red dot indicates the STM tip position. In this case, the STM tip tunnels directly to the gold film. It is clear that in the region where the propagating SPP do not reach the gold nanoparticles, the image is the same as the images obtained on the 50 nm gold film surface without any deposited gold nanoparticles (see figure 4.3(a)). This clearly shows how STM-excited SPP propagate on the gold film surface.

When the propagating SPP reach the gold nanoparticles, two phenomena are seen. The first phenomenon we see is the bright spot at each nanoparticle position, which indicates that the STM-excited propagating SPP are radiatively scattered by the gold nanoparticles.

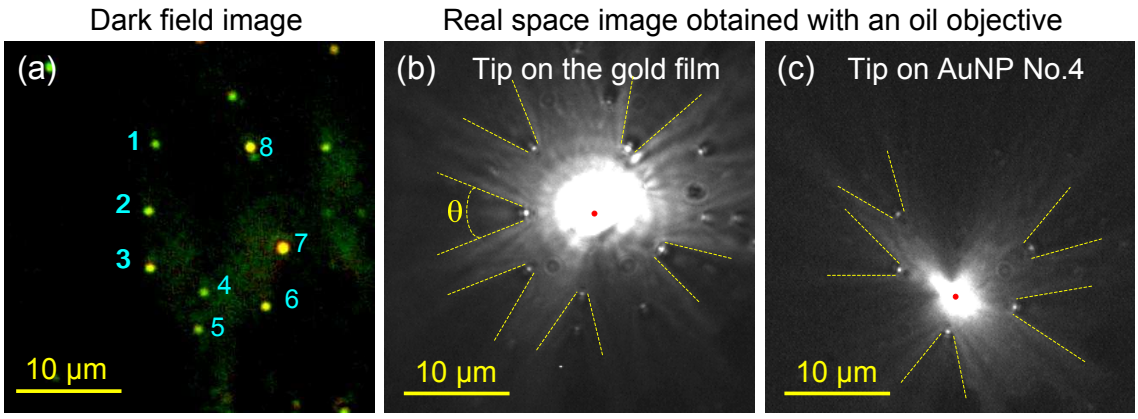

Figure 6.5: (a) The same dark field image as figure 6.2(a) shows the area we study. (b-c) real space radiative and *in-plane* scattering of STM-excited propagating SPP by gold nanoparticles deposited on the 50 nm gold film surface. The images are obtained with the oil objective (100×, NA = 1.45). The red dot indicates the tip position. The *in-plane* scattering angle θ is indicated by the dashed yellow lines for each nanoparticle. In (b) the W tip excites on the gold film and in (c) the W tip excites on gold NP No.4.

This is similar to the real space images using an air objective as shown in figure 6.4(b-c).

The second phenomenon is the *in-plane* scattering of propagating SPP by the gold nanoparticles. In figure 6.5(b), we see that the propagating SPP are blocked by the gold nanoparticles in a region with an angle θ, which is indicated by the yellow dashed lines. This phenomenon is owing to the *in-plane* scattering by the gold nanoparticles. These *in-plane* scattering patterns are similar to the *in-plane* scattering patterns in ref.[132, 134, 135] which are explained by the interference between the excited SPP and the *in-plane* scattered SPP.

A similar experiment is shown in figure 6.5(c). In (c), the STM tip excites on gold nanoparticle No.4 (a detail discussion of the local resonance of the STM tip-gold nanoparticle-gold film system is in Appendix C). Similarly to figure 6.4(c), the intensity is high at the tip position. As explained above, this is mainly related to the localized surface plasmons resonance in the tunneling junction between the STM tip and the gold nanoparticle-gold film system. Similarly to figure 6.5(b), when the propagating SPP do not reach the gold nanoparticles, the image clear shows the propagating SPP on the gold film surface. When the propagating SPP reach the gold nanoparticles, the radiative scattering bright spots and the *in-plane* scattering patterns are seen.

6.3.2 Scattering of STM-excited propagating SPP by a single gold nanoparticle as a function of tip-particle distance

In order to investigate this *in-plane* scattering phenomenon, on the 50 nm gold film surface, we choose an area with only one single nanoparticle. By changing the tip-particle distance, we see the change of the *in-plane* scattering angle θ.

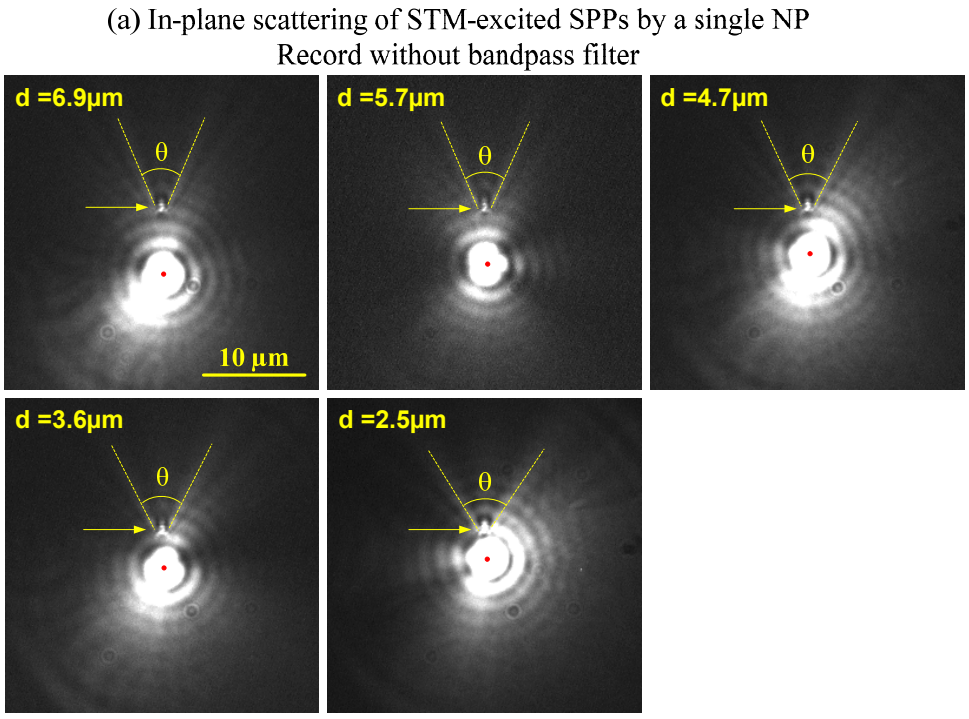

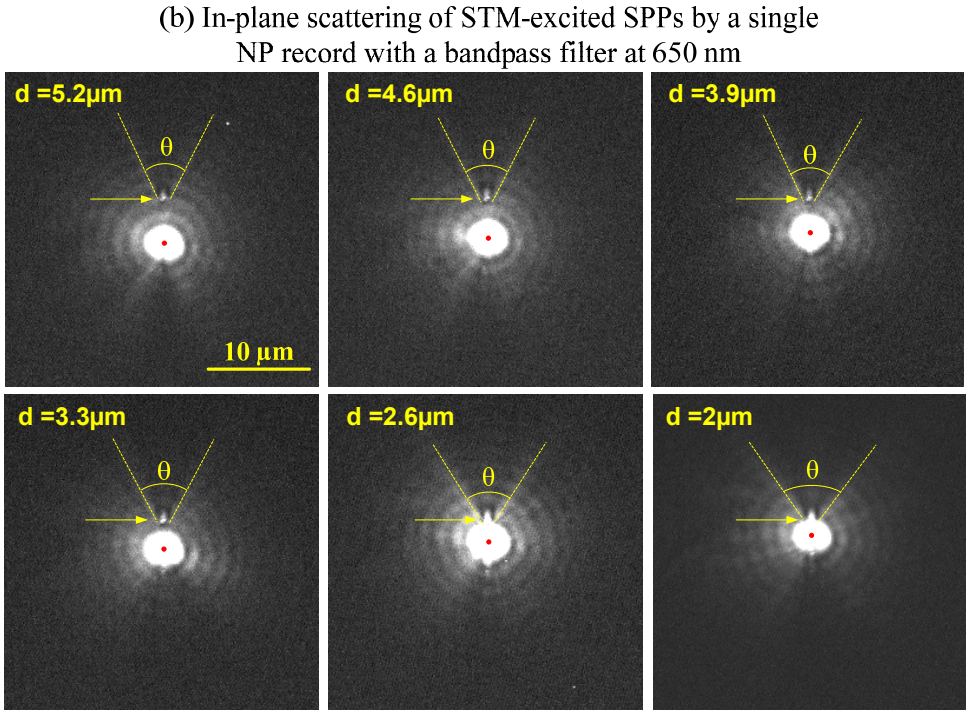

Figure 6.6: *In-plane* scattering of STM-excited propagating SPP by a single nanoparticle in real space: (a) recoded without and (b) with a bandpass filter centered at 650 nm (width 13 nm). The images are obtained using an oil objective (100 ×, NA=1.45). The tip-particle distance d is indicated in each image. The single nanoparticle is indicated by an arrow line and the tip position is indicated by a red dot. The *in-plane* scattering angle θ is indicated by the yellow dashed lines.

Figure 6.6 shows the *in-plane* scattering of STM-excited propagating SPP by a single nanoparticle in real space recorded (a) without a bandpass filter and (b) with a bandpass filter centered at 650 nm (width 13 nm). The images are obtained using an oil objective (100 ×, NA=1.45). In figure 6.6, we clearly see the radiative scattering bright spot and *in-plane* scattering pattern at the particle position for each tip-particle distance d. The tip-particle distance d is indicated for each image and the *in-plane* scattering angle θ is indicated by the yellow dashed lines. It is clear that the θ increases when d decreases.

6.3.3 Model of *in-plane* scattering of 2D circular waves by a point-like scatterer

When propagating SPP are scattered by a nanoparticle or defect, a pronounced *in-plane* scattering pattern is seen. The *in-plane* scattering pattern is related to the interference between the incident SPP and the *in-plane* scattered SPP [132, 135, 136].

From the real space (figure 4.3(a)) and Fourier space (figure 4.12(c)) images of Chapter 4, we know that STM-excited propagating SPP on gold films are circular waves propagating radially from the tip position in all directions. So the pronounced *in-plane* scattering pattern in figure 6.4, figure 6.5 and figure 6.6 can be explained as the interference between the STM-excited propagating SPP and the scattered SPP by the gold nanoparticles.

Figure 6.7(a) shows the sketch of the *in-plane* scattering of 2D circular waves by a single point-like scatterer. The thick black lines indicate the 2D circular waves originating from the point source at (d/2, 0). A single point-like scatterer is at (-d/2, 0). The source-scatterer separation is d. The thin black lines show the *in-plane* scattered 2D circular waves from the scatterer. This interference between the incident 2D circular waves and the *in-plane* scattered 2D circular waves may be calculated as follows.

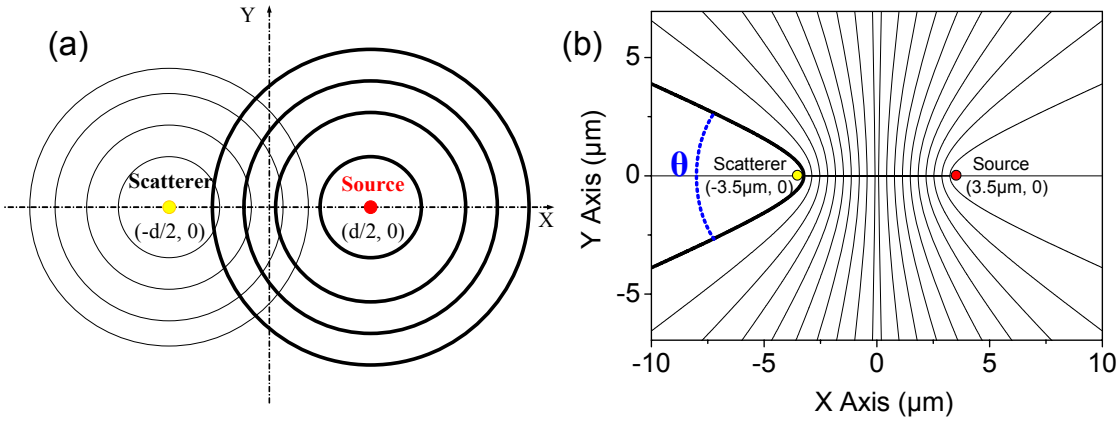

Figure 6.7: (a) Schematic presentation of *in-plane* scattering of 2D circular waves by a single scatterer. The thick black lines indicate the 2D circular waves from the source at (d/2, 0). A single scatterer is at (-d/2, 0) point and the *in-plane* scattered waves are shown as thin black lines. The tip-particle separation is d. (b) The calculated high intensity fringes of the *in-plane* scattering pattern for λ=700 nm. The tip-particle separation d is 7 μm. In (b), the angle θ measured from the fringe closest to the gold nanoparticle (thick black fringe) is named as the *in-plane* scattering angle.

The incident 2D circular waves at position (x,y) can be written as:

$$\begin{aligned} E_1 &= \frac{A_1}{\sqrt{r_1}} \times e^{i\vec{k}_{r_1}\vec{r_1}} \\ |\vec{r_1}| &= \sqrt{(x-d/2)^2+y^2} \end{aligned} \tag{6.1}$$

and the *in-plane* scattered 2D circular waves at position (x,y) can be written as:

$$\begin{aligned} E_2 &= \frac{A_2}{\sqrt{r_2}} \times e^{i\vec{k}_{r_2}\vec{r_2}+i\varphi} \\ |\vec{r_2}| &= \sqrt{(x+d/2)^2+y^2} \end{aligned} \tag{6.2}$$

where $\varphi = \pi/2$ is the phase delay due to the *in-plane* scattering [137]. So the sum intensity of the two fields can be written as:

$$\begin{aligned} I &= |E_1+E_2|^2 = |E_1|^2 + |E_2|^2 + E_1E_2^* + E_1^*E_2 \\ I &= \frac{A_1^2}{r_1} + \frac{A_2^2}{r_2} + 2\frac{A_1A_2}{\sqrt{r_1r_2}}cos(\vec{k}_{r_1}\vec{r_1} - \vec{k}_{r_2}\vec{r_2} - \varphi) \end{aligned} \tag{6.3}$$

The high intensity fringes of this interference can be calculated as:

$$\begin{aligned} &cos(\vec{k}_{r_1}\vec{r_1} - \vec{k}_{r_2}\vec{r_2} - \varphi) = 1 \\ &\vec{k}_{r_1}\vec{r_1} - \vec{k}_{r_2}\vec{r_2} - \varphi = 2\pi m \ (m = 0, 1, 2.....) \end{aligned} \tag{6.4}$$

with

$$\begin{aligned} &|\vec{r_1}| = \sqrt{(x-d/2)^2+y^2} \\ &|\vec{r_2}| = \sqrt{(x+d/2)^2+y^2} \\ &\varphi = \pi/2 \\ &|\vec{k}_{r_1}| = |\vec{k}_{r_2}| = 2\pi/\lambda \end{aligned} \tag{6.5}$$

So the high intensity fringes of this interference are hyperboles written as:

$$y^2 = \frac{((m\lambda+\frac{\lambda}{4})^2 - 2xd)^2 - 4(x-d/2)^2(m\lambda+\frac{\lambda}{4})^2}{4(m\lambda+\frac{\lambda}{4})^2} \tag{6.6}$$

The calculated high intensity fringes of this interference is shown in figure 6.7(b) at λ =700 nm. The source-scatterer separation is 7 μm. The scatterer is at point (-3.5 μm, 0) and the point source is at (3.5 μm, 0). The angle θ measured from the fringe closest to the gold nanoparticle (thick black fringe) is named as the ***in-plane* scattering angle**. In figure 6.7(b), the fringes are calculated without intensity information. In fact, the incident intensity A_1 is much larger than the scattered intensity A_2. Near the scatterer, the intensity difference between A_1 and A_2 is smaller and the interference is more visible. While far from the scatterer, because of the large intensity difference between A_1 and A_2, the interference fringes visibility decreases a lot and the interference can not be seen.

Figure 6.8 shows the calculated high intensity fringes of the *in-plane* scattering pattern at different wavelengths and with different source-scatter separations. Figure 6.8(a) and (b) are calculated for the same wavelength λ=700 nm but different tip-particle separations, d=7 μm and d=4.2 μm respectively. It is very clear that at the same wavelength, when d decreases, the *in-plane* scattering angle θ increases. Figure 6.8 (b) and (c) are calculated for the same source-scatterer separation d=4.2 μm but different wavelengths, λ=700 nm and λ=600 nm respectively. we see that when the wavelength λ decreases, the *in-plane* scattering angle θ decreases a little.

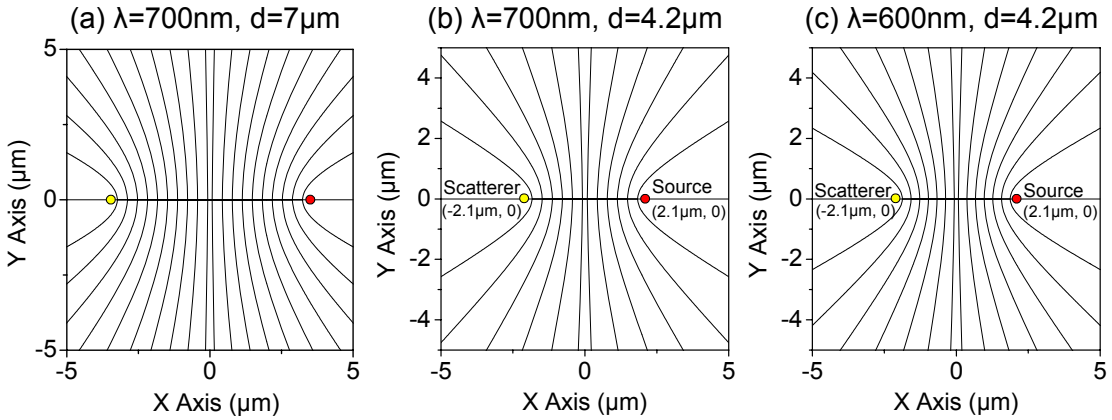

Figure 6.8: The calculated high intensity fringes of the *in-plane* scattering pattern for different wavelengths and different source-scatterer separations. The wavelength in (a) and (b) is 700 nm and the wavelength in (c) is 600 nm. The source-scatterer separation in (a) is d=7 μm and the source-scatterer separation in (b) and (c) is d=4.2 μm.

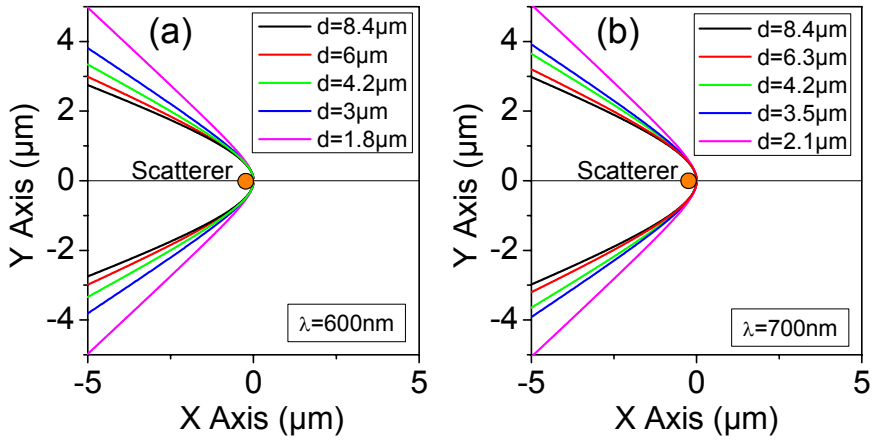

Figure 6.9: The calculated high intensity fringes of the *in-plane* scattering pattern for different source-scatterer separations. In (a), the wavelength is 700 nm and in (b), the wavelength is 600 nm. For each condition, only the fringe closest to the scatterer is plotted.

Figure 6.9 shows the high intensity fringes of the *in-plane* scattering pattern for different source-scatterer separations. The wavelength in (a) is 700 nm and the wavelength in (b) is 600 nm. The large angle scattering fringes with different source-scatterer distance d are plotted together. To make the figure simpler, for each condition only the fringe closest to the scatterer is plotted.

From figure 6.9, we can determine the *in-plane* scattering angle θ for each source-particle distance and wavelength. Figure 6.10 shows how the *in-plane* scattering angle θ changes with the source-particle separation (d) at different wavelengths. The wavelengths are 600 nm (blue line) and 700 nm (red line).

From figure 6.10 we see that at the same source-scatterer separation, the *in-plane* scattering angle θ is a little larger for the longer wavelength. More importantly, it is

clear that the *in-plane* scattering angle θ increases when the source-particle separation d decreases.

6.3.4 Interpretation of real space images using the *in-plane* scattering model

In order to compare the experimental results and the theoretical model of *in-plane* scattering, we measure the *in-plane* scattering angle θ in all the real space images: figure 6.4, figure 6.5 and figure 6.6. In figure 6.10 we plot the measured *in-plane* scattering angle θ together with the theoretical curves determined in last subsection.

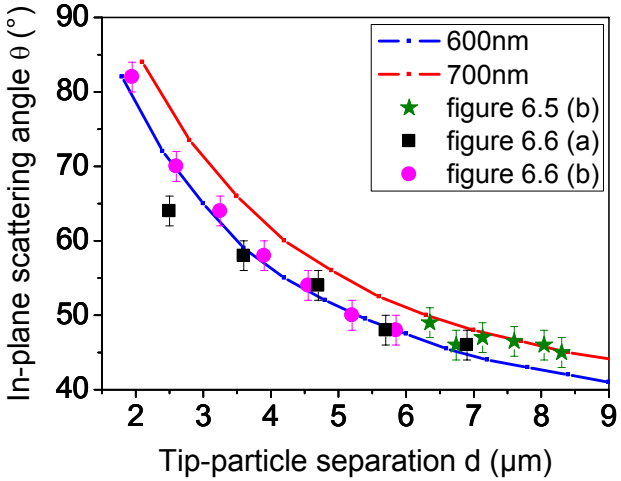

Figure 6.10: Comparison between the measured scattering angle θ and the theoretical curves.

In figure 6.10, almost all the measured scattering angles θ are located between the two theoretical curves for λ=600 nm and λ=700 nm, showing that the experimental results agree well with the theory. These two wavelength are chosen because the free space spectra of STM-excited surface plasmons on a 50 nm thick gold film is centered at $\sim$ 700 nm and the corresponding wavelength of the propagating SPP is $\sim$ 675 nm.

The data in the case of figure 6.6 (with a 650 nm bandpass filter) are closer to the theoretical curve of λ=600 nm. This is because for a 650 nm free space light, the wavelength of the corresponding propagating SPP on a 50 nm gold film is around 620 nm.

The data in the case of figure 6.6 (no bandpass filter used) show a larger deviation from the theoretical curves at small tip-particle distances. This larger deviation is because that the broadband spectrum of STM-excited propagating SPP distorts the interference between the incident SPP and the scattered SPP. At small tip-particle separations, this interference distortion is more significant because more propagating SPP reach the single nanoparticle.

6.4 Fourier space image

6.4.1 Radiative scattering of STM-excited propagating SPP by gold nanoparticles in Fourier space

In order to better understand the gold nanoparticle scattering properties, Fourier space images are also recorded. Figure 6.11(a) shows the Fourier space image when the STM tip is in the same gold nanoparticle area indicated in the dark field image in figure 6.2. The red dashed arrows indicate the tip-particle axes. The red dashed-dot circle indicates a numerical aperture of one (NA=1) and the cyan dashed circle indicates a numerical aperture equals 1.45 (NA=1.45) which is the detection limit of our oil objective. The two circles divided the Fourier space image into three parts: allowed light region (NA<1), forbidden light region (1<NA<1.45) and out of detection region (NA>1.45). As a reference, figure 6.11(b) shows the Fourier space image when the STM tip is far from the gold nanoparticles area.

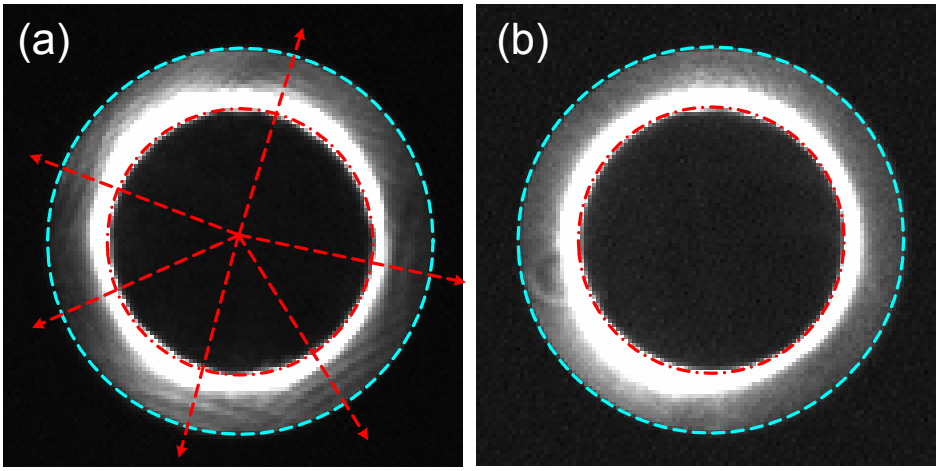

Figure 6.11: Fourier space image when the STM tip is in the gold nanoparticles region (a) and far from gold nanoparticles region (b). The red dashed arrows indicate the tip-particle directions. The red dashed-dot circle indicates the numerical aperture (NA) equals one and the cyan dashed circle indicates the numerical aperture equals 1.45 which is the detection limitation of our oil objective.

In both figure 6.11(a) and (b), there is a bright ring a little larger than the critical angle which is due to the propagating SPP excited by the STM tip (see figure 4.12(a)) [99]. The interesting thing to note here is the fringes in figure 6.11(a), which are perpendicular to the tip-particle axes. In our experiment, these fringes only appear when the STM tip is in the gold nanoparticles area. These fringes must then be due to the interactions between the gold nanoparticle and the STM-excited propagating SPP.

From the real space discussions, we know that the STM-excited propagating SPP can be radiative scattered and *in-plane* scattered by the gold nanoparticle. In the Fourier space image, the *in-plane* scattered SPP is at the same position as the incident STM-excited propagating SPP because they have the same wavenumber. It means that the bright ring a little larger than the critical angle also contains the *in-plane* scattered SPP

contribution. In this case, we can say that the fringes we see in the forbidden light region at large emission angles are related to the radiative scattering by the gold nanoparticle.

6.4.2 Radiative scattering of STM-excited propagating SPP by a single gold nanoparticle as a function of tip-particle separation in Fourier space

In order to better understand the fringes in figure 6.11(a), we repeat the experiment with the STM tip near a single nanoparticle. By changing the tip-particle separation d, we observe an evolution of fringe patterns in Fourier space. A first set of Fourier space images are obtained by decreasing d from 6.9 μm to 2.5 μm (figure 6.12). A second set of Fourier space images are obtained by decreasing d from 5.2 μm to 2.1 μm and with a bandpass filter at 650 nm, 13 nm bandwidth (figure 6.13).

These two sets of images show that the fringes are along the tip-particle direction (unidirectional, see figure 6.12(f)) and the fringes are perpendicular to the tip-particle direction. They also show that the fringes are in the forbidden light region and extend from the critical angle (NA=1) to numerical aperture of the oil objective (NA=1.45). It is clear that the period of the fringe pattern increases when the tip-particle distance d decreases.

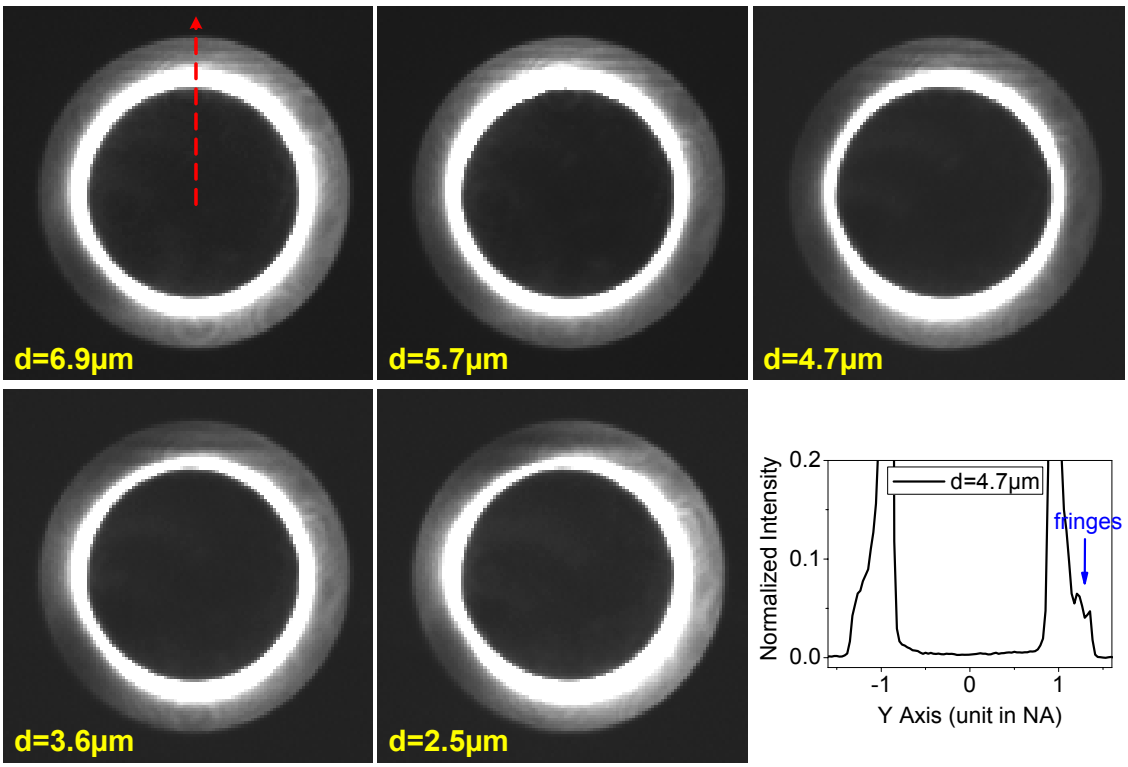

Figure 6.12: Fourier space images when the STM tip excites on the 50 nm gold film near a single scatterer. The tip-particle distance (d) decreases from 6.9 μm to 2.5 μm. The red dashed arrow indicates the tip-particle axis.

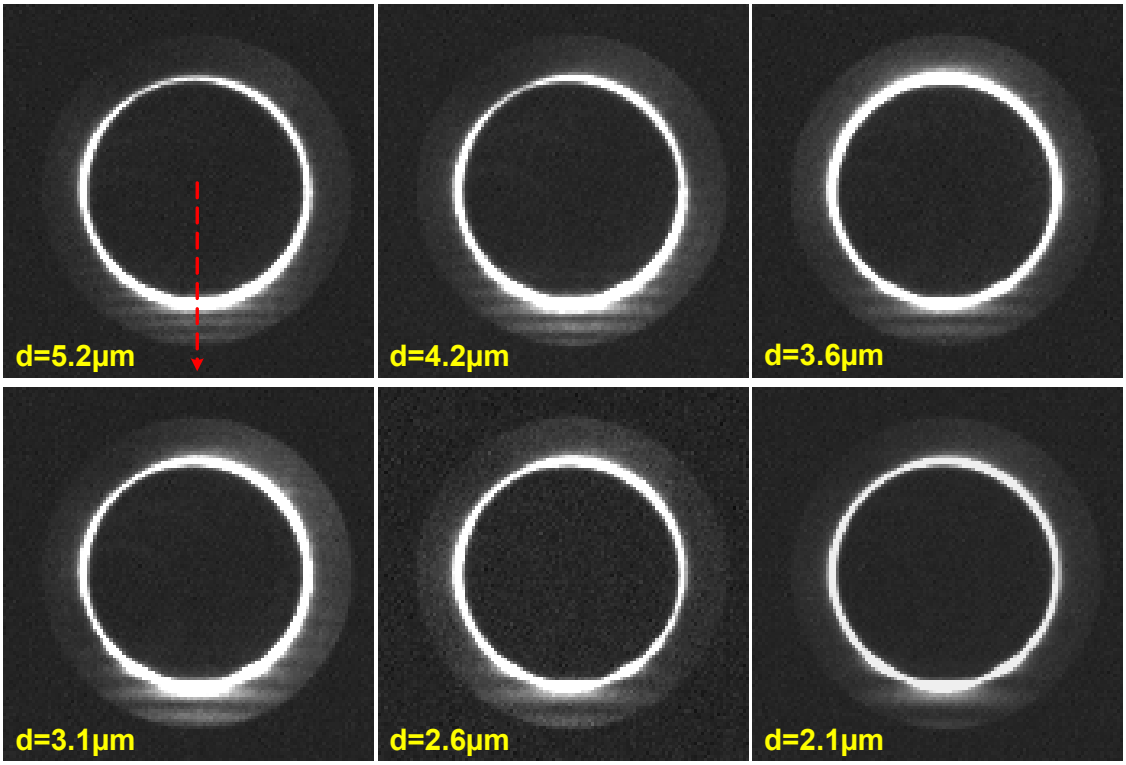

Figure 6.13: Fourier space images when the STM tip excites the 50 nm gold film near a single scatterer. A bandpass filter (central wavelength at 650 nm with 13 nm bandwidth) is placed before the CCD camera. The tip-particle distance (d) decreases from 5.2 μm to 2.1 μm. The red dashed arrow indicates the tip-particle axis.

The measured fringe periods as a function of the tip-particle separation d are plotted in figure 6.14(a). The experimental data from figure 6.12 are plotted as black squares and the experimental data from figure 6.13 are plotted as magenta dots. In figure 6.14(a), we also plot two curves of $lambda$/d for λ=600 nm and λ=700 nm. It is very clear that the experimental data fit well with the two curves of λ/d. This indicates that an interference occurs between two parallel and coherent emissions: one is from the tip position and along $\vec{k}_{tip}$ and one is from the gold nanoparticle position and along $\vec{k}_{NP}$ (see the schematic in figure 6.14(b)). Here $\vec{k}_{NP}$ is parallel to $\vec{k}_{tip}$. According to the experimental images, the angle β (between $\vec{k}_{tip}$ or $\vec{k}_{NP}$ and the optical axis) is in the forbidden light region ($1<1.52sin(\beta)<1.45$, $41.8°<\beta<72.5°$).

6.4.3 Two possible models for the interference fringes in Fourier space

Here we will present two possibilities for the interference in the Fourier space. One is the way we proposed in figure 6.15(a). The other one is shown in figure 6.15(b). In figure 6.15(a), the interference is thought to be between the local emission at the tip position and the radiative scattered propagating SPP (red arrow at the interface) by the single gold nanoparticle. In figure 6.15(b), the interference is thought to be between the radiative scattered propagating SPP by the gold nanoparticle and by the tip. Here, the propagating SPP (red arrow at the interface) are *in-plane* reflected by the gold nanoparticle

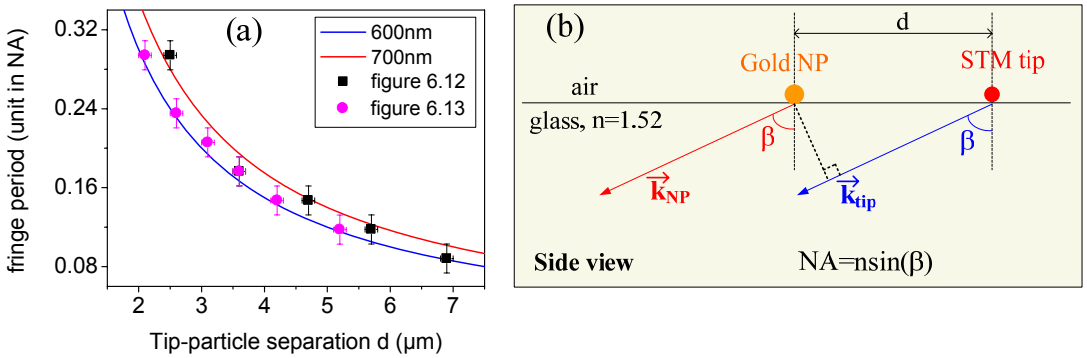

Figure 6.14: (a) Tip-particle separation dependence of the measured fringe periods (experimental data from figure 6.12 and figure 6.13) and the theoretically curves ($lambda$/d). (b) The principle of the interference in Fourier space: the emission at STM tip and gold NP positions are coherent. In Fourier plane, they have a phase difference $k_{glass}dsin(\beta)$.

(blue arrow at the interface). Note that both models will give the same period of the interference fringes.

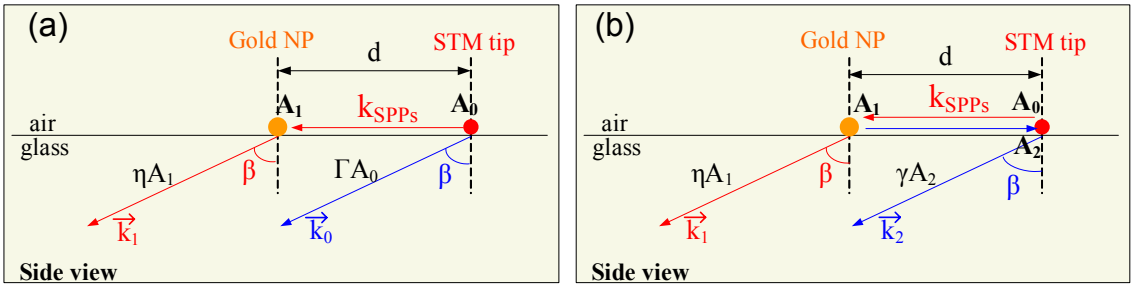

Figure 6.15: Two possible models to explain the interference fringes seen in Fourier space images: (a) The interference is between the local emission at the STM tip and the radiative scattered propagating SPP light from the gold nanoparticle and (b) The interference is between the the radiative scattered propagating SPP light from the gold nanoparticle and from the tip. In (a), the phase difference is given by equation 6.10. Similarly, the phase difference in (b) can be calculated.

Here, d is the tip-particle distance and L_{SPP} is the propagation length of the propagating SPP. Γ is the local emission coefficient (along $\vec{k}_0$) at the tip position. The coefficient η is the radiative scattering coefficient (along $\vec{k}_1$) of the nanoparticle, the coefficient γ is the radiative scattering coefficient (along $\vec{k}_2$) of the tip and the coefficient α is the *in-plane* reflection coefficient of the nanoparticle. For a certain nanoparticle and STM tip, Γ, η, γ and α are constant.

In figure 6.15(a) and (b), the electric field amplitude of the propagating SPP starting from the tip is defined as A_0. The electric field amplitude of the propagating SPP which

reach the gold nanoparticle is defined as A_1. A_1 can thus be written as:

$$A_1 = A_0 \frac{e^{\frac{-d}{2Lspp}}}{\sqrt{d}} \tag{6.7}$$

In the same way, A_2 in figure 6.15(b) can be written as:

$$A_2 = \alpha A_1 \frac{e^{\frac{-d}{2Lspp}}}{\sqrt{d}} = \alpha A_0 \frac{e^{\frac{-d}{Lspp}}}{d} \tag{6.8}$$

It is clear that A_0 is larger than A_1 and A_1 is larger than A_2.

In figure 6.15(a)(case 1), the electric field amplitude of local emission along $\vec{k}_0$ is ΓA_0 and the electric field amplitude of the radiative scattered propagating SPP by the scatter along $\vec{k}_1$ is ηA_1. Here, $\vec{k}_0$ and $\vec{k}_1$ are parallel. The interference fringes seen in Fourier space between these two fields can be written as:

$$I = \Gamma^2 A_0^2 + \eta^2 A_1^2 + 2\eta A_1 \Gamma A_0 cos(\frac{2\pi}{\lambda_0} NAd + \Delta\varphi) \tag{6.9}$$

where $\Delta\varphi$ is the phase difference between $\vec{k}_0$ and $\vec{k}_1$.

$$\Delta\varphi = k_{SPP} d + \delta\varphi - k_{glass} dsin(\beta) \tag{6.10}$$

where $\delta\varphi$ is the phase delay in the radiative scattering process by the gold nanoparticle.

So the intensity of the bright fringes I_{max} and the intensity of the dark fringes I_{min} can be written as:

$$\begin{aligned} I_{max} &= (\Gamma A_0 + \eta A_1)^2 = A_0^2\ \eta^2\ ((\tfrac{\Gamma}{\eta}) + \tfrac{e^{\frac{-d}{2Lspp}}}{\sqrt{d}})^2 \\ I_{min} &= (\Gamma A_0 - \eta A_1)^2 = A_0^2\ \eta^2\ ((\tfrac{\Gamma}{\eta}) - \tfrac{e^{\frac{-d}{2Lspp}}}{\sqrt{d}})^2 \end{aligned} \tag{6.11}$$

the visibility can be written as:

$$\begin{aligned} V &= \tfrac{I_{max}-I_{min}}{I_{max}+I_{min}} = \tfrac{(\eta A_1+\Gamma A_0)^2-(\eta A_1-\Gamma A_0)^2}{(\eta A_1+\Gamma A_0)^2+(\eta A_1-\Gamma A_0)^2} = \tfrac{2\eta A_1 \Gamma A_0}{\eta^2 A_1^2+\Gamma^2 A_0^2} \\ V &= \tfrac{2\eta A_1 \Gamma A_0}{\eta^2 A_1^2+\Gamma^2 A_0^2} = \tfrac{2\eta\Gamma \frac{e^{\frac{-d}{2Lspp}}}{\sqrt{d}}}{\eta^2\ \frac{e^{\frac{-d}{Lspp}}}{d}+\Gamma^2} = \tfrac{2\frac{\Gamma}{\eta} \frac{e^{\frac{-d}{2Lspp}}}{\sqrt{d}}}{\frac{e^{\frac{-d}{Lspp}}}{d}+(\frac{\Gamma}{\eta})^2} \end{aligned} \tag{6.12}$$

if we set $\frac{\Gamma}{\eta} = a$, then for case 1 we will have:

$$\begin{aligned} I_{max} &= A_0^2\ \eta^2\ (a + \tfrac{e^{\frac{-d}{2Lspp}}}{\sqrt{d}})^2 \\ I_{min} &= A_0^2\ \eta^2\ (a - \tfrac{e^{\frac{-d}{2Lspp}}}{\sqrt{d}})^2 \\ V &= \frac{2a\frac{e^{\frac{-d}{2Lspp}}}{\sqrt{d}}}{a^2+\frac{e^{\frac{-d}{Lspp}}}{d}} \end{aligned} \tag{6.13}$$

On the other hand, for case 2 in figure 6.15(b), the field amplitude of the radiatively scattered propagating SPP from the nanoparticle along k_1 is ηA_1 and the radiatively

scattered propagating SPP light from the tip along k_2 is γA_2. Like in figure 6.15(a), k_1 and k_2 are parallel. Using the same calculation as for case 1, if we set $\frac{\eta}{\alpha\gamma} = b$, then for case 2 we will have:

$$\begin{aligned} I'_{max} &= A_0^2\,(\gamma\alpha)^2\,\frac{e^{\frac{-d}{Lspp}}}{d}\,(b+\frac{e^{\frac{-d}{2Lspp}}}{\sqrt{d}})^2 \\ I'_{min} &= A_0^2\,(\gamma\alpha)^2\,\frac{e^{\frac{-d}{Lspp}}}{d}\,(b-\frac{e^{\frac{-d}{2Lspp}}}{\sqrt{d}})^2 \\ V' &= \frac{2b\frac{e^{\frac{-d}{2Lspp}}}{\sqrt{d}}}{b^2+\frac{e^{\frac{-d}{Lspp}}}{d}} \end{aligned} \tag{6.14}$$

From equations 6.13 and 6.14, it is clear that the visibility has the same expression for the two cases and it is not possible to distinguish the two cases using the visibility. However, we can use the visibility equations to fit the d dependent experimental results and get the value of a or b (if we set Lspp=10 μm for example). Also from equations 6.13 and 6.14, it is clear that the I_{max} and I_{min} have different expressions for the two cases, so it may be possible to distinguish the two models using the values of I_{max} and I_{min}. In this way, we can do a quantitative comparison of the two interference models using the experimental data.

From the Fourier space images, we measure I_{max}, I_{min} and the visibility V as a function of d, the tip-particle separation. In figure 6.16, we show the distance dependence of V (figure 6.16(a)), I_{max}-I_{min} (figure 6.16(b)), I_{max} (figure 6.16(c)) and I_{min} (figure 6.16(d)) as derived from the Fourier space images of figure 6.12. The red line is the fit based on model 1 (interference between the local emission at the tip position and the radiative scattered propagating SPP by the single gold nanoparticle), and the blue line is the fitting based on model 2 (interference between the radiative scattered propagating SPP by the gold nanoparticle and by the tip).

In figure 6.16(a) and (b), we see that the visibility V and the I_{max}-I_{min} fits using equations 6.13 and 6.14 are the same and the fittings are quite good. The value of a and b used for the visibility fits are a= b= 3.1 (Lspp=10 μm).

Using this value of a and b, we can fit the d dependent experimental results of I_{max} and I_{min} based on equation equations 6.13 and 6.14. In figure 6.16(c) and (d), we see that the red lines (model 1, equations 6.13) fits very well for both I_{max} and I_{min} data. On the contrary the blue lines (model 2, equations 6.14) cannot fit the experimental data, especially the I_{min} data in figure 6.16(d). This suggests that the model 1 where the interference occurs between the local emission at the tip position and the radiative scattered propagating SPP light by the single gold nanoparticle is more reasonable.

Another similar comparison of the two models is shown in figure 6.16(e-h), as derived from the Fourier space images of figure 6.13. In figure 6.16(e) and (f), we also see that both models are equivalent and the fits are good. Here it is found that a= b= 1.2. In figure 6.16(g) and (h), we see that model 1 (equations 6.13) again fits very well for both the I_{max} and I_{min} data. Similar to figure 6.16(c-d), model 2 (equations 6.14) cannot fit the I_{max} and I_{min} data.

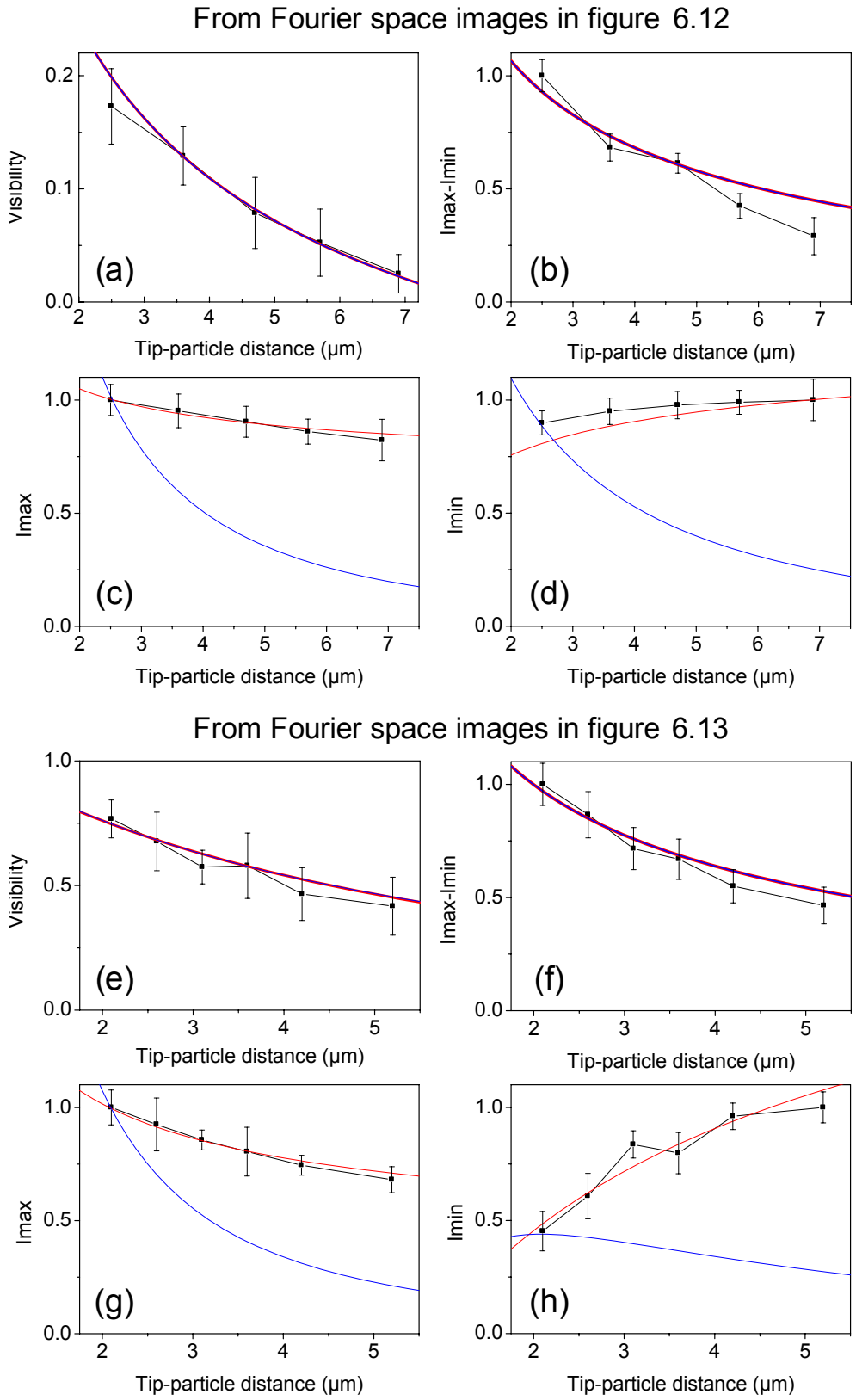

Figure 6.16: Quantitative comparisons of the two interference models using the experimental data of figure 6.12(a-d) and figure 6.13(e-h). (a) Visibility data and the two fits from the models. (b) I_{max}-I_{min} and the two fits. (c) I_{max} and the two fits. (d) I_{min} and the two fits. In all the images, the red lines are the fits from model 1, and the blue lines are the fits from model 2.

From these quantitative comparisons, we conclude that model 1 is the more reasonable explanation of the interference in the Fourier space. The interference observed in Fourier space is most probably between the STM-excited *localized* surface plasmons at the tip position (which radiate at large angles) and the STM-excited *propagating* SPP radiatively scattered by the gold nanoparticle. This is a very interesting phenomenon because it indicates that the STM-excited *localized* surface plasmons and the STM-excited *propagating* surface plasmons are coherent, thus raising the fundamental questions about the nature and origin of STM-excited surface plasmons on thin gold films.

6.5 *In-plane* and radiative interferences

One thing we need to emphasize is that from the real space and Fourier space images, we observe two different kinds of interference in our experiments: the *in-plane* interference seen in real space and the radiative interference seen in Fourier space.

The *in-plane* interference in real space is the interference between the propagating SPP on the gold film surface and the *in-plane* scattered propagating SPP from the gold nanoparticle. The interference in real space is well understood from the theoretical model discussed in subsection 6.3.3. Figure 6.17 shows the *in-plane* interference ((a), (c) and (e)) again as a reminder. Because of the *in-plane* interference, *in-plane* scattering θ increases when the tip-nanoparticle separation d decreases from 5.2 μm to 2 μm.

The radiative interference in Fourier space is the interference between the STM-excited *localized* surface plasmons at the tip position (which radiate at large angles, in the forbidden light region) and the STM-excited *propagating* SPP radiatively scattered by the gold nanoparticle. As discussed in chapter 3 and 4, we know that the STM-excited *localized* surface plasmons at the tip position have the same angular distribution in all the directions. In the side view plane, we show that this localized emission radiates symmetrically with a angle β to the optical axis.

Figure 6.17 shows the radiative interference ((b), (d) and (f)) again as a reminder. φ indicates the radiative scattering range in Fourier space. We see that φ does not change when the tip-nanoparticle separation d decreases from 5.2 μm to 2.1 μm ((b) and (d)). This means that the angular dependence of the radiative scattering of the gold nanoparticle does not depend on the tip-nanoparticle separation d. Because the interference fringes are only seen in the left side, we know that the radiative scattering of the gold nanoparticle is unidirectionally along the tip-NP direction.

By measuring the range indicated by the two canyon dashed lines in (b) and (d), we find that the radiative scattering range $\delta\varphi$ (in (f), the side view plane) of the gold nanoparticle is mainly from critical angle (NA=1) to the numerical aperture of the oil objective (NA=1.45), i.e., β ranges from 41.8° to 72.5° and $\delta\varphi$=72.5°-41.8°=30.7°.

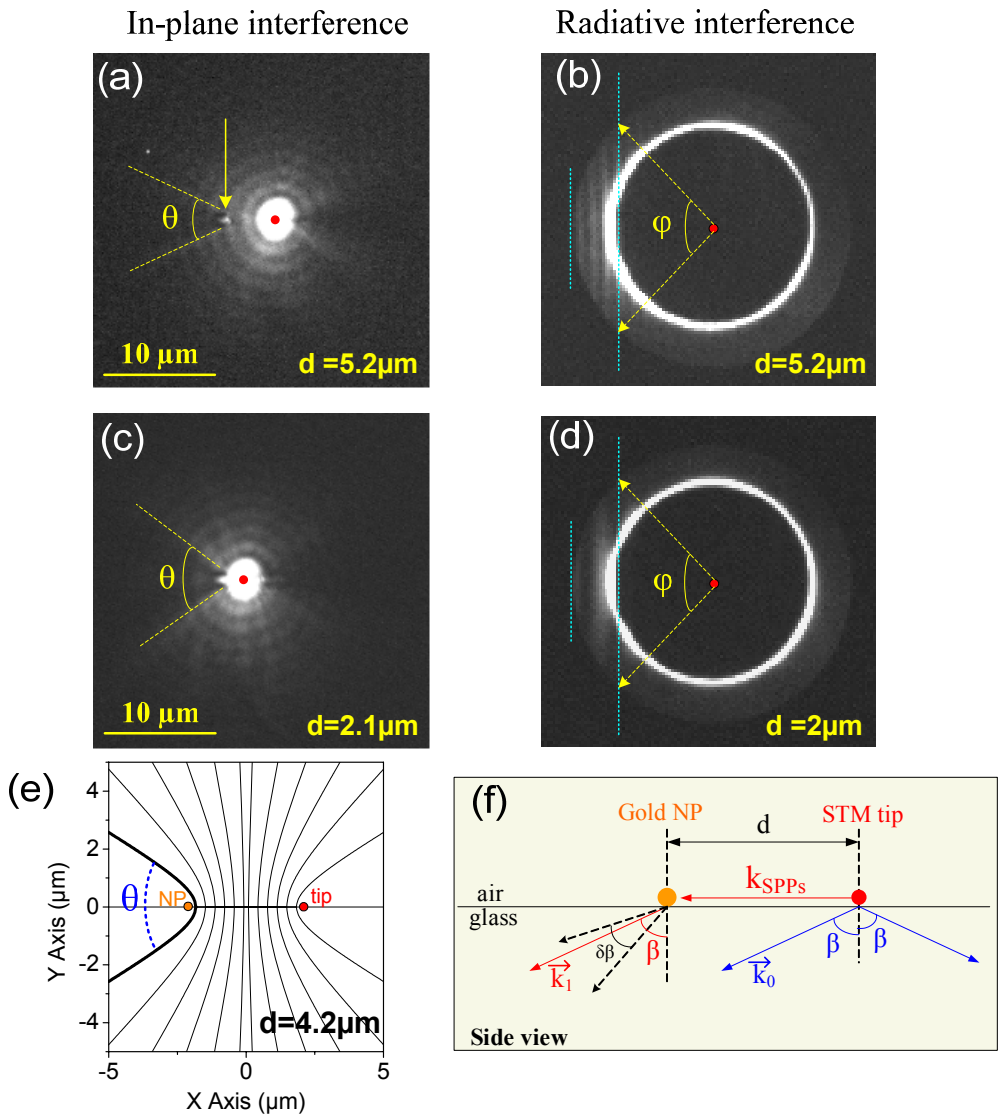

Figure 6.17: *In-plane* and radiative interferences. The experimental images of the *in-plane* interference and radiative interference are shown in (a), (c) and (b), (d) respectively for two tip-nanoparticle separations d. These images are recorded with a bandpass filter at 650 nm, bandwidth=13 nm. The theoretical calculated *in-plane* interference fringes is shown in (e). The schematic of the radiative interference is shown in (f). The red dot in (a) and (c) indicates the tip position. In (a), (c) and (e) θ indicates the *in-plane* scattering angle. The yellow arrow in (a) indicates the gold nanoparticle position. The red dot in (b) and (d) indicates the center of Fourier space. In (b) and (d), φ indicates the radiative scattering range in Fourier space and the two canyon dashed lines indicate the radiative scattering region along the tip-nanoparticle axis. In (f) $\delta\beta$ indicates this radiative scattering range. In (f), β indicates the radiative scattering angle. Note that all the images (a-f) are already shown in the previous discussions of this chapter, here we put them together as a reminder and summary.

6.6 Conclusion

In conclusion, we have shown how the STM-excited propagating SPP are scattered by gold nanoparticles deposited on a 50 nm gold film.

In real space images obtained with an air objective, we observe the radiative scattering bright spots of STM-excited SPP from gold nanoparticles deposited on a 50 nm thick gold film. In real space images obtained with an oil objective, we observe the radiative scattering bright spots and *in-plane* scattering patterns. The *in-plane* scattering is theoretically understood as the interference between the incident SPP launched by the STM tip and the scattered SPP from gold nanoparticles.

According to the radiative scattering bright spots and *in-plane* scattering patterns obtained when STM tip is at the position of gold nanoparticle No.4, it is clear that propagating SPP can also be launched by electrically excitation of gold nanoparticles deposited on the 50 nm gold film with a STM. Meanwhile, because of the gap between the gold nanoparticle and the gold film, the localized emission is enhanced around 10 times.

From Fourier space images obtained with an oil objective, we see interference fringes in the forbidden light region. This indicates that the radiative scattering of STM-excited propagating surface plasmons from the gold nanoparticles can interfere with STM-excited localized surface plasmons which emit at large angles under the STM tip. It follows that STM-excited propagating surface plasmons and STM-excited localized surface plasmons are coherent. This means that the localized and propagating surface plasmons are different components of the same single plasmon produced by inelastic electron tunneling with the STM tip. This result is important in the context of a better understanding about the STM-excited surface plasmons process.

Chapter 7

Conclusions and Perspectives

We have shown that with a scanning tunneling microscope (STM) tip, we electrically excite both broadband localized and propagating surface plasmons on a thin gold film. We demonstrate that by changing the STM tip shape or material we can preferentially excite localized or propagating surface plasmons. This has important implications for the design of electrically driven plasmon nano-sources that require either the excitation of localized plasmon nano-cavity modes for electromagnetic field enhancement or propagating plasmon modes for information transfer. The STM-excited surface plasmons provides a bridge between nano-electronics and nano-optics. Such electrically excited surface plasmons are important in the context of their use in future integrated nano-optics devices such as electro-optical nano-antennas.

We have also explored the unique properties of surface plasmons produced by inelastic electron tunneling (IET) with the STM.

We have investigated the coherence of STM-excited propagating surface plasmons by performing experiments on a 200 nm thick (opaque) gold film punctured by nanoholes. Analogous to Young's double slit experiment, we show that STM-excited propagating surface plasmons are coherent, with a coherence length of 4.7 ± 0.5 μm. This coherent length is very close to the value expected from the spectrum (3.7 ± 1.2 μm), which indicates that the spectrum broadening of STM-excited surface plasmons is homogeneous. This result is very important as it demonstrates a method to produce homogeneous broadband SPP which could be used for the fabrication of nano-lasers or plasmonic lasers. This result is also important for understanding the mechanism of plasmonic inelastic electron tunneling (IET). It indicates that each inelastic tunneling electron has a broadband spectrum of released energy.

We have also studied the in-plane and radiative scattering of STM-excited propagating surface plasmons by gold nanoparticles deposited on a 50 nm thick gold film. In the Fourier space images, interference fringes are observed in the forbidden light region (larger than the critical angle). This interference is between STM-excited localized surface plasmons (radiating at large angles) at tip position and the radiative scattering of STM-excited propagating surface plasmons by the gold nanoparticle. This indicates that STM-excited localized and propagating surface plasmons are coherent. It also means that the localized and propagating surface plasmons are different components of the same single plasmon produced by inelastic electron tunneling with the STM tip.

Appendix A

Quasi-electrostatic approximation of the local electric field in the STM tunneling junction

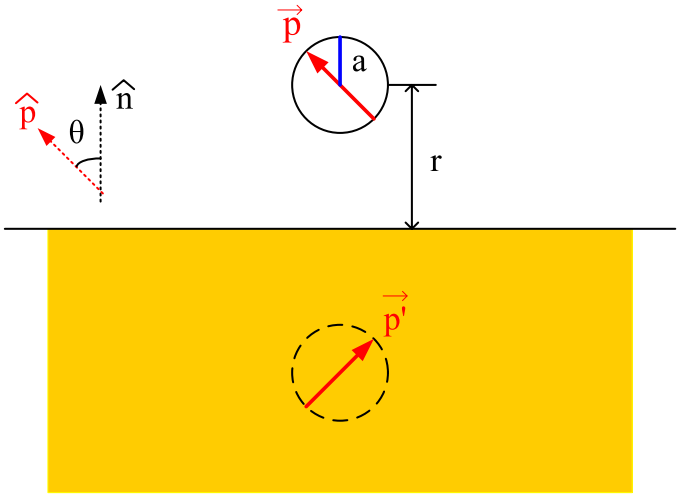

Figure A.1: Sketch of sphere-gold film interaction in the polarizable sphere approximation model. The sphere (radius of a) is polarized when it is excited by a light field (e.g. from the inelastic electron tunneling). The sphere-dipole field $\vec{p}$ induces an image dipole field $\vec{p'}$ located inside the gold film at a distance 2r from the sphere center. The far field light emission pattern contains information about the effective polarizability of the sphere-film tunneling junction.

As shown in figure A.1, the STM tip may be approximated by a spherical particle located at a distance r from the air-gold interface. The radius of the spherical particle is a. If a is very small (a $\ll \lambda$, non-retardation), the polarizability of the sphere can be written as [46]:

$$\alpha_p = 4\pi\varepsilon_0 a^3 \frac{\varepsilon_p - 1}{\varepsilon_p + 2} \tag{A.1}$$

where ε_0 is the vacuum permittivity. ε_p is dimensionless (relative) dielectric constants, i.e.

the vacuum permeability ε_0 is not contained in ε_p. The dimensionless (relative) dielectric constants of air is 1.

The sphere will thus respond to an incident field $\vec{E}_0$ by generating a dipole $\vec{p} = \alpha_p \vec{E}_0$. In the electrostatic limit, the electric field at a generic point $\vec{R}$ is [46]:

$$\vec{E}_p(\vec{R}) = \frac{3(\widehat{d} \cdot \vec{p})\widehat{d} - \vec{p}}{4\pi\varepsilon_0 \left|\vec{R} - \vec{r_p}\right|^3} \tag{A.2}$$

where $\vec{r_p}$ is the spatial position of the sphere-dipole and $\widehat{d} = \frac{\vec{R}-\vec{r_p}}{|\vec{R}-\vec{r_p}|}$.

The gold film has a dielectric constant ε_g. Therefore the polarized sphere will induce an image dipole $\vec{p'}$ (see figure 1). The image dipole is located inside the sample at a distance 2r from the sphere. The image dipole moment is $\vec{p'} = \vec{p}\,\beta$, where $\beta = \frac{\varepsilon_g - 1}{\varepsilon_g + 1}$ [46].

The sphere-gold film interaction can now be calculated by evaluating the effective polarization of the system, as defined by the coupling between the sphere-dipole and its image dipole. At small distances, the effective incident electric field at the sphere-dipole will be enhanced by the image dipole field so that the actual sphere-dipole moment is modified as:

$$\vec{p} = \alpha_p[\vec{E_0} + \vec{E'}(\vec{r_p})] \tag{A.3}$$

where $\vec{E}_0$ is the incident field and

$$\vec{E'}(\vec{r_p}) = \frac{3(\widehat{n} \cdot \vec{p'})\widehat{n} - \vec{p'}}{4\pi\varepsilon_0 \left|\vec{r_p} - \vec{r'}\right|^3} \tag{A.4}$$

Here, $\vec{E'}(\vec{r_p})$ is the electric field of the image-dipole at the sphere position r_p. Here r' is the position of p', and $\vec{r_p}$-$\vec{r'} = 2\mathrm{r}\widehat{n}$ with $\widehat{n}$ normal to the surface. We set the angle between the sphere-dipole $\vec{p}$ and the normal direction $\widehat{n}$ as θ (see figure A.1). In the weak-coupling approximation, $\vec{E'}(\vec{r_p}) \ll \vec{E}_0$, so we can assume $\vec{p}$ to be parallel to $\vec{E}_0$. Therefore the image-dipole $\vec{p'}$ will lay in the incidence plane symmetrically to $\vec{p}$ with respect to $\vec{n}$ (see figure A.1). From equation A.3, we get

$$\vec{p} \cdot \widehat{E}_0 = \alpha_p[E_0 + \frac{3(\widehat{n} \cdot \vec{p'})(\widehat{n} \cdot \widehat{E}_0) - \vec{p'} \cdot \widehat{E}_0}{4\pi\varepsilon_0 \left|\vec{r_p} - \vec{r'}\right|^3}] = \alpha_p[E_0 + \frac{3(cos(\theta))^2 - cos(2\theta)}{32\pi\varepsilon_0 r^3} p'] = |\vec{p}| = p \tag{A.5}$$

where $\widehat{E}_0$ is the unit vector of $\vec{E}_0$. Since $\vec{p'} = p\beta$, we can calculate

$$p = \frac{\alpha_p E_0}{1 - \alpha_p \beta \frac{1+(cos(\theta))^2}{32\pi\varepsilon_0 r^3}} \tag{A.6}$$

and in the same direction as $\vec{p}$, the image-dipole component is

$$p'_{parallel} = \frac{\alpha_p \beta cos(2\theta) E_0}{1 - \alpha_p \beta \frac{1+(cos(\theta))^2}{32\pi\varepsilon_0 r^3}} \tag{A.7}$$

So the effective polarizability is [138, 139]:

$$\alpha_{eff} = \frac{\alpha_p(1 + \beta cos(2\theta))}{1 - \alpha_p \beta \frac{1+(cos(\theta))^2}{32\pi\varepsilon_0 r^3}} \tag{A.8}$$

There are special cases: $\theta = 0$ and $\theta = \pi/2$ in which the sphere-dipole and its image-dipole are respectively parallel and anti-parallel. The effective polarizabilities are $\alpha_{eff}(\theta = 0) = \frac{\alpha_p(1+\beta)}{1-\alpha_p\beta\frac{1}{16\pi\varepsilon_0 r^3}}$ and $\alpha_{eff}(\theta = \pi/2) = \frac{\alpha_p(1-\beta)}{1-\alpha_p\beta\frac{1}{32\pi\varepsilon_0 r^3}}$. In the first case, the two dipoles sum their contributions, while in the second case they tend to cancel each other.

Figure A.2 (a) shows the polarizability of the sphere-dipole based on equation A.1. It is clear that the Ag sphere is more easily polarized than the W sphere. The polarizability of an Ag sphere can be as much as 5 times of that of a W sphere, which leads to a 25 times ($\propto {\alpha_p}^2$) difference of the far field scattering intensity. Thus, the polarization of the W tip is negligible.

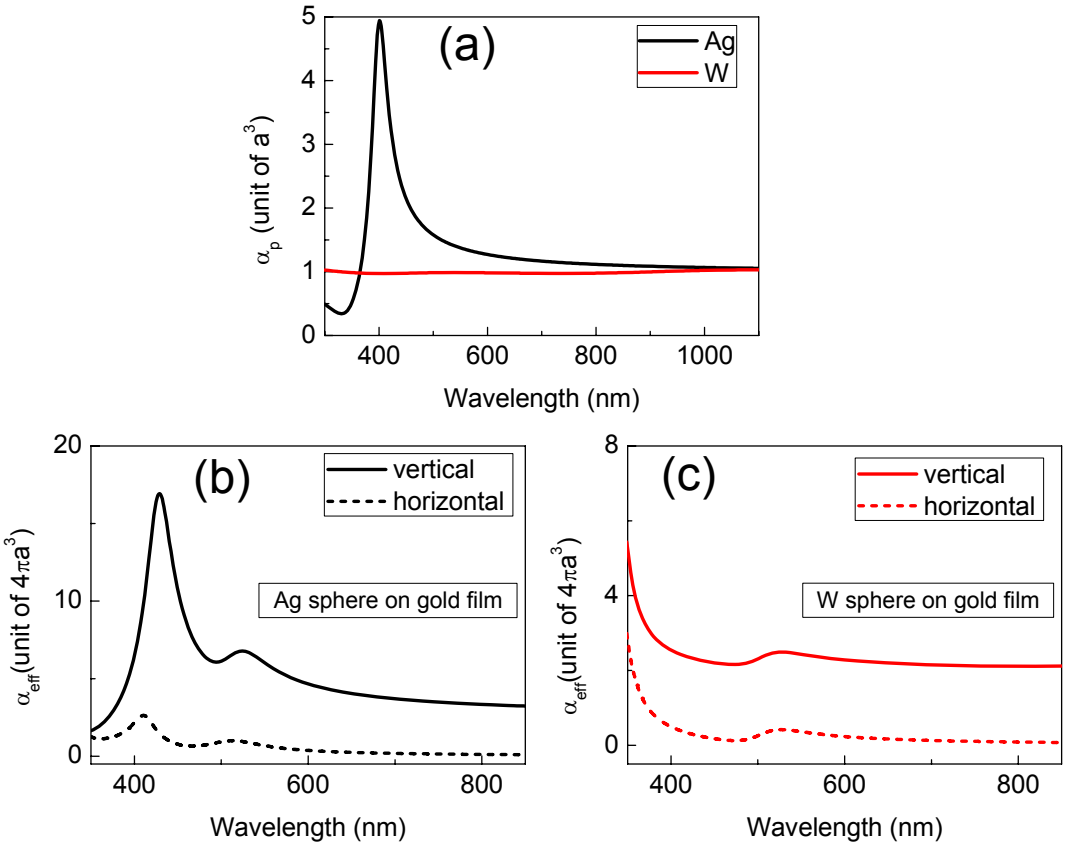

Figure A.2: (a) Polarizability of a W sphere and an Ag sphere as a function of wavelength. (b) Effective polarizability of an Ag sphere on a gold film (r=2a) in vertical and horizontal directions. The dielectric constants of Ag and W are from [41]

The Ag sphere is polarized by the light induced by inelastic electron tunneling. The effective polarizability $\alpha_{eff}(\theta = 0) = \frac{\alpha_p(1+\beta)}{1-\alpha_p\beta\frac{1}{16\pi\varepsilon_0 r^3}}$ and $\alpha_{eff}(\theta = \pi/2) = \frac{\alpha_p(1-\beta)}{1-\alpha_p\beta\frac{1}{32\pi\varepsilon_0 r^3}}$ are plotted in figure A.2(b) as a function of wavelength for a Ag sphere. It is clear that in the horizontal direction (θ=$\pi/2$) the effective polarizability is around 10 times smaller than in the vertical direction ($\theta = 0$). Thus, the vertical component of the effective induced dipole in a Ag sphere-gold film tunneling junction is dominant.

Figure A.2(c) shows the effective polarizability α_{eff} as a function of wavelength for a W sphere in horizontal (θ=$\pi/2$) and vertical ($\theta = 0$) directions. It is clear that the

effective polarizability for a W sphere is smaller than that for a Ag sphere. It is also clear that the effective polarizability in the horizontal direction is around 3 times smaller than in the vertical direction.

Appendix B

Defocusing experiments of STM excited surface plasmons on a 50 nm thick gold film

Figure B.1 shows the real space images of STM excited surface plasmons on a 50 nm thick gold film deposited on a glass substrate (n=1.52) obtained with the oil objective overfocused (i.e. focus above the sample surface). The focus is moved from focus position to 2 μm overfocused. The images are recorded with a bandpass filter (central wavelength= 700 nm, bandwidth= 13 nm). We see that when we overfocus 0.5 μm above the sample surface, both the real space image and the cross-sections are similar to the in focus case. This is because the depth of field of the oil objective is about several hundred nanometer and also because the electric field of the propagating surface plasmons extends several hundred nanometer in the air from the gold film surface. Because of the 2D exponential decay of the propagating surface plasmons on the gold film surface, when the image is more out of focus, the propagating surface plasmons far from the tip position may not be detected due to the low intensity. Meanwhile, the propagating surface plasmons near the tip position can still be detected because the intensity is higher. We can see this effect in the real space images: the concentric rings farther from the tip which is related to the propagating surface plasmons farther from the tip become less obvious when the image is more overfocused. In the cross-sections with the natural logarithmic scale, we see that when the defocusing increases, the fit becomes steeper which means a smaller propagation length or faster intensity decay.

Figure B.2 shows the real space images of STM excited surface plasmons on a 50 nm gold film deposited on a glass substrate (n=1.52) with the image underfocused (i.e. defocused toward the CCD camera). The focus is moved from focus position to 2 μm underfocused. The images are recorded with a bandpass filter (central wavelength= 700 nm, bandwidth= 13 nm). Both the real space image and the cross-sections are similar to the focus case. This is because the depth of focus of the objective is about several hundred nanometer. We see that when the image is overfocused 1 μm (towards the CCD camera), both the real space image and the cross-sections begin to differ from the focused case. These defocused images are similar to the real space images we recorded when we use a quartz substrate to support the gold film (see figure 3.3(a)). To explain this phenomenon,

the first effect is the leakage radiation of the propagating surface plasmons. Because of the leakage radiation, the propagating surface plasmons on the gold film surface radiate to the oil objective all along the same angle (around 45°). So when we defocus the oil objective with a certain distance d, the concentric rings in the real space images which related to the propagating surface plasmons spread out with nearly the same distance d from the tip position and make a dark ring around the central peak. The central peak is related to the localized light emission under the STM tip. In principle, the localized light emission radiates to all the angles. When the oil objective defocused towards the CCD camera, the small angle and large angle radiation of the localized light emission is separated. The small angle part is still at the tip position in the real space images, while the large angle part spread out from the tip together with the propagating surface plasmons. This effect is very similar to the defocusing effect of the quartz substrate (see section 3.4).

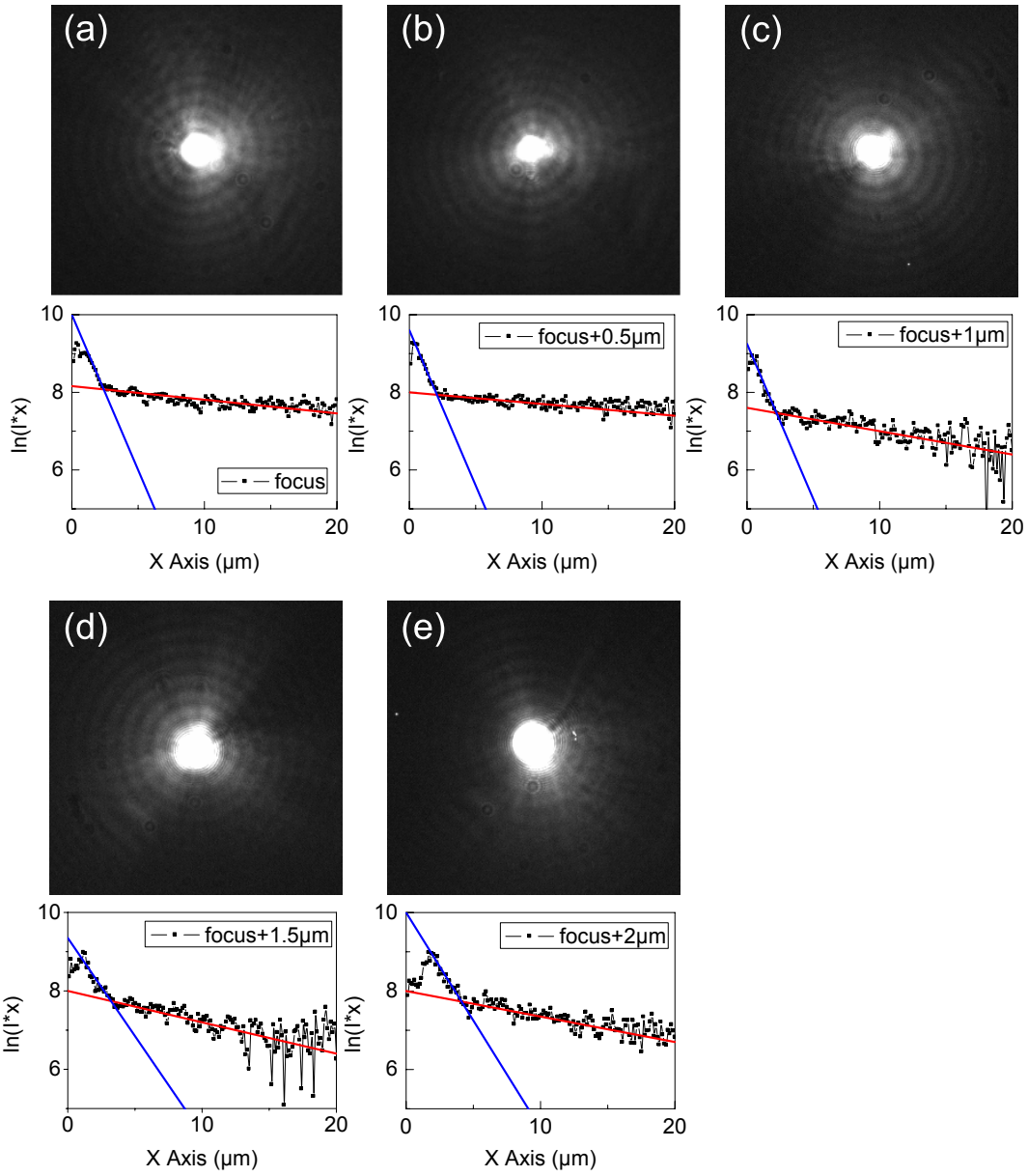

Figure B.1: Real space images of STM excited surface plasmons on a 50 nm gold film. The images are recorded with an oil objective (NA=1.45). From (a) to (e), the images are focused, overfocused 0.5 μm, overfocused 1 μm, overfocused 1.5 μm and overfocused 2 μm. A bandpass filter (central wavelength= 700 nm, bandwidth= 13 nm) is put before the CCD camera. The gold film is deposited on glass substrate (refractive index 1.52).

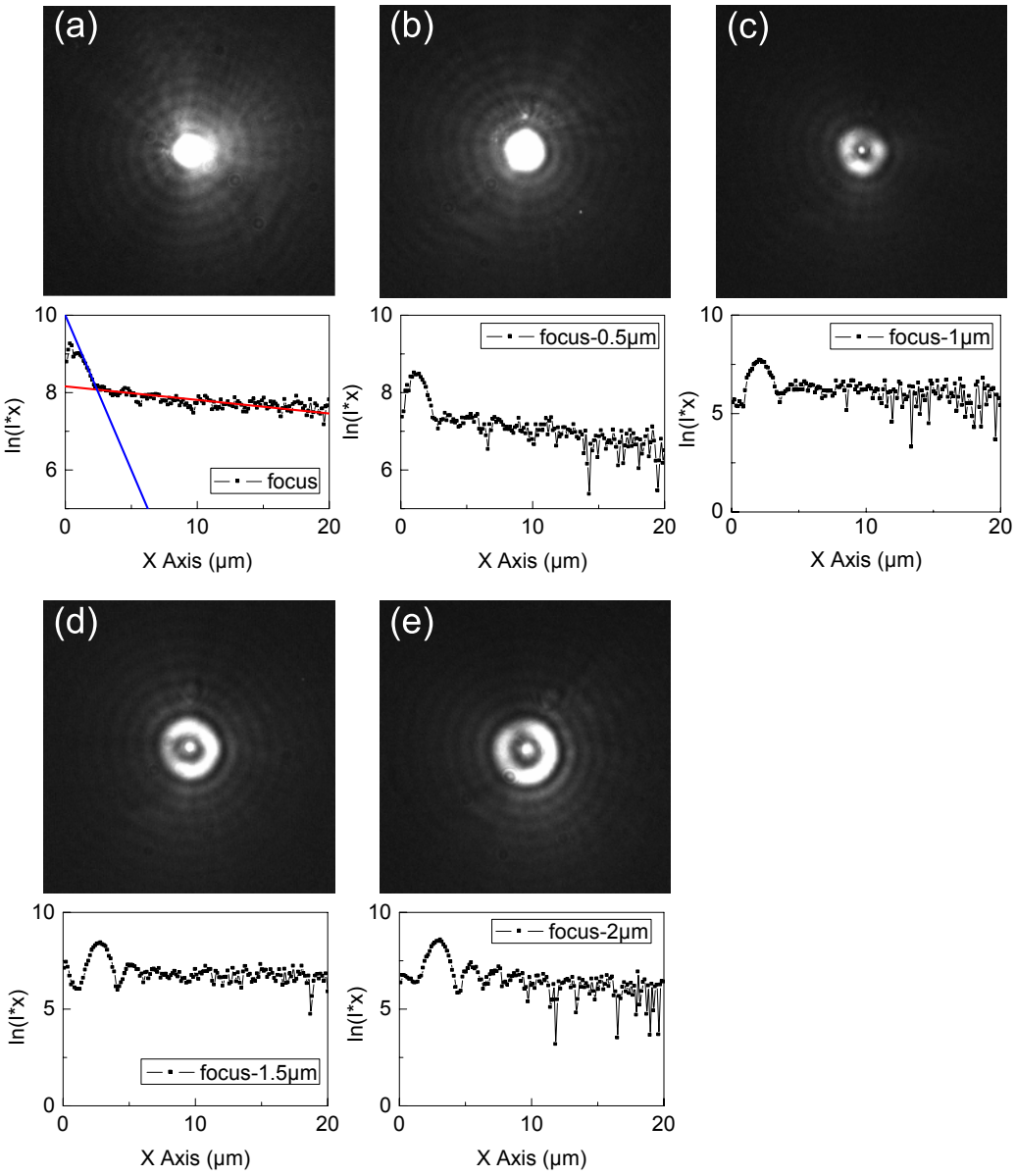

Figure B.2: Real space images of STM excited surface plasmons on a 50 nm gold film. The images are recorded with an oil objective (NA=1.45). From (a) to (e), the images are focused, underfocused 0.5 μm, underfocused 1 μm, underfocused 1.5 μm and underfocused 2 μm. A bandpass filter (central wavelength= 700 nm, bandwidth= 13 nm) is put before the CCD camera. The gold film is deposited on glass substrate (refractive index 1.52).

Appendix C

Local resonance of the STM tip-gold nanoparticle-gold film system

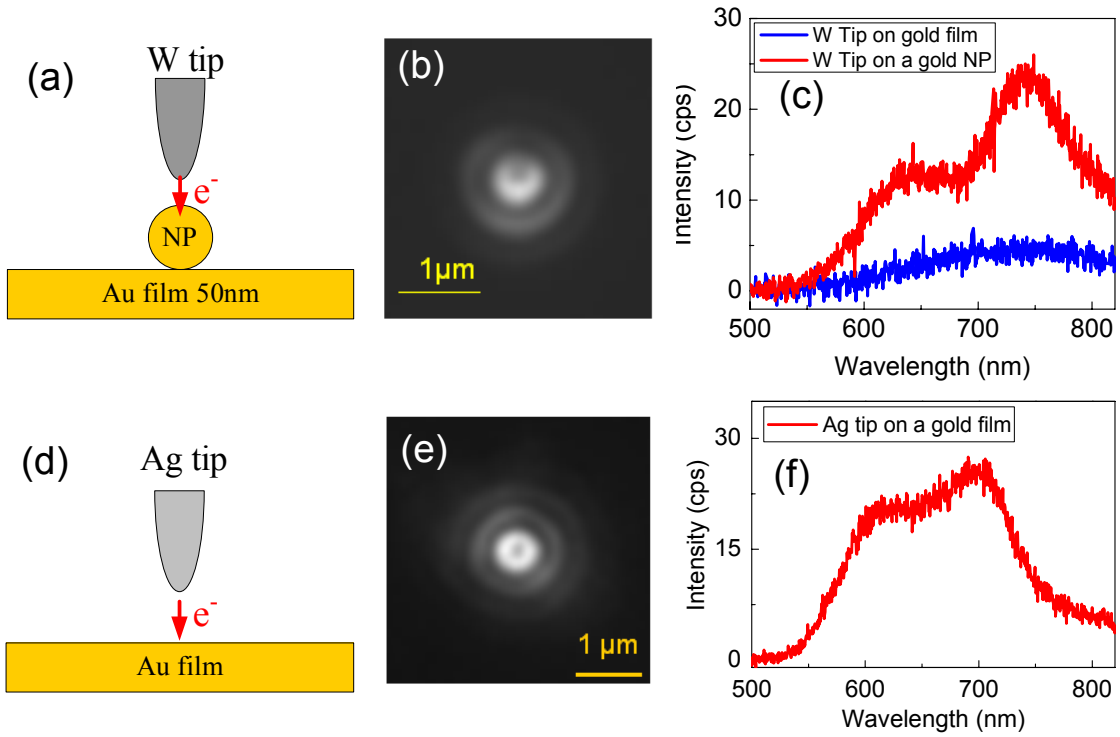

Figure C.1: (a) Schematic of the "W tip–gold nanoparticle–gold film" system. A W STM tip injects electrons into a gold nanoparticle which is deposited on a 50 nm thick gold film. (b) Real space image of the "W tip–gold nanoparticle–gold film" system. This image is recorded using an oil objective (NA=1.45). (c) Spectra resulting from a blunt W tip excitation of the gold film and of the gold nanoparticle which is deposited on the gold film.

Figure C.1(a) shows a schematic of the "W tip–gold nanoparticle–gold film" system. A blunt W tip is used to excite on the gold nanoparticle(NP) which is deposited on a

50 nm thick gold film. Figure C.1(b) shows the real space image of the "W tip–gold nanoparticle–gold film" system. In the center of the real space image, we see a "donut" shape pattern.

A similar donut shape central peak has already been discussed in section 4.3.2 for "Ag tip–gold film" system (presented again in figure C.1(e)). During STM excitation, the Ag tip is approximated as a polarizable sphere which induces a image dipole in the gold film (see Appendix A). The in-plane (parallel to the film) dipole moment of the image dipole is opposite to that of the Ag tip sphere, so that the effective dipole is normal to the surface which rises to a donut shape central peak pattern. From figure C.1(b) and figure C.1(e) we see that in real space "W tip–gold nanoparticle–gold film" system is similar to that of the "Ag tip–gold film" system.

Figure C.1(c) shows the spectra when the W tip excites the gold film directly as well as the gold film via the nanoparticle obtained using an air objective. When the W tip excites the gold film directly, there is only one peak in the spectrum associated to a "film-like" mode [106]. However, when the W tip excites the gold nanoparticle deposited on the gold film, there are two peaks associated to a low-energy "film-like" mode and a high energy "particle-like" mode. A similar phenomenon is seen in figure C.1(f) where we present the spectrum of a Ag tip on a gold film. The two-peaks spectrum in figure 3.6 is due to the local plasmonic resonance of "Ag tip–gold film" system. Similarly, the two peaks spectrum in figure C.1(c) indicates the local plasmonic resonance of "W tip–gold nanoparticle–gold film" system.

In both real space images and the spectra, there are similarities between the "W STM tip–gold nanoparticle–gold film" system and "Ag tip–gold film" system during the STM plasmonic excitation experiments. We thus say that a W tip combined with a gold nanoparticle is similar to a Ag tip during the STM plasmonic excitation experiments. Usually, the STM excitation of surface plasmons(both propagating and localized) with Ag tips is not so stable because the Ag tips are very soft and fragile. Thus, the "W tip–gold nanoparticle" system may substitute for a Ag tip for surface plasmon excitation because the "W tip–gold nanoparticle" system is more robust and stable than Ag tips.

Appendix D

Scattering of STM-excited SPP by a single gold nanoparticle: light confinement

To get more insight into the electromagnetic field confinement around the gold nanoparticle(NP), we zoom the real space image of the gold NP scattering for a tip-NP separation d= 6.9 μm as shown in figure D.1. Figure D.1 (b) is a zoomed region (blue square) of figure D.1(a). In figure D.1(b), the red square indicates the radiative emission of the gold NP and the canyon square indicates an intensity dip. The cross-sections along the tip-NP axis have been plotted for five tip-NP distances in figure D.2.

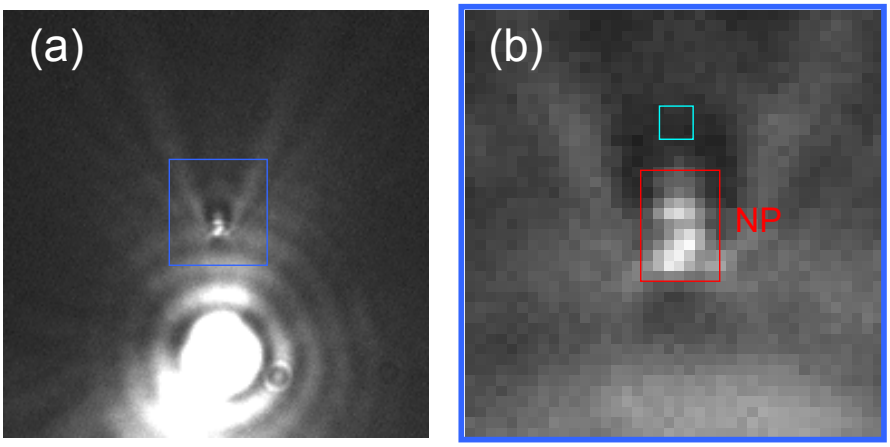

Figure D.1: Real space image of the gold nanoparticle scattering for a tip-NP separation d= 6.9 μm. (b) is a zoomed image of (a). The red square indicates the NP and the canyon square indicates an intensity dip.

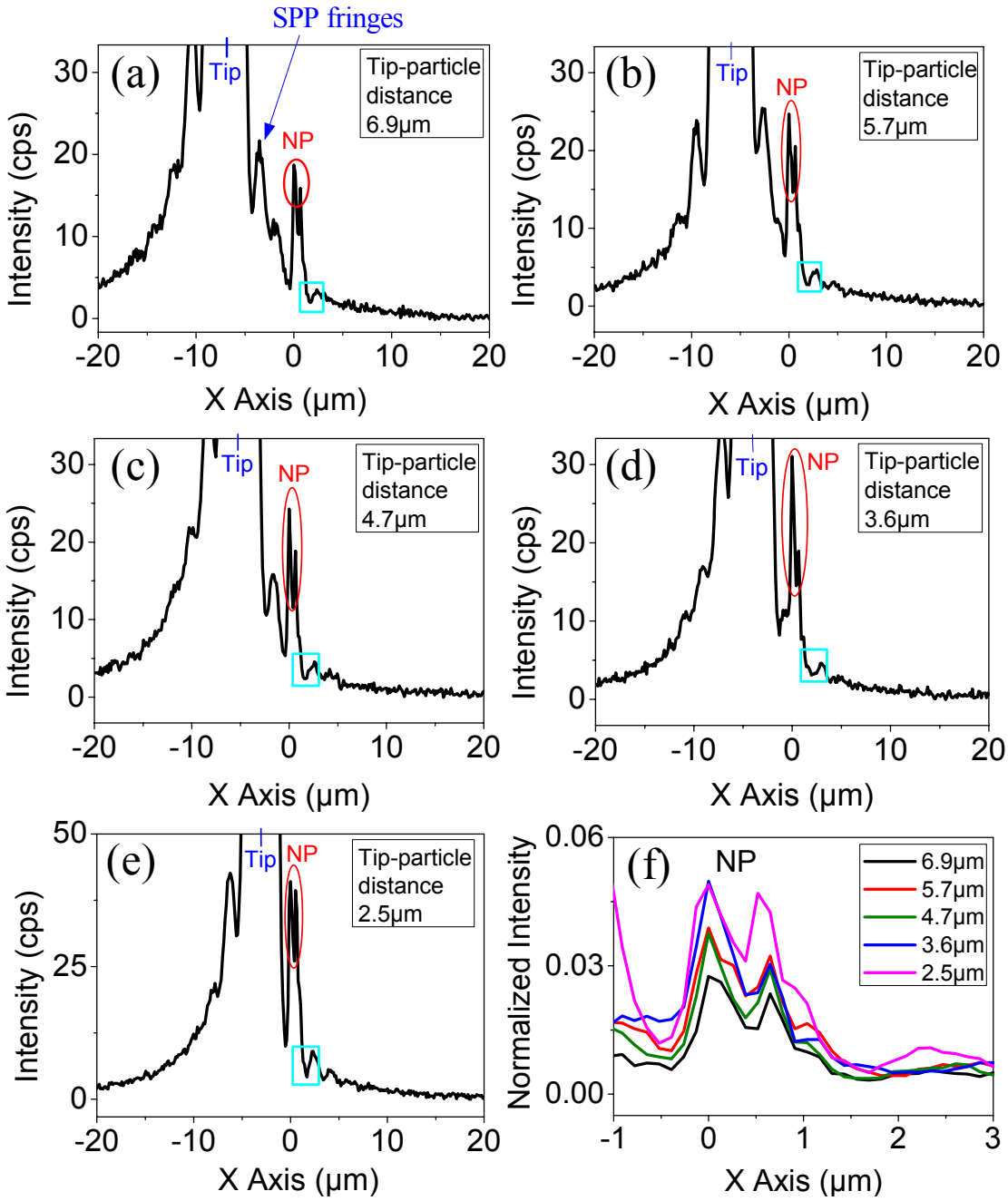

Figure D.2: Cross-sections of the real space images (see figure 6.6) along tip-NP axis. The NP is located at x=0. The tip-NP distance decreases from 6.9 μm (a) to 2.5 μm (e). A zoom view of the cross-sections in (a-e) at the NP position is shown in (f). The canyon squares in (a-e) are the intensity dip seen in the real space image.

In each image of figure D.2, the NP is located at x=0. The STM tip has five successive positions, so the tip–NP distance decreases from 6.9 μm (a) to 2.5 μm (e). Figure 6.6(f) shows a zoom view of cross-sections in (a-e) at the NP position. Note that each cross-section in figure 6.6(f) is normalized to the maximum intensity at the tip position.

Figure D.2 clearly shows that when the tip-NP distance decreases the intensity at the NP position increases. This is easy to understand because when the tip-NP distance

decreases the incident intensity on the NP increases and thus the radiative scattering of the NP increases.

Another interesting point is that in each of the cross-section there is a double-peak shape at the NP position. These double-peak shapes are very similar and with the same peak-to-peak distance $\sim$ 650 nm. Just aside to the double-peak shape

These double-peak shapes show the radiative scattering pattern of the gold NP along the tip-NP axis. Note that along the perpendicular direction of the tip-NP axis, we only see single peak at the NP position (see figure D.1(b)). These peak shapes are similar to the theoretically calculated scattering pattern of a surface protrusion in ref. [140]. The real space image (figure D.1) and the corresponding cross-sections (figure D.2) clearly show how the light field is confined by the gold NP.

List of Figures

List of Tables

Bibliography

[1] John Lambe and S. L. McCarthy. Light emission from inelastic electron tunneling. *Phys. Rev. Lett.*, 37:923–925, 1976.

[2] S. L. McCarthy and John Lambe. Enhancement of light emission from metalinsulatormetal tunnel junctions. *Applied Physics Letters*, 30:427, 1977.

[3] S. Ushioda, J. E. Rutledge, and R. M. Pierce. Prism-coupled light emission from tunnel junctions. *Phys. Rev. Lett.*, 54:224–226, Jan 1985.

[4] S. Ushioda, J. E. Rutledge, and R. M. Pierce. Theory of prism-coupled light emission from tunnel junctions. *Phys. Rev. B*, 34:6804–6812, Nov 1986.

[5] J.K. Gimzewski, B. Reihl, J.H. Coombs, and R.R. Schlittler. Photon emission with the scanning tunneling microscope. *Z. Phys.*, 72:497–501, 1988.

[6] J. K. Gimzewski, J. K. Sass, R. R. Schlitter, and J. Schott. Enhanced photon emission in scanning tunnelling microscopy. *Europhys. Lett.*, 8:435–440, 1989.

[7] Richard Berndt, James K. Gimzewski, and Peter Johansson. Inelastic tunneling excitation of tip-induced plasmon modes on noble-metal surfaces. *Phys. Rev. Lett.*, 67(27):3796–3799, Dec 1991.

[8] K. Takeuchi, Y. Uehara, S. Ushioda, and S. Morita. Prism coupled light emission from a scanning tunneling microscope. *Journal of Vacuum Science & Technology B*, 9:557–60, 1991.

[9] J U Ahamed, T Sanbongi, S Katano, and Y Uehara. Prism-coupled scanning tunneling microscope light emission spectroscopy of Au film covered with self-assembled alkanethiol monolayer. *Japan. J. Appl. Phys*, 49:08LB09, 2010.

[10] Frédéric Rossel, Marina Pivetta, and Wolf-Dieter Schneider. Luminescence experiments on supported molecules with the scanning tunneling microscope. *Surface Science Reports*, 65:129–144, 2010.

[11] X.H. Qiu, G.V. Nazin, and W. Ho. Visualization and spectroscopy of a metal-molecule-metal bridge. *Science*, 302:77–81, 2003.

[12] C. Chen, C. A. Bobisch, and W. Ho. Visualization of fermi's golden rule through imaging of light emission from atomic silver chains. *Science*, 325:981 – 985, 2009.

[13] W. L. Barnes, A. Dereux, and T. W. Ebbesen. Surface plasmon subwavelength optics. *Nature*, 424(6950):824–830, 2003.

[14] S. Lal, S. Link, and N. J. Halas. Nano-optics from sensing to waveguiding. *Nature Photonics*, 1:641–648, 2007.

[15] Jeffrey N. Anker, W. Paige Hall, Olga Lyandres, Nilam C. Shah, Jing Zhao, and Richard P. Van Duyne. Biosensing with plasmonic nanosensors. *Nature Materials*, 7:442–453, 2008.

[16] Harry A. Atwater and Albert Polman. Plasmonics for improved photovoltaic devices. *Nature Materials*, 9:205–213, 2008.

[17] S. Kawata, Y. Inouye, and P. Verma. Plasmonics for near-field nano-imaging and superlensing. *Nature Photonics*, 3(7):388–394, 2009.

[18] D. K. Gramotnev and S. I. Bozhevolnyi. Plasmonics beyond the diffraction limit. *Nature Photonics*, 4(2):83–91, 2010.

[19] Jon A. Schuller, Edward S. Barnard, Wenshan Cai, Young Chul Jun, Justin S. White, and Mark l. Brongersma. Plasmonics for extreme light concentration and manipulation. *Nature Materials*, 9:193–204, 2010.

[20] Pierre Berini and Israel De Leon. Surface plasmon-polariton amplifiers and lasers. *Nature Photonics*, 6:16–24, 2011.

[21] Suljo Linic, Phillip Christopher, and David B. Ingram. Plasmonic-metal nanostructures for efficient conversion of solar to chemical energy. *Nature Materials*, 10:911–921, 2011.

[22] B. Hecht, H. Bielefeldt, L. Novotny, Y. Inouye, and D. W. Pohl. Local excitation, scattering, and interference of surface plasmons. *Phys. Rev. Lett.*, 77(9):1889–1892, Aug 1996.

[23] C. Sönnichsen, A. C. Duch, G. Steininger, M. Koch, G. V Plessen, and J. Feldmann. Launching surface plasmons into nanoholes in metal films. *Appl. Phys. Lett.*, 76:140, 2000.

[24] S. A. Maier, P. G. Kik, H. A. Atwater, S. Meltzer, E. Harel, B. E. Koel, and A. A. G. Requicha. Local detection of electromagnetic energy transport below the diffraction limit in metal nanoparticle plasmon waveguides. *Nature Materials*, 2:229 – 232, 2003.

[25] M. Brun, A. Drezet, H. Mariette, N. Chevalier, J.C. Woehl, and S. Huant. Remote optical addressing of single nano-objects. *Europhys. Lett.*, 64:634, 2003.

[26] M. V. Bashevoy, F. Jonsson, A. V. Krasavin, N. I. Zheludev, Y. Chen, and M. I. Stockman. Generation of traveling surface plasmon waves by free-electron impact. *Nano Letters*, 6(6):1113–1115, 2006.

[27] J. T. van Wijngaarden, E. Verhagen, A. Polman, C. E. Ross, H. J. Lezec, and H. A. Atwater. Direct imaging of propagation and damping of near-resonance surface plasmon polaritons using cathodoluminescence spectroscopy. *Applied Physics Letters*, 88(22):221111, 2006.

[28] J. Nelayah, M. Kociak, O. Stéphan, F. J. García de Abajo, M. Tencé, L. Henrard, D. Tavernaand I. Pastoriza-Santos, L. M. Liz-Marzán, and C. Colliex. Mapping surface plasmons on a single metallic nanoparticle. *Nature Physics*, 3:348–353, 2007.

[29] W. Cai, R. Sainidou, J. J. Xu, A. Polman, and F. J. G. de Abajo. Efficient generation of propagating plasmons by electron beams. *Nano Letters*, 9(3):1176–1181, 2009.

[30] F. J. García de Abajo. Optical excitations in electron microscopy. *Reviews of Modern Physics*, 82:209–275, 2010.

[31] P. J. Schuck, D. P. Fromm, A. Sundaramurthy, G. S. Kino, and W. E. Moerner. Improving the mismatch between light and nanoscale objects with gold bowtie nanoantennas. *Phys. Rev. Lett.*, 94:017402, Jan 2005.

[32] Jean-Jacques Greffet. Nanoantennas for light emission. *Science*, 308:1561–1563, 2005.

[33] P. Mühlschlegel, H.-J. Eisler, O. J. F. Martin, B. Hecht, and D. W. Pohl. Resonant optical antennas. *Science*, 308:1607–1609, 2005.

[34] J. N. Farahani, D. W. Pohl, H.-J. Eisler, and B. Hecht. Single quantum dot coupled to a scanning optical antenna: A tunable superemitter. *Phys. Rev. Lett.*, 95:017402, Jun 2005.

[35] Lukas Novotny. Effective wavelength scaling for optical antennas. *Phys. Rev. Lett.*, 98:266802, Jun 2007.

[36] T. H. Taminiau, F. D. Stefani, F. B. Segerink, and N. F. van Hulst. Optical antennas direct single-molecule emission. *Nature Photonics*, 2:234–237, 2008.

[37] Jean-Jacques Greffet, Marine Laroche, and Fran çois Marquier. Impedance of a nanoantenna and a single quantum emitter. *Phys. Rev. Lett.*, 105:117701, Sep 2010.

[38] A. G. Curto, G. Volpe, T. H. Taminiau, M. P. Kreuzer, R. Quidant, and N. F. van Hulst. Unidirectional emission of a quantum dot coupled to a nanoantenna. *Science*, 329:930–933, 2010.

[39] Lukas Novotny and Niek van Hulst. Antennas for light. *Nature Photonics*, 5:83–90, 2011.

[40] Lukas Novotny and Bert Hecht. *Principles of nano-optics*. Cambridge University Press, 2006.

[41] Sergio G. Rodrigo, F. J. Garcia-Vidal, and L. Martin-Moreno. Influence of material properties on extraordinary optical transmission through hole arrays. *Phys. Rev. B*, 77:075401, Feb 2008.

[42] P. B. Johnson and R. W. Christy. Optical constants of the noble metals. *Phys. Rev. B*, 6:4370–4379, Dec 1972.

[43] Heinz Raether. *Surface Plasmons on Smooth and Rough Surfaces and on Gratings*. Springer-Verlag, 1988.

[44] A Drezet, A Hohenau, D Koller, A Stepanov, H Ditlbacher, B Steinberger, F.R Aussenegg, A Leitner, and J.R Krenn. Leakage radiation microscopy of surface plasmon polaritons. *Materials science and engineering: B*, 149(3):220–229, 2008.

[45] A. Drezet, A. Hohenau, J.R. Krenn, M. Brun, and S. Huant. Surface plasmon mediated near-field imaging and optical addressing in nanoscience. *Micron*, 38:427–437, 2006.

[46] John David Jackson. *Classical Electrodynamics*. 1998.

[47] M. Andreas Lieb, James M. Zavislan, and Lukas Novotny. Single-molecule orientations determined by direct emission pattern imaging. *JOSA B*, 21:1210–1215, 2004.

[48] B. C. Buchler, T. Kalkbrenner, C. Hettich, and V. Sandoghdar. Measuring the quantum efficiency of the optical emission of single radiating dipoles using a scanning mirror. *Phys. Rev. Lett.*, 95:063003, 2005.

[49] X. Brokmann, L. Coolen, M. Dahan, and J. P. Hermier. Measurement of the radiative and nonradiative decay rates of single CdSe nanocrystals through a controlled modification of their spontaneous emission. *Phys. Rev. Lett.*, 93:107403, 2004.

[50] G. Lévêque, O. J. F. Martin, and J. Weiner. Transient behavior of surface plasmon polaritons scattered at a subwavelength groove. *Phys. Rev. B*, 76:155418, 2007.

[51] Y. Alaverdyan, B. Sepúlveda, L. Eurenius, E. Olsson, and M. Käll. Optical antennas based on coupled nanoholes in thin metal films. *Nature Physics*, 3:884, 2007.

[52] Aitzol García-Etxarri, Isabel Romero, F. Javier García de Abajo, Rainer Hillenbrand, and Javier Aizpurua. Influence of the tip in near-field imaging of nanoparticle plasmonic modes: Weak and strong coupling regimes. *Phys. Rev. B*, 79:125439, 2009.

[53] Palash Bharadwaj, Alexandre Bouhelier, and Lukas Novotny. Electrical excitation of surface plasmons. *Phys. Rev. Lett.*, 106(22):226802, JUN 2 2011.

[54] W Lukosz and R E Kunz. Light emission by magnetic and electric dipoles close to a plane interface. i. total radiated power. *JOSA*, 67:1607–1615, 1977.

[55] W Lukosz and R E Kunz. Light emission by magnetic and electric dipoles close to a plane dielectric interface. ii. radiation patterns of perpendicular oriented dipoles. *JOSA*, 67:1615–1619, 1977.

[56] W Lukosz. Light emission by magnetic and electric dipoles close to a plane dielectric interface. iii. radiation patterns of dipoles with arbitrary orientation. *JOSA*, 69:1495–1503, 1979.

[57] Xavier Brokmann. *Propriétés de fluorescence de nanocristaux de CdSe individuels*. PhD thesis, LKB (Jussieu) - Laboratoire Kastler Brossel, l'Université Paris VI, 2004.

[58] Henk Arnoldus, F; Foley, and John T. Spatial separation of the traveling and evanescent parts of dipole radiation. *Optics Letters*, 28:1299, 2003.

[59] L Novotny, B Hecht, and D.W Pohl. Interference of locally excited surface plasmons. *Journal of Applied Physics*, 81(4):1798–1806, FEB 15 1997.

[60] Ignacy Gryczynski, Joanna Malicka, Zygmunt Gryczynski, and Joseph R. Lakowicz. Surface plasmon-coupled emission with gold films. *J. Phys. Chem. B*, 108:12568–12574, 2004.

[61] F. D. Stefani, K. Vasilev, N. Bocchio, N. Stoyanova, and M. Kreiter. Surface-plasmon-mediated single-molecule fluorescence through a thin metallic film. *Phys. Rev. Lett.*, 94:023005, 2005.

[62] Lieven Penninck, Saso Mladenowski, and Kristiaan Neyts. The effects of planar metallic interfaces on the radiation of nearby electrical dipoles. *Journal of Optics*, 12(7):075001, JUL 2010.

[63] A. Cuche, O. Mollet, A. Drezet, and S. Huant. "deterministic" quantum plasmonics. *Nano Letters*, 10(11):4566–4570, 2010.

[64] A. Drezet, A. Hohenau, A. L. Stepanov, H. Ditlbacher, B. Steinberger, N. Galler, F. R. Aussenegg, A. Leitner, and J. R. Krenn. How to erase surface plasmon fringes. *Applied Physics Letters*, 89(9):091117, 2006.

[65] http://www.horiba.com/scientific/products/optics-tutorial/diffraction-gratings/.

[66] Max Born and Emil Wolf. *Principles of optics*. Cambridge University Press, 1999.

[67] Eugene Hecht. *Optics (Fourth Edition)*. Addison Wesley, 2007.

[68] Luru Dai, Ingo Gregor, Iris von der Hocht, Thomas Ruckstuhl, and Jörg Enderlein. Measuring large numerical apertures by imaging the angular distribution of radiation of fluorescing molecules. *Optics Express*, 13:9409–9414, 2005.

[69] Harald Ditlbacher, Andreas Hohenau, Dieter Wagner, Uwe Kreibig, Michael Rogers, Ferdinand Hofer, Franz R. Aussenegg, and Joachim R. Krenn. Silver nanowires as surface plasmon resonators. *Phys. Rev. Lett.*, 95(25):257403, 2005.

[70] A. Bouhelier, Th. Huser, H. Tamaru, H.-J. Güntherodt, D. W. Pohl, Fadi I. Baida, and D. Van Labeke. Plasmon optics of structured silver films. *Phys. Rev. B*, 63(15):155404, Mar 2001.

[71] J. Grandidier, S. Massenot, G. Colas des Francs, A. Bouhelier, J.-C. Weeber, L. Markey, A. Dereux, J. Renger, M. U. González, and R. Quidant. Dielectric-loaded surface plasmon polariton waveguides: Figures of merit and mode characterization by image and Fourier plane leakage microscopy. *Phys. Rev. B*, 78(24):245419, Dec 2008.

[72] M. Lastapis, M. Martin, D. Riedel, L. Hellner, G. Comtet, and G. Dujardin. Picometer-scale electronic control of molecular dynamics inside a single molecule. *Science*, 308(5724):1000–1003, 2005.

[73] V. Sivel, R. Coratger, F. Ajustron, and J. Beauvillain. Control of photon emission by scanning tunneling microscopy in air. *Phys. Rev. B*, 50(8):5628–5634, Aug 1994.

[74] Ph. Dumas, C. Syrykh, I. V. Makarenko, and F. Salvan. STM-induced light emission of supported silver nanocrystallites. *Europhys. Lett.*, 40(4):447, 1997.

[75] Fabien Silly, Alexander O. Gusev, Abdelhafed Taleb, Fabrice Charra, and Marie-Paule Pileni. Coupled plasmon modes in an ordered hexagonal monolayer of metal nanoparticles: A direct observation. *Phys. Rev. Lett.*, 84(25):5840–5843, Jun 2000.

[76] Y. Uehara and S. Ushioda. Atomic-site-dependent light emission from $Au(110)-(2\times 1)$ surface induced by scanning tunneling microscope. *Phys. Rev. B*, 66(16):165420, Oct 2002.

[77] Karen Perronet, Luc Barbier, and Fabrice Charra. Influence of the Au(111) reconstruction on the light emission induced by a scanning tunneling microscope. *Phys. Rev. B*, 70(20):201405, Nov 2004.

[78] P Dawson and Michael G Boyle. Light emission from scanning tunnelling microscope on polycrystalline au films: what is happening at the single-grain level? *Journal of Optics A: Pure and Applied Optics*, 8(4):S219, 2006.

[79] D. G. Walmsley, T. S. Tan, and P. Dawson. Light emission from gold and silver thin films in a scanning tunneling microscope: role of contamination and interpretation of grain structure in photon maps. *Surface Science*, 572(2-3):497–520, 2004.

[80] M. Sakurai, C. Thirstrup, and M. Aono. New aspects of light emission from STM. *Applied Physics A-materials Science & Processing*, 80(6):1153–1160, 2005.

[81] M. J. Romero, J. van de Lagemaat, G. Rumbles, and M. M. Al-Jassim. Plasmon excitations in scanning tunneling microscopy: Simultaneous imaging of modes with different localizations coupled at the tip. *Applied Physics Letters*, 90(19):193109, 2007.

[82] Michael G Boyle, J Mitra, and Paul Dawson. The tip-sample water bridge and light emission from scanning tunnelling microscopy. *Nanotechnology*, 20(33):335202, 2009.

[83] Natalia L. Schneider, Guillaume Schull, and Richard Berndt. Optical probe of quantum shot-noise reduction at a single-atom contact. *Phys. Rev. Lett.*, 105(2):026601, Jul 2010.

[84] J U. Ahamed, T. Sanbongi, S. Katano, and Y. Uehara. Prism-coupled scanning tunneling microscope light emission spectroscopy of Au film covered with self-assembled alkanethiol monolayer. *Japan. J. Appl. Phys.*, 49:08LB09, 2010.

[85] S. Egusa, Y. H. Liau, and N. F. Scherer. Imaging scanning tunneling microscope-induced electroluminescence in plasmonic corrals. *Applied Physics Letters*, 84(8):1257–1259, 2004.

[86] M. Hu, A. Ghoshal, M. Marquez, and P. G. Kik. Single particle spectroscopy study of metal-film-induced tuning of silver nanoparticle plasmon resonances. *Journal of Physical Chemistry C*, 114(16):7509–7514, 2010.

[87] G. Baffou, A. J. Mayne, G. Comtet, and G. Dujardin. State selective electron transport through electronic surface states of 6H-SiC (0001)-3 x 3. *Phys. Rev. B*, 77(16):165320, 2008.

[88] Roman. Kiyan, Carsten. Reinhardt, Sven. Passinger, Andrei L. Stepanov, Andreas. Hohenau, Joachim R. Krenn, and Boris N. Chichkov. Rapid prototyping of optical components for surface plasmon polaritons. *Optics Express*, 15:4205–4215, 2007.

[89] S. Hell, G. Reiner, C. Cremer, and Ernst H. K. Stelzer. Aberrations in confocal fluorescence microscopy induced by mismatches in refractive index. *Journal of Microscopy*, 169:391–405, 1993.

[90] M. J. Booth and T. Wilson. Refractive-index-mismatch induced aberrations in single-photon and two-photon microscopy and the use of aberration correction. *Journal of Biomedical Optics*, 6(3):266–272, 2001.

[91] A. Hohenau. Private communications. 2011.

[92] Peter Johansson, R. Monreal, and Peter Apell. Theory for light emission from a scanning tunneling microscope. *Phys. Rev. B*, 42:9210–9213, Nov 1990.

[93] Peter Johansson. Light emission from a scanning tunneling microscope: Fully retarded calculation. *Phys. Rev. B*, 58:10823–10834, Oct 1998.

[94] J. Aizpurua, S. P. Apell, and R. Berndt. Role of tip shape in light emission from the scanning tunneling microscope. *Phys. Rev. B*, 62:2065–2073, Jul 2000.

[95] Y. Uehara, Y. Suda, S. Ushioda, and K. Takeuchi. Tip shape dependence of the light emission efficiency for the scanning tunneling microscope. *Applied Physics Letters*, 79:1718, 2001.

[96] Kazuyuki Meguro, Kenji Sakamoto, Ryuichi Arafune, Minoru Satoh, and Sukekatsu Ushioda. Origin of multiple peaks in the light emission spectra of a Au(111) surface induced by the scanning tunneling microscope. *Phys. Rev. B*, 65:165405, Apr 2002.

[97] Shiwei Wu and D. L. Mills. STM induced enhancement of dynamic dipole moments on crystal surfaces: Theory of the lateral resolution. *Phys. Rev. B*, 65:205420, 2002.

[98] Ping Chu and D. L. Mills. Plasmonic response of STM tips. *Phys. Rev. B*, 84:045430, Jul 2011.

[99] T Wang, E Boer-Duchemin, Y Zhang, G Comtet, and G Dujardin. Excitation of propagating surface plasmons with a scanning tunnelling microscope. *Nanotechnology*, 22:175201, 2011.

[100] A. Hohenau, J. R. Krenn, A. Drezet, O. Mollet, S. Huant, C. Genet, B. Stein, and T. W. Ebbesen. Surface plasmon leakage radiation microscopy at the diffraction limit. *Optics Express,*, 19:25749–25762, 2011.

[101] DT Pierce, A Davies, JA Stroscio, and RJ Celotta. Polarized light emission from the metal-metal STM junction. *Appl. Phys. A*, 66(Part 1, S):S403–S406, MAR 1998.

[102] Jack J. Mock, Ryan T. Hill, Aloyse Degiron, Stefan Zauscher, Ashutosh Chilkoti, and David R. Smith. Distance-dependent plasmon resonant coupling between a gold nanoparticle and gold film. *Nano Letters*, 8:2245–2252, 2008.

[103] Shiuan-Yeh Chen, Jack J Mock, Ryan T Hill, Ashutosh Chilkoti, David R Smith, and Anne A Lazarides. Gold nanoparticles on polarizable surfaces as raman scattering antennas. *ACS Nano*, 4:6535–6546, 2010.

[104] N. Yamamoto, S. Ohtani, and F. J. García de Abajo. Gap and mie plasmons in individual silver nanospheres near a silver surface. *Nano Letters*, 11:91–95, 2011.

[105] Henk F. Arnoldus. Reflection and refraction of multipole radiation by an interface. *J. Opt. Soc. Am. A*, 22:190–198, 2005.

[106] Vladimir D. Miljkovic, Timur Shegai, Mikael Käll, and Peter Johansson. Mode-specific directional emission from hybridized particle-on-a-film plasmons. *Optics Express*, 19:12856–12864, 2011.

[107] Z. C. Dong, X. L. Zhang, H. Y. Gao, Y. Luo, C. Zhang, L. G. Chen, R. Zhang, X. Tao, Y. Zhang, J. L. Yang, and J. G. Hou. Generation of molecular hot electroluminescence by resonant nanocavity plasmons. *Nature Photonics*, 4:50–54, 2010.

[108] R. Marty, A. Girard, C.and Arbouet, and G. C. des Francs. Near-field coupling of a point like dipolar source with a thin metallic film: Implication for STM plasmon excitations. *Chemical Physics Letters*, 532:100–105, 2012.

[109] H. F. Schouten, N. Kuzmin, G. Dubois, T. D. Visser, G. Gbur, P. F. A. Alkemade, H. Blok, G. W. 't Hooft, D. Lenstra, and E. R. Eliel. Plasmon-assisted two-slit transmission: Young's experiment revisited. *Phys. Rev. Lett.*, 94:053901, 2005.

[110] G. Gay, O. Alloschery, B. Viaris de Lesegno, J. Weiner, and H. J. Lezec. Surface wave generation and propagation on metallic subwavelength structures measured by far-field interferometry. *Phys. Rev. Lett.*, 96:213901, Jun 2006.

[111] Leonard Mandel and Emil Wolf. *Optical Coherence and Quantum optics*. Cambridge University Press, 1996.

[112] Aurélien Drezet. Private communication.

[113] I A Vartanyants, A P Mancuso, A Singer, O M Yefanov, and J Gulden. Coherence measurements and coherent diffractive imaging at flash. *J. Phys. B: At. Mol. Opt. Phys.*, 43:194016, 2010.

[114] Maurice Françon. *Diffraction: coherence in optics*. Pergamon Press, 1966.

[115] Ludovic Douillard and Fabrice Charra. High-resolution mapping of plasmonic modes: photoemission and scanning tunnelling luminescence microscopies. *J. Phys. D: Appl. Phys.*, 44:464002, 2011.

[116] Natalia L. Schneider, Guillaume Schull, and Richard Berndt. Optical probe of quantum shot-noise reduction at a single-atom contact. *Phys. Rev. L*, 105:026601, 2010.

[117] H Ditlbacher, JR Krenn, N Felidj, B Lamprecht, G Schider, M Salerno, A Leitner, and FR Aussenegg. Fluorescence imaging of surface plasmon fields. *Applied Physics Letters*, 80(3):404–406, JAN 21 2002.

[118] JC Weeber, Y Lacroute, A Dereux, E Devaux, T Ebbesen, C Girard, MU Gonzalez, and AL Baudrion. Near-field characterization of bragg mirrors engraved in surface plasmon waveguides. *Phys. Rev. B*, 70(23):235406, DEC 2004.

[119] M. U. González, J.-C. Weeber, A.-L. Baudrion, A. Dereux, A. L. Stepanov, J. R. Krenn, E. Devaux, and T. W. Ebbesen. Design, near-field characterization, and modeling of 45° surface-plasmon bragg mirrors. *Phys. Rev. B*, 73:155416, 2006.

[120] I. P. Radko, S. I. Bozhevolnyi, G. Brucoli, L Martin-Moreno, F J Garcia-Vidal, and A. Boltasseva. Efficiency of local surface plasmon polariton excitation on ridges. *Phys. Rev. B*, 78:115115, Sep 2008.

[121] I P Radko, S I Bozhevolnyi, G Brucoli, L Martin-Moreno, F J Garcia-Vidal, and A Boltasseva. Efficient unidirectional ridge excitation of surface plasmons. *Optics Express*, 17:7228, 2009.

[122] Igor I. Smolyaninov, David L. Mazzoni, Joseph Mait, and Christopher C. Davis. Experimental study of surface-plasmon scattering by individual surface defects. *Phys. Rev. B*, 56:1601–1611, Jul 1997.

[123] J. R. Krenn, H Ditlbacher, G Schider, A Hohenau, A Leitner, and F. R. Aussenegg. Surface plasmon micro- and nano-optics. *J.Microscopy*, 209:167–172, 2003.

[124] A.L. Stepanov, J.R. Krenn, H. Ditlbacher, A. Hohenau, A. Drezet, B. Steinberger, A. Leitner, and F.R. Aussenegg. Quantitative analysis of surface plasmon interaction with silver nanoparticles. *Optics Letters*, 30:1524, 2005.

[125] Sergey I. Bozhevolnyi, John Erland, Kristjan Leosson, Peter M.W. Skovgaard, and Jørn M. Hvam. Waveguiding in surface plasmon polariton band gap structures. *Phys. Rev. Lett.*, 86:3008, 2001.

[126] Sergey I. Bozhevolnyi, Valentyn S. Volkov, Kristjan Leosson, and Alexandra Boltasseva. Bend loss in surface plasmon polariton band-gap structures. *Applied Physics Letters*, 79:1076, 2001.

[127] Sergey I. Bozhevolnyi and Valentyn S. Volkov. Multiple-scattering dipole approach to modeling of surface plasmon polariton band gap structures. *Optics Communications*, 198:241–245, 2001.

[128] T. Søndergaard and S. I. Bozhevolnyi. Vectorial model for multiple scattering by surface nanoparticles via surface polariton-to-polariton interactions. *Phys. Rev. B*, 67:165405, 2003.

[129] Thomas Søndergaard and Sergey I. Bozhevolnyi. Theoretical analysis of finite-size surface plasmon polariton band-gap structures. *Phys. Rev. B*, 71:125429, 2005.

[130] Ilya P Radko, Thomas Søndergaard, and Sergey I Bozhevolnyi. Adiabatic bends in surface plasmon polariton band gap structures. *Optics Express*, 14:4107, 2006.

[131] A.-L. Baudrion, J.-C. Weeber, A. Dereux, G. Lecamp, P. Lalanne, and S. I. Bozhevolnyi. Influence of the filling factor on the spectral properties of plasmonic crystals. *Phys. Rev. B*, 74:125406, 2006.

[132] Sergey I. Bozhevolnyi and Victor Coello. Elastic scattering of surface plasmon polaritons: Modeling and experiment. *Phys. Rev. B*, 58:10899–10910, 1998.

[133] W. Abidi, B. Pansu, R. Krishnaswamy, P. Beaunier, H. Remita, and M. Imperor-Clerc. Gold nanoparticles confined in lamellar mesophases. *RSC Advances*, 1:434–439, 2011.

[134] Sergey I. Bozhevolnyi, Igor I. Smolyaninov, and Anatoly V. Zayats. Near-field microscopy of surface-plasmon polaritons: Localization and internal interface imaging. *Phys. Rev. B*, 51:17916–17924, Jun 1995.

[135] A. V. Shchegrov, I. V. Novikov, and A. A. Maradudin. Scattering of surface plasmon polaritons by a circularly symmetric surface defect. *Phys. Rev. Lett.*, 78:4269–4272, 1997.

[136] A. B. Evlyukhin and S. I. Bozhevolnyi. Point-dipole approximation for surface plasmon polariton scattering: Implications and limitations. *Phys. Rev. B*, 71:134304, 2005.

[137] Jeppe Morch Norgaard and Rene Petersen. Scattering of surface plasmon polaritons by gold nanoparticles. Master's thesis, Institute of Physics and Nanotechnology, Aalborg University, Denmark, 2007.

[138] Bernhard Knoll and Fritz Keilmann. Enhanced dielectric contrast in scattering-type scanning near-field optical microscopy. *Optics Communications*, 182:321–328, 2000.

[139] R. Hillenbrand, T. Taubner, and F. Keilmann. Phonon-enhanced light-matter interaction at the nanometre scale. *Nature*, 418:159–162, 2002.

[140] Christian Girard, Alain Dereux, Olivier J. F. Martin, and Michel Devel. Generation of optical standing waves around mesoscopic surface structures: Scattering and light confinement. *Phys. Rev. B*, 52:2889–2898, Jul 1995.